THE CREEP CRACK GROWTH OF T92 AND A NEW HEAT-RESISTANT STEEL BG12CR

Ke Liu

A thesis submitted to The University of Birmingham

for the degree of

Doctor of Philosophy

School of Metallurgy and Materials

College of Engineering and Physical Science

The University of Birmingham

March 2025

Synopsis

The increasing global demand for electricity encourages improvements in the efficiency of fossil fuel-fired power plants to reduce CO_2 emissions and conserve resources. A promising strategy to enhance efficiency is by increasing steam temperatures in ultra-supercritical power plants. However, this demands materials with superior creep resistance, thermal stability, corrosion resistance and low cost. T/P92 martensitic heat-resistant steels have been widely used in power plants up to 620℃, but they have limitations in corrosion resistance at higher temperatures such as 650℃.To address this, a new 12Cr martensitic heat-resistant steel, BG12Cr, has been developed, which offers enhanced corrosion resistance and thermal stability for long-term operation at high steam temperatures and pressures. In addition to creep strength, creep crack growth resistance is crucial for the material's longevity in real-world applications under creep conditions. This study aims to examine the creep crack growth resistance of BG12Cr and T92 at various temperatures (600°C, 650°C, and 700°C) and loadings (3 kN, 6 kN, and 10 kN) and research the creep crack growth mechanisms of them. Fracture surface and cross-sectional observations further help the understanding of the creep crack growth mechanism.

To support research on crack growth resistance, this study conducts an in-depth microstructural investigation of both BG12Cr and T92 steels. Optical microscopy, scanning electron microscopy (SEM), transmission electron microscopy (TEM), and energy-dispersive X-ray spectroscopy (EDX) on as-received, heat-treated, and post-test specimens were used in this study. In the as-received BG12Cr, tempered martensite with minor amounts of δ-ferrite was observed. Additionally, $M_{23}C_6$ carbide type which is mainly (Cr, Mo, W)-rich carbides and fine

MX type of (Nb, V)(C, N) and V(C, N) carbon nitrides were found located on the prior austenite grain boundaries, martensite colony boundaries and lath boundaries. Notably, a significant number of Cu particles (20-30nm in size) were discovered within the martensite lath. And in the as-received T92, the main particles at the lath boundaries and prior austenite grain boundaries are $M_{23}C_6$ carbides ((Cr, Mo, W)-rich carbides), (Nb, V)(C, N), V(C, N) and Ti-rich carbides and some $(Fe, Cr)_2(Mo, W)$ Laves phases were also found at prior austenite grain boundaries.

In the post-test specimens, abnormal acceleration in microstructure degradation was observed adjacent to crack faces. This area showed not only a higher density of precipitates than regions farther from the crack but also a new type of precipitate, Z Phase, not present in the as-received specimens. This acceleration is attributed to stressing and oxidation-induced Cr outward diffusion. Hardness tests conducted on heat-treated specimens showed that BG12Cr had higher hardness values than T92 across all conditions, which can be attributed to its higher content of Cr and Co, a greater number of Cu particles, and finer lath width. Moreover, hardness decreased with increasing temperature and time in both materials, indicating coarsening of precipitates.

Creep crack growth tests were conducted on compact tension (CT) specimens at temperatures of 600°C, 650°C, and 700°C, with stable loadings of 3 kN, 6 kN, and 10 kN over a test period ranging from 158 to 2587 hours. The resistance to creep crack growth was evaluated using two parameters: one from linear elastic fracture mechanics (LEFM), K_n, and another from elastic-plastic time-dependent fracture mechanics, denoted as C*. Although C* correlated well with the crack growth rate, it was not sufficiently sensitive to distinguish the crack growth resistance of BG12Cr and T92. This is due to similar da/dt - C* slopes observed in both steels under

equivalent loading conditions. On the other hand, Kn, though not as closely correlated with crack growth rate, provided a more straightforward comparison of material performance under identical conditions and specimen geometry. Overall, BG12Cr displayed better creep crack growth resistance than T92 under investigated test conditions within 2587h, except under loading of 10kN at 600°C.

Based on observations of the fracture surfaces and cross-sections of post-test specimens, the mechanism of creep crack growth is characterized by the formation and growth of microvoids, as well as their subsequent linking and coalescence. These processes are accelerated by elevated temperatures and stress conditions. In T92 steel, microvoids primarily form and grow at the triple points of prior austenite grains. In BG12Cr, microvoids tend to form both at these triple points and along the boundaries of the prior austenite grains. However, compared to T92, the void density is lower, and the growth of coalescences is slower, which contributes to its better creep crack growth resistance.

Acknowledgements

First and foremost, I would like to extend my deepest gratitude to Professor Paul Bowen for his invaluable guidance and for introducing me to the scholarship opportunity that made this project possible. I also want to thank my another supervisor, Dr. Hangyue Li, for her patient teaching and consistent guidance.

I would like to express my sincere thanks to BaoWu Steel for generously providing both funding and the necessary materials for this study.

Special acknowledgement goes to Dr. Suyang Yu for his expert advice on testing methodologies, and to Dr. Rengen Ding for his major contribution in conducting the TEM analysis for this study. I am also grateful to Mr. David Price for the technical support that greatly facilitated my lab work.

On a personal note, I wish to thank my father, Shaomin Liu, for his unceasing encouragement and emotional support. Equal thanks go to my mother, Chi Huang, whose unwavering belief in me relieved much of the pressure I faced.

Lastly, I extend my heartfelt thanks to Dr. Zeyu Jiang, Enbang Ti and Xuan Huang for their companionship, encouragement and emotional support during the darkest periods of my life have meant the world to me.

Contents

Abbreviation	Definition
A-USC	Advanced Ultra-Supercritical
BF	Bright Field
CMOD	Crack Mouth Opening Displacement
CCG	Creep Crack Growth
CT	Compact Tension
DBTT	Ductile-Brittle Transition Temperature
d.c.p.d	Direct Current Potential Drop
EDX	Energy-Dispersive X-ray Spectroscopy
fcc	Face-Centred Cubic
HAADF	High Angle Annular Dark Field
IG	Intergranular Failure
LEFM	Linear Elastic Fracture Mechanics
PAG	Prior Austenite Grain
PAGB	Prior Austenite Grain Boundaries
SAD	Selected Area Diffraction Pattern
SEM	Scanning Electron Microscopy
STEM	Scanning Transmission Electron Microscopy
TEM	Transmission Electron Microscopy

CHAPTER 1 Introduction

Introduction of T92 and BG12Cr

The global demand for electricity is growing rapidly every year, and although most countries are developing and investing huge amounts of money in renewable energy, the predominant resource for electricity generation is still coal, which accounts for 35% of the world's electricity and nearly 61% in China in 2024 (1). Improving the efficiency of fossil fuel-fired power plants is still crucial to reducing CO_2 emissions, conserving non-renewable fossil fuel resources and reducing costs. The best and most economical way to do this is to raise the steam temperature. The ultra-supercritical power plant operates at 650℃ and a pressure of 26 MPa, which can increase the efficiency to almost 50%. The harsher environment for the material requires better creep resistance, thermal stability and corrosion resistance.

T/P92, the martensitic heat-resistant steel developed by Nippon Steel Corporation from T/P91, is widely used in fossil fuel-fired power plants for manufacturing steam pipes. T/P92 has better creep rupture strength than T/P91 due to the addition of W and B, which allows T/P92 to operate at higher steam temperatures. The working temperature limit for T/P92 is 625℃, as the corrosion resistance is not sufficient for higher temperatures, but the steam temperature of a USC power plant is 650℃. For better corrosion resistance, a relatively higher Cr content is required. To meet the requirements of the USC power plant, a new 12Cr martensitic heat-resistant steel, BG12Cr, was developed by BaoWu Steel Company. Compared to T/P92, BG12Cr contains more Cr for better corrosion resistance, more Co for better strength and thermal stability, and the addition of Cu for microstructure strengthening.

For the long-term operation of the power plant at high steam temperature and pressure, creep strength is another key property. However, the crack initiation could occur from the microstructural defects or overheated region of the large practical components, so the creep crack growth resistance is also an important property for the material working in the creep condition.

The objective of this project

The objectives of this project are to investigate the creep crack growth behaviour and mechanism of BG12Cr and T92, and to evaluate and compare the creep crack resistance of BG12Cr at different temperatures with T92. As a newly developed material, the microstructure of BG12Cr has been studied to better understand its strengthening mechanisms and thermal stability. The microstructural changes in both BG12Cr and T92 during the creep crack growth tests were also analyzed.

The work involved in the project

Optical microscopy, SEM and TEM observation, along with EDX analysis has been carried out on T92 and BG12Cr steels in 3 stages: in as-received conditions, after various heat-treated treatments and after creep crack growth tests, to characterize their microstructures.

Creep crack tests were conducted on two types of heat-resistant martensitic steels, T92 and BG12Cr, under three different temperature conditions: 600℃ (the working temperature of T92), 650℃ (the target working temperature of BG12Cr), and 700℃ (representing the temperature in overheated regions). The tests were performed with three different loadings: 3 kN, 6 kN, and 10 kN. Observations on the fracture surface and cross-section of specimens after creep crack growth to evaluate the creep crack growth mechanism of BG12Cr and T92.

Evaluate the different growth behaviour of crack growth and crack mouth opening displacement during the creep crack growth test of BG12Cr and T92. Compare the crack growth resistance between BG12Cr and T92 with K_n and C* under creep conditions.

To obtain the creep crack growth data and C*-da/dt curves for predicting the remaining life of BG12Cr and T92.

CHAPTER 2 Literature Review

2.1 The development of fossil-fueled power plant

The origins of coal-fired electricity generation can be linked to 1866 when Werner von Siemens introduced the first dynamo specifically designed for power production. Then the first central power plant which used low-pressure saturated or slightly superheated steam was built by Thomas Edison in 1882. In 1884, the initial steam turbine generator was engineered by Sir Charles Parsons, with a thermal efficiency of 1.6% (2). From 1910 to 1980, steam pressure in fossil-fuel power plants increased from 4 MPa to 31 MPa, and steam temperature rose from 370 °C to 621 °C, resulting in an improvement in thermal efficiency from approximately 15% to 40%. Figure 2. 1 shows this development for US turbine generators (3). In the US, the thermal efficiency of power plants improved to around 15% in the 1920s. These power plants operated at a steam pressure of 4 MPa and a temperature of 370℃, limitations dictated by the use of carbon steel. The addition of Mo in steel has enhanced the operating conditions in power plants, increasing the steam pressure to 10 MPa and the steam temperature to 480℃. In the 1950s, the CrMo steel was developed for the construction of power plants that operated at a higher steam pressure and temperature than before which were 17 MPa and 566℃, respectively (3). The first commercial supercritical steam power unit, Philo 6, was constructed in 1957. It operated at 31 MPa and 621℃/566℃/538℃, respectively, achieving a thermal efficiency of around 40%. Steam enters a supercritical phase when it exceeds the critical point of water, set at 22.1 MPa and 374°C (4). The operating conditions for supercritical power plants typically involve a steam pressure of around 22-24 MPa and a steam temperature of approximately 597℃. These plants could achieve an efficiency of up to 45% (5). However, due to material limitations, although

Philo 6 reached a steam pressure of 31 MPa, most subsequent power plants reduced the operating steam pressure and temperature to 24 MPa and 538°C. For example, John E. Amos Unit 2, built in 1972 in Saint Albans, USA, operated at 538°C with double reheat temperatures of 552°C and 565°C under a steam pressure of 24 MPa, achieving a thermal efficiency of 39.4% (6). From the 1960s for over two decades, steam conditions remained stable at either a pressure of 24 MPa and a temperature of 538°C or a pressure of 19MPa and a temperature of 566°C, due to the development of nuclear power plants and the electricity demand shifted (3). However, the increasing demand, rising fuel costs and the global urgency to minimize CO_2 emissions drove the development of power plant technology, leading to increases in steam pressure and temperature (7). With advancements in materials, Denmark constructed one of the world's most efficient ultra-supercritical coal-fired power plants, operating at 580°C/580°C/580°C under 29 MPa and achieving 47.0% efficiency. In China, the Huaneng Yuhuan Power Plant, commissioned in 2006, became the country's first ultra-supercritical coal-fired power plant, operating at 600°C/600°C/600°C with 26.2 MPa and delivering a net efficiency of 45.2% (8). In 2021, China built the highest-efficiency coal-fired power plant to date, Pingshan Phase II, which operates at 610°C/630°C/630°C with 31 MPa of pressure and achieves a net efficiency of 49.4% (9). Figure 2. 2 shows the development trend in China. Advanced Ultra-Supercritical (A-USC) power plants were designed to achieve higher efficiency, characterized by a main steam pressure exceeding 26 MPa and a main steam temperature surpassing 700°C. These plants are nearing a thermal efficiency of 50% (5).

2.2 Heat-resistant martensitic steel

Compared to austenitic steel and nickel-based alloys, martensitic steel offers smaller thermal expansion, greater conductivity, and lower costs, making it well-suited as a material for heavy

components in power plants (10).

2.2.1 History of Heat-resistant martensitic steel

At the beginning of the 20th century, hot tensile tests were utilized to assess the properties of materials used in high-temperature, high-pressure steam environments. During this period, the maximum steam temperature and pressure reached 350°C and 1.5 MPa, respectively, and the materials used were primarily non-alloyed carbon steels. However, hot tensile tests were of limited duration and could not accurately determine long-term strength under high-temperature conditions. Additionally, the impact and importance of alloying elements like N, Al and Mn were not well-understood during this period (10).

Beginning in the early 1920s, the development of low-alloyed steels with enhanced heat-resistant properties was accelerated due to the operational needs of power plants, which were running at 450°C and 3.5 MPa (10). Molybdenum (Mo) was found to significantly improve high-temperature strength; the 10^5 hours creep strength of 0.15%C-0.3Mo steel reached 260 MPa at 450°C, up from 70 MPa for unalloyed 0.15%C steel. The increase in strength is contributed by the solution hardening and precipitation of Mo_2C. However, when the Mo content exceeded approximately 0.35%, the precipitation of graphite led to a reduction in ductility under creep stress conditions. Fabritius conducted further research on the influence of Mo and chromium (Cr) in steels like 0.13%C-0.3%Mo, 0.13%C-1%Cr-0.5%Mo, and 0.13%C-2.25%Cr-1%Mo. His studies showed that 1%Cr achieved the highest creep strength at 500°C. Increasing the content of Mo and Cr in the case of 0.13%C-2.25%Cr-1%Mo steel further boosted the creep rupture strength at 550°C (11). Vanadium (V) was also examined; 0.14%C-0.6%Mo-0.3%V steel exhibited higher creep-rupture strength than 0.13%C-2.25%Cr-1%Mo

steel (12). Japan developed an improved weldable low-alloy steel known as HCM2S (0.06%C-2.25%Cr-2%Mo-1.6%W-0.25%V-0.05%Nb-0.02%N-0.003%B), which was easy to weld and the post-weld treatment was not required. It exhibited higher creep rupture strength than both 0.15%C-0.5%Mo and 0.13%C-1%C-0.5%Mo steels (10)(13).

In the 1950s, steam temperatures increased from 538℃ to 566℃, and by the 1980s, supercritical technology in power plants was developed, requiring temperatures of 600-650℃ and supercritical pressures ranging from 22.1 MPa to 35 MPa. To meet the demands of power plants operating at these elevated temperatures and pressures, 9-12% Cr steels were developed starting in the 1980s. The United States, Japan, and Europe have each initiated specific projects to further the development of these 9-12% Cr steels (10), as shown in Figure 2. 3. Figure 2. 4 illustrates the historical progression and 10^5 hours creep rupture strength of high-chromium steels developed between 1950 and 1995 (10).

In the 1950s, the alloy X22CrMoV was developed, benefiting from solution hardening and $M_{23}C_6$ precipitates for enhanced strength and it was employed in power plants for several decades. UK developed H46 and FV448, and France developed 56T5 which were strengthened by the addition of 0.30-0.45% Nb to form MX precipitations including VN and Nb(C, N), but the significant improvement in creep strength was only in a short-term period at 600℃ due to Nb content caused serious segregations in thick-walled components (10). Japan developed TAF from European Nb alloyed steels with an addition of up to 0.040% boron, the $M_{23}C_6$ carbides can be stabilised by boron with the formation of $M_{23}(C, B)_6$ (14). A USA company, General Electric Company, developed a rotor steel 11%CrMoVNbN with a lower content of Nb to 0.08% to avoid the segregation of a rotor. The published rupture strength of this steel is 85-90 MPa at

600°C for 10^5 hours (15).

In the late 1970s, the United States introduced a newer generation of 9-12% Cr steel, mod.9Cr1Mo (P91). With a lower carbon content of 0.10% and only 9% Cr, P91 boasts a creep strength of 94 MPa for 10^5 hours at 600°C. This material is now commonly used in new Japanese and European power plants (16).

In the mid-1980s, Japan developed a new 12% Cr steel, HCM12 (0.10%C-1%Mo-1%W-0.25%V-0.05%Nb-0.03%N), characterized by a unique duplex structure of delta-ferrite and tempered martensite, strengthened by fine VN nitrides. The relatively high Cr content (12%) contributed to the good corrosion resistance of this steel (13).

Under the European cooperation programme COST501, several advanced steels were developed including X18CrMoVNbB 91, X12CrMoWVNbN and E911. X18CrMoVNbB 91 was a 9% CrMoVNb steel, originating from the TAF steel but with a lower content of Cr, Nb, and B for manufacturing the large components. Creep tests conducted on 900 mm diameter pilot rotors showed results consistent with those on 600 mm diameter rotors, demonstrating a creep strength of approximately 120 MPa at 600°C. X12CrMoWVNbN has a lower creep strength of around 90 MPa. Its composition includes 12% Cr, 0.06% B, 1% Mo, and 0.8% W (10). E911 contains 9% Cr and has reduced Ni content. It has an estimated creep rupture strength of 98MPa for 10^5 hours at 600°C (17).

In the 1980s, the P92 and P122 were developed by Japan. The P92 has an estimated creep rupture strength of 113MPa for 10^5h at 600°C with alloy content of 0.10%C-1.8%W-0.5%Mo-0.2%V-0.06%Nb-0.05%N-0.003%B after tempered at 750°C (18). P122 has a higher Cr content of 11% and an addition of 1% Cu for reducing the formation of delta-ferrite and an estimated

creep rupture strength of 101MPa for 10^5h at 600°C(19,20). The P92, P122 and E911 have now served in new advanced steam power plants for decades years (10).

To expand the working temperature from up to 620℃ to 650℃, new 9-12%Cr steel needs to be developed. The goal is to achieve a creep strength of 100 MPa for 10^5 hours. An alloy with 11% Cr content is targeted as it offers dependable oxidation resistance (10).

One noteworthy steel is VM12, with a composition of 11.5% Cr, 1.5% W, 1.62% Co, 0.29% Mo, and 0.115% C. When compared to E911, VM12 exhibited similar rupture strength in creep tests lasting less than 15,000 hours at 625°C. However, at creep stresses below 85 MPa and longer testing durations, the rupture life of VM12 became shorter than that of E911 under the same stress conditions. The decrease in creep rupture life was due to the formation of the Z phase in VM12 (21,22).

2.2.2 The role of alloy chemical composition

The chemical composition fundamentally determines microstructural stability, creep resistance, and degradation behaviour at elevated temperatures. Therefore, alloying design is critical for steels intended for advanced power plant use. Figure 2. 5 illustrates the alloy design strategy for high-Cr ferritic steels developed by NIMS for 650°C applications, including the roles of individual elements (10).

(a) C

Carbon (C) is the necessary element to form the martensitic microstructure in rapid cooling after normalizing. C is an interstitial solid solution element that can increase the hardenability of steel but the weldability of high-content C steel is poor. The relatively low solubility of C in the ferrite compared to austenite caused the C atom precipitation from the matrix to form

carbide with other elements, such as Cr to form $Cr_{23}C_6$ during the tempering process (23). Taneike et al. (24) prepared six 9Cr-3W-3Co-0.05N-0.007B steel with different C content to investigate the C content effect on the $M_{23}C_6$ and MX precipitation behaviour after heat treatment, the amount of $M_{23}C_6$ was increased with C content but the amount of MX is not influenced significantly by the C content. Also, the distribution of $M_{23}C_6$ and MX is changed with C content, almost no $M_{23}C_6$ in the steel with 0.002% C and instead, the MX carbonitride is sited at the grain boundaries. In replicas with 0.018% C, the large $M_{23}C_6$ carbides were at the triple point and relatively small $M_{23}C_6$ sited at grain boundaries in replicas with 0.047% to 0.16% C (24).

(b) N

Like carbon, Nitrogen (N) is also an important interstitial solid solution element, it can strengthen the steel but reduces the weldability. The difference in solubility of N between austenite and ferrite promotes MX carbonitride precipitation and the “M” are mainly niobium and vanadium in 9-12%Cr heat-resistant steel. The MX-type carbonitride is fine and stable, mainly precipitated in the matrix and at lath boundaries during the tempering which can retard the moving of dislocation and the Cr content affects the solubility of N in steel (23).

(c) Cr

The presence of chromium (Cr) in heat-resistant steel is crucial for its oxidation and corrosion resistance. As a ferritic stabilizer, chromium encourages the formation of the ferrite phase in steel. Moreover, it forms chromium carbides, specifically $Cr_{23}C_6$, mainly at prior austenite grain boundaries in conjunction with carbon providing precipitate strengthening for heat-resistant steels. Traditionally, 9% chromium content has been found to offer the longest creep life for heat-resistant steels. However, when it comes to applications requiring service

temperatures up to 650℃, 9% Cr may not provide adequate oxidation resistance. In such cases, the chromium content is often increased to 12% to improve the material's resistance to high-temperature oxidation, even though this higher chromium content might lead to some loss in rupture life (25). Danielsen and Hald have researched ten steels with different Cr content (8.3% to 12.2%) to investigate the behaviour of the Z phase after prolonged thermal exposure at 600 to 650℃, Z phase has been found in all steels but there are higher Z phase precipitation rate in relatively high Cr content steel (11 to 12.2%) than that in lower Cr content steel (9% and lower) at 650℃. That reveals the higher Cr content encourages the formation of the Z phase which is a large precipitate and this precipitation consumes fine carbonitride MX reducing the creep stability in long-term service (26).

(d) Mo and W

Molybdenum (Mo) and Tungsten (W) are both commonly used alloying elements that enhance the creep strength of heat-resistant steel. Their efficacy is generally attributed to solid solution strengthening, but each element offers additional mechanisms to improve material properties. In the case of Mo, its atomic radius is different from that of iron, and this difference is believed to hinder creep deformation through the solute drag effect, particularly when Mo content reaches around 1% (23). On the other hand, Tungsten (W) serves to slow down the recovery process of the martensitic matrix and reduce the self-diffusion rate in the material. This contributes to the greater stability of precipitates at elevated temperatures. However, it's important to note that both Mo and W have been observed to encourage the formation of the Laves phase during long-term creep exposure (27).

(e) Si and Ni

Silicon (Si) serves multiple roles in the alloying process for heat-resistant steel. One of its

primary benefits is its capacity to enhance oxidation resistance, even more effectively than Cr when used in appropriate concentrations. Another benefit is the solubility of C in the metal could be decreased by Si (28). However, it's important to be aware that higher Si content can encourage the formation of the Laves phase, particularly when Mo is also present in the alloy. This occurs because Si reduces the solubility of Mo in the ferrite phase (29).

Nickel (Ni) serves as an austenitic stabilizer which can help to reduce the formation of δ-ferrite. Both the material's ductility and its high-temperature strength can be improved by the addition of Ni in high-Cr steel (28).

(f) Nb, Ta and V

Niobium (Nb), tantalum (Ta), and vanadium (V) can form MX-type carbonitrides with N, contributing to the precipitation strengthening of heat-resistant steel. Both V and Nb carbonitrides serve as intragranular precipitates, which are stable and exhibit a slow coarsening rate at elevated temperatures. These carbonitrides enhance the creep strength of the material by retarding creep deformation at high temperatures (23)(27). However, high content of Nb decreases the toughness of steel (23).

(g) B

Boron (B) can reduce the Ostwald ripening rate near the prior austenite grain boundaries, which leads to the stabilization and slower coarsening of $M_{23}C_6$ carbides. When the boron content is relatively high, carbon in $M_{23}C_6$ can be replaced by boron, resulting in a new $M_{23}(B, C)_6$ that is more stable and resistant to coarsening compared to the regular B-free $M_{23}C_6$ (30). The fine and stable $M_{23}C_6$ carbides can enhance the steel's creep strength through precipitate strengthening. However, the boron content must be carefully balanced with the nitrogen content; otherwise, they can form large BN particles, causing the boron to lose its

effectiveness (27).

(h) Co and Mn

Cobalt (Co) and Manganese (Mn) are austenite stabilizers and are used to inhibit the formation of δ-ferrite above the austenitization temperature. Co can increase the Curie point and diminish the coarsening rate of $M_{23}C_6$ carbides by slowing down atomic diffusion (27,31,32). Additionally, Co exhibits low solubility in the precipitate phase but high solubility within the ferritic matrix. This means that Co can remain in the matrix and provide stable solid-solution strengthening (33). Manganese aids in the deoxidization process during steel manufacturing. However, it can adversely impact the material's creep rupture strength if its content exceeds 0.5% (23).

(i) Cu

The effect of Cu particle for a 9%Cr base Cu bearing steels which contain 1 to 4wt% Cu has been researched by Y. Futamur et al (34). They discovered that, when compared to Cu-free steel, the steels with Cu exhibited a substantially longer creep rupture life—up to six times longer. Moreover, a higher Cu content was associated with further improvement of creep rupture life. This is contributed by precipitate strengthening from the Cu (34).

2.2.3 The precipitates and secondary phase in 9-12%Cr heat-resistant steel

$M_{23}C_6$-type carbides and MX-type carbonitride are the most common types of precipitates found in 9-12%Cr heat-resistant steel. The Laves phase and Z phase were normally formed in the 9-12%Cr heat-resistant steel after long-term creep or thermal ageing. A summary of precipitates and secondary phases in 9-12Cr% heat-resistant steel is provided in Table 2. 1.

$M_{23}C_6$-type carbides are the primary carbides in heat-resistant steel and have an fcc (face-

centred cubic) structure with a lattice parameter ranging from a=1.06 to 1.07 nm. These carbides primarily precipitate at prior austenite grain boundaries (PAGB), block boundaries and lath boundaries, with sizes between 100-200 nm after the tempering process (28,35). The "M" in $M_{23}C_6$ mainly represents chromium but can be replaced by elements like Fe, Ni, Mn, and Mo (28). The addition of boron can substitute for carbon to form $M_{23}(B, C)_6$, which is more stable than regular $M_{23}C_6$ (30).

Another major type of precipitate contributing to creep strength is MX-type carbonitride, which has an fcc structure with a lattice parameter ranging from a=0.42 to 0.45 nm. These precipitates are fine and dispersed along lath boundaries and within the matrix, usually measuring less than 50 nm after post-heat treatment (28,35). It can improve the creep strength by retard the movement of dislocations (36).

The Laves phase has a hexagonal structure with lattice parameters of a=0.47 nm and c=0.78 nm. This phase typically forms near $M_{23}C_6$ precipitates under creep exposure (28). Common compositions of Laves phases include Fe_2W, Fe_2Mo, or $(Fe, Cr)_2(W, Mo)$, which are enriched in W or Co. The formation of Laves phases depletes W and Co in the matrix, leading to a loss of solute hardening (37).

Z phase primarily consists of Cr(V, Nb)N and has a tetragonal structure with lattice parameters of a=0.29 nm and c=0.74 nm. This phase is formed from the conversion of MX particles, which absorb Cr from the matrix under high-temperature thermal exposure. This transformation leads to a reduction in fine MX particles, resulting in the loss of precipitate hardening. Additionally, Z phases found at PAGBs are generally larger, further diminishing the effect of precipitate strengthening (37,38). A higher Cr content (above 10.5%) significantly accelerates the

formation of the Z phase, explaining why 12%Cr steels degrade more quickly than P92 steels after long-term creep tests (26,39).

In steels with high chromium concentrations, specifically above around 10%, the material manifests as a dual-phase composition of martensite and δ-ferrite. This dual-phase structure has implications for its mechanical properties: both the creep rupture strength is reduced and the Ductile-Brittle Transition Temperature (DBTT) is raised as the chromium concentration increases. This is correlated with an increased volume fraction of δ-ferrite in the material. For example, in 12%Cr-2W and 15%Cr-2W steels, the volume fraction of δ-ferrite is 0.16% and 0.60%, respectively. Notably, this δ-ferrite phase lacks carbides and subgrains and exhibits a relatively low dislocation density (37,40). In addition, the tensile strength of steel decreased by increasing the amount of δ-ferrites at high temperatures (41). Figure 2. 6 shows the optical images of δ-ferrites in martensite structure (41).

2.2.4 The strengthening mechanism

The high strength of 9-12% Cr heat-resistant steel is attributed to several mechanisms, including solid solution strengthening, precipitation strengthening, dislocation hardening, as well as boundary and sub-boundary hardening (37,42).

Solid solution strengthening

The primary substitutional solute elements in 9-12% Cr steels are Mo and W, both of which have significantly larger atomic sizes compared to the iron matrix. The addition of molybdenum (Mo) and tungsten (W) in the steel can sometimes lead to the formation of Fe2(Mo, W) Laves phases, as well as promoting the fine distribution of $M_{23}C_6$ carbides. Therefore, it's crucial to note that the strengthening effects of Mo and W in solid solution to the overall creep strength

are not stand-alone; they work together with other strengthening mechanisms, such as precipitation strengthening (43).

Precipitate strengthening

Two types of precipitates provide the main sources of precipitate strengthening for 9-12% heat-resistant steels: $M_{23}C_6$ and MX. $M_{23}C_6$ primarily precipitates at the boundaries of laths, blocks, packets, and prior austenite grains. This serves to significantly inhibit the coarsening of the laths and blocks, further retarding the transformation of lath structures into subgrain structures (30,44). MX precipitates are mostly distributed within laths and act to hinder the movement of dislocations (36).

The minimum stress required for a dislocation to pass through precipitate particles is called the threshold stress. Multiple theories have been proposed to explain this, including the Orowan mechanism, local climb mechanism, general climb mechanism and Srolovitz mechanism (45). For the Orowan mechanism, the Orowan stress σ_{or} is given by the following equation:

$$\sigma_{or} = 0.8MGb/\lambda \qquad Equation\ 2.1$$

Where M is the Taylor factor (=3), G is the shear modulus, b is the magnitude of the Burgers vector, and λ is the mean inter-particle spacing (42).

In 9 to 12%Cr steels, certain changes in the microstructure, such as the coarsening of fine precipitates like $M_{23}C_6$, MX, and Fe_2(W, Mo) Laves phase, along with the dissolution of fine MX particles to form larger Z phase precipitates, have been observed. These transformations lead to an increase in the λ term in Equation 2.1, causing a reduction of the Orowan stress. The creep resistance of the material can be significantly reduced due to the coarsening and

dissolution of precipitates, leading to premature creep rupture (46).

Dislocation hardening

Dislocation hardening is crucial for determining a material's properties at room temperature. The concept of dislocation hardening is based on the assumption that existing dislocations act as obstacles to any moving dislocation (43). The dislocation hardening is given by the following equation:

$$\sigma_{or} = 0.5MGb(\rho_f)^{1/2} \qquad Equation\ 2.2$$

Where ρ_f is the free dislocation density in the matrix (42). Even after undergoing post-heat treatment processes like tempering, tempered martensitic 9–12% Cr steels still maintain a high dislocation density in the matrix. This density is typically in the range of $1–10\times10^{14}m^{-2}$ (43,47). However, the benefits of cold-work hardening are diminished due to the recovery of excess dislocations and the recrystallization of the deformed microstructure, leading to a reduction in creep strength at elevated temperatures. Therefore, dislocation hardening only contributes to short-term creep strength (43).

Boundary and sub-boundary hardening

After the appropriate normalising and tempering process, 9-12%Cr steels exhibit a tempered martensite microstructure. This structure is composed of laths and blocks featuring a high concentration of dislocations. Additionally, fine $M_{23}C_6$ are dispersed along both the lath, block and packet boundaries as well as fine MX within the matrix. The lath and block can be regarded as elongated sub-grains. Sub-boundary hardening contributed by lath and block boundaries is given by:

$$\sigma_{or} = 10Gb/\lambda_{sg} \qquad Equation\ 2.3$$

where λ_{sg} is the short width of elongated subgrains (42).

As creep strain progresses, particularly in the tertiary or acceleration creep region, there's a noticeable coarsening of the laths and blocks within the material (48). This coarsening effect leads to an increase in the λ_{sg} term in the Equation 2.3. The smaller width could provide more lath boundary strengthening for the material as found by Nikitin I et al. and Mitsuhara M et al. (49,50).

2.2.5 Evolution of microstructure in creep crack growth

Microstructure after post-heat treatment

The 9-12%Cr steels exhibit a tempered martensite microstructure with a high density of dislocation after the appropriate normalising and tempering process. The larger particles $M_{23}C_6$ (M = Cr, Fe) carbides, which have a size range of 100-200 nm are primarily distributed along the lath boundaries and the prior austenite grain boundaries. The smaller scale pertains to MX (M = V, Ta, Nb; X = C, N) carbonitrides, with sizes below 50 nm are mainly dispersed within the matrix (35).

During testing

During the creep process, high temperatures and elevated stress levels accelerate microstructural evolution. This evolution encompasses a range of changes in both the subgrain structure and the distribution of precipitates. In terms of subgrain modifications, the process includes lath widening, disappearance of prior austenite grain boundaries, emergence of subgrains, formation of subgrains and growth of subgrain. On the other hand, the evolution of precipitates involves the coarsening of fine particles, such as $M_{23}C_6$ and MX, as well as the

formation and enlargement of new precipitate phases, like the Laves phase and Z phase (25). The existing fine particles were also consumed by the precipitation of the new particles.

As creep strain accumulates, particularly during the tertiary period, the laths and blocks coarsen. This coarsening weakens sub-boundary hardening and leads to material softening (37). The migration of subgrain boundaries in the material is largely controlled by the pinning force exerted by particles dispersed along these boundaries. $M_{23}C_6$ are mainly located on subgrain boundaries, contributing to the thermal stability of the subgrains (25). According to research conducted by Maruyama et al, $M_{23}C_6$ precipitates are more influential than MX precipitates in regulating subgrain coarsening (51). This is primarily attributed to the proximity of small $M_{23}C_6$ particles to the subgrain boundaries, where they apply Zener pinning forces (52). Chromium diffuses from the matrix to the boundaries due to both strain and thermal factors, resulting in the coarsening of $M_{23}C_6$ precipitates (25). These coarsened precipitates lose their pinning effect, thereby accelerating the coarsening of laths and blocks (37). Significant growth of $M_{23}C_6$ carbides in P91 steel after prolonged creep exposure exceeding 10^5 hours at 600°C was observed by Panait et al. (53). Specifically, the average equivalent diameter of these carbides expanded significantly, moving from an initial range of 150-180 nm to a considerably larger size of 300 nm. Besides the thermal factor, the coarsening of $M_{23}C_6$ could also promoted by the strain. In addition to thermal influences, the strain also appears to contribute to the coarsening of $M_{23}C_6$ carbides (54).

During long-term thermal exposure at high temperatures, Laves and Z phases form. The typical Laves phases are compounds like Fe_2W, Fe_2Mo, or $(Fe, Cr)_2(W, Mo)$, which are enriched with W or Mo. Their formation consumes W and Mo from the matrix, resulting in a loss of solute

hardening (37). Apparently, the increase in W and Mo content could promote the formation of Laves phase. And also, the incorporation of Co can facilitate the formation of this phase by reducing the solubility of W and Mo in the matrix (55). MX precipitates are smaller and more resistant to coarsening compared to $M_{23}C_6$. However, it could convert to the Z phase by incorporating Chromium from the matrix (38). This conversion reduces the number of fine MX particles and leads to the formation of larger Z phase particles thereby causing a loss in precipitate hardening (37). Unlike finer MN nitrides that contribute to creep strength, the coarser particles of Z phase do not offer the same benefit. In fact, Z phase precipitation has been identified as a key factor leading to the early degradation of creep strength in certain 11-12% Cr heat-resistant steels, particularly after relatively short-term creep exposure of less than 15,000 hours (56,57). The formation of the Z phase led to a dramatic reduction in creep resistance of TAF 650 at 650°C was observed by Sklenička V et al. (58). However, the Z phase is not always harmful to the material. Two experimental steels were developed by Masoud Rashidi et al.: Z-steel with a composition of 11.79% Cr, 2.9% W, 7.3% Co, and 0.002% C by weight, and ZCuC-steel with a composition of 12.1% Cr, 2.47% W, 3.5% Co, 1.95% Cu, and 0.06% C by weight which are using Z phase for strengthening. Remarkably, the creep rupture strengths of these newly developed steels were found to be comparable to both P91 and P92 when tested at 650°C. Additionally, they outperformed X20, another commercially available 12% Cr steel (59). Similar to $M_{23}C_6$, the creep deformation could also accelerate the growth of MX precipitates and Z phase particles (54,60,61).

2.3 Creep

2.3.1 Creep curve

Creep refers to the time-dependent plastic deformation that materials experience when

subjected to constant stress at elevated temperatures. In a typical creep test, a specimen is placed under a constant load or stress, and the resulting strain is monitored and recorded over time. The typical creep strain curve is shown in Figure 2. 9 (62). In primary creep, the creep rate rises rapidly at first and then slows down with time. In this stage, the strain hardening reduces the creep rate. In secondary creep, the material exhibits a nearly constant creep rate, denoted as $\dot{\varepsilon}_{min}$. This is the longest phase in the creep life cycle and is often considered the "steady-state" creep rate. In this phase, the effect of work hardening was balanced by the recovery softening. In tertiary creep, the creep rate starts to accelerate again until rupture. This acceleration is typically due to localized necking, as well as the formation of creep cavities or voids (63).

2.3.2 Creep mechanism

Creep deformation in metals occurs primarily through three mechanisms: dislocation creep, diffusion creep, and grain boundary sliding. The contribution of each mechanism depends on stress level, temperature, and grain structure.

Dislocation creep

Dislocation creep typically dominates under relatively high stress and moderate temperature. It occurs through the motion of dislocations within the crystal lattice. At low temperatures, dislocations are pinned by barriers such as grain boundaries or precipitates. When temperature increases, vacancies assist dislocations in climbing over these obstacles. This process, known as climb, enables dislocations to move out of their original slip planes. After bypassing the obstacle, the dislocation continues gliding on a different slip plane, as shown in Figure 2. 7 (64). This climb-glide process repeats and contributes to time-dependent plastic deformation. The creep rate in this regime is strongly influenced by stress. In heat-resistant steels like T92 and

BG12Cr, fine $M_{23}C_6$ carbides and MX carbonitrides effectively hinder dislocation motion, thereby enhancing creep resistance.

Diffusion creep

Diffusion creep is a mechanism that allows the material to deform through atomic diffusion, without the movement of dislocations which is different from the dislocation creep. Diffusion creep becomes significant when materials are subjected to low stress and high temperature. In this mechanism, atoms diffuse from regions of high compressive stress toward regions under uniaxial tensile stress, resulting in gradual elongation along the loading direction. Two types of diffusion creep exist depending on the diffusion path: Nabarro-Herring creep and Coble creep (65,66). Figure 2. 8 illustrates diffusion creep via both grain boundary diffusion and lattice (bulk-crystal) diffusion. Nabarro-Herring creep occurs via lattice diffusion through the grain interior and becomes dominant at higher homologous temperatures. In contrast, Coble creep is governed by grain boundary diffusion, where atoms move along grain boundaries instead of through the lattice. Since grain boundary diffusion has a lower activation energy than lattice diffusion, it dominates at lower temperatures where lattice diffusion is not yet active.

Grain boundary sliding

Grain boundary sliding refers to the relative motion between adjacent grains along their boundaries (67). It tends to become more prominent at elevated temperatures and is also facilitated by high stresses, often associated with tertiary creep or accelerated creep stages.

Figure 2. 10 shows the schematic deformation mechanism map which indicates the operating condition for different creep mechanisms. The creep mechanisms in primary and secondary creep regions are diffusional creep and dislocation creep (68).

2.3.3 The minimum creep rate

The slope of the creep curve (dε/dt) is known as the creep rate. The stationary creep rate observed in the secondary creep stage is typically the lowest across all stages of the creep process. For this reason, it's commonly termed the "minimum creep rate." This rate is often used as a standard measure to evaluate a material's resistance to creep deformation. The minimum (or steady-state) creep rate, denoted as $\dot{\varepsilon}_{min}$ usually expressed by the following equation:

$$\dot{\varepsilon}_{min} = A\sigma^n \qquad Equation\ 2.4$$

σ is the creep stress, n is the stress exponent and A is the material constants.

2.4 Creep crack growth

2.4.1 The Fundamental of Creep Crack Growth

Creep crack growth is the progressive extension of a crack on a cracked component under sustained loading at elevated temperatures, where the time-dependent deformation or "creep" mechanism dominates.

Creep zone growth

The development of creep zones in front of the crack tip during creep crack growth is illustrated in Figure 2. 11 (69). In the early stage of creep crack growth, only a small area in front of the crack tip undergoes primary creep (as shown in Figure 2. 11 a). As time progresses, the zone experiencing secondary creep expands within the region initially affected by primary creep, eventually becoming comparable in size to the uncracked ligament (Figure 2. 11 b). With increasing creep time, the primary creep zone covers the whole uncracked ligament with a significant secondary creep zone (Figure 2. 11 c). Figure 2. 11 d illustrates the condition where

secondary creep dominates the entire uncracked ligament which is called the extensive creep condition.

2.4.2 C^* and C(t)

The C*-integral, initially introduced by Landes and Begley (70), and Nikbin et al. (71)in 1976, serves as an elastic-plastic fracture mechanics counterpart to the J-integral. This parameter can be understood as the difference in the energy rates between two similarly loaded structures with varying crack sizes:

$$C^* = \int_{\tau}^{-} (\dot{w}dy - T \cdot \frac{\partial \dot{u}}{\partial x} ds) \qquad Equation\ 2.5$$

where ẇ is the strain energy rate per unit volume, u̇ is the displacement vector rate.

The C^*-integral was developed to describe the stress and strain-rate fields at the tip of a crack under significant creep deformation. Additionally, $C^*$is associated with the changes in the rate of potential energy release as the crack extends (70). Like the J-integral, C^*has been shown to be path-independent, meaning that any contour around the crack tip will yield an identical C^*value.

In 1988, Hyde conducted calculations for the C^*using two types of test specimens: Compact Tension (CT) and Thumbnail (72).

Following the ASTM E1457-23 (73), C^*can be calculated based on the CT specimen with the equation:

$$C^* = \frac{P\dot{\Delta}^{CMOD}}{B_N(W-a)} H^{CMOD} \eta^{CMOD} \qquad Equation\ 2.6$$

$$H^{CMOD} = \frac{N}{N+1} \qquad Equation\ 2.7$$

where F is the force applied, B_N is the net width of the sample, $\dot{\Delta}^{CMOD}$ is the crack mouth displacement change rate measured from the clip-on gauge, η^{CMOD} equals to 2.20 and N is the creep index of the material at the same temperature.

The relationship between crack growth rate with C^* is:

$$\dot{a} = D(C^*)^q \qquad Equation\ 2.8$$

$\dot{a}$ is creep crack rate, D and q are material constants.

In creep ductile materials, the contour integral C^* serves as a good correlational parameter for crack growth. And for creep brittle material, the stress intensity factor K_I is preferred (74).

Following ASTM E1457-23, the total rate of crack mouth opening displacement measured in an experiment ($\dot{\Delta}_{CMOD}$) is composed of an instantaneous elastic part ($\dot{\Delta}_e$) and a time-dependent part ($\dot{\Delta}_c$). The elastic part can be calculated by Equation below:

$$\dot{\Delta}_e = \frac{\dot{a}B}{P}\left[\frac{2K^2}{E'}\right] \qquad Equation\ 2.9$$

Where,

$\dot{a}$= crack growth rate,

P= applied force,

B= specimen thickness, it was replaced by B_N in this study.

K=stress intensity factor

E'= elastic constraint modulus, for the plane strain, it is equal to $E/(1-v^2)$.

Therefore, the ($\dot{\Delta}_c$) can be derived by $\dot{\Delta}_c = \dot{\Delta}_{CMOD} - \dot{\Delta}_e$.

Only when $\frac{\dot{\Delta}_c}{\dot{\Delta}_{CMOD}} > 0.5$ the $C^*$is applicable.

Also, $C^*$is applicable only in extensive creep, and in small-scale creep and transition creep, C(t) should be applied.

Small scale creep

For the C(T) specimen, the $C(t)$ is given in Equation (75):

$$C(t) = \frac{P\dot{V}_c}{BW}(F'/F) \qquad Equation\ 2.10$$

P is the applied load, F is the K-calibration factor, F`= dF/d(a/W), B is the thickness of specimens, a is the crack length and W is the width of the specimen.

Transition creep

Transition creep is between the small-scale creep stage and the extensive secondary creep stage. In the case of transition creep, C(t) serves to describe the immediate stress and strain field surrounding a static crack tip, gradually converging to the C^*value as time progresses. Over extended periods of creep, C(t) stabilizes to a constant value (76). Typically, the value of C(t) is much higher than that of C^*. For conditions of plane strain small-scale creep, the expression for C(t) is as follows:

$$C(t) = \frac{K^2(1-\upsilon^2)}{E(n+1)t} \qquad Equation\ 2.11$$

where K is the stress intensity factor, ν is Poisson's ratio, E is the modulus of elasticity, n is the

creep exponent in Norton's law and t is the time.

When C^* becomes equal to C(t), the time 't' marks the transition time t_T from the small-scale creep phase to the extensive secondary creep stage. Hence the time for extensive creep established t_T can be calculated by (77):

$$t_T = \frac{K^2(1-v^2)}{E(n+1)C^*} \qquad Equation\ 2.12$$

2.5 The microstructure and properties of 9%Cr and 12%Cr heat-resistant steel

2.5.1 The microstructure of 9%Cr

Figure 2. 12 shows the microstructure of typical 9%Cr heat-resistant steel. 9-12% Cr heat-resistant steels exhibit a tempered martensitic microstructure, where prior austenite grains (PAGs) are subdivided into packets, blocks, and laths, forming a hierarchical structure. As shown in Figure 2. 13, $M_{23}C_6$ carbides are predominantly precipitated along lath and block boundaries, enhancing boundary strengthening, whereas MX-type carbonitrides are uniformly distributed within laths and contribute to dispersion strengthening (78).

2.5.2 The effect of normalizing and tempering temperature on P92

Different heat treatment conditions significantly affect the microstructure and mechanical properties of P92.

Saini N. et al. investigated the effect of normalizing temperature on P92 steel through a series of experiments and microstructural observations (79). They found that normalizing temperature significantly influences the microstructure and mechanical properties of P92, even with a fixed

tempering temperature of 760 °C. When tempered at 760 °C, increasing the normalizing temperature from 950 °C to 1150 °C results in a steady increase in prior austenite grain size, as shown in Figure 2. 14. This grain coarsening trend is accompanied by changes in precipitate distribution: fine MX carbonitrides remain dispersed within the lath matrix, while coarse $M_{23}C_6$ carbides accumulate along prior austenite grain boundaries (PAGBs) at higher normalizing temperatures. The accumulation of coarse $M_{23}C_6$ precipitates along PAGBs and the uniform distribution of fine MX particles within the matrix are clearly visible in the microstructure (Figure 2. 15) (79).

These microstructural changes are directly correlated to the degradation of mechanical properties. Both hardness and tensile strength decrease with increasing normalizing temperature, reaching minimum values at approximately 1100 °C. For example, Vickers hardness declines from ~236 HV at 950 °C to ~215 HV at 1100 °C, while yield strength and ultimate tensile strength drop by over 60 MPa and 80 MPa, respectively (Figure 2. 16 and Figure 2. 17). A slight recovery is observed at 1150 °C, which may be attributed to the reduced grain boundary area associated with larger grain size, thereby retaining more carbon in the matrix (79). This indicates that excessive grain growth and precipitate coarsening at high normalizing temperatures reduce dislocation hardening, resulting in decreased strength and hardness (79).

In addition to the effect of normalising temperature, Barbadikar D et al. also investigated how tempering temperature influences the microstructure and mechanical properties of P92 steel (80). Grain size shows limited sensitivity to tempering temperature (Figure 2. 18). A slight reduction in average grain size is observed across all tempering conditions, with consistent trends under varying normalising temperatures. In contrast, lath width increases with tempering temperature (Figure 2. 19). For specimens normalised at 1313 K, 1333 K, and 1353 K, elevated

tempering temperatures promote martensite recovery, as indicated by broader laths (80). The average size of precipitates also increased with tempering temperature, indicating coarsening of $M_{23}C_6$ carbides. This effect was observed regardless of normalizing temperature and reflects the thermally driven diffusion and growth of carbides during tempering. Accordingly, hardness consistently decreases with tempering temperature across all normalising conditions (Figure 2. 20) (80). This decline is attributed to both lath coarsening and precipitate growth, which reduce the effectiveness of boundary and dispersion strengthening mechanisms.

These findings indicate that while tempering at higher temperatures promotes microstructural recovery and precipitate coarsening, it also compromises mechanical strength. Therefore, the optimisation of both normalising and tempering conditions is necessary to achieve a balance between hardness, strength, and thermal stability in P92 steel.

2.5.3 The creep and creep crack growth properties of P92

Figure 2. 21 illustrates the creep strain curves of P92 steel tested at 650 °C under various applied stresses. The results indicate that increasing the applied stress significantly reduces the creep rupture life (81).

Figure 2. 22 presents the creep rupture life of P92 at different temperatures under different stress levels. As the temperature increases, the rupture life of P92 decreases markedly, demonstrating the thermal degradation of creep strength (82).

Figure 2. 23 shows the variation of creep strain rate with time for P92 steel tested at 923 K (650 °C) under different applied stresses (81). Higher applied stresses result in higher minimum creep rates and earlier onset of the tertiary creep stage The lowest strain rate observed at each stress level corresponds to the minimum (or steady-state) creep rate, which is used to derive the

stress exponent in Figure 2. 24.

The relationship between steady-state creep rate and applied stress is shown in Figure 2. 24. This log-log plot is used to determine the creep stress exponent *n*, which is critical for calculating C^* during CCG analysis (81).

Kim B. et al. investigated the creep crack growth resistance of P92 and its weld metal at 600 °C. Figure 2. 25 shows the relationship between crack extension and C_t. Their results revealed that both base metal and welds exhibit time-dependent crack propagation, with the weld metal generally showing faster growth due to its coarser microstructure and lower ductility (83).

Tanner D. et al. conducted a similar study at 675 °C, where the creep crack growth rate (da/dt) was plotted against the C* parameter, as shown in Figure 2. 26. Their data confirm that the da/dt–C* relationship follows a power-law trend, consistent with creep-ductile behaviour. The slope of the log(da/dt) vs log(C*) curve provides the material constant q, which is required for remaining life prediction under long-term creep crack conditions (84).

CHAPTER 3 Experimental

3.1 Material

3.1.1 Chemical composition

The T92 and BG12Cr materials used in the current research were both provided by Baowu Steel, China. The nominal chemical compositions of these two materials are shown in Table 3. 1.

Compared to T92 steel, BG12Cr contains 3 wt% more Cr, 1.6 to 3.0 wt% Co, 0.5 wt% Cu, and lower amounts of Mo and Mn. Additionally, BG12Cr does not include some minor alloying elements such as Ni, Al, Ti, or Zr. Most of the BG12Cr materials used in this research were taken from the thick wall tubes and machine to C(T) specimens and cylindrical bars. The manufacturing process of the thick wall tubes was continuous casting, primary rolling, piercing, continuous hot rolling and cold rolling. And then, the tubes from BG12Cr and T92 were normalized at a temperature of 1060℃ for 60 mins and cooled to room temperature followed by tempering with the temperature of 780℃ for 90 mins. The tensile properties of T92 and BG12Cr provided by the manufacturer are shown in Table 3. 2. And the tensile properties of P92 tested by BaoWu steel under various temperatures as shown in Figure 3. 3. The tensile strength of P92 reduced from around 650 MPa at 200°C to around 300 MPa at 650°C.

3.1.2 Tempering at different temperatures

To investigate the effect of tempering temperature on the microstructure of T92 and BG12Cr steel, additional heat treatments have been carried out on cylindrical bar specimens. The cylindrical bars were sealed individually into the quartz tubes with Argon gas to prevent severe oxidation during the normalizing at elevated temperatures before the heat treatment. The specimens were firstly normalized at 1080℃ for 1 hour and then, the tubes were taken from the

furnace and broken intermittently to allow the specimen to contact the air directly for air cooling. The specimens were tempered at 760,780,800,820℃ individually for 1.5 hours after being cooled to room temperature. An 8mm length of bars was cut off from one end of the bar for microstructure investigation. Sample with normalizing alone is noted as N, while those with tempering are noted as N+T760 etc. The matrix of heat treatment is shown in Table 3. 3.

3.2 Microstructure characterization

3.2.1 Sample preparation for observation

Following the final fracture along the crack, most C(T) specimens were sectioned along the mid-thickness using an Al_2O_3 cutting disc. Exceptions include the T92 specimen tested at 600 °C under 10 kN, the specimen tested at 650 °C under 6 kN, and both BG12Cr and T92 specimens from interrupted tests, which were sectioned by electrical discharge machining (EDM) without final fracture. The sectioning path is shown in Figure 3.1. These EDM-sectioned specimens were prepared specifically to examine the crack tip and the region ahead of it. Subsequently, all sectioned C(T) specimens were mounted in conductive Bakelite at 180 °C for metallographic preparation.

The mounted samples were ground by SiC grinding papers of grit size 120, 240, 400, 800, 1200, and 2500 in sequence with water as the lubricant. After grounding, the samples were polished on the cloth polishing discs with diamond suspensions in the order of 6,3 um and finally OP-S. The samples were cleaned with water and acetone and dried between each grounding and polishing step. The polished samples were etched with Kalling`s reagent (40 ml HCl, 40 ml ethanal and 2 g Cupric Chloride) for 10s.

TEM samples were 3mm in diameter thin foils taken from C(T) samples. The samples were

electropolished with a twin-jet electropolisher at 25 voltages and -20°C using a solution of 10 pct perchloric acid+ 90 pct ethanol.

3.2.2 Optical observation

A Keyenece VHX-6000 optical microscope was used to image the fracture surface of the tested C(T) specimens and the microstructure of the as-received and re-heat treated samples.

3.2.3 Scanning electron microscope(SEM) and Energy dispersive X-ray spectroscopy (EDX)

A Philips XL-30 FEG ESEM and a JOEL 6060 were used to image the fracture surface of the tested C(T) specimens and the microstructure of the as-received and re-heat treated samples. A JOEL 7000F was used to image the cross-section of tested C(T) specimens with 20kV accelerating voltage and 10mm working distance.

3.2.4 Transmission electron microscope (TEM)

A scanning transmission electron microscope (STEM) was used to examine the microstructures including precipitates of both as-received T92 and BG12Cr materials. The TEM observation was carried out on an FEI Talos 200F microscope equipped with Silicon Drift Detector (SDD) for energy-dispersive X-ray spectrometry (EDS). The accelerating voltage for EDS Mapping with STEM is 200kV voltage.

3.2.5 Primary Austenite Grain(PAG) size distribution and average lath width

To measure the PAG size distribution in as-received T92, BG12Cr, and BG12Cr N+T780, 10 SEM images were acquired for each material at 100× magnification. A least 300 PAGs were measured per condition. The prior austenite grain boundaries (PAGBs) were outlined, and both the number and projected area of PAGs were quantified using ImageJ software. These data were used to calculate the average grain size and assess the grain size distribution for each

condition. The average lath width in as-received T92 and BG12Cr was determined from five TEM images at 10,000× magnification, with at least 50 laths measured for each material. The average lath width was calculated by dividing the cumulative lath width by the number of laths.

3.3 Creep crack growth test

The creep crack growth (CCG) tests were carried out on C(T) test pieces in accordance with ASTM standard E1457-23. All these tests were conducted on a screw-driven servo-electric closed loop controlled mechanical testing machine, Zwick 100. The direct current potential drop (d.c.p.d) method was used to monitor crack growth and the crack mouth opening displacement (CMOD) was recorded by a high temperature-resistant clip-on extensometer during the tests. Crack length and CMOD data were analyzed to calculate the crack growth rates and the corresponding fracture mechanics parameters which are stress intensity factor K and the elastic-plastic parameter C* after each test. The typical setup of experiment is shown in Figure 3. 2.

3.3.1 Testpiece preparation

Compact tension (C(T)) test pieces were designed following ASTM E1457-23 for CCG tests and the geometry of the specimen is shown in Figure 3. 1. The width of the test piece (W) is 26 mm and the thickness (B) is 13 mm. To regulate the crack shape, 1 mm depth side- grooves were machined to each side of the test piece, leaving the effective thickness of the test piece (B_n) at 11mm. To correspond to an a/W ratio of 0.35, the initial notch depth is 9.1mm which for achieving a/W=0.4 with a minimum precrack (a is the crack length and W is the width of the testpiece). For mounting the clip-on extensometer which is used for CMOD measurements, two knife edges were machined and the tips of the edges are in line with the loading line.

3.3.2 Crack length monitoring method

To monitor the crack growth during the test, the d.c.p.d method was applied in the CCG tests. Two pairs of wires were spot-welded onto the test piece, one is current wires for applying a constant direct current with a power supply, and another pair is potential wires which were linked to a voltage metre to record the potential change across the crack as a function of time during the test. Both current wires and potential wires are made by Brightray which is a Ni-Cr alloy with good oxidation resistance and stability at elevated temperatures. As the crack grows, the path between the two potential wires increases, and the potential measured across the crack rises consequently. After testing, the recorded potential data were converted into physical crack length using a calibration function, as detailed in the crack length calibration section below.

3.3.3 Test procedure

All test pieces were thoroughly cleaned in Acetone using an ultrasonic cleaner to remove any contamination that could affect the mechanical properties of the material at elevated temperatures before testing. Before loading the test pieces on the machine, both pairs of wires were spot-welded on the test pieces and covered by ceramic fibre sleeves which protect the wires and prevent short circuits. Precracking was applied on each test piece before CCG tests to create a sharp crack while removing the influence of the machined notch. And according to the ASTM E1457-23, the calculation of the C* parameter is only valid for a/W values ranging from 0.4 to 0.7, the a/W would be around 0.4 after precracking. All the precrackings in this project were carried out on an Amsler Vibrophone at a frequency of 60Hz and a stress ratio(minimum stress/maximum stress) of 0.1. The maximum force used in precracking was the same as the loading used in the following CCG test except for the CCG tests with the loading of 3 kN. The maximum force of 3 kN was too low for precracking on the both T92 and BG12Cr

C(T) test pieces, the maximum force of 6 kN was used to speed up the precracking process and finished by precracking with a maximum force of 3 kN to achieve the target crack length.

The test pieces were transferred to the screw-driving testing machine which is equipped with a resistance furnace after precracking. Two loading pins made of high-strength nickel alloys were used during the long-term testing to prevent bending and consequent uneven loading at high temperatures. To ensure the test temperature is stable and accurate during testing, the temperature needs to be checked regularly. A thermocouple was used to measure the temperature of the testpiece and it was attached without welding to the middle section of the test piece and linked to a calibrated thermometer. After loading the testpiece, a static load of 0.5 kN was applied and the clip-on extensometer was mounted on the testpiece. The high current will heat the test piece, so a constant direct current of 10A was applied through the test piece before reaching the target temperature.

When the target temperature is reached and stabilized, the loading would be increased to the test loading slowly (0.1kN/s). At these test conditions, the normal CCG tests may take thousands of hours until the crack length reaches about a/W =0.7. However, it is not possible to do all tests in this way in three years, a sine waveform fatigue was intruded to accelerate the crack growth after a limited crack growth under static loading (1^{st} CCG) if the extremely low crack growth rate was observed. This fatigue was conducted on the same testing machine and temperature at a frequency of 0.25 Hz and a stress ratio of 0.1, the maximum loading was the same as the static loading. When the crack length grew to a certain amount, the loading was switched to static loading again, and the second creep crack growth (2^{nd} CCG) was started with a longer crack length. Since the loading of the 2^{nd} CCG was the same as that of the 1^{st} CCG,

the crack driving force would be larger with the longer crack length and the crack growth rates increased which allowed the tests to be completed faster. After a certain amount of crack growth in the 2nd CCG, the static loading is stopped before a/W=0.7. To protect the creep crack tip and easy to do the crack length calibration, the 2nd fatigue loading was applied with the same condition as the previous high-temperature fatigue. The furnace was turned off after certain fatigue crack growth. The test pieces were split into two parts after being cooled to room temperature.

3.3.4 Test matrix

In order to investigate the creep crack growth resistance of T92 and BG12Cr at different temperatures, five CCG tests have been done for each material in this project, the test conditions were 6 kN and 10 kN of loading at 600℃, 3 kN and 6 kN of loading at 650℃ and 3kN of loading at 700℃. The test matrix for creep crack growth was shown in Table 3. 4.

3.3.5 Crack length calibration

A Keyence VHX-6000 optical microscope was used to examine the fracture surfaces of the tested specimens. The crack length corresponding to each beach mark—formed due to changes in the loading waveform—was identified based on differences in morphology and contrast. Post-test observations revealed that the crack front was non-uniform and arched, making surface crack measurements insufficient to represent the actual crack size. To address this, an area-based calibration method was introduced(85). The area between successive beach marks was measured, and the corresponding average crack length was calculated by dividing the measured area by the specimen thickness. A linear relationship was then established between the measured d.c.p.d signal and the calculated equivalent crack length, including the initial

length at the onset of creep crack growth.

3.3.6 K and C* calculation

The stress intensity factors K and C* can be calculated with the crack length at any given time. K can be calculated using the following equations, according to ASTM E1457-23.

$$\mathrm{K} = \mathrm{Y(a/W)}\sigma\sqrt{a} \qquad Equation\ 3.1$$

$$\mathrm{Y} = \sqrt{\frac{W}{a}}\left[\frac{2+\frac{a}{W}}{\left(1-\frac{a}{W}\right)^{\frac{3}{2}}}\right] f\left(\frac{a}{W}\right) \qquad Equation\ 3.2$$

$$\mathrm{f}\left(\frac{a}{W}\right) = 0.886 + 4.64\left(\frac{a}{W}\right) - 13.32\left(\frac{a}{W}\right)^2 + 14.72\left(\frac{a}{W}\right)^3 - 5.6\left(\frac{a}{W}\right)^4 \qquad Equation\ 3.3$$

$$\sigma = \frac{F}{BW} \qquad Equation\ 3.4$$

where σ is the monotonic stress applied, Y is the compliance, F is the force applied. The stress intensity factor for side-grooved specimens used in this study K_n can be derived by:

$$K_n = K\sqrt{\frac{B}{B_n}} \qquad Equation\ 3.5$$

Corresponding C^* values are calculated using the equations below.

$$C^* = \frac{P\dot{\Delta}^{CMOD}}{B_N(W-a)} H^{CMOD}\eta^{CMOD} \qquad Equation\ 2.6$$

$$H^{CMOD} = \frac{N}{N+1} \qquad Equation\ 2.7$$

where F is the force applied, B_N is the net width of the sample, $\dot{\Delta}^{CMOD}$ is the crack mouth

displacement change rate measured from the clip-on gauge, η^{CMOD} equals to 2.20 according to ASTM1457-23 with test piece geometry (C(T)) and a/W range (0.45-0.7) and N is the creep index of the material at the same temperature.

According to the ASTM standard E1457-23, only data obtained after the onset of extensive creep(t_T) and after 0.2 mm of crack extension ($t_{0.2}$) are valid for C* calculation.

3.4 Microhardness measurement

The microhardness measurements were carried on as-received T92 and BG12Cr test pieces, the T92 and BG12Cr with additional heat treatment. The Vicker hardness value of each material was tested on the Struers Durascan 40 machine with a load of 0.1kg for 10 seconds. 450 measurements were carried out on each polished metallographic sample. The indents typically measure between 0.025 mm and 0.03 mm. The indents were placed in a 2.9 x 1.4 mm rectangular with a space of 0.1 mm between the indents.

CHAPTER 4 Microstructure of T92 and BG12Cr

4.1 Microstructure of as-received material

This section presents the initial microstructure of T92 and BG12Cr before any heat treatment or testing. Optical microscopy, SEM, and TEM were used to compare key features, including martensite lath structure, precipitates, and second-phase particles.

4.1.1 Optical images of the microstructure of as-received T92 and BG12Cr

The optical micrographs of T92 and BG12Cr with the same magnification in as received condition are shown in Figure 4. 1. The microstructure of T92 and BG12Cr are both tempered martensite structures, but as shown in Figure 4. 1(b), there are some δ-ferrites sited at prior austenite grain boundaries which are formed in the normalizing process. Both images are taken at the same magnification for direct comparison

4.1.2 SEM images of the microstructure of as-received T92 and BG12Cr

Figure 4. 2 shows the SEM images of T92 and BG12Cr in as-received condition. The PAG size in the T92 is smaller than in the BG12Cr. In BG12Cr, most δ-ferrite formed at the PAGBs as Figure 4. 2(d)&(e) but still some of them formed in the PAG shown in Figure 4. 2(f). There are some large particles formed around δ-ferrite and along the PAGBs, and small particles formed along the lath boundaries and within the lath.

4.1.3 TEM results of the microstructure of as-received T92

The bright field (BF) and high angle annual dark field (HAADF) STEM images have been shown in Figure 4. 3. Figure 4. 3a shows that there are a lot of large precipitates on the PAGBs, and lath boundaries are decorated with few small precipitates.

The EDS mapping results with HAADF STEM image are shown in Figure 4. 4 which are used

to identify the precipitates. The particles are distributed on the PAGBs containing Cr, W, Mo and C which are identified as (Cr, Mo, W) rich carbides(e.g. particle a). The bottom part of the large particle a shows higher W and Mo content than the rest part of the particle suggesting that is another particle which may be (W, Mo)-rich intermetallics (particle b). The Ti-rich carbonitride (particle d) is covered by (Nb, V)-rich carbonitride (particle c). And the small V-rich carbonitride (e.g. particle e) is distributed in the PAGs and the large V-rich carbonitride (particle f) is distributed on the PAGBs.

The elements of particles in the PAG are confirmed by the EDS spectrums shown in Figure 4. 5 a&b which suggests they are (Nb, V)-rich carbonitride and V-rich carbonitride.

The EDS spectrum from the particle on PAGB is shown in Figure 4. 6 a which shows that is (Cr, Mo, W)-rich carbide and the Selected area diffraction pattern (SAD) of [11-2] from this particle is shown in Figure 4. 6 b. The particle on the boundary is fcc $M_{23}C_6$ carbide with a lattice parameter of a=1.06 nm which is indicated by diffraction analysis.

There are some particles on the PAGBs that show brighter contrast than $M_{23}C_6$ in the HAADF image (e.g.Figure 4. 7a). The element Map EDS analysis in Figure 4. 4 shows they are rich in W and Mo. The line scan path has been shown in Figure 4. 7 a, and EDS analysis in Figure 4. 7 b shows that particles contained 51.7%Fe, 13.4%Cr, 20.2%W, 13.1%Mo, 0.8% Mn and 0.8%C and the elements are confirmed by the EDS spectrum in Figure 4. 7 c. Diffraction analysis (Figure 4. 7 c and d) indicates that this particle is a hexagonal structure $(Fe, Cr)_2(Mo, W)$ Laves phase with a = 0.48 nm and c = 0.78 nm. The Cr enrichment at PAGBs is detected by line scan shown in Figure 4. 8.

4.1.4 TEM results of the microstructure of as-received BG12Cr

The typical BF and HAADF STEM images of BG12Cr are shown in Figure 4. 9, a high density of dislocation was found in the laths.

Figure 4. 10 shows the HAADF STEM and elemental EDS maps of BG12Cr. The EDS maps show the (Cr, Mo, W)-rich carbides are mainly at PAGBs (e.g. particle a), (Nb, V)-rich carbonitrides (particle b) at PAGB and Cu particle (e.g. particle c) in the PAG.

Figure 4. 11 shows the high magnification HAADF STEM image and elemental EDS maps of BG12Cr. The high magnification EDS maps show that the size of (Cr, Mo, W)-rich carbides are less than 100 nm and some small particles are (Nb, V)-rich carbonitrides or Cu particles with the size of 20~30 nm.

The EDS spectrum from the carbide on boundary and diffraction analysis indicated that the (Cr, Mo, W)-rich carbide is fcc $M_{23}C_6$ carbide with the lattice parameter of a =1.06 nm, shown in Figure 4. 12 a&b.

There are a number of nanoparticles were formed interior grain. Figure 4. 13 shows the small particles pining the dislocation which can increase the strength of BG12Cr.

The EDS maps were used to identify the type of particles pinning the dislocation. As shown in Figure 4. 14, they are (Cr, Mo, W)-rich carbide which is the small $M_{23}C_6$ carbide and some of them are Cu particles.

Both T92 and BG12Cr exhibit tempered martensite microstructures with $M_{23}C_6$-type carbides and MX-type carbonitrides. The key difference is the presence of δ-ferrite and Cu nanoparticles in BG12Cr.

4.2 Microstructure after different heat treatments

This section presents the microstructural differences between T92 and BG12Cr after tempering at different temperatures.

4.2.1 Microstructure of T92 after heat treatment

The microstructures of T92 after different heat treatments are shown in Figure 4. 15. At lower tempering temperatures, the precipitates are finer and fewer, while higher tempering temperatures promote coarsening and increased precipitation. Lath structure recovery is observed in the microstructure tempered at 820 °C.

4.2.2 Microstructure of BG12Cr after heat treatment

The microstructures of BG12Cr after different heat treatments are shown in Figure 4. 16. All BG12Cr samples show tempered martensite microstructure and the precipitates outline the PAGBs. Only a few fine particles were found on the PAGBs and lath boundaries in the microstructure of the sample which was tempered at 760°C as shown in Figure 4. 16a. As shown in Figure 4. 16 b2, more and larger particles were found on PAGBs and some fine particles in the PABs in the microstructure of BG12Cr T780. Continuous particles were found on the PAGBs in both microstructures of BG12Cr T800 and BG12Cr T820, but more and larger particles sit in the PAGs in the microstructure of BG12Cr T820 than that of BG12Cr T800, as shown in Figure 4. 16 c2&d2. In addition, the spherical δ-ferrites are found in all samples sited at PAGBs and within the PAGs.

Heat treatment leads to visible changes in precipitate distribution and size in both materials. The higher tempering temperatures result in increased particle size and density, especially at PAGBs. The presence of δ-ferrite remains stable in BG12Cr.

4.3 Microstructure after CCG tests

This section compares the microstructural changes in T92 and BG12Cr after creep crack growth (CCG) testing. Observations were made in regions near and far from the crack. The combined thermal and stress effects during CCG influence microstructural evolution and precipitate behaviour.

4.3.1 Microstructure of T92 after CCG tests

The microstructure of the as-received T92 and away-from-crack region on T92 after the CCG test at 650°C were shown in Figure 4. 17 . Basically, no clear particles were found with as-received condition with the magnification of 1000x, but after heated at 650°C for 188h, there are many spherical particles were found on the PAGBs. After the test last 2348.6h at 650°C, there are more and larger spherical particles were found on the PAGBs and also some small particles formed in the PAGs were found.

Figure 4. 18 shows the microstructure of T92 after tests at 650°C with the loading of 3 kN in different regions. Compared to the away-from-crack region, the particles in the near-crack region were more and larger and some rod-like particles which were darker than the matrix were found in this region.

4.3.2 Microstructure of BG12Cr after CCG tests

The microstructure of as-received BG12Cr and away-from-crack region on BG12Cr after the CCG test were shown in Figure 4. 19. Similar to T92, the particles could not be clearly found in the as-received BG12Cr with the magnification of 1000x, but after the test at 650°C with the loading of 6kN which is last 886.9h, many spherical particles were clearly found at PAGBs and few in the PAGs in the away-from-crack region. After the test at 650°C with the loading of 3

kN (2587.2h), the larger spherical particles were found at PAGBs and the particles in the PAGs were more and larger in the away-from-crack region.

Figure 4. 20 shows the microstructure of BG12Cr tested at 650°C with the loading of 3kN in different regions. Compared to the away-from-crack region, the near-crack region contained some new particles which were rod-like and dark. In the region with a short crack length (K_n=14.3 MPa√m), the dark rod-like particles were dominant on the PAGBs and lath boundaries. And in the region with a longer crack length (K_n=15 MPa√m), there were fewer and smaller dark rod-like particles and they were immediately adjacent to grey particles.

The microstructure of BG12Cr tested at 650°C with the loading of 6 kN is shown in Figure 4. 21. Small grey particles close to the dark rod-like particles were found in the near crack region.

Post-CCG microstructures of both materials exhibited precipitate coarsening. Compared to the away-from-crack region, both T92 and BG12Cr showed localized microstructural degradation near the crack, including further coarsening and the formation of new rod-like particles.

4.4 The coarsening zone and Cr depletion zone

The near-crack region shows a different microstructure from the away-from-crack region on both materials. To facilitate direct microstructural comparison across regions, additional SEM and backscattered electron images for BG12Cr and T92 tested at 650 °C under 3 kN are provided below.

4.4.1 The SEM images of the Microstructure

The whole creep crack of BG12Cr tested at 650°C with the loading of 3kN is shown in Figure 4. 22. As shown in Figure 4. 22, there is a precipitate coarsening zone close to the crack, and

the zone width is 82 um in the short crack region, 60um in the mid crack region, 21 um in the long crack region and no obvious precipitates coarsening were found at the end of the crack.

Figure 4. 23a shows the three zones with different microstructure features below the fracture surface. And Figure 4. 23 b&c shows the different microstructure features in three zones clearly with higher magnification SEM images. Zone 1 is the region right below the fracture surface with few or no obvious precipitates, Zone 2 is the region beneath Zone 1 with a larger amount of precipitates and Zone 3 is the region away from the crack which means less affected by the stress and the oxidation. Backscatter image Figure 4. 23d shows there are two types of precipitate in Zone 2, the bright spherical particles are mainly on the PAGBs and the rod-like particles on the martensite lath boundaries. The bright spherical particles are also found in zone 3.

As shown in Figure 4. 24 a&b, similar to tested BG12Cr, three different feature zones with two types of precipitate were found in the T92 test. Figure 4. 24 c&d shows the two types of precipitate, the spherical particles are mainly on the PAGBs, and some individual particles are within the PAGs or coalesced with rod-like precipitates. The rod-like precipitates are mainly on the martensite lath boundaries.

4.4.2 EDX result

As shown in Figure 4. 25, compared to spectrum 25 which is the matrix, the bright particle (spectrum 26) is (Cr, W, Mo)-rich carbide, rod-like precipitates (spectrum 27&28) are Cr-rich nitride and grey particle(spectrum 29) in the lath is the Cr-rich carbon-nitride.

Figure 4. 26 shows the EDX map result from the BG12Cr tested at 650°C with the loading of 3kN. Particle a is a grey rod-like particle within PAG which is the (Cr, V)-rich carbon nitride.

Particle b is a large bright particle on the PAGB which is a (Cr, W, Mo)-rich carbide. Particle c is a small Nb-rich nitride. The Cu particles were widely distributed in the PABs and on the PAGBs with a size of 180 - 700 nm.

The EDX map result from the P92 tested at 650°C with the loading of 3 kN is shown in Figure 4. 27, particle a is the bright particle on the PAGBs which is the (Cr, W, Mo)-rich carbide, particle b is a V-rich carbon-nitride under a rod-like particle, particle c is the Nb-rich carbon-nitride on the PAGB and particle d is the rod-like precipitate in the lath which is (Cr, V)-rich carbon-nitride.

The EDX result of P92 tested at 650°C with the loading of 3kN is shown in Figure 4. 28. The Cr content of Zone 1(spectrum 5: 5.64% and spectrum 3:4.67%) is lower than that of Zone 2 (spectrum 6: 8.93% and spectrum 4:10.42%).

Precipitate coarsening zones were identified near the crack regions in both T92 and BG12Cr, with the width of the affected area decreasing along the crack growth direction. Three distinct microstructural zones were observed below the fracture surface, each with different precipitate morphology and density. EDX analysis confirmed Cr depletion in the region closest to the crack, particularly in Zone 1.

4.5 Distribution of prior austenite grain size

This section presents the measurements and comparison of prior austenite grain (PAG) size and distribution in as-received and heat-treated conditions for T92 and BG12Cr. PAG size is a key microstructural parameter that influences mechanical performance, particularly creep resistance and fracture behaviour.

All BG12Cr materials have a larger average PAG size than T92. The average PAG size is

similar in as-received BG12Cr (46um) to that of BG12Cr N+T780 which is 49 um. The average PAG in T92 is around 16 um which is obviously smaller than in BG12Cr. In T92, the PAGs distribution range is narrow, over 75% of PAGs are between 5 um and 15 um, and all BG12Cr materials have a broad PAG size distribution which is between 2.5 um to 135 um. The BG12Cr and BG12Cr N+780 contained some very large PAGs which are over 100 um.

4.6 Hardness

This section presents the hardness values of T92 and BG12Cr under various conditions, including as-received, after heat treatments, and post-CCG tests. As hardness is sensitive to microstructural features, the measurements provide insight into microstructural changes such as recovery, precipitation, and phase stability resulting from thermal exposure.

4.6.1 The hardness of T92

Figure 4. 30 shows the hardness of T92 under different heat treatments. The hardness of as -as-received T92 is around 236 HV which is similar to T92 N+T780 which means the re-normalizing has no significant effect on the hardness of T92. After normalizing, the sample achieves the highest hardness (467 HV) which drops after tempering. The hardness of tempered samples decreased as the tempering temperature raising, from 257 HV for T92 N+T760 to 219 HV for T92 N+T820.

4.6.2 The hardness of as received, after re-heat treatment and post-test BG12Cr

As shown in Figure 4. 31, the BG12Cr N has the highest hardness value (391 HV). The tempering temperature effect on hardness is different from T92 to BG12Cr, although tempering still reduces the hardness value of BG12Cr. The specimen with the lowest hardness value is the material tempered at 780°C and the value of hardness for BG12Cr raised with increasing

tempering temperature from 780°C to 820°C. The N+T820 has the highest hardness value in tempered material.

The hardness of tested BG12Cr specimens is shown in Figure 4. 32. The hardness of tested BG12Cr specimens was lower than the as-received BG12Cr. The specimen tested at 650°C for 2587h had the lowest hardness value (220 HV) and the specimen tested at 600°C for 1611h had the highest hardness value (26 7HV) in the tested specimen. The hardness value of the specimen tested at 650°C for 887h (254 HV) is higher than that of the specimen tested at 700°C for 195h (233 HV).

T92 exhibits a conventional softening trend with increasing tempering temperature. In contrast, BG12Cr shows a non-monotonic response, with a minimum hardness at 780°C and increased values at higher tempering temperatures. Post-creep tests show hardness reduction in both steels, more pronounced after longer durations, suggesting precipitate coarsening and matrix recovery. BG12Cr retains higher hardness than T92 under all examined conditions.

CHAPTER 5 Creep crack growth behaviour

5.1 Experiment results

Table 5. 1 shows the details of the creep crack growth tests with the test condition, materials of specimens, the value of initial stress intensity factor K_i, the crack growth length and the test time during the creep crack growth stages, the time to establish extensive creep t_T for each creep region and the time for the initial 0.2 mm crack growth $t_{0.2}$. The crack length growth is very short for some creep crack regions because the creep crack growth rate is relatively low in these regions. To reduce the test time, fatigue is introduced to increase the crack length for a higher driving force and a higher crack growth rate. The reason that t_T and $t_{0.2}$ were not determined for these creep regions was that the test time in these regions was not enough to establish extensive creep or the crack length growth was less than 0.2 mm. The value of initial stress intensity factor K_i are close in two materials (typically < 2 MPa√m) with the same testing condition (test temperature and loading) and all specimens have the same testpieces geometry which means the crack tip condition is similar in the specimens of two material after the pre-crack process.

The experiment results of CMOD and crack length for the CCG tests at different temperatures are shown in Figure 5. 1 to Figure 5. 3. At the beginning of the test, both crack growth and CMOD grow rapidly with a deceleration growth rate in a very short term (stage 1) and it grows constantly in the middle period of the test (stage 2), as shown in Figure 5. 4 to Figure 5. 11, at the later stage of the test, the growth rate accelerated (stage 3) (Figure 5. 1 to Figure 5. 3). In some of the tests, there is no obviously accelerating stage which is might because the test time of 1st Creep is not enough for them to reach that stage.

For comparing the growth behaviour of CMOD and crack length in the CCG test, the CMOD

and crack growth of each testpiece were plotted separately. To identify the different stages in the crack length–time and CMOD–time curves, a fitted straight line was introduced—similar to the method used to define the secondary stage in conventional creep curves. An example is shown in Figure 5. 4. The crack growth and CMOD of T92 600°C 6kN are shown in Figure 5. 4. The CMOD reached stage 2 at around 420h, which is earlier than the crack length which is at 475h. For T92 650°C 3kN, stage 2 of CMOD was around 60-1600h and the acceleration stage of crack growth was from around 600h which is shown in Figure 5. 5. As shown in Figure 5. 6, the time for crack growth achieved the acceleration stage (70h) was later than the time for CMOD which were 160h respectively for T92 650°C 6kN. The Crack growth of T92 700°C 3kN had a constant growth rate until 55h and the time of stage 2 is about 25 to 65h for its CMOD which is shown in Figure 5. 7.

For BG12Cr 600°C 6kN, stage 2 of crack growth is from around 250 to 500h, while the CMOD did not reach stage 2 in 1st creep test time which is shown in Figure 5. 8. As shown in Figure 5. 9, The CMOD grew at a constant growth rate from around 35h to 300h but crack growth was from around 200h to 500h for BG12Cr 650°C 3kN. For BG12Cr 650°C 6kN, its CMOD took about 100h to reach stage 2 and about 500h to reach stage 3, while crack growth took about 65h and 300h, as shown in Figure 5. 10. Figure 5. 11 shows that the CMOD of BG12Cr 700°C 3kN achieved stage 2 after about 90h and stage 3 after around 450h, and for its crack growth, stage 2 is from about 65h to 280h.

5.2 C* for T92 and BG12Cr

The creep crack growth resistant curves in the form of crack growth rate da/dt vs C* were shown in Figure 5. 12. Compared to the curves in Figure 5. 12 b, d and f, the curves in Figure

5. 12 a, c and e included the data points before extensive creep was established and $t_{0.2}$. Follow the ASTM standard E1457-23, only the data of crack length and CMOD after extensive creep established and $t_{0.2}$ are valid for the calculation of C*. As shown in Figure 5. 12 b, the lines of data points for each test have a similar slope, regardless of the test conditions and materials. Figure 5. 12 d shows that the curves of T92 tested at 650°C and 700°C are close and the curves for 600°C are a little further away from the previous two curves. As shown in Figure 5. 12 f, all data points were basically on a straight line which for BG12Cr tested with different test conditions.

For a clear comparison, the curves for both materials tested at a temperature of 600°C,650°C and 700°C are shown in Figure 5. 13 a, b and c respectively and the curves for both materials tested with the loading of 3 kN, 6 kN and 10 kN are shown in Figure 5. 13 d, e and f respectively.

In Figure 5. 13 a the curve of BG12Cr is above the curve of T92 which means with the same C*, the crack growth rate of BG12Cr is higher than that of T92 at 600°C. The data from tests on BG12Cr at 600°C are on a line even with different loading, the only difference is the position of the curves and some of them are overlapped. But for the data from tests on T92, the data from the 2nd creep with the loading of 6kN is out of the line formed by the data from the 1st creep with the loading of 6kN and the data from the test with the loading of 10 kN. And similar to the curves of BG12Cr, the test with the loading of 6 kN has a lower creep crack growth rate and lower value of C* than with the loading of 10 kN on T92.

As shown in Figure 5. 13 b, all data points from tests at 650°C were within a narrow band, but the positions of curves for BG12Cr and T92 were different, even though the test conditions were the same.

The curves of tests at 700°C are shown in Figure 5. 13 c, the data from tests on BG12Cr and T92 were essentially on the same line.

As shown in Figure 5. 13 d, the four curves are from the tests with the loading of 3kN at different temperatures and on different materials, but they were still on a narrow band. And the tests at 700°C have higher initial C* and da/dt than the tests at 650°C.

For the tests with the loading of 6 kN, the curves are shown in Figure 5. 13 e, except the 1st creep of the test on T92 at 600°C with the loading of 6 kN, other data from tests at 600°C and 650°C on both materials were on a narrow band. The tests at 600°C have lower initial C* and da/dt than the tests at 650°C.

As shown in Figure 5. 13 f, BG12Cr has higher da/dt than T92 with the same C* but the T92 has higher initial C* and da/dt at 600°C with the loading of 10 kN.

5.3 K for T92 and BG12Cr

Due to the curved and non-uniform crack front observed post-test, surface crack length was not representative of the actual crack geometry. Therefore, an equivalent crack length—defined as the average length corresponding to the same fractured area—was used for stress intensity factor (K) calculations. This area-based approach accounts for the reduction in load-bearing section and provides a geometrically representative input for fracture mechanics analysis. The method is consistent with ASTM E647-22 and prior studies (85), where average or equivalent lengths are adopted to address tunnelling or arched crack fronts.

Figure 5. 14 shows the curves of da/dt vs K_n for both material tests at 600,650 and 700°C. This figure can be used to compare the crack growth resistance of two materials at the same loading, temperature and testpiece geometry. The initial K_n for tests with the same loading at 650°C and

700°C on both materials is close. The difference in crack growth resistance between BG12Cr and T92 is not obvious with the loading of 3 kN, the T92 has a higher crack growth rate than BG12Cr with the same K_n value and the gap of crack growth rate is slightly increased with the higher K_n value at 650°C and 700°C. For the tests with the loading of 6 kN at 650°C, the crack growth resistance between T92 and BG12Cr is the highest, the crack growth rate of T92 just slightly higher than BG12Cr at the beginning with K_n= 22 MPa√m, but the difference of crack growth rate increased rapidly with the increase K_n. At 600°C with the loading of 6 kN, in 2nd creep for both materials, the T92 still has a higher crack growth rate with K_n= 29 MPa√m but the crack growth rate of BG12Cr raised rapidly with a tiny increase of K_n and the slope of the curves of BG12Cr is greater than that of T92. For the tests at 600°C with the loading of 10 kN, the difference in crack growth resistance between BG12Cr and T92 is small, the curve of T92 has a higher slope than BG12Cr and they cross at around 48 MPa√m of K_n.

5.4 The fraction of CMOD growth rate from the creep

Figure 5. 15 shows the fraction of CMOD growth rate induced by the creep ($\Delta \dot{c}$). As shown in Figure, all the CMOD growth rates are 100% creep-induced at the beginning of the tests, and keep dropping with the test's time increase. In the tests at 600°C with the loading of 10 kN on T92, the $\Delta \dot{c}$ fraction dropped rapidly after 75h and reached nearly 65% at the end of the test. At the end of 2nd creep in the test at 600°C with the loading of 6 kN on BG12Cr, the the $\Delta \dot{c}$ fraction dropped to around 86%. And $\Delta \dot{c}$ fraction is over 90% for remaining tests at the end of tests.

5.5 Cross-section of T92 and BG12Cr specimens after test

5.5.1 Cross-section of T92 test-pieces backscatter images

The cross-section of the creep crack tested at 600°C with the loading of 6 kN on T92 is shown in Figure 5. 16. In 1st creep region, the voids were mainly formed and stayed alone within the PAGs, and only a few void coalescences are found at the near crack region and some void coalescences are linked with the crack, shown in Figure 5. 16 b. The secondary crack was found in the 2nd creep region, shown in Figure 5. 16 a, it was growing into a PAG and the most of voids coalesced within PAGs and at the PAGBs in the 2nd creep region.

Figure 5. 17 shows the representative backscatter cross-section view of T92 tested at 600°C with a loading of 10 kN. The voids distributed at PAGBs and within the PAGs, some void coalescences were found within PAG and a secondary crack was growing through the PAGs. And also, a large void connected with a secondary crack was found shown in Figure 5. 17 b), both void and crack were in the PAG.

The cross-section view of T92 tested at 650°C with the loading of 3kN is shown in Figure 5. 18. As shown in Figure 5. 18 c), at the very beginning of the creep region ($14.4<K_n<14.5$ MPa√m), the voids were small, the voids became larger with higher K_n ($14.5<K_n<14.6$ MPa√m) and the voids started to grow together at the near crack region. The void coalescences dominated the rest of the creep region ($K_n>14.6$ MPa√m) in the short crack region. The voids coalescences were found both on PAGBs and within PAGs but mainly within PAGs on all three regions of the crack. Some void coalescences distributed on PAGBs and within PAGs were linked to form a larger void coalescence as shown in Figure 5. 18 c3. The secondary cracks growing across the PAGBs were found on both the mid and the long crack region as shown in Figure 5. 18

a2&b3. More void coalescences were found in the middle crack region than in the short crack region and their sizes were larger. And the size of void coalescences in the long crack region is larger than in the mid crack region and some of them were growing together to form secondary cracks.

The backscatter electron images of the cross-section views for creep crack growth regions on T92 tested at 650°C with 6 kN are shown in Figure 5. 19. Similar to T92 tested at 650°C with 3kN, the voids were main just at the very beginning of creep crack region, the void coalescences were found on both PAGBs and mainly within PAGs. And the void coalescences on PAGBs and within PAGs were growing to form a larger void coalescence as shown in Figure 5. 19 c3. And the secondary cracks growing through PAGs were found in both the short crack and middle crack regions. In the middle crack region, larger void coalescences connections were found in front of the secondary crack as shown in Figure 5. 19 b2, and most of the void coalescences were formed within the PAGs. Very severe plastic deformation was found at the long crack region and the voids in this region were very large and mainly within PAGs as shown in Figure 5. 19 a1.

Figure 5. 20 shows the cross-section views for creep crack growth regions on T92 tested at 700°C with 3 kN. Small voids were found mainly at the very beginning of the crack region both on PAGBs and within PAGs and some void coalescences were found at the short crack region shown in Figure 5. 20 c. As shown in Figure 5. 20 b, more void coalescences were found both on the PAGBs and within PAGs in the middle crack region, and some large void coalescences within PAGs connected to form the secondary crack, the void coalescences. However, there were also some void coalescences on the PAGBs connected to form the secondary crack which

is in front of the first secondary crack. A large secondary crack was found across the PAGs in the long crack region shown in Figure 5. 20 a.

5.5.2 Cross-section of BG12Cr test-pieces backscatter images

The cross-section views for creep crack growth regions on BG12Cr tested at 600°C with 6 kN are shown in Figure 5. 21. The voids were found both on the PAGBs and within PAGs in both creep regions. A secondary crack was found in the 1st creep region and it grew through the PAGs. Some δ-ferrites and a few void coalescences were found in both regions. The secondary crack in 2nd creep was formed by voids distributed on PAGBs and the voids are mainly on the PAGBs shown in Figure 5. 21 a, the voids in the 2nd creep region were mainly on the PAGBs.

Figure 5. 22 shows the cross-section views of the BG12Cr test piece tested at 600°C with 10 kN. The voids were mainly formed on the PAGBs in the whole creep region. A secondary crack formed by voids on the PAGBs was found in the short crack region as shown in Figure 5. 22 c. Compared to the short crack region, More voids were found in the mid crack region and few void coalescences were found on the PAGBs as shown in Figure 5. 22 c. As shown in Figure 5. 22 a, a larger secondary crack on the PAGBs was found in the long crack region.

The cross-section views of BG12Cr tested at 650°C with 3 kN are shown in Figure 5. 23. In the short crack region, very few voids were found on PAGBs and within PAGs. The size of voids in the mid-crack region is larger than in the short-crack region and a few void coalescences were found on the PAGBs and within PAGs. More voids grew to form void coalescences in the long crack region.

Figure 5. 24 shows the cross-section views for creep crack growth regions on BG12Cr tested at 650°C with the loading of 6 kN. At the beginning of the crack, the voids were mainly found on

PAGBs and a few voids were found within the PAGs, and only a few void coalescences were mainly found on the PAGBs as shown in Figure 5. 24 c. At the mid-crack region, more large voids and void coalescences were found both on PAGBs and within PAGs. Some void coalescences on the PAGBs and within PAG were growing together to form larger void coalescences which are shown in Figure 5. 24 b2. A large secondary crack across PAGs was found in the long crack region which is shown in Figure 5. 24 a. The δ-ferrites were found on all three crack regions.

5.6 Fractography of T92 and BG12Cr

5.6.1 Optical images of the Fracture surface of T92 and BG12Cr

Figure 5. 25 shows the optical fractography of test pieces for both materials.

The crack area exposed in the high-temperature environment shows dark and grey, and the silver area is caused by room temperature fatigue or the process of pulling the test pieces into two halves which is for observing the fracture surface. The dark areas are the creep regions, and the grey areas between the two dark areas on some test pieces are the high-temperature fatigue. High-temperature fatigue is used to increase the crack length for 2nd creep and protect the crack area of creep which are the grey areas before the silver colour area.

5.6.2 SEM images of the fracture surface of T92

The SEM fractography of both creep crack regions tests at 600°C with the loading of 6 kN on T92 are shown in Figure 5. 26. The fracture surface of the 1st creep region is covered by thick oxides (e.g. Figure 5. 26 a), but still can find some dimple-like features which are the representative features of ductile fracture at the deep layer of fracture surface in Figure 5. 26 b. In the 2nd creep region, the surface is covered by oxide but there are many voids and dimples

that still can be found in Figure 5. 26 c&d.

Figure 5. 27 shows the fractography of creep crack regions tested at 600°C with the loading of 10kN with SEM images. The dimples feature covered by oxide and the secondary crack in the short creep region are shown in Figure 5. 27 a&b. The dimples features are more clearly shown in Figure 5. 27 c&d which is not many oxides formed on the surface of the long crack region due to the short time exposed to the air.

The SEM fractography of both creep crack regions tested at 650°C with the loading of 3 kN on T92 is shown in Figure 5. 28. A lot of large voids can be found in both creep regions.

The fracture surface of creep crack regions tested at 650°C with the loading of 6 kN on T92 with SEM images is shown in Figure 5. 29. The fracture surface is dimples-like feature dominant and a secondary crack is found in Figure 5. 29 b.

The SEM fractography of both creep crack regions tested at 650°C with the loading of 3 kN on T92 are shown in Figure 5. 30. At the beginning of the creep region, there are few intergranular failure (IG) features which are cracks along PAGBs, but the rest of creep crack region is a completely ductile fracture, featuring large voids and severe plastic deformation and some linkage of voids can be found.

5.6.3 SEM images of the fracture surface of BG12Cr

The SEM fractography of this test is shown in Figure 5. 31. The fracture surface is covered by very thick oxides but a mixture of IG features and dimples can be found in both creep regions.

Figure 5. 32 shows SEM images of fractography of creep crack regions tested at 600°C with the loading of 10 kN on BG12Cr. The ice cube feature is very clearly shown in Figure 5. 32

which is the feature of intergranular failure. One of the ice cube features is measured in Figure 5. 32 b, the size of it is around 60um which is close to the PAG size of BG12Cr.

The SEM fractography of this test is shown in Figure 5. 33. A mixture of IG features and dimples is found in both creep regions. As shown in Table 5. 1, the test time of this test is the longest in all the creep crack growth tests and there are not only thick oxides but also some chromium crystals covering the fracture surface of the 1st creep region.

The SEM fractography taken at different crack lengths along the creep crack growth tested at 650°C with the loading of 6 kN on BG12Cr is shown in Figure 5. 34. A transition of failure mechanism is found in this test piece. It is found the main feature of the fracture surface is IG features at the beginning of the creep region. After some crack growth, the dimples feature is found and it dominates the end of the creep crack.

Figure 5. 35 shows the fracture surface of this test piece. Similar to the test piece after the creep cracks growth test at 650°C with the loading of 6 kN, the transition of failure mechanism is found in this test piece. At the beginning of the crack, the ice cube feature is dominant and one of them has a size of 50.3 um which is close to the PAG size of BG12Cr. The mixture of IG features and dimples is found in the middle length of the crack, and the dimples are the main feature at the end of the crack with some voids. A secondary crack across the void is found at the end of the crack area.

5.7 The observation on the crack tips of interrupted tests

5.7.1 Optical images of interrupted test on T92 and BG12Cr

Figure 5. 36 and Figure 5. 37 shows the unbroken crack of BG12Cr and T92 after the interrupted test. The test temperature of T92 and BG12Cr was 650°C with a loading of 6 kN with a similar

pre-crack length. The pre-crack tip opening of T92 after the interrupted test is 192 um with 437um of creep crack growth length and that of BG12Cr is only 39um with 1054um of creep crack growth length. And the voids formed during the creep crack tests were visible on the optical images. The distribution area of voids around the creep crack of T92 is much larger than that of BG12Cr whose voids were mainly around the front part of the creep crack of BG12Cr.

5.7.2 SEM images of interrupted test on T92 and BG12Cr

As shown in Figure 5. 39, there are many large voids around the crack and they were distributed both on the PAGBs and within the PAGs. There are three large voids connected just in front of the crack which is shown in Figure 5. 38 c.

Figure 5. 39 shows the SEM images of BG12Cr after the interrupted test. There were some small voids connected on the PAGB and formed the crack in front of the crack tip, as shown in Figure 5. 39 a. And some large voids were connected on the PAGB above the main crack which is shown in Figure 5. 39 b. Figure 5. 39 c and d show that the voids around the crack were mainly on the PAGBs and some dark rod-like particles were found close to the crack.

CHAPTER 6 Discussion

This study aimed to investigate the microstructure and creep crack growth behaviour of BG12Cr, compare the creep crack growth resistance of BG12Cr with T92, figure out the creep crack growth mechanism and understand the microstructure evolution of BG12Cr during the creep crack growth testing.

6.1 The difference between the microstructure of BG12Cr and T92

As the most widely used heat-resistant steel in the thermal power plant industry, T92 has a tempered martensitic structure with fine precipitates e.g., $M_{23}C_6$ and MX which provide good creep resistance, oxidation resistance and thermal stability at high temperatures. However, the maximum working temperature for T92 is limited to 625℃. In response to this limitation, Baowu Steel designed a new 12Cr martensitic steel with superior oxidation resistance, BG12Cr, which aims to achieve better creep resistance than T92, enabling it to operate for extended periods in the power plant at a temperature of 650℃. Understanding the microstructure of BG12Cr and the difference between the B12Cr and T92 is important for the further development of BG12Cr.

The fundamental microstructure of both T92 and BG12Cr are tempered martensitic structures, which are lath structures decorated by nano-sized precipitates at lath boundaries and PAGBs (Figure 4. 1, Figure 4. 2, Figure 4. 3 and Figure 4. 9). The principal differences between T92 and BG12Cr are that there are few δ-ferrite in BG12Cr and it has a larger average PAG size and thinner lath width (around 0.284 um) than the T92 (around 0.509 um) (Figure 4. 1, Figure 4. 2 and Figure 4. 29). The δ-ferrites are mainly at PAGBs and some also located within the PAGs. For improved comprehensive properties, many alloying elements are added in BG12Cr

which include ferrite stabilizer elements (Cr, W, V and Nb). The ferrite stabilizer element prompted the formation of δ-ferrites by reducing its formation temperature.

The increasing amount of δ-ferrites reduces the tensile strength of steel at high temperatures (86). The δ-ferrites improved short-term creep resistance due to their high W and Cr content, which is favoured by nucleation of the fine laves phases. However, the formation of the Laves phase may reduce microstructural stability and creep rupture strength during the long-term creep (41).

The average size of PAG in T92 is concentrated in the range of 5-15 um, the number of PAGs in this range is near 75% of the total PAGs. Compared to the T92, BG12Cr has a broad average PAG size distribution ranging from 5um to 130um (Figure 4. 29). The larger PAG size is normally suggested to have a higher minimum creep rate when the PAG size is less than 50 um (87,88). In addition, the lath width of BG12Cr (0.27um) is smaller than that of T92 (0.41um) which provides more lath boundaries, potentially enhancing strength via lath boundary strengthening (49,50).

In the T92 sample, five types of precipitates were identified: (Cr, Mo, W)-rich carbide ($M_{23}C_6$) and $(Fe, Cr)_2(Mo, W)$ Laves phases, which mainly decorate on the PAGBs, and MX type carbonitride which are Ti-rich carbonitride, (Nb, V)-rich carbonitride and V-rich carbonitride (Figure 4. 4 to Figure 4. 8). Compared to the T92, the BG12Cr samples lacks both the laves phase and Ti-rich carbonitride. However, a large quantity of nano-size Cu particles, measuring 20-30 nm were observed (Figure 4. 10 to Figure 4. 14). These precipitates which decorated the PAGBs and lath boundaries, enhance the material`s strength by retarding the movement of free dislocations and the coarsening of subgrain. Furthermore, they exhibit relative stability at high

temperatures which can retain the creep strength (10).

The extra Cr content of BG12Cr promoted the formation of Cr-containing particles, providing further precipitate hardening. However, the higher content of Cr may reduce the thermal stability of BG12Cr, favouring precipitate coarsening and formation of the new precipitates, the Z phase (26). The incorporation of Co in BG12Cr also contributes to the solid solution strengthening, enhanced strength and creep-resistant properties (31). And also, the Co remains uniformly distributed in the matrix and did not tend to form any precipitate in the microstructures of BG12Cr specimens after testing, demonstrating it can provide the solid solution strengthening stably at the elevated temperature (Figure 4. 10, Figure 4. 25 and Figure 4. 26). This high stability is attributed to the high solubility of Co in ferrite and its poor solubility in the precipitates (32). And also, as an austenite stabilizer, Co can suppress the formation of δ-ferrites (32). The addition of Cu provides precipitate hardening due to the low solubility of Cu in ferrite promoting the formation of Cu-rich particles (33). The nano-sized Cu particles (20-30nm) can improve the creep resistance of the material (31).

6.2 The influence of tempering temperature and ageing on the hardness of T92 and BG12Cr

Tempering temperature plays an important role in the properties of heat-resistant steel. In this study, the normalizing condition and the tempering time of all samples are the same. The hardness result is shown in Figure 4. 30 and Figure 4. 31, BG12Cr exhibits greater hardness than T92 after tempering which indicates that BG12Cr is stronger than T92, which is contributed by the more Cr content, Cu and Co element addition and thinner lath width.

After homogenisation, both materials exhibit peak hardness, primarily due to the formation of

a fully martensitic microstructure upon air cooling from the austenitising temperature. The as-quenched martensite retains a high dislocation density and fine lath substructure, contributing to increased hardness. The matrix also remains highly strained due to the presence of supersaturated carbon, which further enhances solid solution strengthening.

After tempering, the microstructure of the samples was transformed into the tempered martensitic microstructure. During this process, the dislocation density is reduced and the solute atom diffusion from the matrix to the formed precipitates on the PAGBs and lath boundaries and the hardness of the samples drops (89). For the T92 steel normalized at 1060℃ for 1h and 1.5h tempering time, the hardness of samples dropped with raising the tempering temperature from 760℃ to 820℃. The lath size, precipitate size and area fraction of precipitates increased and the dislocation density reduced might be the reason for the hardness reduction of T92 with raising the tempering temperature (89,90).

However, the hardness behaviour of BG12Cr with various tempering temperatures is different, the lowest hardness is achieved by the sample tempered at 780℃, and the increasing tempering temperature raises the hardness of BG12Cr, as shown in Figure 4. 32. There is a high content of alloy elements in BG12Cr which tend to form a large number of precipitates e.g. Carbides, carbonitride and Cu particles. These fine precipitates provide precipitates hardening on BG12Cr microstructure. Typically, the higher tempering temperatures result in the formation of more precipitates during tempering which is beneficial for steel strength, but at the same time, the precipitates tend to grow and coarsen, negating their pinning effect on dislocation movement and reducing the strength of the material. However, the presence of Co can retard the coarsening process of $M_{23}C_6$ and promote the formation of Cr-rich particles. Consequently, a larger amount

of fine precipitates remains in the microstructure of BG12Cr at higher tempering temperatures, and these fine precipitates also retards the recovery of martensite (Figure 4. 16) (31–33). A large amount of fine precipitate contributed to inhibiting the recovery of dislocation, strengthening the PAGB and further increasing the hardness of BG12Cr at higher tempering temperatures. Similar to increasing tempering temperature, Liu Z et al. found that the hardness increased in the first hundreds of ageing at 540℃ on a 12Cr steel containing 5.1% Co (91).

6.3 Microstructure evolution during creep crack growth tests

6.3.1 Effects of thermal exposure on the microstructure of BG12Cr and T92

In the away-from-crack region, the stress effect on microstructure development is minimal, with thermal exposure being the primary factor influencing microstructure development. The effect of thermal exposure is determined by both temperature and exposure time, test time becomes the only variable parameter in the away-from-crack region of specimens tested at the same temperature. The microstructures of BG12Cr and T92 subjected to different test times at 650℃ are shown in Figure 4. 17 &Figure 4. 19, It can be observed that prolonged thermal exposure leads to the precipitation of more and larger particles on PAGBs and within PAGs.

As mentioned earlier, the particle coarsening can result in the loss of pinning effect on dislocation movement. This is evident in the hardness of BG12Cr 650°C 3kN (2587.2h) has a lower hardness value than BG12Cr 650°C 6kN (886.9h). Xu Y et al. reported a similar trend of hardness reduced with the ageing time on a 10.5Cr steel at 650℃ (92). After long-term thermal exposure, the coarsening of $M_{23}C_6$ type and MX type precipitates, formations and coarsening of new phases which are the Laves phase and Z phase, the lath coarsening to form subgrain and dislocation density all contribute to the degradation of creep strength, tensile

strength and impact toughness on 9Cr and 12Cr martensite heat-resistant steel (58,61,92). However, due to the time limit for tests, the longest tests only last 2587.2h, and no severe microstructure degradation has been observed in the away-from-crack region.

6.3.2 Factors that cause particle coarsening and new particle precipitation in the near-crack region of BG12Cr and T92

Abnormal microstructure development in the near-crack region

Figure 4. 18, Figure 4. 20 and Figure 4. 21 illustrate that the near-crack regions have significant differences from the away-from-crack regions in microstructure on both the tested BG12Cr and T92 specimens. The near-crack region is divided into two zones: Zone 1, which contains only fewer particles, and Zone 2, which not only contains a higher concentration of larger particles but also features a new type of particle which is a rod-like particle, as shown in Figure 4. 20, Figure 4. 21, Figure 4. 23 and Figure 4. 24. The new type of particle is a (Cr, V)-rich nitride with a rod-like shape and mainly formed at lath boundaries next to the V-rich nitride (Figure 4. 25, Figure 4. 26 and Figure 4. 27), it might be the Z phase Cr(V, Nb)N (26). The formation of the Z phase normally occurs after several thousand hours of ageing in 12Cr steel and over 10000 hours in P92 steel at 650℃ (26). However, the Z phase can be found in the near-crack region of BG12Cr 650°C 3kN (2587.2h) and T92 650°C 3kN (2348.6h). Additionally, the large (Cr, Mo, W)- rich carbides on both BG12Cr and T92 might be the Laves phase.

Zone 1 has a lower Cr content than other regions which might be the reason for the fewer Cr-contained particles and no rod-like particles found in this region (Figure 4. 28).

Factors that cause the particle coarsening and precipitation of new particles

The presence of rod-like particles was observed across most of the specimens (Figure 5. 16 to

Figure 5. 24), even in the BG12Cr specimen after the interrupted test (Figure 5. 39). The width of the precipitate coarsening zone (zone 2) appears to decrease as the crack length increases, as shown in Figure 4. 22. The longest test time in this research is around 2500 hours. Two factors might explain the accelerated formation of the Z phase and the coarsening of precipitates.

The first factor is the impact of strain and/or stress, Sawada K. et al. reported that in creep test specimens of T92 and T122 exposed to 600℃ for 22,000 to 40,000 hours, the gauge portion exhibited a Z-phase number density two to four times higher than that of the grip portion (93). In addition, the plastic deformation accelerated the transformation from V-rich MX into Z phase (60). Plastic deformation also can encourage the coarsening of $M_{23}C_6$ in the tertiary creep region (54).

Another potential factor is oxidation. During crack growth, the formation of oxides consumes the Cr content in the region immediately adjacent to the crack, and the difference in the concentration gradient of Cr promotes the diffusion of Cr from the matrix to the crack surface, which improves the possibility of Cr-containing particles formation and coarsening. Typically, a dense oxide film formed on the surface would hinder the subsequent oxidation process. However, during the CCG process, the growth of the crack exposes new surfaces to the air, negating the protective ability of the oxide film against oxidation. In the initial stages of crack growth, the crack growth rate is low, allowing for more time for Cr diffusion which can explain why this region exhibits the greatest width. The effect of oxidation and diffusion of Cr on the coarsening and formation of Cr-containing particles can be researched in future work.

However, the impact of the accelerated degradation of microstructure beneath the crack on the properties of BG12Cr and T92 is not clear which can be a potential avenue for future work.

6.4 Creep crack growth resistance curves

6.4.1 Validity of test results

The methods recommended by the ASTM standard E1457-23 were used to validate the test result.

Firstly, the data points before reaching the extensive creep conditions were excluded for the calculation of C* which was collected before the transition time t_T. And then, only the data collected after the initial 0.2 mm crack expansion can be used to calculate the da/dt.

Furthermore, C* is recommended for the creep ductile material and K is suitable for the creep brittle material. For evaluating the validity of using C*, the proportion of the time-dependent CMOD rate to the total CMOD rate $\dot{\Delta}_c/\dot{\Delta}_{CMOD}$ was plotted against time which is calculated from Equation 2.9, as shown in Figure 5. 15. In both T92 and BG12Cr, it was observed that all the $\dot{\Delta}_c/\dot{\Delta}_{CMOD}$ were over 50% during the entire testing period in all tests. This suggests that both materials were considered as creep ductile under the test conditions of this study. In the test on BG12Cr at 600 °C under 10 kN loading, the $\dot{\Delta}_c/\dot{\Delta}_{CMOD}$ ratio dropped rapidly after approximately 70 hours. This could be attributed to the high loading condition and the net-section stress increased progressively as the crack extended. The raised stress, combined with stress concentration at the crack tip, strongly promoted non-creep deformation mechanisms. In contrast, this sharp drop was not observed in the T92 specimen tested under the same temperature and load. This difference may be attributed to the stronger crack tip blunting and stress relaxation observed in T92 compared to BG12Cr, as confirmed by the interrupted test results shown in Figure 5. 36 and Figure 5. 37. The more pronounced blunting in T92 helps maintain creep-dominated crack propagation for a longer period. Additionally, BG12Cr

exhibits lower $\dot{\Delta}_c/\dot{\Delta}_{CMOD}$ values than T92, indicating that BG12Cr is relatively less creep-ductile than T92.

6.4.2 da/dt- C* curves

The da/dt-C* curves for all ten creep crack growth tests on BG12Cr and T92 at different temperatures and with different loading were shown in Figure 5. 12 b. All ten curves were within a narrow band and had a similar slope which shows good consistency on the trend of da/dt-C* for the BG12Cr and T92, regardless of the material, the test temperature and the test load. This means the da/dt-C* curves can be used to predict the lifetime of the material and evaluate the remaining lifetime of the component with a crack under creep conditions. However, although all ten curves were with a narrow band and a similar slope, the gap between the curves of T92 is larger than that of BG12Cr. The curves of T92 have good consistency on the tests with 3kN loading and the 2nd creep region of tests with 6 kN. The curve of T92 650°C 6kN has good consistency with that of the 1st creep region on T92 600°C 6kN and they have larger intercepts than the curves of T92 with 3 kN loading. The curves of T92 600°C 10kN have the largest intercepts. The different intercept on the curves of T92 shows that the 6 kN load and 10 kN load may be too high for the T92 CT specimen, and then the C* from the CCG test with high load and stress may not be reliable enough to predict the lifetime of T92. Unlike the T92, the curves of BG12Cr show high consistency, all curves have a similar slope and intercept including the tests with the loading of 6 kN and 10 kN, and the C* from high load and stress is reliable for the lifetime prediction on BG12Cr.

Although all da/dt-C* curves exhibit similar slopes and close intercepts, C* remains ablility to distinguish creep crack resistance. This is because data points from different tests are positioned

differently within the plots, reflecting variations in crack growth behaviour under different conditions. For example, under identical initial crack length, BG12Cr exhibits a lower initial crack growth rate and C* value than T92 at 700 °C under 3 kN loading, indicating superior creep crack resistance (Figure 5. 3 a &Figure 5. 13 c).

6.4.3 Effect of temperature and loading on the da/dt-C* curves

As discussed above, the da/dt-C* curves of all tests have similar slopes and close intercepts but the positions of the curves are different.

At the beginning of the test, all specimens had a similar initial crack. As shown in Figure 5. 13 d&e, BG12Cr 650°C 3kN has a lower initial C* value than BG12Cr 700°C 3kN and BG12Cr 600°C 6kN has a lower initial C* than BG12Cr 650°C 6kN. The C* data points from lower test temperatures overlapped with the data points from higher test temperatures. This overlap indicated a good correlation between C* and crack growth rate. Similar to BG12Cr, the T92 tests at 650°C and 600°C have lower C* values than those tested at 700°C and 650°C with the same load, respectively. This trend is attributed to the thermally activated nature of creep deformation. At elevated temperatures, enhanced atomic diffusion and dislocation activity accelerate creep strain accumulation near the crack tip. An increase in temperature leads to higher crack mouth opening rates and consequently higher C* values under identical loading conditions.

With the same test temperature, the specimens tested with a lower load have a lower initial C* than the specimens with a higher load (Figure 5. 13 d&e). Especially, the end of the BG12Cr 600°C 6kN curve is the start of the BG12Cr 650°C 6kN curve.

However, using C* curves to compare creep crack resistance is not intuitive because the slopes

and intercepts of the curves are similar, making it difficult to differentiate materials based on curve shape alone, as shown in Figure 5. 12 (b). For example, BG12Cr at 600°C, 10kN exhibits a higher crack growth rate than T92 under the same conditions at the same C* value,as shown in Figure 5. 13 (a). However, at the beginning of the test, BG12Cr 600°C, 10kN has a lower crack growth rate and C* than T92 600°C, 10kN, despite having a similar initial crack length.

The comparison can only be made by evaluating the positions of data points under the same crack length condition—where data points located toward the lower-left corner indicate lower C* values and slower crack growth rates, as shown in Figure 5. 12 and Figure 5. 13. However, since crack length is not explicitly represented in the C* curve, this makes direct comparisons more challenging in C* curves.

6.4.4 C(t) in small-scale creep and transition creep

When the entire ligament of the specimen is dominated by secondary creep, it is considered to be under extensive creep conditions (69). According to the ASTM standard E1457-23, the parameter C*(t) is used to characterize the local stress-strain rate at any given moment in the vicinity of the crack front in extensive creep conditions. The C*(t) value that corresponds to the steady-state conditions is referred to as C*. However, the C*(t) is not path-independent under small-scale creep and transition creep conditions. Therefore, the C_t parameter is used in the small-scale creep and transition creep regime which extends from the C*(t)-integral concept. For the C(T) specimen, the C_t is given in Equation (75):

$$C(t) = \frac{P\dot{V}_c}{BW}(F'/F) \qquad Equation\ 2.10$$

P is the applied load, F is the K-calibration factor, F`= dF/d(a/W), B is the thickness of

specimens, a is the crack length and W is the width of the specimen.

However, no data were collected before t_T due to the t_T is extremely short relative to the entire test time. Park et al., also found the transition time from small-scale to extensive creep ranges from 0.3% to 0.8% of the specimen failure time. This was determined from the CCG tests conducted on X20CrMOV121 steel, including both base metal and weld joint.

6.4.5 da/dt-K_n curves

K_n is the stress intensity factor which is normally used to compare the crack resistance in brittle fractures. Figure 5. 14 shows the da/dt against K_n curves under variable test conditions. In the tests conducted at 700℃ with 3kN loading, both BG12Cr and T92 curves exhibit similar slopes and intercepts. However, under the same conditions, the BG12Cr curve displays a lower crack growth rate with the same K_n value and slope than T92 at 650℃ with 3kN loading. At the beginning of the curves, the difference between the crack growth rate of BG12Cr 650 6kN and T92 650℃ 6kN with the same K_n value was small, yet it became significant with the increase of K_n. At a temperature of 600℃ and loading of 6kN, the 1st creep of the BG12Cr curve appears to lie on the line of the 1st and 2nd creep of the T92 curve. However, the 2nd creep of BG12Cr shows a lower crack growth rate with the same K_n value, despite having a steeper slope. The difference between T92 and BG12Cr tested at 600℃ with 10kN loading is minor but the T92 curve displays a steeper slope.

Unlike C* curves, the K_n curves of the same material exhibit different slopes and intercepts, even under identical test temperatures and loading conditions. A key limitation is that for the same material under different conditions, the same K_n value corresponds to different crack growth rates. For example, under the same 3kN load, BG12Cr tested at 650℃ exhibits a

significantly different crack growth rate compared to BG12Cr tested at 700°C, despite having the same stress intensity factor, as shown in Figure 5. 14. Another issue with K_n is its inconsistency across different stages within a single test, where variations in slope and intercept are observed, e.g. 1st and 2nd creep of BG12Cr tested at 600°C with the 6kN loading and 1st and 2nd creep of T92 tested at 650°C with 3 kN loading, shown in Figure 5. 14. Since K_n does not maintain a stable correlation with the creep crack growth rate under varying conditions or even across different stages of the same test, its applicability is limited. Consequently, K_n curves cannot be reliably used to predict the remaining lifetime of a component in the presence of an existing crack under creep conditions..

6.4.6 Effect of temperature and loading on the da/dt-K curves

As indicated by Equation 1, K_n is directly related to stress. And the B_n and initial crack length are similar in each specimen which suggests the dominant effect of loading on the K_n. Therefore, specimens tested under high loadings exhibit higher K_n values with the same crack growth rate than those subjected to lower loadings. Similarly, when tested at high temperatures, specimens tend to show higher initial K_n values compared to those tested at lower temperatures. In the entire creep crack growth process, the crack growth rates in T92 and BG12Cr are lower at 600°C than at 650°C, and lower at 650°C than at 700°C, with the same K_n, respectively.

6.5 The growth behaviour of crack length and CMOD on T92 and BG12Cr

Except for a few tests or creep stages that are too short for the specimens to achieve the third acceleration stage, the results from most tests exhibit three stages in both CMOD curves and crack growth curves which are very similar to the creep curve. As discussed in Section 6.4.1, the CMOD is largely influenced by the creep, so the CMOD curves that are similar to the creep

curve are reasonable. In the crack growth against time curves, after the application of static loading, the crack growth rate decreased due to work hardening. When the secondary creep dominated the entire ligament of the specimen, extensive creep was established, and the voids grew, nucleated and accumulated in uncracked regions continuously. The increase in crack length reduces the cross-section along the direction of the crack, thereby raising the net-section stress. These creep damage accumulations promote crack growth with the net-section stress increase. During the steady-state stage, they were counterbalanced by work hardening, resulting in a constant crack growth rate. In the third stage, referred to as the acceleration stage, the crack grows rapidly due to net-section stress much higher than the initial one and high-density void coalescences.

In the material that demonstrates high ductility at creep conditions during the CCG test, the application of static load results in blunting at the crack tip, with the plastic zone spreading over time, relieving the stress concentration in the vicinity of the crack tip. The stress relaxation is caused by the creep deformation ahead of the crack tip and it causes a significant reduction of stress. The effect of stress relaxation in the crack tip is directly related to the ductility of the material under test conditions. Therefore, in the material that shows high creep ductility, more creep damage is necessary for crack propagation. As illustrated in Figure 5. 36, this situation is characterised by the crack propagation accompanied by high CMOD, along with more, larger and widely distributed voids around the crack area.

Conversely, in material that exhibits lower ductility, the crack could grow with small CMOD which is due to crack tip blunting having less effect on the stress concentration, the crack could grow with less creep damage. As shown in Figure 5. 37, the crack growth with small CMOD,

fewer and smaller voids, and these voids are only formed in close regions of the crack.

In most tested specimens in this study, the crack growth is not simultaneous with the CMOD growth. In the specimen with high ductility, the CMOD achieve the steady-state phase earlier than the crack length which is due to the crack tip blunting and crack propagation needing the aid from the accumulation of creep damage (Figure 5. 4 and Figure 5. 5). However, the higher applied stress will strongly promote the creep process, the crack could grow with less creep damage and reduce the transition time t_T, so the crack length achieves steady state earlier than CMOD. The higher temperature has the same effect by reducing the strength of the material and promoting creep damage (Figure 5. 5&Figure 5. 7 and Figure 5. 4&Figure 5. 6). The crack length achieves the acceleration stage earlier than CMOD because of the increased net-section stress and accumulation of creep damage in the steady-state stage. The net section of specimens withstands the stress reduced during the crack growth which raises the net-section stress and causes the effect of net-section stress to be dominant in the final stage of crack growth, so the acceleration of crack length growth is earlier than CMOD.

However, the creep ductility of the material affects the crack tip blunting and stress relaxation effect. From the data provided by the manufacturer, the T92 has an elongation rate of 22% at 20℃ and 30 % at 600℃, while the BG12Cr only has an elongation rate of 20% at 20℃ and 22% at 600℃. In the BG12Cr specimens which exhibit lower ductility, the crack length could grow with less creep deformation and damage, and the crack length could achieve the steady-state stage earlier than CMOD (Figure 5. 8, Figure 5. 10 and Figure 5. 11). And in the BG12Cr 650℃ 3kN, the time of achieving steady-state stage is less in CMOD than in crack length and the acceleration of CMOD is earlier than that of crack length. That is might because the stress

of 3kN loading is too small compared to the strength of BG12Cr at 650℃, the accumulation of creep damage dominates the propagation of crack growth. And also, the relatively low crack growth rate allows more time for creep damage accumulation.

6.6 The fracture mechanism of creep crack growth on T92 and BG12Cr

Understanding the creep crack growth mechanism is important for discerning what occurs during the crack propagation and developing a solution to retard the crack propagation and further extend the lifetime of the material.

T92

At the outset of the crack on T92 tested at 600°C with a loading of 6kN (K_n=21.7 MPa√m), the voids nucleated both on the PAGBs and within PAGs, and the void coalescences were only found near the crack tip region (Figure 5. 16 b). As the K_n increased to 26.5 MPa√m, most of the voids grew to interconnect, forming voids coalescences. These coalescences formed on the PAGBS and within PAGs, and a secondary crack grew into a PAGB (Figure 5. 16 a). And some fracture features were consistent with the average PAG size of T92 which is considered to be an intergranular feature and dimple features were also found in the fracture surface of the T92 600°C 6kN at the beginning of the crack (Figure 5. 26 c&d). This suggests a mixture of intergranular fracture and transgranular fracture initially. Only the dimple features were observed in the region with K_n=28.9 MPa√m (Figure 5. 26 a&b). Transgranular fracture is dominant in this region with high K_n and long crack length. The crack growth along PAGBs was considered to be the intergranular fracture and across the PAGs was considered to be the transgranular fracture in this study.

In the cross-section of T92 600°C 10kN, both voids and some large void coalescences within

PAGs were found in the region with K_n=47.4 MPa√m and a long secondary crack was found across many PAGs (Figure 5. 17). And dimple features in the region K_n=42 MPa√m was found (Figure 5. 27). The prevailing fracture mechanism in this specimen is the transgranular fracture, particularly in areas with high K_n and long crack length.

For T92 650°C 3kN, small and large voids were predominantly located at the very beginning of the crack, and then they were subsequently replaced by the void coalescences in the remaining region. The void coalescences were mainly distributed within the PAG in all three observed regions, and their density increased with the increase of K_n. Secondary cracks across the PAGs were found in both the mid-crack and long-crack regions (Figure 5. 18). However, the fracture surface was heavily covered by oxide, obscuring the specific fracture features (Figure 5. 28). Therefore, the fracture mechanism is transgranular fracture dominant in the T92 650°C 3kN.

Similar to T92 650°C 3kN, there were many small voids found mainly within the PAGs in the area underneath the very beginning of the crack on the T92 650°C 6kN. In contrast to the initial area, the remaining part of the short-crack region mainly exhibited a high density of small void coalescences mainly within PAGs (Figure 5. 19 c). The secondary cracks across PAGs were found in both the short-crack and mid-crack regions. With a high K_n= 25.7 MPa√m, these voids coalesce leading to the formation of a secondary crack (Figure 5. 19 b). In the long-crack region with K_n= 38.1 MPa√m, there were large amount of void coalescences and voids within the PAGs were found, along with significant deformation (Figure 5. 19 a). Similar to the fracture surface of T92 650°C 3kN, the surface of T92 650°C 6kN was covered by an oxide layer, and only a few dimples features could be identified (Figure 5. 29). Based on the feature on the cross-

section and fracture surface, the primary fracture mechanism of T92 650°C 6kN is a transgranular fracture.

In the short-crack region (K_n=11.6 MPa√m) of T92 700°C 3kN, both voids and void coalescences were found on the PAGBs and within PAG (Figure 5. 20 c). In the mid-crack region (K_n=12.1 MPa√m), there were mainly void coalescences both on the PAGBs and within the PAG, and some void coalescences within PAGs connected to form a secondary crack (Figure 5. 20 b). The voids bridged to form micro-crack and void coalescences can be found both on the PAGBs and within the PAG in the long-crack region (K_n=13 MPa√m) (Figure 5. 20 a). The intergranular features were found at the beginning of the crack, and the interlinkings of voids to form micro-cracks were found (Figure 5. 30). The fracture mechanism for T92 700°C 3kN is a mixture of intergranular and ductile fracture.

The K_n is 22.0 at the crack tip of the T92 specimen (650 6kN) with the interrupted test. The main crack was growth across PAGs and voids and void coalescence were mainly within the PAGs. Three large voids within PAGs were connected in front of the crack tip. The fracture mechanism is ductile fracture for this specimen.

In T92 specimens, only a few IG features were found in T92 600°C 6kN and T92 700°C 3kN at the very beginning of the crack. In other regions and specimens, the fracture mechanisms were mainly ductile fracture or ductile dominant mixture fracture.

BG12Cr

The voids were mainly distributed on the PAGBs and few of them were within the PAGs, and only a few void coalescences were found in both the 1st creep and 2nd creep region on the BG12Cr 600°C 6kN (Figure 5. 21). In 2nd creep, a sub-crack was identified along the PAGB

and it appeared to be attempting to connect the voids located in front of the crack tip and on the PAGB. And also some voids on PAGBs tended to form a sub-crack (Figure 5. 21 a). On the fracture surface, many intergranular features were found on both the 1st and 2nd creep region and some dimple features were also found (Figure 5. 31). Intergranular fracture is the dominant mechanism combined with a few ductile fractures on the BG12Cr 600°C 6kN.

The main fracture mechanism for BG12Cr 600°C 10kN is the intergranular fracture. This was corroborated by the observation of voids mainly on the PAGBs, some of them connected to form a sub-crack. The clear "ice cube" features are seen on the fracture surface, which is close to the size of the PAGs in BG12Cr, further, confirming this mechanism (Figure 5. 22 and Figure 5. 32).

The voids and void coalescences on the BG12Cr 650°C 3kN were less than other specimens. Particularly in the short-crack region, only a few voids were on the PAGBs and void coalescences were within PAGs in the near-crack area (Figure 5. 23 c). The voids and void coalescences grew larger and many voids were nucleated on the PAGBs in the mid-crack region (Figure 5. 23 b). In the long-crack region, more voids and voids coalescences were nucleated within the PAGs (Figure 5. 23 a). And the mixture of intergranular features and dimples was found on the fracture surface (Figure 5. 33). The fracture mechanism for BG12Cr 650°C 3kN seems to be dominantly intergranular fracture with low K and C*, transitioning to a mixture of intergranular and ductile fracture and ductile fracture becoming dominant at the end of the crack with high K_n and C*.

A similar transition in the fracture mechanism was also observed in the BG12Cr 650°C 6kN. In the short-crack region with low K and C*, the voids and void coalescences were mainly

located on the PAGBs, and some of them were linked to form sub-cracks (Figure 5. 24 c). In the mid-crack region with K_n=26.0 MPa√m &C*=1.03E-01, more and larger voids and void coalescences were found, and large void coalescences linked to form sub-crack on the PAGBs. And also, more voids and void coalescences were nucleated within the PAGs (Figure 5. 24 b). The voids and void coalescences on the PAGBs were still found in the long-crack region with high K_n/C*, but more voids and void coalescences were within PAGs and a large 2nd crack across PAGs was found (Figure 5. 24 a). The fracture surface revealed intergranular features dominated the short-crack region and dimple features dominated the long-crack region (Figure 5. 34). The fracture mechanism for BG12Cr 650°C 6kN is thus seen to be the primarily intergranular fracture in the short-crack region with low K_n/C*, and fraction of ductile fracture increase as of K_n and C* rises, the long-crack region with high K_n /C* was the ductile fracture dominant.

In the fracture surface of BG12Cr 700°C 3kN, both IG feature and dimples were clearly found in the transition area with K_n=13.4 MPa√m, C*=7.71E-02 (Figure 5. 35 c&d). The IG features were predominantly found in the short-crack region, while dimples were primarily located in the long-crack region.

On the BG12Cr specimen (650°C 6kN) with the interrupted test, the K_n =24.8 MPa√m at the crack tip and the voids and sub-crack were mainly on the PAGBs around the crack, only a few voids were within PAGs. The main crack propagated along the PAGBs, and a sub-crack formed by PAGB voids was found in front of the crack tip which indicated the fracture mechanism here is mainly intergranular fracture.

The summary of fracture mechanism in T92 and BG12Cr with vary test conditions is shown in

Table 6. 1.

6.6.1 The effect of stress and temperature on the fracture mechanism

In this study, it was observed that different fracture mechanisms occurred in different specimens or even within various regions of a single specimen. These mechanisms were influenced by factors such as loading conditions, temperature, and initial stress.

Under a high loading condition of 10kN, the fracture mechanism was identified as an intergranular (IG) fracture. And then, a mixture of IG and ductile fracture mechanism was found in the specimen subjected to lower loading at 6kN and 600℃. Furthermore, the critical values of C* and K_n for the transition from IG fracture to ductile fracture were lower in the specimen exposed to 3kN than in the specimen subjected to 6kN at 650℃. These results suggest that initial stress promoted IG fracture in BG12Cr at both 600℃ and 650℃. The high crack growth rate resulting from high initial stress restricted the time available for void nucleation and growth. And the observation of IG fracture in the high initial stress test suggests the strength of PAGB is lower than that of PAGs in BG12Cr, leading to the formation of most voids mainly on the PAGBs. Consequently, crack growth occurred primarily along the PAGBs. The ductile fracture was primarily found in the region with extended crack length, which endures higher net-section stress but high initial stress promoted the IG fracture. The net-section stress might be similar in the short-crack region in the specimen with high loading and in the long-crack region of the specimen with lower loading, but their microstructure is different. The long-crack region in specimens with lower loading experienced longer test durations and consequently accumulated more severe creep damage; the distribution of voids/void coalescence is different. That suggests the net-section stress could not determine the fracture mechanism alone in the CCG process.

It was also observed that the transition of fracture mechanism occurred earlier in BG12Cr 650°C 6kN and BG12Cr 700°C 3kN compared to BG12Cr 600°C 6kN and BG12Cr 650°C 3kN, respectively, as shown in Figure 5. 33 to Figure 5. 35. That indicated the transition of the fracture mechanism in BG12Cr was earlier at high temperatures than at low temperatures. That suggests that the temperature promoted the transition of the fracture mechanism.

The high temperature and longer test time in specimens with low loading promoted the nucleation and growth of voids and void coalescences. That suggests the creep damage or the deformation and accumulation of voids/ void coalescences might be fundamental in driving the transition of the fracture mechanism.

6.6.2 The effect of stress and temperature on voids behaviour

Figure 5. 18 c1 clearly shows the distribution of voids and void coalescences across different regions. In the initial stages of the crack, the voids are predominantly individual and small. However, as the crack propagated, more and larger voids formed, with some linking together to form void coalescences or micro-cracks in the region near the crack. Notably, the distribution change of voids closer to the crack was more rapid than in regions farther away. Several factors contribute to the differences in void distribution, including net-section stress, the distance from the crack tips and the test time. When static loading is applied to the specimen, the small-scale primary creep first occurs around the initial crack tip, leading to the void nucleation in the immediate vicinity. The creep zone grows with time and after a transition time t_T, the extensive secondary creep dominates the entire uncracked ligament, allowing voids to form farther from the crack tip. With the crack propagation, the stress on the cracked region rapidly drops to zero eliminating the driving force for void growth and formation. In the region just ahead of the

crack tip, the growth and nucleation of voids will be strongly promoted by the tertiary creep zone around the crack tip, leading to the linkage of voids and then forming the void coalescences. The long-crack region experienced a longer test time and higher net-section stress causing more and larger voids and void coalescences to form.

In the region underneath the initial crack, T92 650°C 3kN contains smaller and fewer voids compared to T92 650°C 6kN, As shown in Figure 5. 18 c1 & Figure 5. 19 c1. A similar situation could be found between BG12Cr 650°C 3kN and BG12Cr 650°C 6kN, as shown in Figure 5. 23 c1&Figure 5. 24 c2. These findings suggest that the loading/ initial stress could encourage the formation and growth of voids. Similar to the effect of stress, high temperature could promote the formation and growth of voids. This is evidenced in T92 700°C 3kN, which contains larger and more voids in the region underneath the initial crack than T92 650°C 3kN, as shown in Figure 5. 18 c1&Figure 5. 20c.

6.6.3 The mechanism of creep crack growth

The region ahead of the crack tip is expected to undergo a creep deformation process similar to that in plane-sided specimens, progressing from the primary stage to the secondary stage, and ultimately leading to crack growth in the tertiary stage. The stress level decreases with increasing distance from the crack tip. When a static load is applied to a specimen with a sharp pre-crack induced by room temperature fatigue, the crack tip region experiences primary creep deformation, which causes crack tip blunting (observed as increasing CMOD but only slight growth of the crack). With continued creep deformation, the crack tip region enters the secondary creep phase, during which the region adjacent to the crack tip region undergoes primary creep. In the secondary phase, creep deformation and void diffusion promote

nucleation and growth of voids and the crack tip continues blunting. Once the size and density of voids reach a critical level, the tertiary creep phase begins, and the crack begins to propagate. As the crack propagates, the tertiary, secondary, and primary creep zones occur in sequence at different distances from the crack tip. The creep crack growth can be considered as a series of continuous small sections before the crack tip experiences the creep stages and fractures. However, the creep crack growth process is more complicated than the creep alone. One key difference lies in the change in stress; in a creep test, the stress change before fracture is mainly due to cross-section reduction caused by necking, whereas in the C(T) specimen, the main reason for stress change is the reduction in net section due to crack propagation. While area reduction in creep is mainly observed in the tertiary stage, in creep crack growth, it occurs from the beginning to the end of the test. Additionally, the condition of the section ahead of the crack tip is distinct. Accumulation of voids caused by creep deformation and diffusion occurs in the uncracked region after extensive creep is established during crack propagation. This suggests that the creep process occurs in regions with pre-existing voids, void coalescence, and micro-cracks, with their density and size increasing during crack propagation. The raised density and size of voids reduce the effective cross-section of the specimen and create shortcuts for crack growth. This is evidenced by the discovery of sub-cracks formed ahead of the crack tip, shown in Figure 5. 38 and Figure 5. 39.

6.6.4 The transition of the mechanism during the crack growth in BG12Cr

From the images of the cross-section and fracture surface, the transition of the fracture mechanism can be found in BG12Cr 650°C 3kN, BG12Cr 650°C 6kN and BG12Cr 700°C 3kN. Fracture mechanism from intergranular fracture transit to the ductile transgranular fracture with crack propagation. The transition is also reflected on the C*-da/dt curve.

As shown in Figure 6. 1, the slope of C*-da/dt changed twice during the test on BG12Cr 650°C 6kN. Before turning point 1, the relation between C* and da/dt is

$$da/dt = 0.0400C^{*0.72}$$

In the transition period, is

$$da/dt = 0.9758C^{*0.23}$$

After turning point 2, is

$$da/dt = 0.0543C^{*0.48}$$

The crack length of the turning points is shown in Figure 6. 2, Turning point 1 is at a=11.51 mm and turning point 2 is at a=12.71 mm which is close to the crack length of the transition point on the fracture surface. The shift in fracture mechanism from ductile fracture to brittle intergranular fracture observed when C* level drops were also found by Tan et al. (94) . This change in fracture mechanism change further influences the slope of the C*-da/dt curves.

In addition, the voids nucleated and grew during the crack growth. At the beginning of the crack growth, the voids were fewer, smaller and mainly on PAGBs. The PAGs remained a strong matrix and the connection of voids on PAGBs with crack tip became the easiest way for crack propagation. After the extensive creep is established, the creep damage accumulates in the uncracked region during the crack growth. When more voids nucleated and grew, the chance for voids within PAGs was increased. After the number and size of voids with PAGs increase to a certain level, the distance between the voids will be reduced, and the local necking occurs between voids and voids connect to form the sub-crack which leading to the ductile fracture and transgranular creep fracture (95). The rupture between voids is also promoted by high net-

section stress. The equivalent strength of the PAGs will drop during the voids nucleated, grow and coalesce and finally, the crack tips connect the sub-crack in the PAGs. The time of transition also can be found in Figure 6. 2, the test time of transition point 1 is around 750h and that of transition point 2 is around 850h which is both in the acceleration stage. Therefore, the density and size of voids are relatively high in the crack-tip region. And also, the density of voids and the fraction of voids area reduce the strength in PAGs leading to transgranular fracture.

As discussed above, the all test duration of CCG tests in this study is relatively short, which limits the impact of thermal exposure on the microstructure. In particular, for the BG12Cr 650 3kN sample, which had the longest test duration (2587.2h), only some coarsening of particles on PAGBs was observed in the microstructure after the CCG test.

However, the creeping progress generates strain that can encourage microstructure development. Specifically, the strain can promote the nucleation and coarsening of particles, including the newly formed particles, such as the Z phase, within the PAG. Moreover, the solid solution atom may diffuse from the matrix to the PAGBs, further reducing the matrix`s strength. Additionally, the presence of a large number of large particles provides additional sites for void nucleation, which can lead to a reduction in matrix strength and the formation of more voids within PAGs, strongly promoting intergranular fracture. Therefore, it is possible that the microstructure changes induced by strain may also play a role in the transition of the fracture mechanism in BG12Cr material.

6.7 The comparison between T92 and BG12Cr

In this study, the comparison of T92 with BG12Cr from the following aspects: time for initial 0.2 mm crack growth $t_{0.2}$, transition time for extensive creep established t_T, the experiment result

crack length, the C*-da/dt curves and K_n-da/dt curves, the void distribution after the interrupted test.

6.7.1 $t_{0.2}$ and t_T

The value of $t_{0.2}$ can be used to compare the rate of crack growth in the initial stage of creep. In the tests conducted at 650℃ with the loading of 6kN, and at 700℃ with a loading of 3kN, T92 exhibited a lower value of $t_{0.2}$ (58h and 38h, respectively) than BG12Cr ($t_{0.2}$=93h and 253h, respectively). That indicates that the creep crack growth in T92 is faster than in BG12Cr in the initial stages of creep under these test conditions. When testing with the same loading on T92, the $t_{0.2}$ is shorter at higher temperatures ($t_{0.2}$ =74h at 650℃ and $t_{0.2}$ =38h at 700℃ with the loading of 3kN, $t_{0.2}$ =334h at 600℃ and $t_{0.2}$ =58h at 650℃ with the loading of 6kN).

With the same loading of 6 kN on T92, the t_T is much longer than in the test at 600℃ which is 35h than at 650℃ which is only 2h. That reveals the increase in test temperature strongly prompted the rate to establish extensive creep. The same trend is apparent in the comparison of t_T between tests at 650℃ (t_T=21h) and at 700℃ (t_T=1h) with the loading of 3 kN on T92.In the tests (650℃,6 kN and 700℃,3 kN), the t_T on BG12Cr is much longer than on T92, indicating that it requires more time for BG12Cr to achieve extensive creep compared to T92.

6.7.2 Crack Length

In tests conducted at 600°C under a 6 kN load, BG12Cr exhibited a crack growth length of 0.22 mm over 759 hours, which is less than T92's 0.3 mm over 729 hours, despite BG12Cr having a higher initial stress intensity factor (Ki) of 23.7 MPa √ m and an initial crack length of 11.0 mm, compared to T92's Ki of 21.6 MPa √ m and initial crack length of 10.5 mm. The differences between BG12Cr and T92 became more significant at 650℃ with the loading of 6 kN. The

crack length of T92 reaches 7.8 mm within 188h and that of BG12Cr is only 4.95 mm within 886h, while the value of K_i for T92 is 21.1 MPa√m and 20.5 MPa√m for BG12Cr. The test temperature showed a significant effect on the creep crack growth rate in T92, with the same loading of 6 kN, the crack growth length is only 0.3 mm at 600℃ within 729h and 7.8 mm at 650℃ within 188h and they have almost the same value of K_i. The result from tests with the loading of 3 kN at 650℃ and 700℃ shows the same trend on T92, the crack length extension is 0.64 mm within 1836h at 650℃ and 2.88 mm within only 158h.

The difference between T92 and BG12Cr at 600℃ with the loading of 6 kN was clearly shown in Figure 5. 1. In the 2nd creep, the start crack length of BG12Cr is around 12.5um and that of T92 is around 12.25um, but the stable stage of BG12Cr is longer than that of T92, the acceleration of crack length of T92 is earlier than that of BG12Cr. That means in the test at 600℃ with the loading of 6 kN, the BG12Cr has better creep crack growth resistance than T92 with a long crack length.

6.7.3 Creep crack growth resistance

da/dt-C curves*

As discussed in Section 6.4.2 C* is highly co-related with da/dt, but the curves could not be used directly in comparing the crack growth resistance of materials. Because all da/dt-C* curves have a similar slope and intercept except the curves from the tests conducted at 600 ℃. In the tests conducted at 600℃, BG12Cr has a higher intercept on both 6 kN and 10 kN curves. However, in the tests conducted at 600℃ and 650℃ with the loading of 6 kN, and at 700℃ with the loading of 3 kN, all BG12Cr specimens exhibited lower initial C* values and crack growth rates even though all specimens have similar initial crack lengths. That indicated

BG12Cr has better creep crack growth resistance than T92 under these test conditions.

da/dt-K_n curves

As discussed in section 6.4.5, da/dt-K_n plot has some limitations in describing the creep crack growth in creep ductile material. However, using da/dt-K_n plots can provide a more straightforward perspective on the comparison of the crack growth resistance on different materials under the same test conditions. The value of K_n is only related to the geometry of the test piece, the crack length and the loading. Therefore, if the same loading and test piece geometry are utilised, the crack growth rate corresponding to a specific K_n value could be interpreted as the rate at an equivalent crack length. According to this, a higher crack growth rate with the same K_n value might be poorer crack growth resistance. In the tests conducted at 600℃, the difference between T92 and BG12Cr is not obvious. But in the tests conducted at 650℃ and 700℃, the T92 exhibited a higher crack growth rate with the same K_n value, especially, in tests at 650℃ with the loading of 6 kN, the crack growth rate difference between T92 and BG12Cr became more significant with the raised K_n value. That indicates that the BG12Cr has a better crack growth resistance than T92.

6.7.4 The void distribution in the interrupted test

The amount and size of voids and void calescence in the T92 specimen were higher than that in the BG12Cr specimen with the same test conditions. Especially, in the interrupted test T92 specimen, the voids are widely distributed, and many small voids can be found even at a distance of around 0.95 mm from the crack perpendicular to the direction of crack growth. In the interrupted test BG12Cr specimen, only a few small voids can be found at a distance of around 0.35 mm from the crack perpendicular to the direction of crack growth. That indicates

the creep damage zone is larger in T92 than in BG12Cr during the crack growth. The larger creep damage zone is also evidence showing the higher creep ductility in T92 than in BG12Cr.

In conclusion, through the comparison of the $t_{0.2}$ and t_T, crack length behaviour and da/dt-C* curves and da/dt-K_n curves, the BG12Cr has a better creep crack resistance under the test conditions involved in this study.

As discussed in Section 6.1 and 6.2, the BG12Cr contain a higher content of Cr, added the Co and Cu, These elements contribute to more substitutional strengthening and second-phase strengthening. Additionally, BG12Cr exhibits a finer lath width, which leads to better hardness and strength than T92. This enhanced strength contributes to better creep crack resistance. Even T92 has better creep ductility which can redistribute the creep deformation but still has poorer creep crack resistance than BG12Cr.

6.8 Summary

This chapter systematically investigated the creep crack growth (CCG) behaviour of BG12Cr and T92 steels and discussed the results with reference to microstructural observations, creep crack growth behaviour and fracture mechanism.

The comparison of initial microstructures confirms that both steels possess tempered martensitic structures, with BG12Cr exhibiting finer lath widths and larger PAG sizes than T92. The microstructure and precipitate types, distributions, and sizes agree with the literature (28,35,78,96). The presence of Co and Cu in BG12Cr is known to enhance solid solution and precipitation hardening and the observed higher hardness and crack resistance of BG12Cr is consistent with this (31). However, the high Cr content, the presence of δ-ferrite and the

absence of Ti-rich carbonitride in BG12Cr may influence long-term stability due to increased sensitivity to Z-phase formation, in line with concerns raised in earlier work (93).

The softening trends in T92 with increasing tempering temperature due to lath recovery and precipitate coarsening agree with prior studies (80,97,98). However, BG12Cr displayed an unconventional increase in hardness when the tempering temperature was raised from 780°C to 820°C. This unusual trend contrasts with the findings of Tao X. et al. on X12CrMoWVNbN10 steel, which showed a softening trend from 500°C to 800°C (99). This may be attributed to Co's ability to retard $M_{23}C_6$ coarsening (100), but this trend is not widely reported in the literature and warrants further long-term validation. In addition, thermal softening was observed in both BG12Cr and T92, consistent with hardness reduction over ageing time in previous thermal ageing studies on P92, attributed to Laves phase formation and early-stage precipitate coarsening (61,92,101,102).

The observation of accelerated particle coarsening and Z-phase formation in the near-crack regions within ~2500 h at 650°C contradicts reports that such phases typically appear after 10,000+ hours (103). This accelerated precipitation may be related to local stress, as discussed by Sawada et al. (93). Another possible contributing factor is oxidation, which warrants further investigation in future work.

Creep crack growth resistance analysis showed that BG12Cr exhibited lower crack growth rates and higher $t_{0.2}$ and t_T values than T92 under equivalent conditions. This is consistent with the expected strengthening effect of Cu and Co additions and refined substructures. The da/dt–C* trends in this study exhibit similar slopes across different conditions, in agreement with previous CCG studies on 9–12Cr steels (83,84,104). A summary of da/dt–C* parameter

compared with literature values is presented in Table 6. 2. The slope of T92 da/dt–C*at 600°C and 650°C is close to that of P92 da/dt–C* in literature (62,83).

Fractographic analysis revealed a transition from intergranular to transgranular fracture modes with increasing Kn and C*, particularly in BG12Cr specimens. The summary of fracture mechanisms in this study is shown in Table 6. 1 . Tan et al. reported similar transitions occurring at C* ~ 10^{-4} MPa·m/h (94). In this study, the transition appeared at higher C* values (e.g. >10^{-3} MPa·m/h), suggesting that the presence of high void density and size, or elevated stress levels due to long crack lengths, may shift the critical threshold to.

Overall, the results largely confirm the superior creep crack resistance of BG12Cr compared to T92 under the tested conditions, while also highlighting areas—such as accelerated Z-phase formation and tempering-induced hardening in BG12Cr—that deviate from established literature and deserve further investigation.

CHAPTER 7 Conclusion

1. The as-received microstructure of BG12Cr is a tempered martensite microstructure with a small number of δ-ferrites. Different types of precipitates are found in the material: one is $M_{23}C_6$ type, (Cr, Mo, W)-rich carbides; another is MX type of (Nb, V)(C, N) and V(C, N) carbon nitrides. Both are distributed mainly on prior austenite grain boundaries, martensite colony boundaries and lath boundaries. A large number of Cu particles with a size of 20-30nm were also found evenly distributed within martensite lathes. In the as-received T92, the microstructure is also tempered martensite and the main particles at the lath boundaries and prior austenite grain boundaries are $M_{23}C_6$ carbides ((Cr, Mo, W)-rich carbides), (Nb, V)(C, N), V(C, N) and Ti-rich carbides. Some $(Fe, Cr)_2(Mo, W)$ Laves phases were also found at prior austenite grain boundaries.
2. The hardness of BG12Cr is higher than T92 in the as-received and different tempered conditions applied, which is attributed to its higher content of Cr, additional Co, large amount of nano Cu particle and finer lath width.
3. The precipitate size and distribution are affected by the tempering temperature. High tempering temperatures promoted the formation and coarsening of precipitates in BG12Cr. In addition, an unusual trend of increased hardness with an increase in tempering temperature (from 780 to 820°C) is observed, attributed to the addition of Co retard the coarsening of $M_{23}C_6$ carbides during the tempering.
4. Hardness measurements on the post-testing samples (with a testing time of 158 h to 2525 h at temperatures of 600, 650 and 700°C respectively) suggest coarsening of

precipitates at all cases for both alloys, and the hardness values reduce with an increase of temperature and testing time.

5. The microstructure evolution adjacent to crack faces is much faster than the region further away from the crack faces for both alloys. The acceleration of microstructural degradation is affected by stressing and oxidation-induced Cr outward diffusion.
6. Creep crack growth, manifested by the formation and growth of voids, and voids linking and coalescence, is promoted by high temperature and high stress. It was found that in T92, microvoids predominantly form and grow at triple points of prior austenite grains, whereas in BG12Cr microvoids tend to form both at the triple points and along prior austenite grain boundaries.
7. With one exception of an applied load of 10 kN at 600°C, the crack growth rate measured for T92 is higher than that of BG12Cr in all cases when compared under the same test conditions of applied load, temperature and crack length; In addition, BG12Cr possesses a lower C* value than that of T92. This suggests that for the investigated test conditions and within a certain testing period (~2500 h), BG12Cr has a better creep crack growth resistance than T92, especially at 650℃ and 700℃.

CHAPTER 8 Future work

Due to limitations in experimental time and resources, several aspects remain to be explored to deepen the understanding of BG12Cr's fundamental properties, as well as the creep crack growth (CCG) behaviour and microstructural stability of both BG12Cr and T92. The following directions are proposed for future investigation:

1. Carry out tensile tests on BG12Cr and T92 across a range of temperatures and heat treatment conditions. Establishing a full set of tensile properties will support the understanding of temperature-dependent strength and ductility.
2. Investigate the effect of different heat treatment conditions on CCG behaviour by testing specimens of BG12Cr and T92 subjected to varied normalising and tempering procedures. These tests will help clarify how initial microstructure influences crack propagation under creep conditions and assist in identifying optimal heat treatment parameters for improved creep crack resistance.
3. Conduct long-term CCG tests on BG12Cr and T92 under low-stress conditions. The results should be compared with those from high-stress tests to evaluate the influence of applied stress on creep crack growth behaviour and creep crack growrth mechanisms.
4. Perform CCG tests using alternative specimen geometries, such as round-bar or circular cross-section specimens, to validate the path independence and applicability of the C* parameter under different loading and constraint conditions.
5. Investigate the microstructural evolution of BG12Cr and T92 after long-term thermal ageing (e.g. 5,000 h, 10,000 h, and 20,000 h). These tests will help evaluate the

thermal stability of precipitates and grain structures and provide insight into ageing-induced degradation in mechanical properties.

6. Study the relationship between microstructural degradation and creep performance by examining the impact of precipitate coarsening, subgrain formation, and Z-phase development on the creep resistance and fracture behaviour of both steels.
7. Perform high-resolution TEM analysis on selected specimens after CCG testing to identify the types and distributions of precipitates in regions near and away from the crack. This will help explain localised microstructural changes caused by stress gradients and oxidation during crack propagation.

Reference

1. Energy Institute. Statistical Review of World Energy 2024 [Internet]. 2024. Available from: https://www.energyinst.org/statistical-review

2. Termuehlen H, Emsperger W. Evolutionary Development of Coal-Fired Power Plants. In: Termuehlen H, Emsperger W, editors. Clean and Efficient Coal-Fired Power Plants: Development Toward Advanced Technologies [Internet]. ASME Press; 2003. p. 0. Available from: https://doi.org/10.1115/1.801942.ch1

3. Masuyama F. History of power plants and progress in heat resistant steels. ISIJ International. 2001;41(6):612–25.

4. Wheeldon JM, Shingledecker JP. Materials for boilers operating under supercritical steam conditions [Internet]. Ultra-Supercritical Coal Power Plants: Materials, Technologies and Optimisation. Woodhead Publishing Limited; 2013. 81–103 p. Available from: http://dx.doi.org/10.1533/9780857097514.1.81

5. Zhang D. Introduction to advanced and ultra-supercritical fossil fuel power plants [Internet]. Ultra-Supercritical Coal Power Plants: Materials, Technologies and Optimisation. Woodhead Publishing Limited; 2013. 1–20 p. Available from: http://dx.doi.org/10.1533/9780857097514.1

6. Nicol Kyle. Application and development prospects of double-reheat coal-fired power units. IEA Clean Coal Centre; 2015.

7. Narula RG, Koza D, Wen H. Impacts of steam conditions on plant materials and operation in ultra-supercritical coal power plants [Internet]. Ultra-Supercritical Coal Power Plants: Materials, Technologies and Optimisation. Woodhead Publishing Limited; 2013. 23–56 p. Available from: http://dx.doi.org/10.1533/9780857097514.1.23

8. Fan H, Zhang Z, Dong J, Xu W. China's R&D of advanced ultra-supercritical coal-fired power generation for addressing climate change. Vol. 5, Thermal Science and Engineering Progress. Elsevier Ltd; 2018. p. 364–71.

9. Patel S. China's Pingshan Phase II Sets New Bar as World's Most Efficient Coal Power Plant [Internet]. Power Magazine; 2023. Available from: https://www.powermag.com/chinas-pingshan-phase-ii-sets-new-bar-as-worlds-most-efficient-coal-power-plant/

10. Abe F, Kern TU, Viswanathan R. Creep-resistant steels. Elsevier; 2008.

11. Fabritius H. ENTWICKLUNGSSTAND VON WARMFESTEN UND KORROSIONSBESTAENDIGEN STAEHLEN FUER DIE ERDOL-UND ERDGASINDUSTRIE. 1973;

12. Foldyna V, Purmenský J, Prnka T, Kadulová M. Einfluß des Molybdängehaltes auf die

Zeitstandfestigkeit von Chrom-Molybdän-Vanadin-Stählen mit niedrigem Kohlenstoffgehalt. Archiv für das Eisenhüttenwesen. 1971;42(12):927–32.

13. Masuyama F. Steam plant material developments in Japan. In: Proceedings of the 6th International Conference on Materials for Advanced Power Engineering, Liege. 1998.

14. TAKAHASHI N, FUJITA T. The Effect of Boron on the Long Period Creep Rupture Strength of the Modified 12% Chromium Heat Resisting Steel. Transactions of the Iron and Steel Institute of Japan. 1976;16(11):606–13.

15. Curran RM. Progress in the Development of Large Rotor Forgings. In: Proc 5 th Internat Forgemaster Meeting, Arti Grafiche Nobili, Terni, Italy 1972, 658-577, 875-894. 1972.

16. Brinkman CR, Alexander DJ, Maziasz PJ. Modified 9Cr-1Mo steel for advanced steam generator applications. Oak Ridge National Lab.(ORNL), Oak Ridge, TN (United States); 1990.

17. Orr J, Buchanan LW, Everson H. The commercial development and evaluation of E911, a strong 9% CrMoNbVWN steel for boiler tubes and headers. In: Advanced heat resistant steels for power generation (San Sebastian, 27-29 April 1998, preprints). 1998.

18. Hald J. ECCC E911-P92 Assessment. In: ECCC Data Sheet, presented in September 2005 at the ECCC conference Creep & Fracture in High Temperature Components. 2005.

19. Iseda A. Development of a new 0.1 C-11Cr-2W-0.4 Mo-1Cu steel for large diameter and thick wall pipe for boilers. Creep: Characterization, Damage and Life Assessments. 1992;389–97.

20. Kimura K. Assessment of long-term creep strength and review of allowable stress of high Cr ferritic creep resistant steels. In: ASME Pressure Vessels and Piping Conference. 2005. p. 237–44.

21. Zielinska-Lipiec A, Bendick W, Koziel T, Hahn B, Czyrska-Filemonowicz A. Effect of creep deformation at 625°C on microstructure development of VM12 steel. Materials at High Temperatures. 2010;27(1):73–8.

22. Zieliński A, Dobrzański J, Sroka M. Changes in the structure of VM12 steel after being exposed to creep conditions. Archives of Materials Science and Engineering. 2011;49(2):103–11.

23. Hasegawa Y. Grade 92 creep-strength-enhanced ferritic steel. In: Coal Power Plant Materials and Life Assessment [Internet]. Elsevier; 2014. p. 52–86. Available from: https://linkinghub.elsevier.com/retrieve/pii/B9780857094315500023

24. Taneike M, Sawada K, Abe F. Effect of carbon concentration on precipitation behavior of M23C6 carbides and MX carbonitrides in martensitic 9Cr steel during heat treatment. Metall Mater Trans A Phys Metall Mater Sci. 2004;35 A(4):1255–62.

25. Yan W, Wang W, Shan YY, Yang K. Microstructural stability of 9-12%Cr ferrite/martensite heat-resistant steels. Front Mater Sci. 2013;7(1):1–27.

26. Danielsen HK, Hald J. Behaviour of z phase in 9–12%Cr steels. Energy Materials: Materials Science and Engineering for Energy Systems. 2006;1(1):49–57.

27. Rojas D, Garcia J, Prat O, Sauthoff G, Kaysser-Pyzalla AR. 9%Cr heat resistant steels: Alloy design, microstructure evolution and creep response at 650°C. Materials Science and Engineering A [Internet]. 2011;528(15):5164–76. Available from: http://dx.doi.org/10.1016/j.msea.2011.03.037

28. Hu ZF. Heat-Resistant Steels, Microstructure Evolution and Life Assessment in Power Plants. Thermal Power Plants. 2012.

29. Aghajani A, Richter F, Somsen C, Fries SG, Steinbach I, Eggeler G. On the formation and growth of Mo-rich Laves phase particles during long-term creep of a 12% chromium tempered martensite ferritic steel. Scr Mater [Internet]. 2009;61(11):1068–71. Available from: http://dx.doi.org/10.1016/j.scriptamat.2009.08.031

30. Kaibyshev R, Mishnev R, Fedoseeva A, Dudova N. The role of microstructure in creep strength of 9-12%Cr steels. Materials Science Forum. 2017;879(November):36–41.

31. Shen X, Liu J, Xu Z. The effect of Co and Cu on the creep properties of high chromium (12%Cr) ferritic steel. In: Advanced Materials Research. 2011. p. 944–7.

32. Helis L, Toda Y, Hara T, Miyazaki H, Abe F. Effect of cobalt on the microstructure of tempered martensitic 9Cr steel for ultra-supercritical power plants. Materials Science and Engineering A. 2009 Jun 15;510–511(C):88–94.

33. Rojas D, Garcia J, Prat O, Carrasco C, Sauthoff G, Kaysser-Pyzalla AR. Design and characterization of microstructure evolution during creep of 12% Cr heat resistant steels. Materials Science and Engineering A [Internet]. 2010;527(16–17):3864–76. Available from: http://dx.doi.org/10.1016/j.msea.2010.02.056

34. Futamura Y, Tsuchiyama T, Takaki S. Strengthening mechanism of Cu bearing heat resistant martensitic steels. ISIJ international. 2001;41(Suppl):S106–10.

35. Wang H, Yan W, van Zwaag S, Shi Q, Wang W, Yang K, et al. On the 650 °C thermostability of 9–12Cr heat resistant steels containing different precipitates. Acta Mater [Internet]. 2017;134:143–54. Available from: http://dx.doi.org/10.1016/j.actamat.2017.05.069

36. Sawada K, Kubo K, Abe F. Creep behavior and stability of MX precipitates at high temperature in 9Cr–0.5 Mo–1.8 W–VNb steel. Materials Science and Engineering: A. 2001;319:784–7.

37. Abe F. Precipitate design for creep strengthening of 9% Cr tempered martensitic steel for ultra-supercritical power plants. Sci Technol Adv Mater. 2008;9(1).

38. Cipolla L, Danielsen HK, Venditti D, Di Nunzio PE, Hald J, Somers MAJ. Conversion of MX nitrides to Z-phase in a martensitic 12% Cr steel. Acta Mater [Internet]. 2010;58(2):669–79. Available from: http://dx.doi.org/10.1016/j.actamat.2009.09.045

39. Danielsen HK, Hald J. Influence of z-phase on long-term creep stability of martensitic 9 to 12 % Cr steels. VGB PowerTech. 2009;89(5).

40. Wang P, Lu SP, Xiao NM, Li DZ, Li YY. Effect of delta ferrite on impact properties of low carbon 13Cr-4Ni martensitic stainless steel. Materials Science and Engineering A. 2010 May;527(13–14):3210–6.

41. Li S, Eliniyaz Z, Zhang L, Sun F, Shen Y, Shan A. Microstructural evolution of delta ferrite in SAVE12 steel under heat treatment and short-term creep. Mater Charact. 2012 Nov;73:144–52.

42. Maruyama K, Sawada K, Koike JI. Strengthening mechanisms of creep resistant tempered martensitic steel. ISIJ International. 2001;41(6):641–53.

43. Abe F. Progress in Creep-Resistant Steels for High Efficiency Coal-Fired Power Plants. Journal of Pressure Vessel Technology, Transactions of the ASME. 2016;138(4).

44. Zhou X, Liu C, Yu L, Liu Y, Li H. Phase Transformation Behavior and Microstructural Control of High-Cr Martensitic/Ferritic Heat-resistant Steels for Power and Nuclear Plants: A Review. J Mater Sci Technol [Internet]. 2015;31(3):235–42. Available from: http://dx.doi.org/10.1016/j.jmst.2014.12.001

45. Maruyama K, Nakashima H. Materials Science for High Temperature Strength. Uchida-Rokakuho: Tokyo, Japan. 1997;

46. Abe F. Development of creep-resistant steels and alloys for use in power plants. Structural Alloys for Power Plants: Operational Challenges and High-Temperature Materials. 2014. 250–293 p.

47. Ridley N, Maropoulos S, Paul JDH. Effects of heat treatment on microstructure and mechanical properties of Cr–Mo–3· 5Ni–V steel. Materials science and Technology. 1994;10(3):239–49.

48. Abe F, Nakazawa S, Araki H, Noda T. The role of microstructural instability on creep behavior of a martensitic 9Cr-2W steel. Metallurgical Transactions A. 1992;23:469–77.

49. Mitsuhara M, Yamasaki S, Miake M, Nakashima H, Nishida M, Kusumoto J, et al. Creep strengthening by lath boundaries in 9Cr ferritic heat-resistant steel. Philos Mag Lett. 2016 Feb 1;96(2):76–83.

50. Nikitin I, Fedoseeva A, Kaibyshev R. Strengthening mechanisms of creep-resistant 12%Cr–3%Co steel with low N and high B contents. J Mater Sci. 2020 Jun 1;55(17):7530–45.

51. Ghassemi Armaki H, Chen R, Maruyama K, Igarashi M. Creep Behavior and Degradation of Subgrain Structures Pinned by Nanoscale Precipitates in Strength-Enhanced 5 to 12áPct Cr Ferritic Steels. Metallurgical and Materials Transactions A. 2011;42:3084–94.

52. Kostka A, Tak KG, Hellmig RJ, Estrin Y, Eggeler G. On the contribution of carbides and micrograin boundaries to the creep strength of tempered martensite ferritic steels. Acta Mater. 2007;55(2):539–50.

53. Panait CG, Bendick W, Fuchsmann A, Gourgues-Lorenzon AF, Besson J. Study of the microstructure of the Grade 91 steel after more than 100,000 h of creep exposure at 600 C. International journal of pressure vessels and piping. 2010;87(6):326–35.

54. Ghassemi Armaki H, Chen R, Kano S, Maruyama K, Hasegawa Y, Igarashi M. Strain-induced coarsening of nanoscale precipitates in strength enhanced high Cr ferritic steels. Materials Science and Engineering A [Internet]. 2012;532:373–80. Available from: http://dx.doi.org/10.1016/j.msea.2011.10.105

55. Hu P, Yan W, Sha W, Wang W, Guo Z li, Shan Y yin, et al. Study on Laves phase in an advanced heat-resistant steel. Front Mater Sci China. 2009;3:434–41.

56. Hald J. Microstructure and long-term creep properties of 9-12% Cr steels. International Journal of Pressure Vessels and Piping. 2008;85(1–2):30–7.

57. Hald J, Danielsen HK. Z-phase strengthened martensitic 9–12% Cr steels. In: Proceedings of 3rd Symposium on Heat Resistant Steels and Alloys for High Efficiency USC Power Plants, National Institute for Materials Science, Tsukuba, Japan. 2009. p. 2–6.

58. Sklenička V, Kuchařová K, Svoboda M, Kloc L, Buršík J, Kroupa A. Long-term creep behavior of 9-12%Cr power plant steels. Mater Charact. 2003;51(1):35–48.

59. Rashidi M, Johansson L, Andrén HO, Liu F. Microstructure and mechanical properties of two Z-phase strengthened 12%Cr martensitic steels: the effects of Cu and C. Materials Science and Engineering A. 2017;694(March):57–65.

60. Fedoseeva A, Nikitin I, Dudova N, Kaibyshev R. Strain-induced Z-phase formation in a 9% Cr-3% Co martensitic steel during creep at elevated temperature. Materials Science and Engineering A. 2018 May 2;724:29–36.

61. Sun N, Jiang Y, Weng XX, Gong JM. Microstructural Evolution of P92 Steel During Long-Term Aging. Journal of Failure Analysis and Prevention. 2017;17(5):882–9.

62. Saber M. Experimental and finite element studies of creep and creep crack growth in P91 and P92 weldments. PhD thesis, University of Nottingham [Internet]. 2012; Available from: http://etheses.nottingham.ac.uk/2197/

63. Penny RK, Marriott DL. Design for creep. Springer Science & Business Media; 1995.

64. Jones DRH, Ashby MF. Mechanisms of Creep, and Creep-Resistant Materials. In: Engineering Materials 1. Elsevier; 2019. p. 381–94.

65. Herring C. Diffusional viscosity of a polycrystalline solid. J Appl Phys. 1950;21(5):437–45.

66. Coble RL. A model for boundary diffusion controlled creep in polycrystalline materials. J Appl Phys. 1963;34(6):1679–82.

67. Zhang JS, editor. 11 - Mechanisms of Grain Boundary Sliding. In: High Temperature Deformation and Fracture of Materials [Internet]. Woodhead Publishing; 2010. p. 172–81. Available from: https://www.sciencedirect.com/science/article/pii/B9780857090799500112

68. Jones DRH, Ashby MF. Engineering materials 2: an introduction to microstructures and processing. Butterworth-Heinemann; 2012.

69. Saxena A. CREEP CRACK GROWTH IN HIGH TEMPERATURE DUCTILE MATERIALS? Vol. 40, hhgtneedng Fracture Mechanics. 1991.

70. Landes JD, Begley JA. A fracture mechanics approach to creep crack growth. Astm Stp. 1976;590:128–48.

71. Nikbin KM, Webster GA, Turner CE. Relevance of nonlinear fracture mechanics to creep cracking. In: Cracks and fracture. ASTM International; 1976.

72. Hyde TH. Creep crack growth in 316 stainless steel at 600 C. High Temperature Technology. 1988;6(2):51–61.

73. Standard Test Method for Measurement of Creep Crack Growth Times in Metals 1. Available from: www.astm.org,

74. Riedel H, Detampel V. Creep crack growth in ductile, creep-resistant steels. Int J Fract. 1987;33(4):239–62.

75. Saxena A. Fracture mechanics seventh conference. ASTM STP. 1986;905:185–201.

76. Park YK, Kim KS, Chung YK, Park JJ. Creep crack growth in X20CrMoV 12 1 steel and its weld joint. J Pressure Vessel Technol. 2001;123(2):191–6.

77. Riedel H, Rice JR. Tensile cracks in creeping solids. Fracture mechanics. 1980;12:112–30.

78. Abe F. Precipitate design for creep strengthening of 9% Cr tempered martensitic steel for ultra-supercritical power plants. In: Science and Technology of Advanced Materials. 2008.

79. Saini N, Pandey C, Mahapatra MM. Characterization and evaluation of mechanical properties of CSEF P92 steel for varying normalizing temperature. Materials Science

and Engineering A [Internet]. 2017;688(February):250–61. Available from: http://dx.doi.org/10.1016/j.msea.2017.02.022

80. Barbadikar DR, Deshmukh GS, Maddi L, Laha K, Parameswaran P, Ballal AR, et al. Effect of normalizing and tempering temperatures on microstructure and mechanical properties of P92 steel. International Journal of Pressure Vessels and Piping. 2015 Aug 1;132–133:97–105.

81. Isaac Samuel E, Choudhary BK, Rao Palaparti DP, Mathew MD. Creep deformation and rupture behaviour of P92 steel at 923 K. Procedia Eng. 2013;55:64–9.

82. Mohyla P, Kubon Z, Cep R, Samardzic I. Evaluation of creep properties of steel P92 and its welded joint [Internet]. Vol. 53, METALURGIJA. 2014. Available from: https://www.researchgate.net/publication/286160852

83. Kim B, Jeong C, Lim B. Creep behavior and microstructural damage of martensitic P92 steel weldment. Materials Science and Engineering A. 2008;483–484(1-2 C):544–6.

84. Tanner DWJ, Saber M, Sun M, Hyde TH. Creep behavior of P92 and P92 welds at 675°C. Journal of Pressure Vessel Technology, Transactions of the ASME. 2013;135(5).

85. Bär J. Crack detection and crack length measurement with the DC potential drop method–possibilities, challenges and new developments. Applied Sciences (Switzerland). 2020 Dec 1;10(23):1–14.

86. Shang Z, Shen Y, Ji B, Zhang L. Effect of δ-ferrite evolution and high-temperature annealing on mechanical properties of 11Cr3W3Co ferritic/martensitic steel. Metals and Materials International. 2016 Mar 1;22(2):171–80.

87. Kimura K, Ohi N, Shimazu K, Matsuo T, Tanaka R, Kikuchi M. Effect of prior austenite grain size on high temperature creep properties of Cr□Mo□V rotor steel. Scripta Metallurgica [Internet]. 1987;21(1):19–22. Available from: https://www.sciencedirect.com/science/article/pii/0036974887903991

88. Hong SH, Yu J. Effect of prior austenite grain size on creep properties and on creep crack growth in 3.5Ni□Cr□Mo□V steel. Scripta Metallurgica [Internet]. 1989;23(7):1057–62. Available from: https://www.sciencedirect.com/science/article/pii/0036974889902998

89. Yan P, Liu Z, Bao H, Weng Y, Liu W. Effect of tempering temperature on the toughness of 9Cr-3W-3Co martensitic heat resistant steel. Mater Des [Internet]. 2014;54:874–9. Available from: http://dx.doi.org/10.1016/j.matdes.2013.09.017

90. Saini N, Mulik RS, Mahapatra MM. Study on the effect of ageing on laves phase evolution and their effect on mechanical properties of P92 steel. Materials Science and Engineering A [Internet]. 2018;716(November 2017):179–88. Available from: https://doi.org/10.1016/j.msea.2018.01.035

91. Liu ZB, Zhang BN, Sha G, Jin SB, Yang ZY, Liang JX, et al. Effect of cobalt on

precipitation in Fe-Cr-Co-Mo-Ni-C stainless steels. Mater Lett. 2021 Apr 15;289.

92. Xu Y, Nie Y, Wang M, Li W, Jin X. The effect of microstructure evolution on the mechanical properties of martensite ferritic steel during long-term aging. Acta Mater [Internet]. 2017;131:110–22. Available from: http://dx.doi.org/10.1016/j.actamat.2017.03.045

93. Sawada K, Kushima H, Kimura K. Z-phase formation during creep and aging in 9-12% Cr heat resistant steels. ISIJ International. 2006;46(5):769–75.

94. Tan JP, Tu ST, Wang GZ, Xuan FZ. Effect and mechanism of out-of-plane constraint on creep crack growth behavior of a Cr-Mo-V steel. Eng Fract Mech. 2013 Feb;99:324–34.

95. Ashbyt MF, Gandhi C, Taplins DMR. OVERVIEW NO. 3 FRACTURE-MECHANISM MAPS AND THEIR CONSTRUCTION FOR F.C.C. METALS AND ALLOYS.

96. Vivas J, Celada-Casero C, San Martín D, Serrano M, Urones-Garrote E, Adeva P, et al. Nano-precipitation Strengthened G91 by Thermo-mechanical Treatment Optimization. Metall Mater Trans A Phys Metall Mater Sci. 2016 Nov 1;47(11):5344–51.

97. Abe F. Effect of quenching, tempering, and cold rolling on creep deformation behavior of a tempered martensitic 9Cr-1W steel. Metall Mater Trans A Phys Metall Mater Sci. 2003;34 A(4):913–25.

98. Dudko V, Belyakov A, Kaibyshev R. Effect of tempering on mechanical properties and microstructure of a 9% Cr heat resistant steel. In: Materials Science Forum. Trans Tech Publications Ltd; 2012. p. 841–6.

99. Tao XG, Han LZ, Gu JF. Effect of tempering on microstructure evolution and mechanical properties of X12CrMoWVNbN10-1-1 steel. Materials Science and Engineering A. 2014;618:189–204.

100. Fedoseeva A, Dudko V, Dudova N, Kaibyshev R. Effect of Co on the strengthening mechanisms of the creep-resistant 9% Cr-2%W-MoVNb steel. J Mater Sci. 2022 Dec 1;

101. Sakthivel T, Laha K, Parameswaran P, Panneer Selvi S, Chandravathi KS, Mathew MD. Effect of Thermal Aging on Microstructure and Mechanical Properties of P92 Steel. Transactions of the Indian Institute of Metals [Internet]. 2015;68(3):411–21. Available from: http://dx.doi.org/10.1007/s12666-014-0480-x

102. Fedorova I, Belyakov A, Kozlov P, Skorobogatykh V, Shenkova I, Kaibyshev R. Laves-phase precipitates in a low-carbon 9% Cr martensitic steel during aging and creep at 923K. Materials Science and Engineering A [Internet]. 2014;615:153–63. Available from: http://dx.doi.org/10.1016/j.msea.2014.07.046

103. Abe F. Creep rates and strengthening mechanisms in tungsten-strengthened 9Cr steels. Materials Science and Engineering A. 2001;319–321:770–3.

104. Kobayashi KI, Shimizu S, Fuji A, Yokobori AT, Hirohashi M. PERFORMANCE OF CREEP CRACK GROWTH ON W STRENGTHENED 9-12Cr STEEL.

105. Kim WG, Sah I, Kim SJ, Lee HY, Kim ES. Creep and creep crack growth behaviors for base, weld, and heat affected zone in a grade 91 weldment. Nuclear Engineering and Technology. 2021 Feb 1;53(2):572–82.

106. Speicher M, Klenk A, Roos E, Maile K. Creep Crack Assessment of Components at High Temperatures.

Tables and Figures

Table 2. 1 Summary of precipitates and secondary phases in 9-12Cr% heat resistant steel

Precipitate Phase	Crystal Structure	Lattice Parameters (nm)	Precipitation Sites	Size (nm)	Composition	Effect on Creep Strength	Formation Process	References
$M_{23}C_6$	fcc	a=1.06-1.07	PAGBs, block boundaries, lath boundaries	100-200	Cr-rich, can include Fe, Ni, Mn, Mo; B can substitute for C	Provides grain boundary strengthening, stable at medium temperatures	During tempering	24, 31, 26
MX	fcc	a=0.42-0.45	Lath boundaries, within the matrix	<50	(Nb, V)(C, N)	Hinders dislocation movement	During tempering	24, 31, 32
Laves Phase	Hexagonal	a=0.47, c=0.78	Near $M_{23}C_6$ precipitates	Varied	Fe_2W, Fe_2Mo, $(Fe, Cr)_2(W, Mo)$	Depletes W and Co, reducing solute hardening	Long-term creep exposure	24, 33
Z Phase	Tetragonal	a=0.29, c=0.74	Converted from MX, typically at PAGBs	Varied	Cr(V, Nb)N	Reduces precipitate strengthening, accelerates creep	Long-term creep exposure, transforms from MX	33, 34, 22, 35
δ-ferrite	bcc	a=2.85	Forms in high-Cr steels (>10%)	Micro-scale	Fe	Reduces creep rupture strength, increases DBTT	During solidification	33, 36, 37

Table 3. 1 Nominal chemical composition of T92 and BG12Cr heat-resistant steel studied in this research (wt%).

	C	Si	Mn	Cr	Mo	W	Co	V	Nb	B	N	Ni	Al	Ti	Zr	Cu	Fe
T92	0.07-0.13	0-0.50	0.30-0.60	8.50-9.50	0.30-0.60	1.50-2.00	-	0.15-0.25	0.04-0.09	0.001-0.006	0.030-0.070	0-0.40	0-0.02	0-0.01	0-0.01	-	Balance
BG12Cr	0.08-0.12	0.40-0.60	0.15-0.45	11.0-12.0	0.20-0.40	1.00-2.00	1.60-3.00	0.20-0.30	0.03-0.08	0.003-0.006	0.030-0.070	-	-	-	-	0.5	Balance

Table 3. 2 Tensile properties of T92 and BG12Cr studied (data provided by the manufacturer).

Material	**Temperature (°C)**	**Yield Stress (MPa)**	**Tensile Strength (MPa)**	**Elongation (%)**
T92	20	577	743	22
	600	318	386	30
BG12Cr	20	660	813	20
	600	368	438	22

Table 3. 3 Heat treatment condition in T92 and BG12Cr

Material	Sample ID	Normalizing Temperature((°C)	Tempering Temperature (°C)
T92	T92 N	1080	-
	T92 N+T760		760
	T92 N+T780		780
	T92 N+T800		800
	T92 N+T820		820
BG12Cr	TWT N	1080	-
	TWT N+T760		760
	TWT N+T780		780
	TWT N+T800		800
	TWT N+T820		820

Table 3. 4 Test matrix for creep crack growth test on T92 and BG12Cr

Temperature (°C)	**Load (kN)**	**Material**
600	6	T92
		BG12Cr
	10	T92
		BG12Cr
650	3	T92
		BG12Cr
	6	T92
		BG12Cr
700	3	T92
		BG12Cr

Table 5. 1 Summary of creep crack growth testing results. Note that two values in the same cell correspond to two creep crack growth regions in the same testpiece. NA means that such a value was not determined or measured during the test.

Temperature (°C)	**Load (kN)**	**Material**	**K_i (MPa√m)**	**Crack extension (mm)**	**Duration (h)**	**t_T (h)**	**$t_{0.2}$ (h)**
600	6	T92	21.6/25.7	0.30/1.17	729/568	35/10	334/282
		BG12Cr	23.7/27.7	0.22/0.45	759/479	NA/42	716/304
	10	T92	39.1	2.29	193	2	36
		BG12Cr	36.4	3.24	265	20	71
650	3	T92	11.3/14.4	0.64/2.14	1863/235	21/3	74/121
		BG12Cr	10.9/14.1	0.10/1.38	557/1968	NA/26	NA/763
	6	T92	21.1	7.80	188	2	58
		BG12Cr	20.5	4.95	886	18	93
700	3	T92	11.6	2.88	158	1	38
		BG12Cr	11.1	4.30	836	8	253

K_i is the initial stress intensity factor

t_T is the time to establish extensive creep

$t_{0.2}$ is the time for initial 0.2 mm crack growth

Table 6. 1 The summary of fracture mechanism in T92 and BG12Cr with vary test conditions.

Temperature (°C)	**Load (kN)**	**Material**	**Fracture Mechanism**	**Key Evidence**
600	6	T92	intergranular (IG) → transgranular	Figure 5. 16&Figure 5. 26
		BG12Cr	IG	Figure 5. 21&Figure 5. 31
	10	T92	Transgranular	Figure 5. 17&Figure 5. 27
		BG12Cr	IG	Figure 5. 22&Figure 5. 32
650	3	T92	Transgranular	Figure 5. 18&Figure 5. 28
		BG12Cr	IG → mixed of IG and duitle fracture → duitile fracture	Figure 5. 23&Figure 5. 33
	6	T92	Transgranular	Figure 5. 19&Figure 5. 29
		BG12Cr	IG → mixed of IG and duitle fracture → duitile fracture	Figure 5. 24&Figure 5. 34
700	3	T92	Mixture of IG and dutile	Figure 5. 20&Figure 5. 30
		BG12Cr	IG → mixed of IG and duitle fracture → duitile fracture	Figure 5. 35

Table 6. 2 Comparison of da/dt–C* with literature value

Reference	Material	Temperature (°C)	Slope (n)	Intercept (log C*, MPa·m/h)
Current Study	BG12Cr	600	0.71	0.0037
		650	0.72	0.040
		700	0.78	0.020
Current Study	T92	600	0.88	0.038
		650	0.70	0.0212
		700	0.65	0.050
Kim et al. (105)	Modified P91	550	0.77	0.009
Saber M (62)	P92	650	0.76	0.069
Kim et al. (83)	P92	600	0.71	0.032
Speicher et al. (106)	P122	650	1.13	0.679

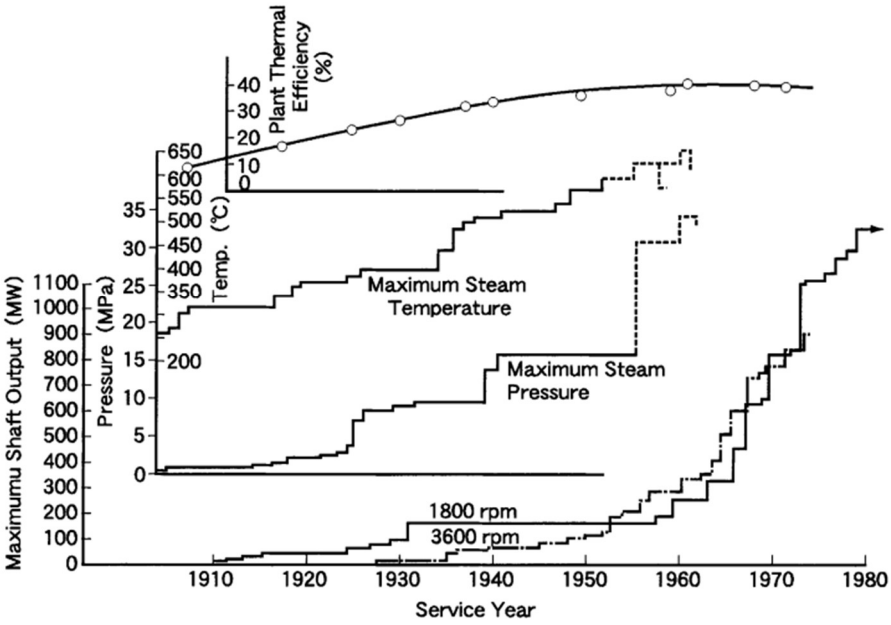

Figure 2. 1 The development history of fossil-fueled turbine generators (3).

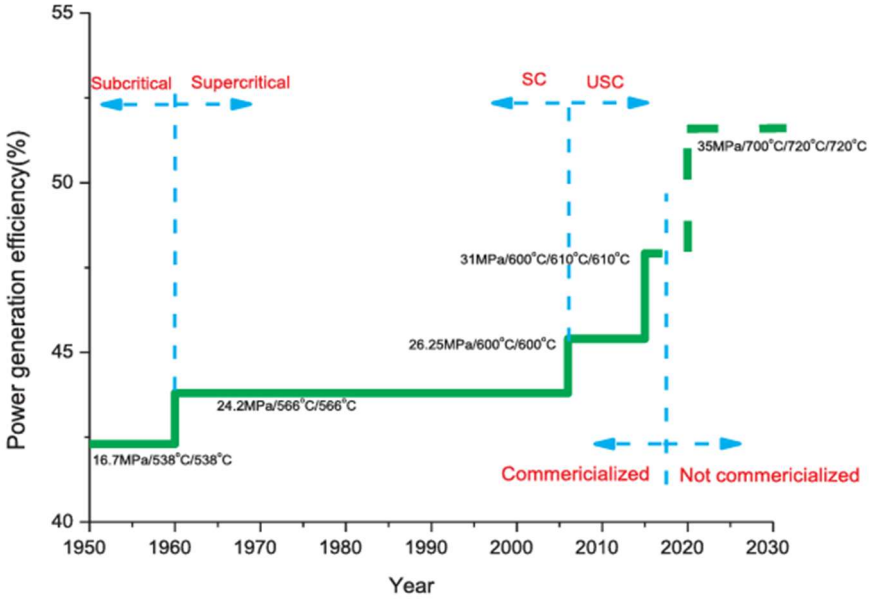

Figure 2. 2 The development of coal-fired power plant in China (8).

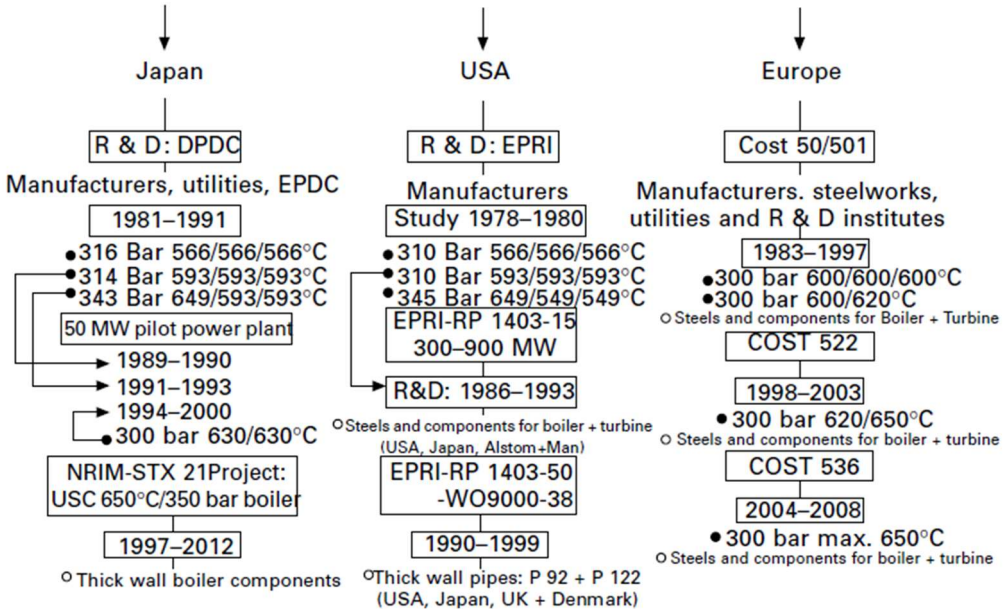

Figure 2. 3 Overview of the advancement in heat-resistant steel development for advanced power plant applications since 1978 (10).

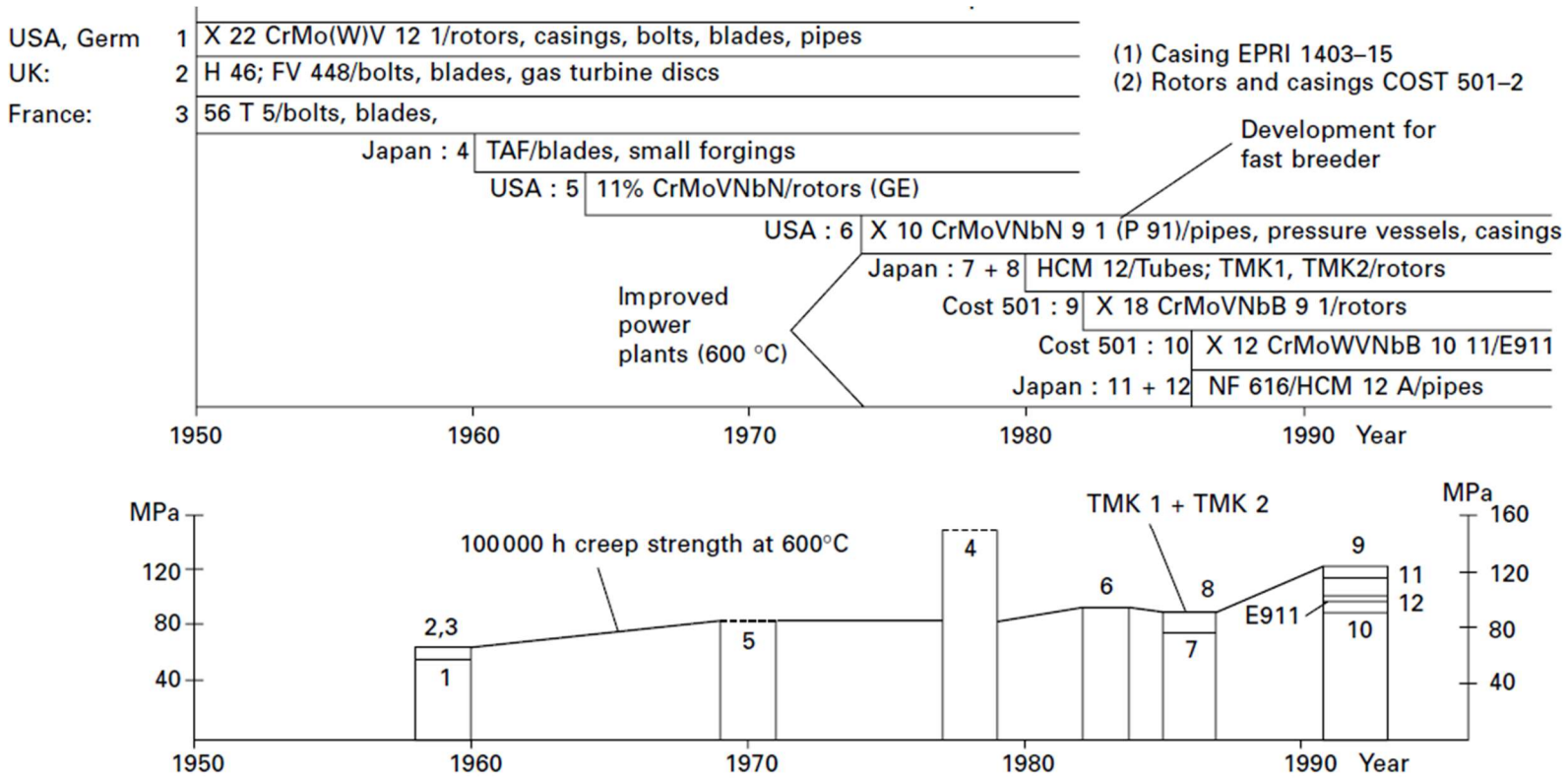

Figure 2. 4 Overview of the historical development of 9–12% Cr heat-resistant steels (1950–1995) and their 10^5 hours creep rupture strengths at 600 °C (10).

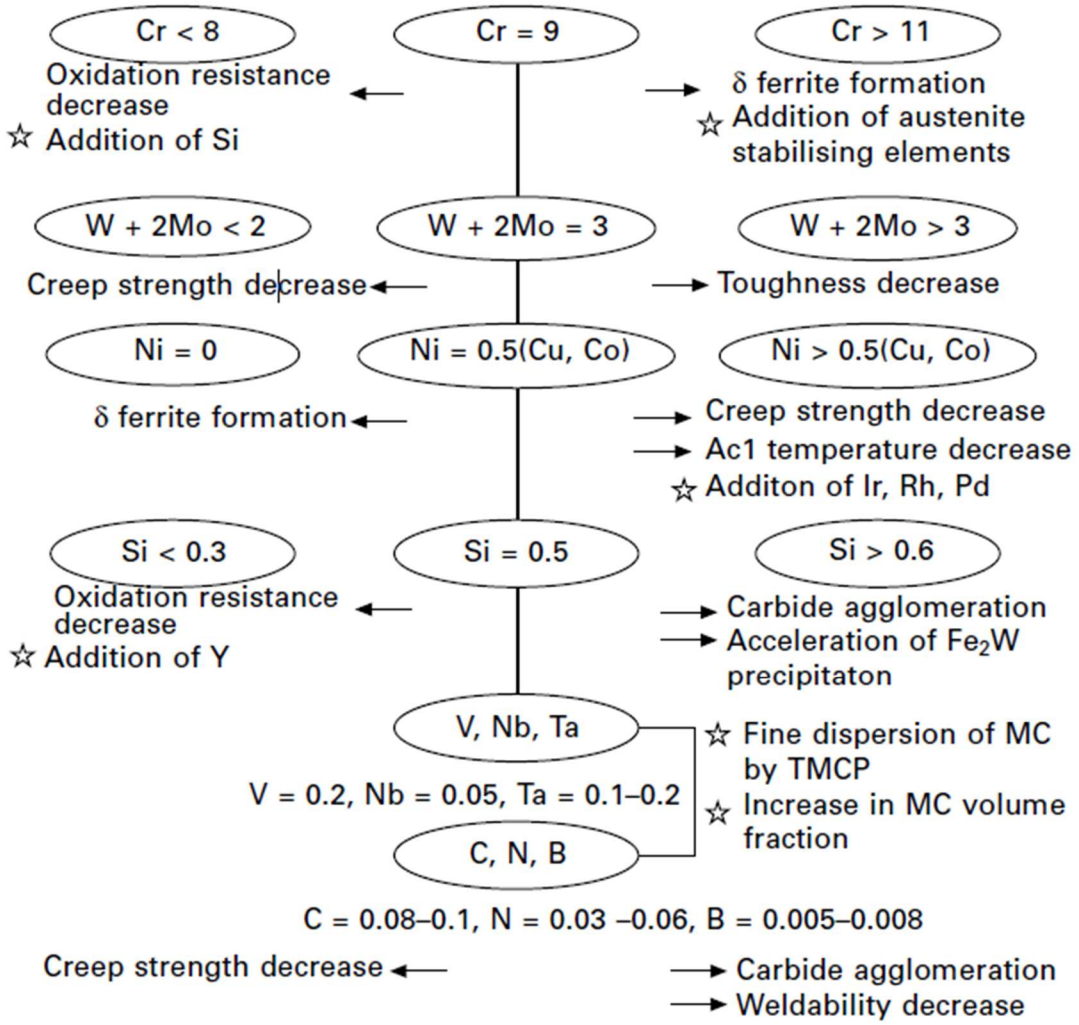

Figure 2. 5 Alloy design approach developed by Janpanese NIMS reserch project for high-chromium ferritic steels intended for 650°C ultra-supercritical (USC) boiler applications (10).

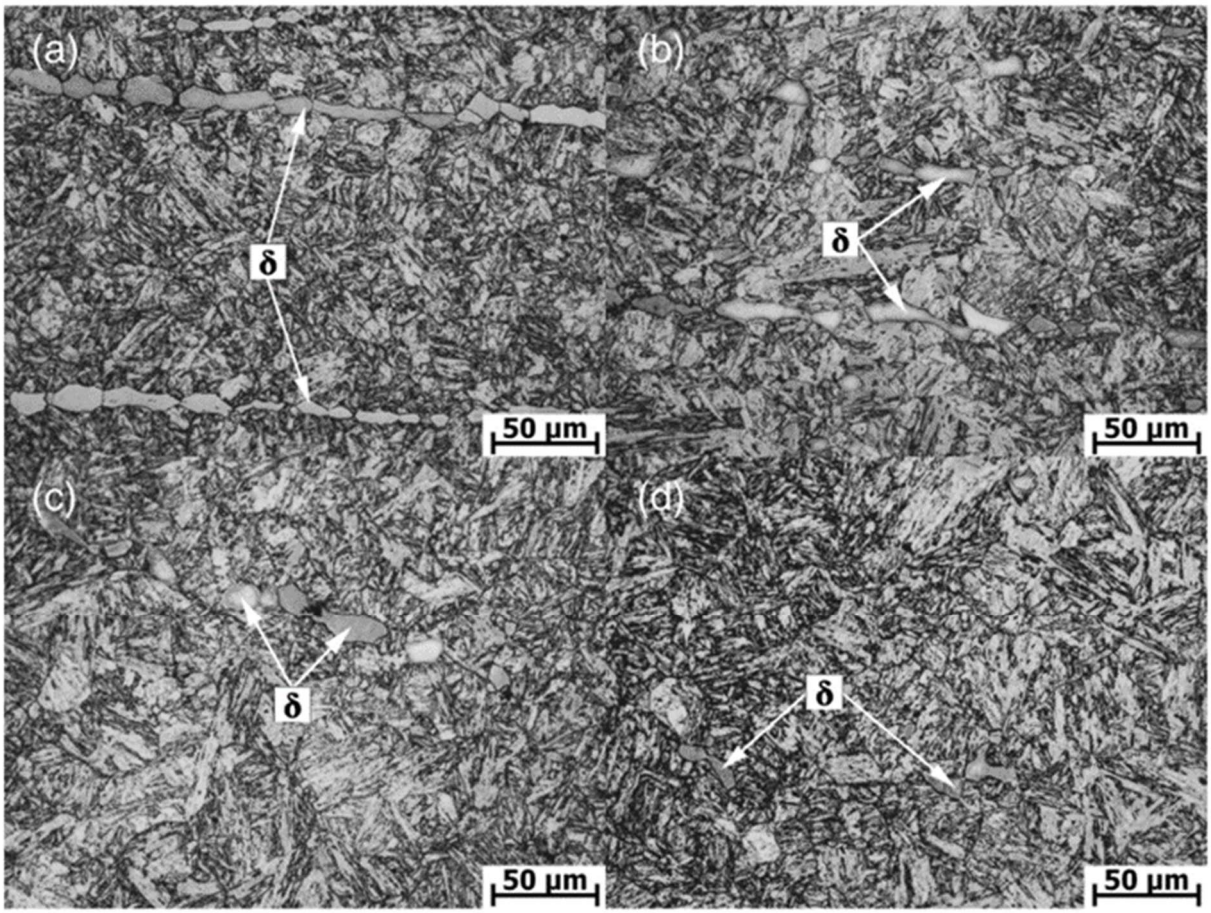

Figure 2. 6 The optical images of δ-ferrites in specimens with different annealing times at 100°C a) 0.5h, b) 3h, c) 6h, d) 10h (41).

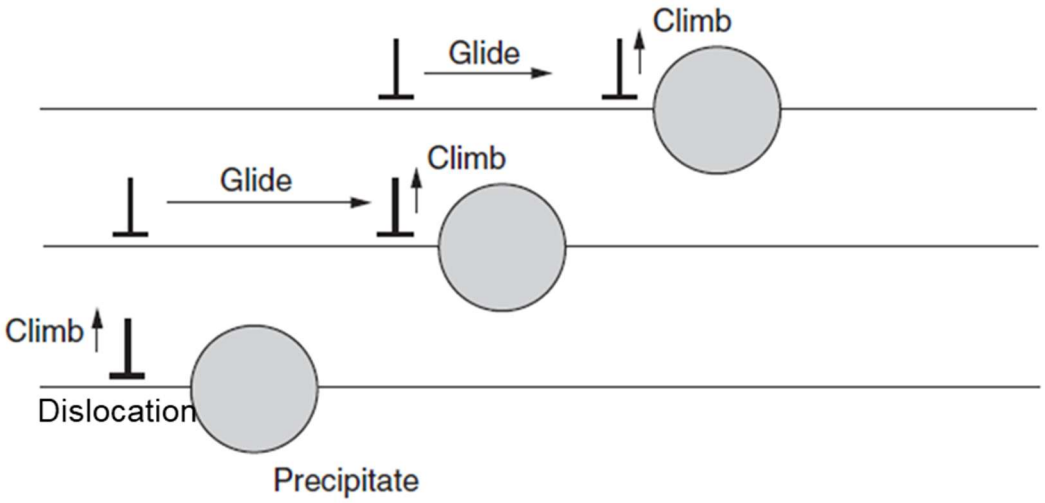

Figure 2. 7 Dislocation creep mechanism illustrated by the climb–glide process of dislocation movement (64).

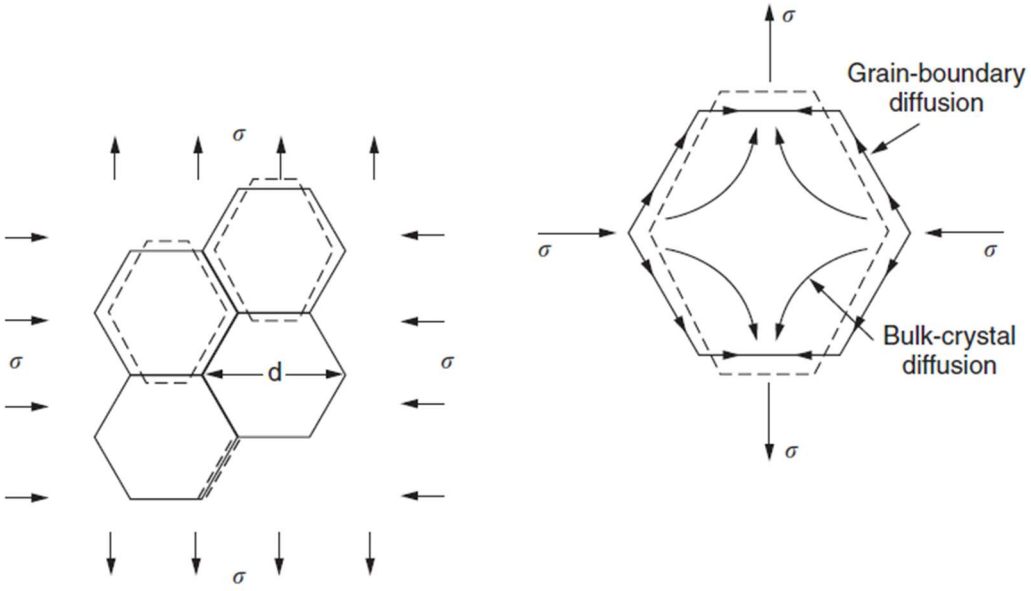

Figure 2. 8 Schematic illustration of diffusion creep mechanisms (64).

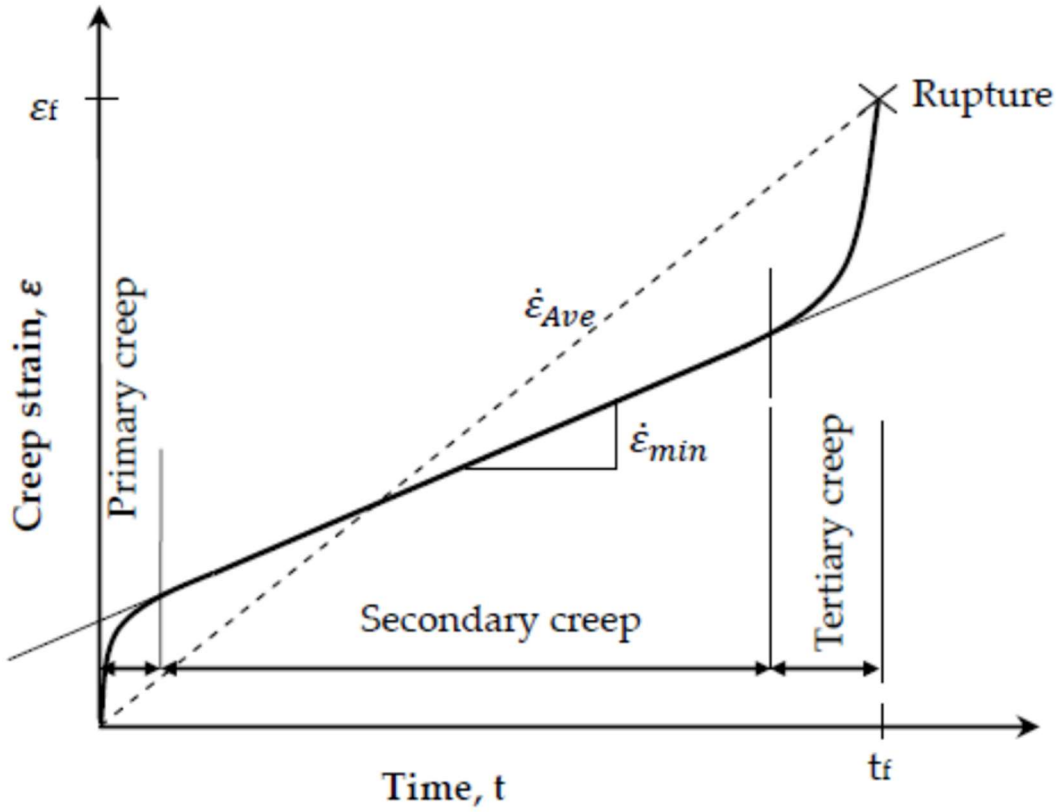

Figure 2. 9 Typical creep strain curves (62).

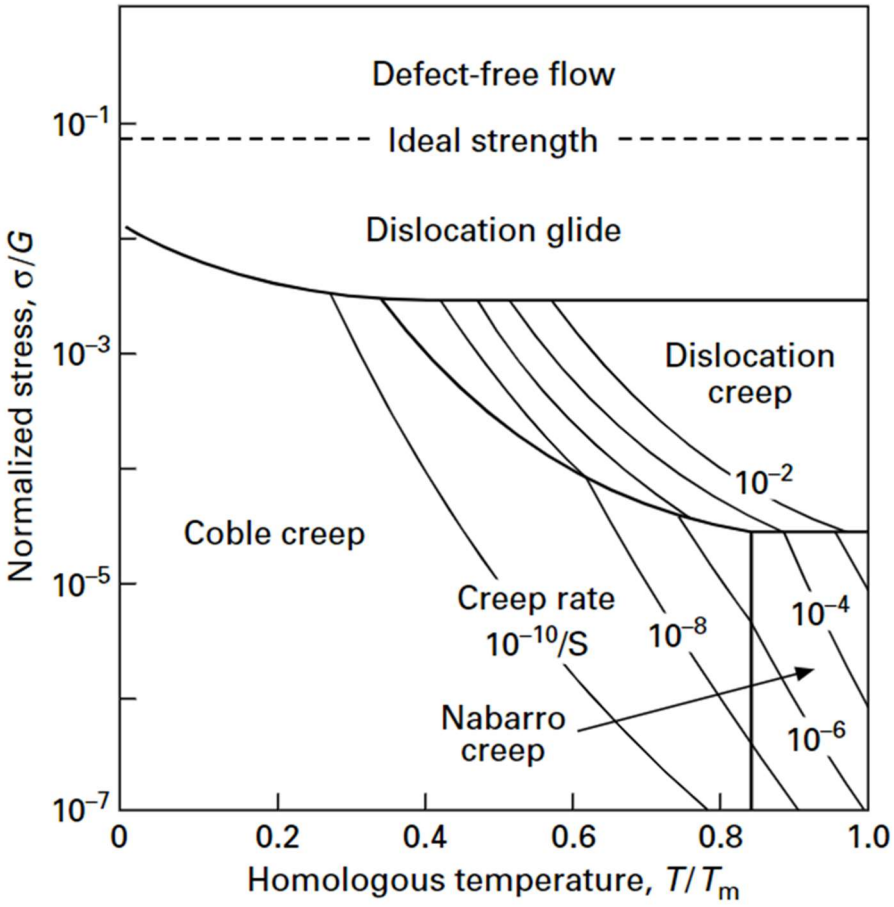

Figure 2. 10 Schematic deformation mechanism map (10).

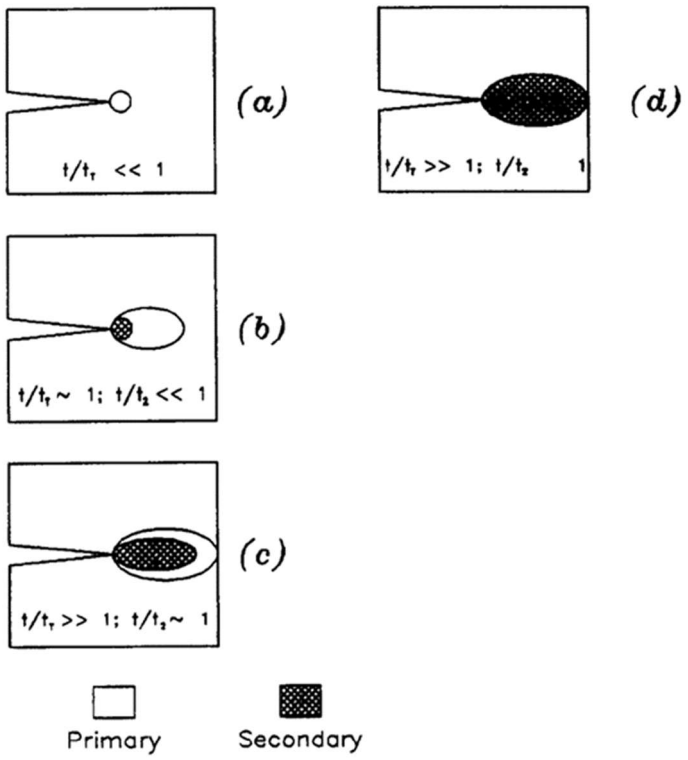

Figure 2. 11 Stages of creep deformation in cracked specimens undergoing both primary and secondary creep deformation under static loading (69). (a) Small-scale primary creep. (b) The secondary creep zone expands within the primary creep zone, reaching a size comparable to the uncracked ligament. (c) Extensive primary creep condition with a significant secondary creep zone. (d) Extensive secondary creep conditions .

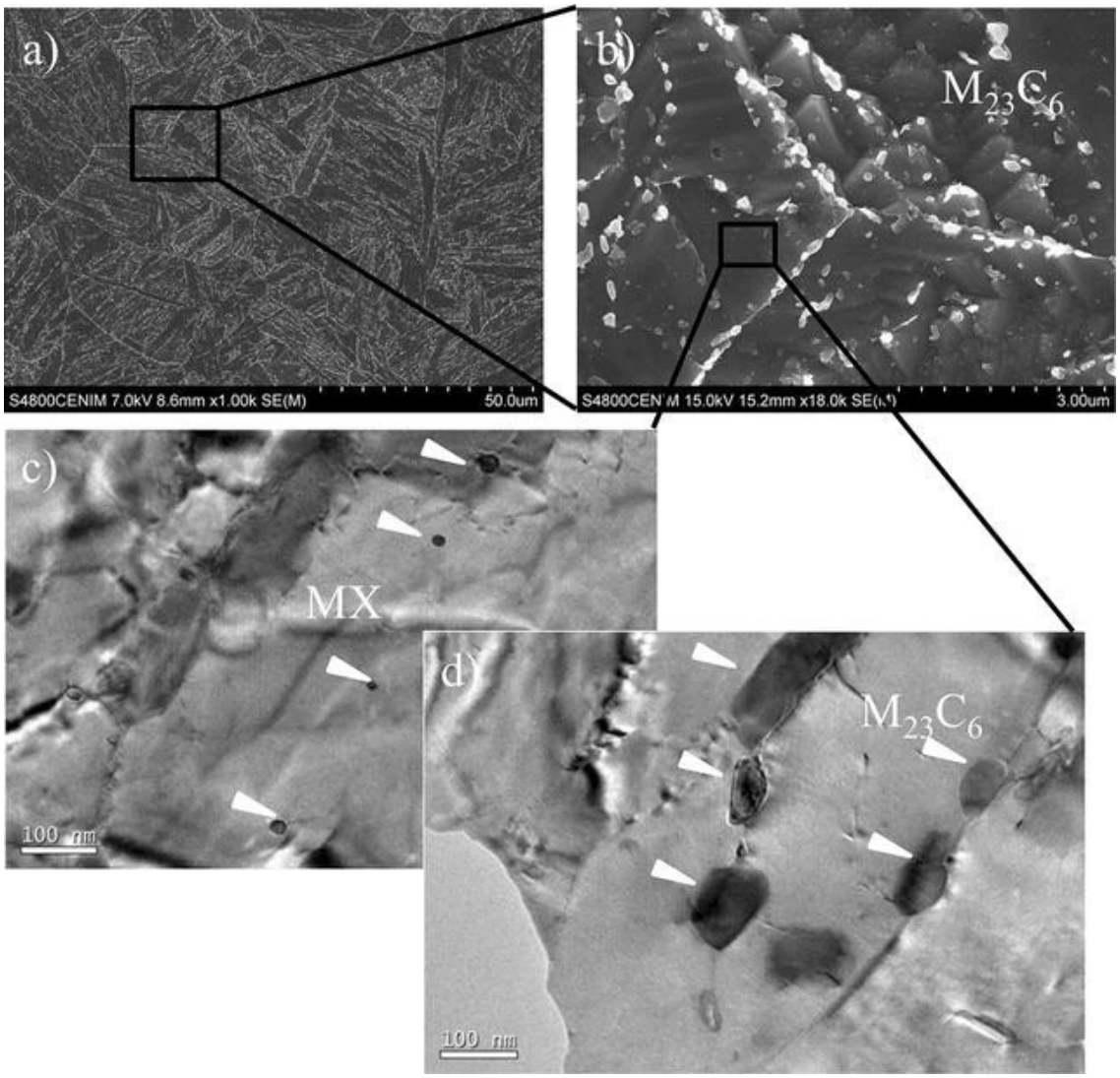

Figure 2. 12 Microstructure of a typical 9% Cr heat-resistant steel (P91): (a) SEM image at low magnification; (b) SEM image at high magnification; (c) TEM image showing MX precipitates located within lath; (d) TEM image showing $M_{23}C_6$ carbides formed along lath boundaries (96).

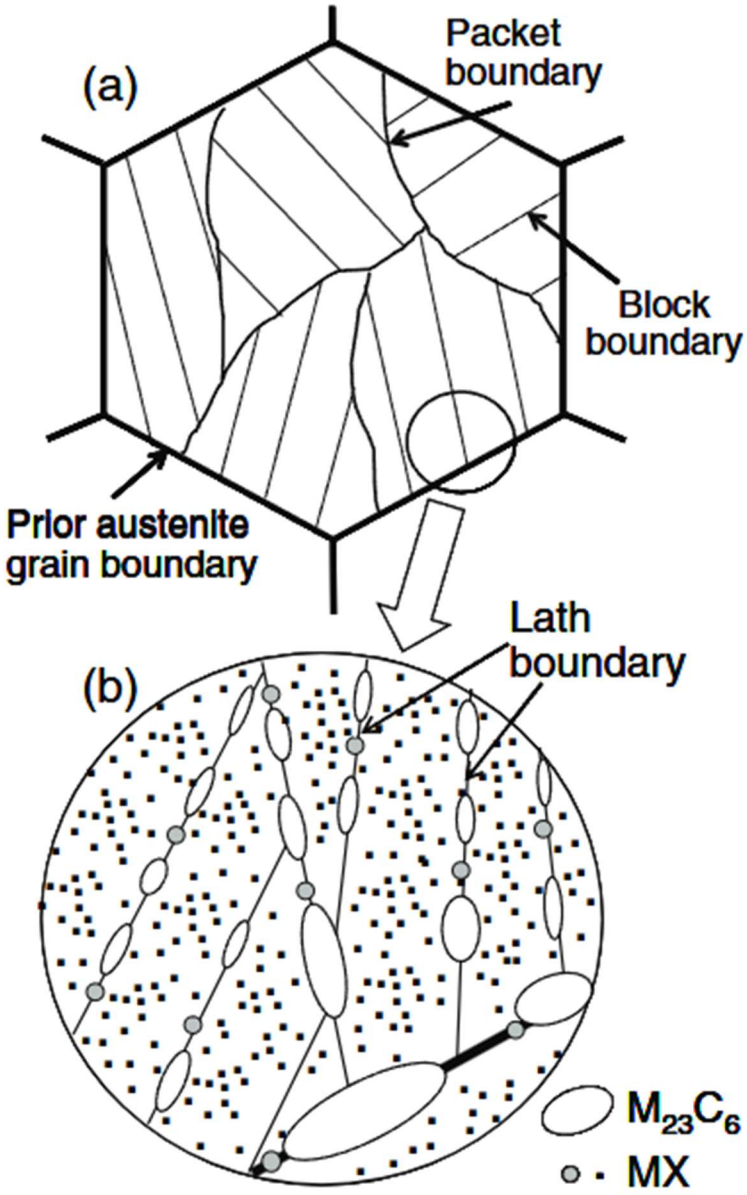

Figure 2. 13 Schematic illustration of hierarchical martensitic microstructure in 9–12%Cr steels (78).

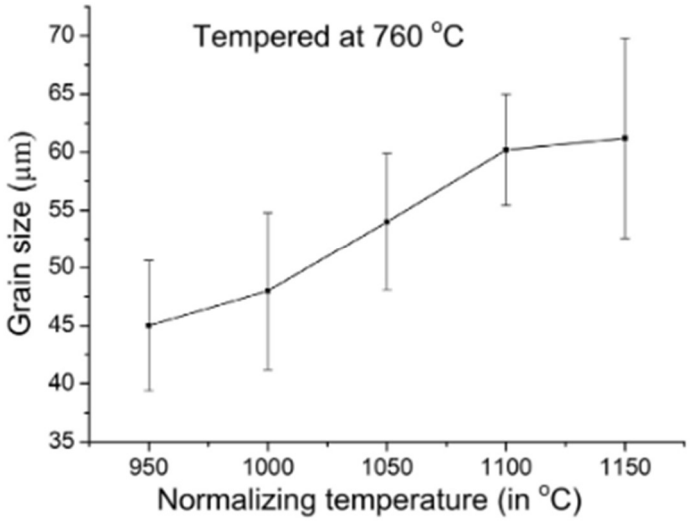

Figure 2. 14 Variation of grain size with different normalizing temperature (79).

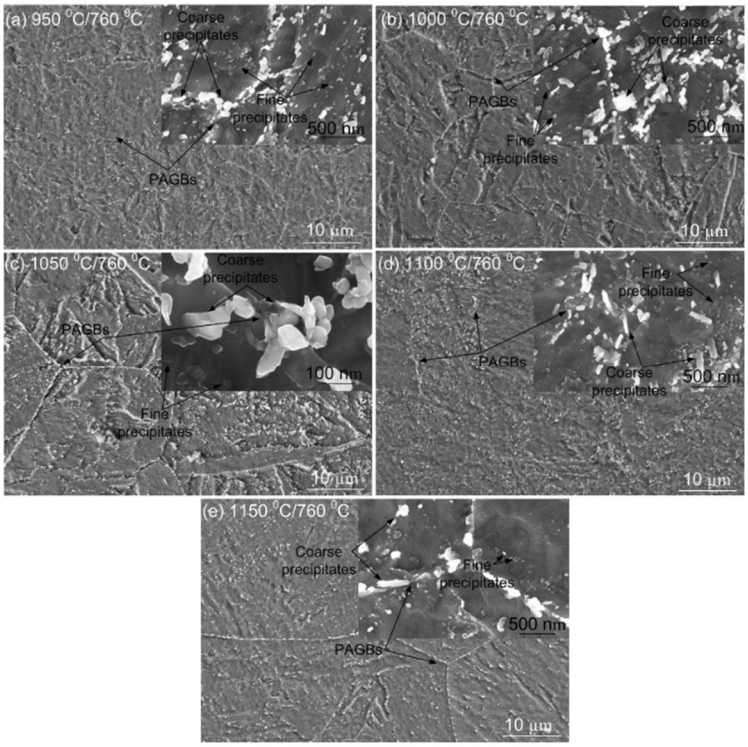

Figure 2. 15 SEM images of samples with different normalizing and after tempering at 760°C: a) 950°C; b) 1000°C; c) 1050°C; d)1100°C; e) 1150°C (79).

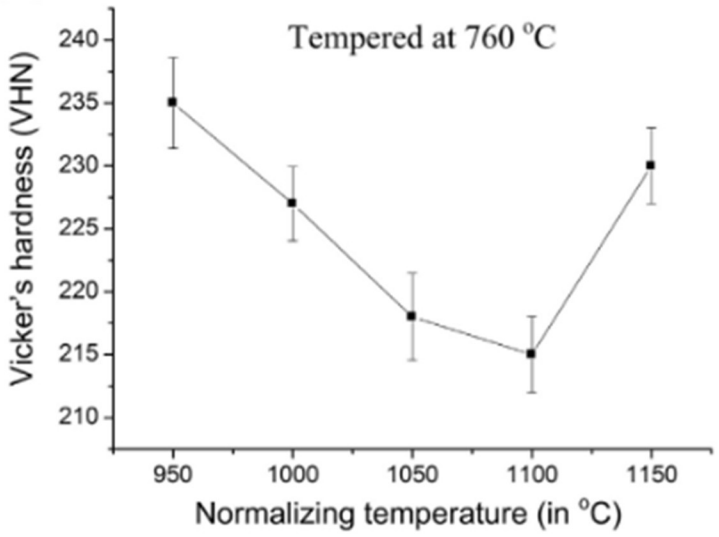

Figure 2. 16 Variation of microhardness with different normalizing temperature and after tempering at 760°C (79).

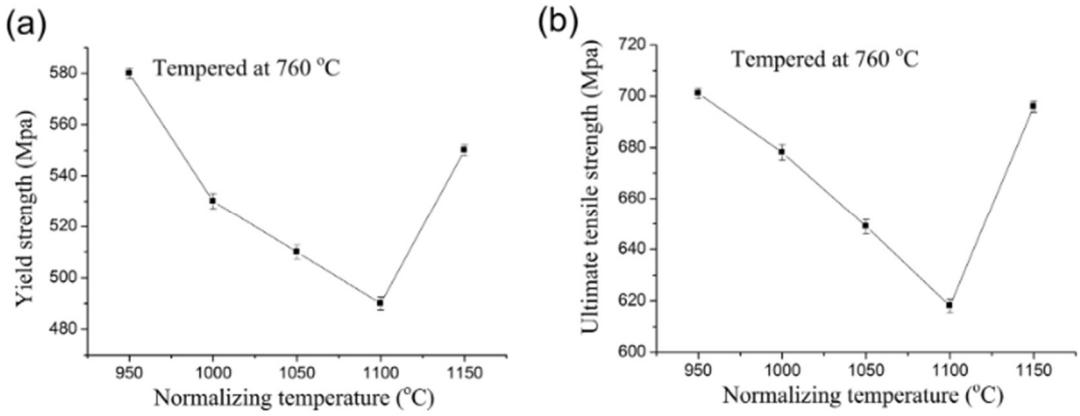

Figure 2. 17 Variation of yield strength and ultimate tensile strength with different normalizing temperature and after tempering at 760°C (79).

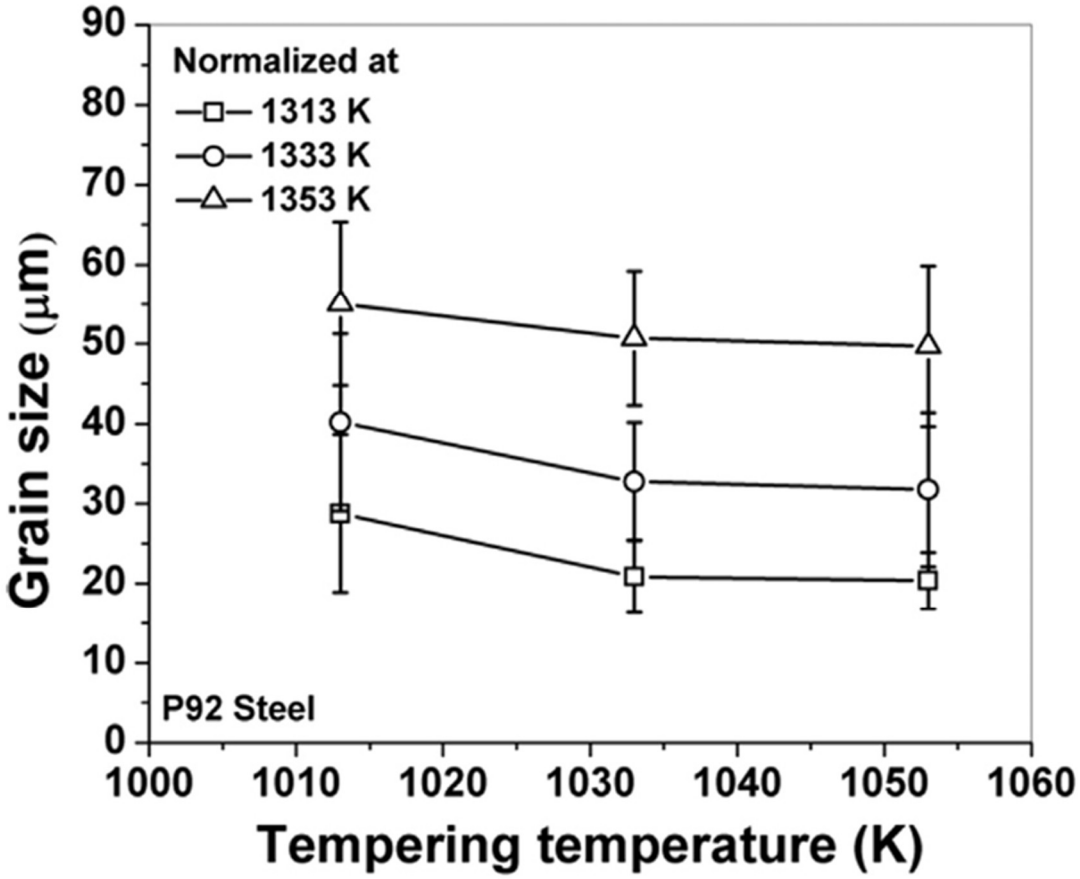

Figure 2. 18 Variation of grain size with different normalizing temperature and tempering temperature (80).

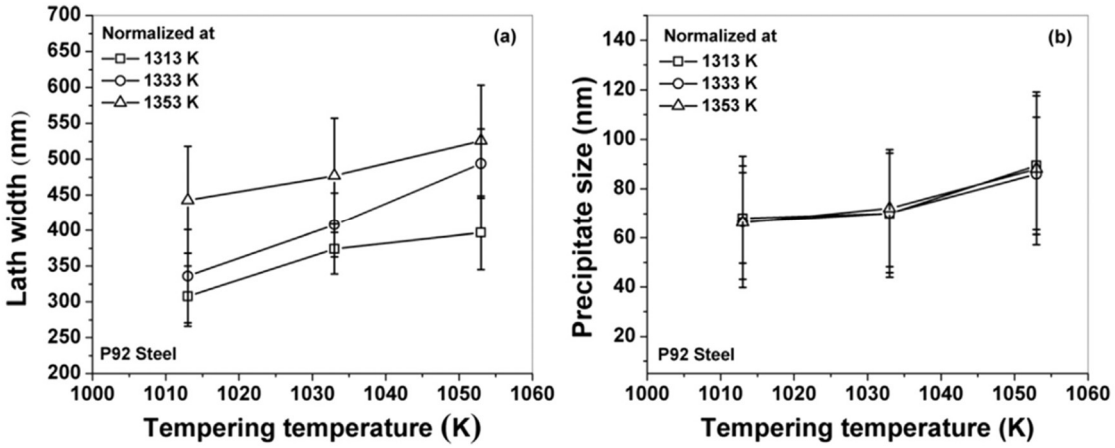

Figure 2. 19 Variation of lath width and $M_{23}C_6$ carbides with different normalizing temperature and tempering temperature (80).

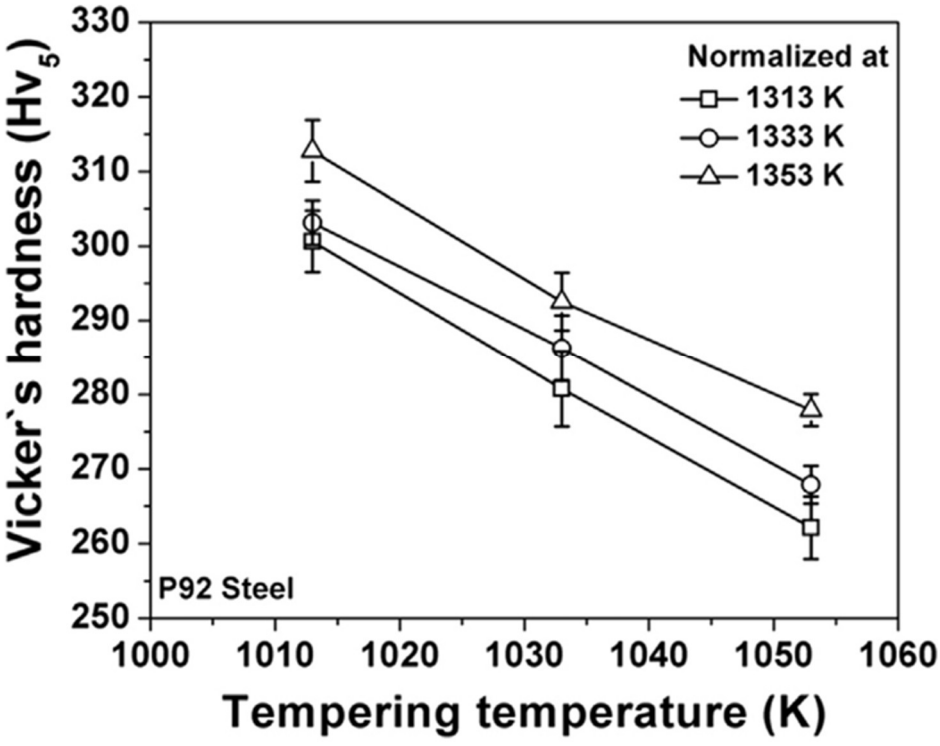

Figure 2. 20 Variation of hardness with different normalizing and tempering condition (80).

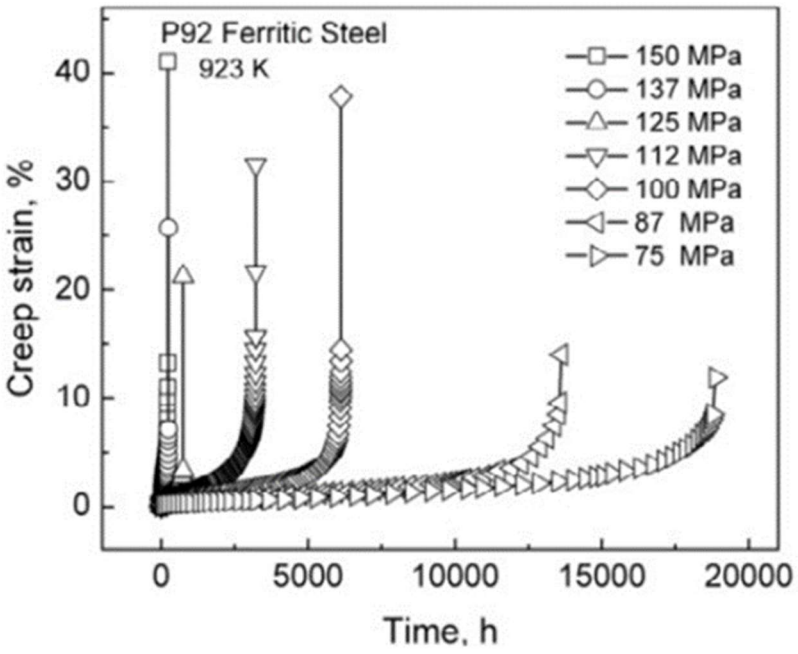

Figure 2. 21 The creep curves at different stress at 650°C (81).

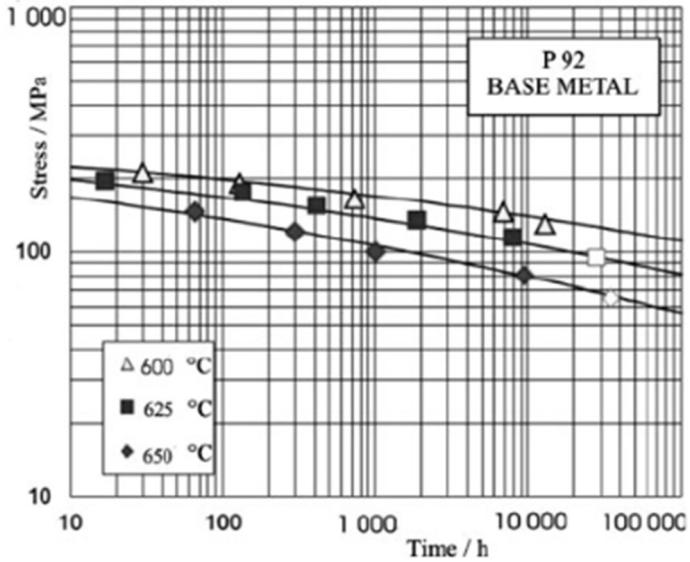

Figure 2. 22 Creep rupture life of P92 steel under various temperatures and stress conditions (82).

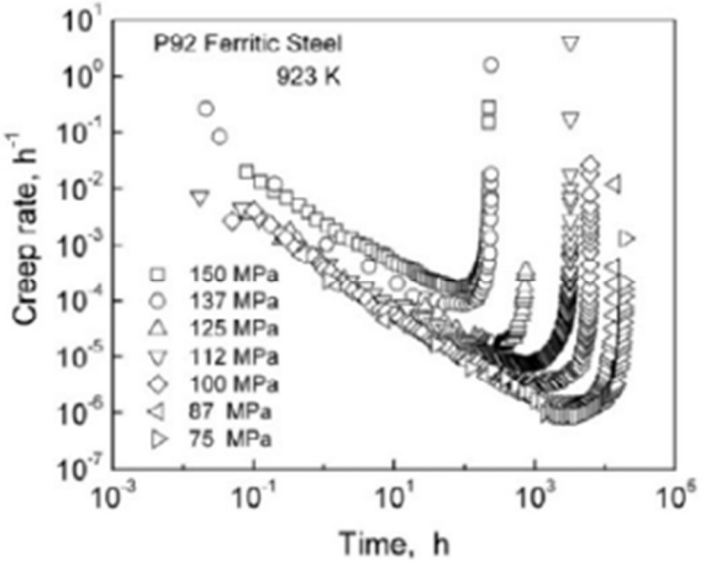

Figure 2. 23 Variation of creep strain rate with time for P92 steel tested at 923 K (650 °C) under different applied stresses (81).

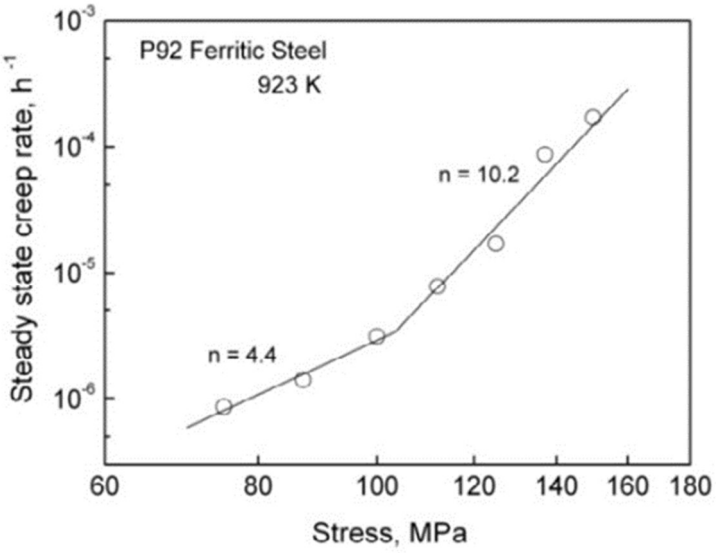

Figure 2. 24 Different minimum creep rate with applied stress at 650°C for P92 steel (81).

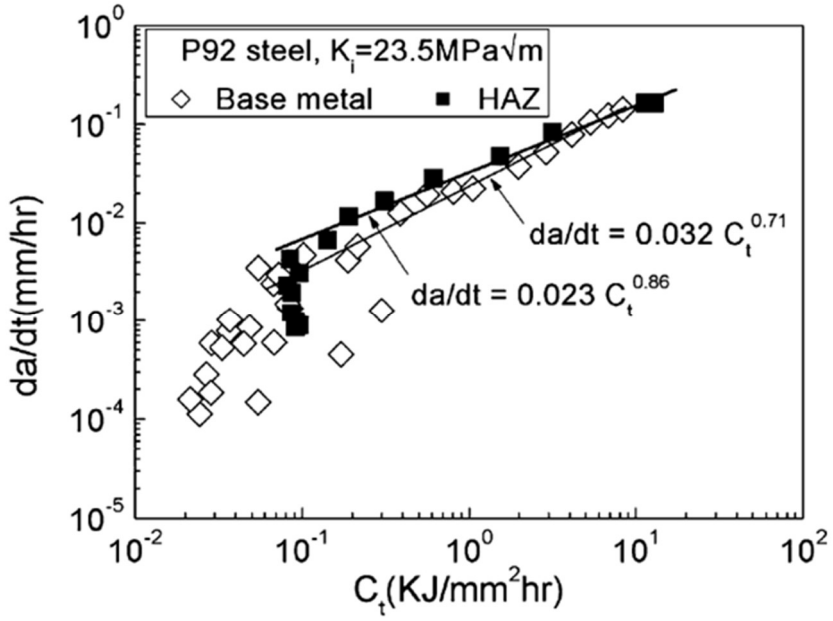

Figure 2. 25 Crack rate, da/dt aginst C_t on P92 and its weld at 600 °C (83).

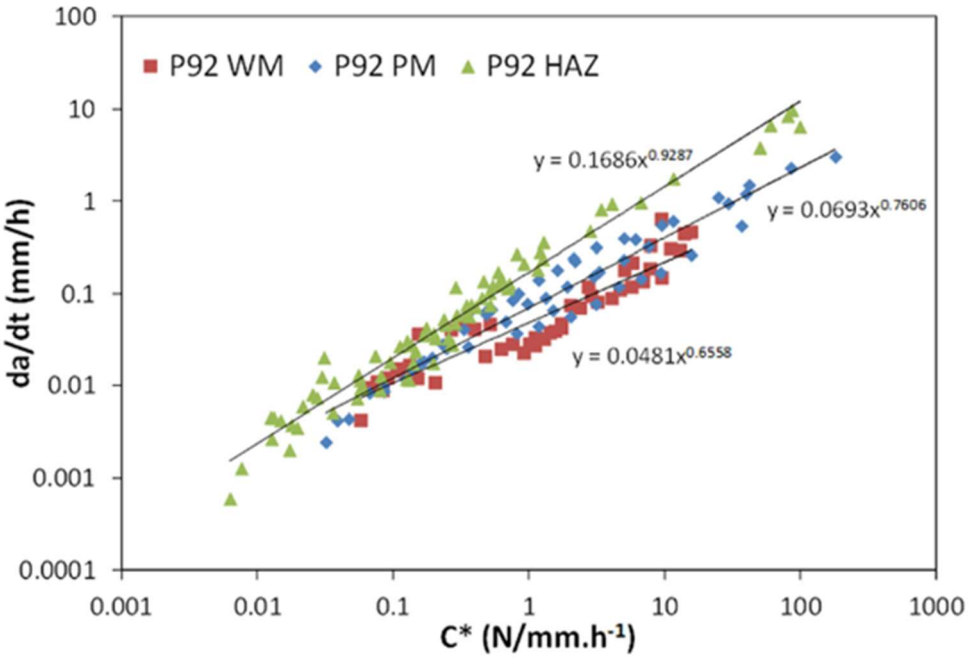

Figure 2. 26 Crack rate, da/dt aginst C* on P92 and its weld at 675 °C (84).

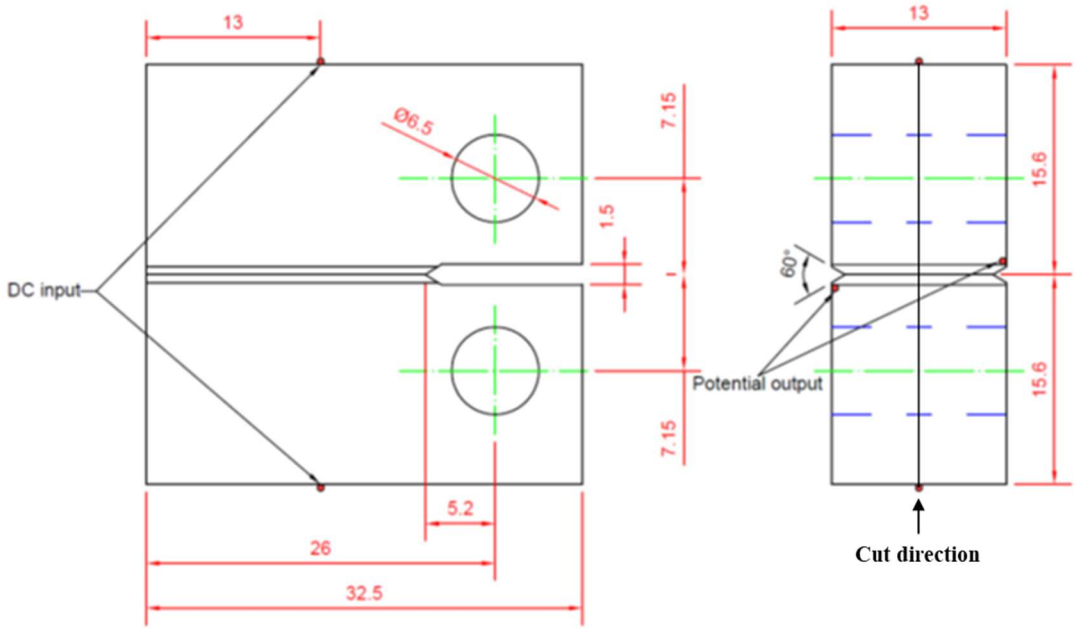

Figure 3. 1 The schematics of sample geometry, the wired points of DC input and potential output, the cut direction for microstructure characterisation

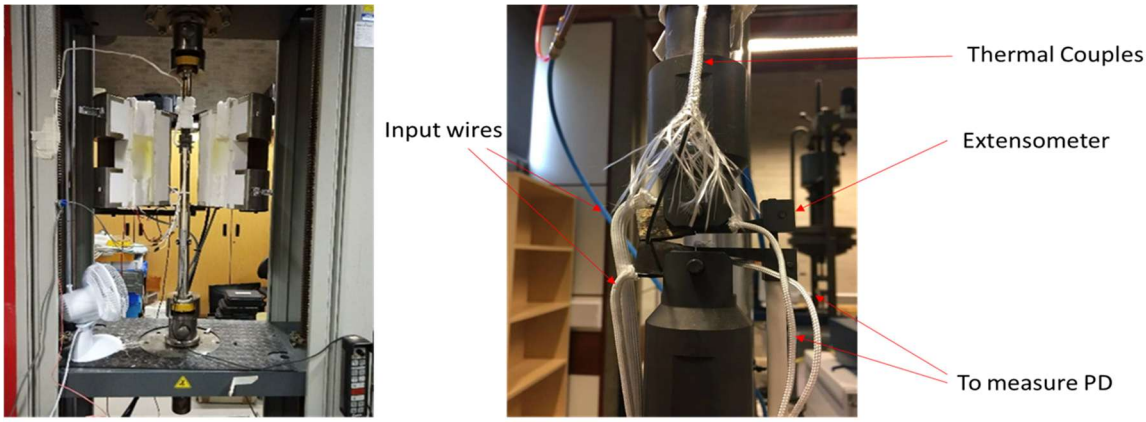

Figure 3. 2 (a) Zwick 100 testing machine with a high-temperature furnace; (b) Mounted C(T) specimen with welded input wires, potential output wires, attached thermocouple, and mounted extensometer.

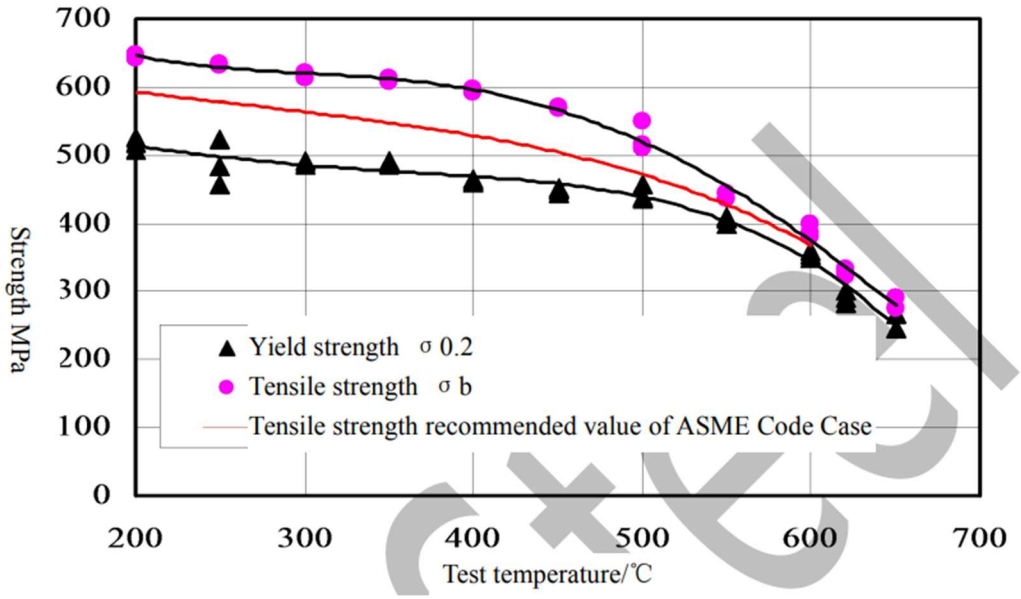

Figure 3. 3 The tensile properties of P92 at from 200°C to 650°C, provided by BaoWu steel.

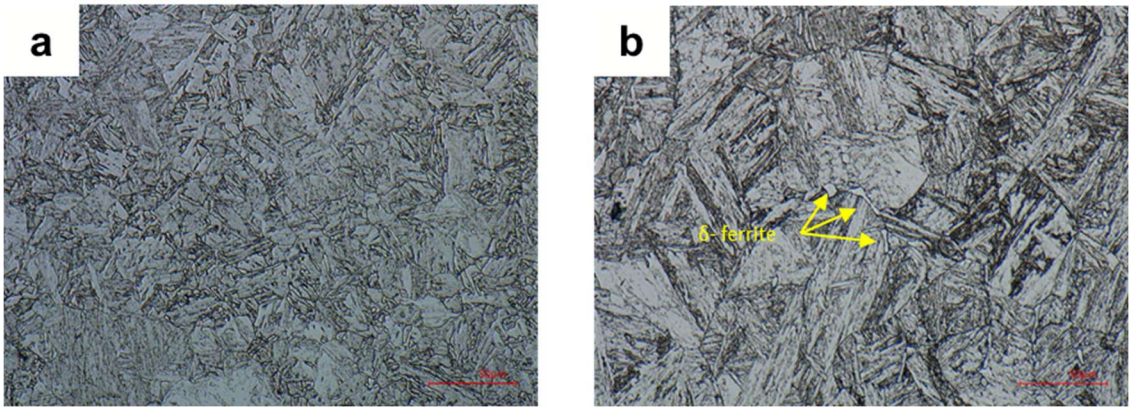

Figure 4. 1 Optical image showing the microstructure of As received (a)T92 and (b)BG12Cr.

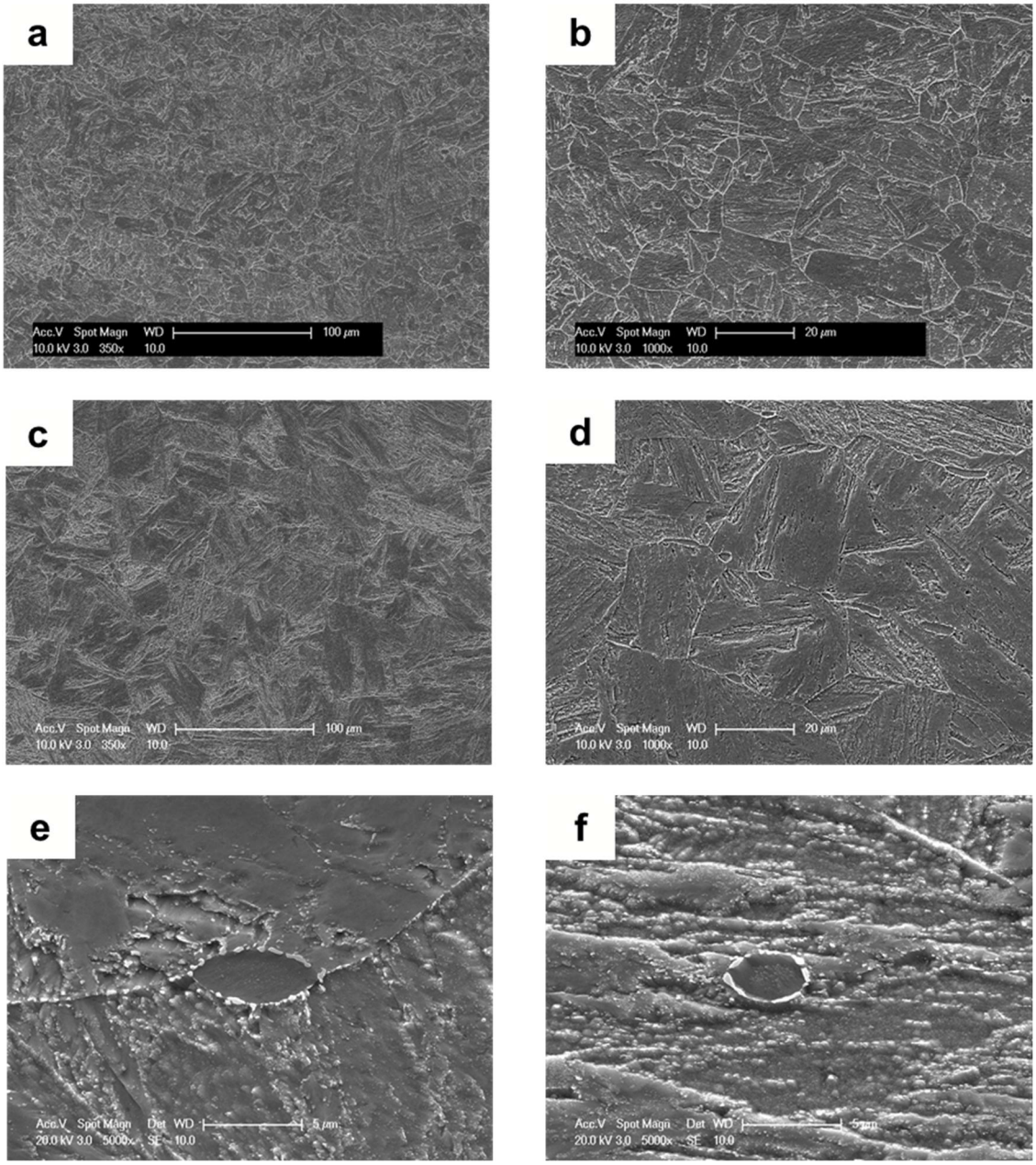

Figure 4. 2 SEM micrographs of as-received T92 and BG12Cr: a) T92 at low magnification; b) T92 at high magnification; c) BG12Cr at low magnification; d) BG12Cr at high magnification; e) δ-ferrite at PAGB in BG12Cr; f) δ-ferrite within prior PAG in BG12Cr.

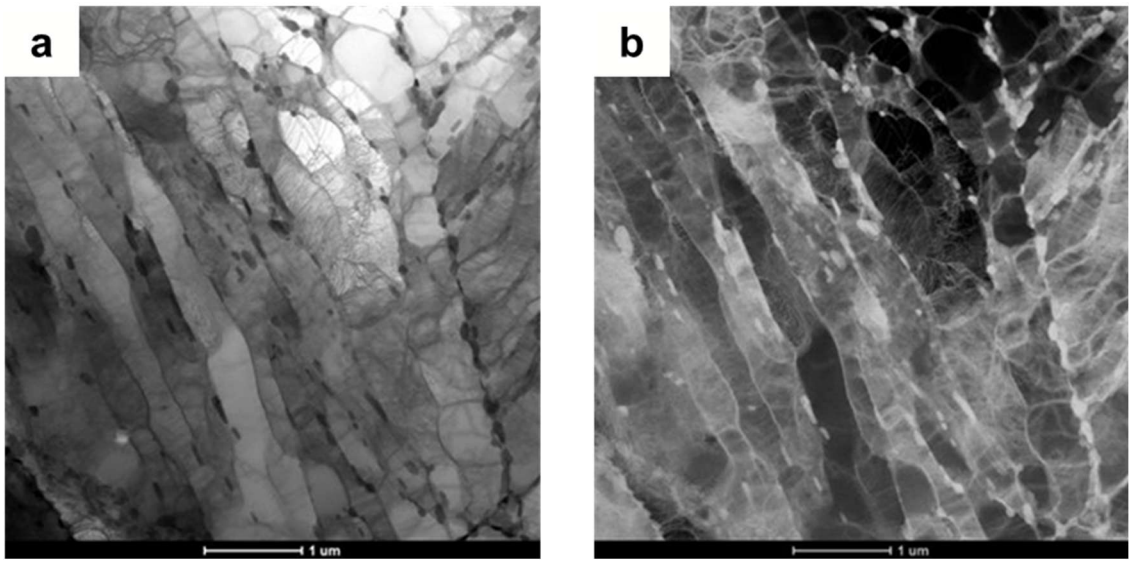

Figure 4. 3 TEM images of T92: a) BF-STEM image, b) HAADF-STEM image

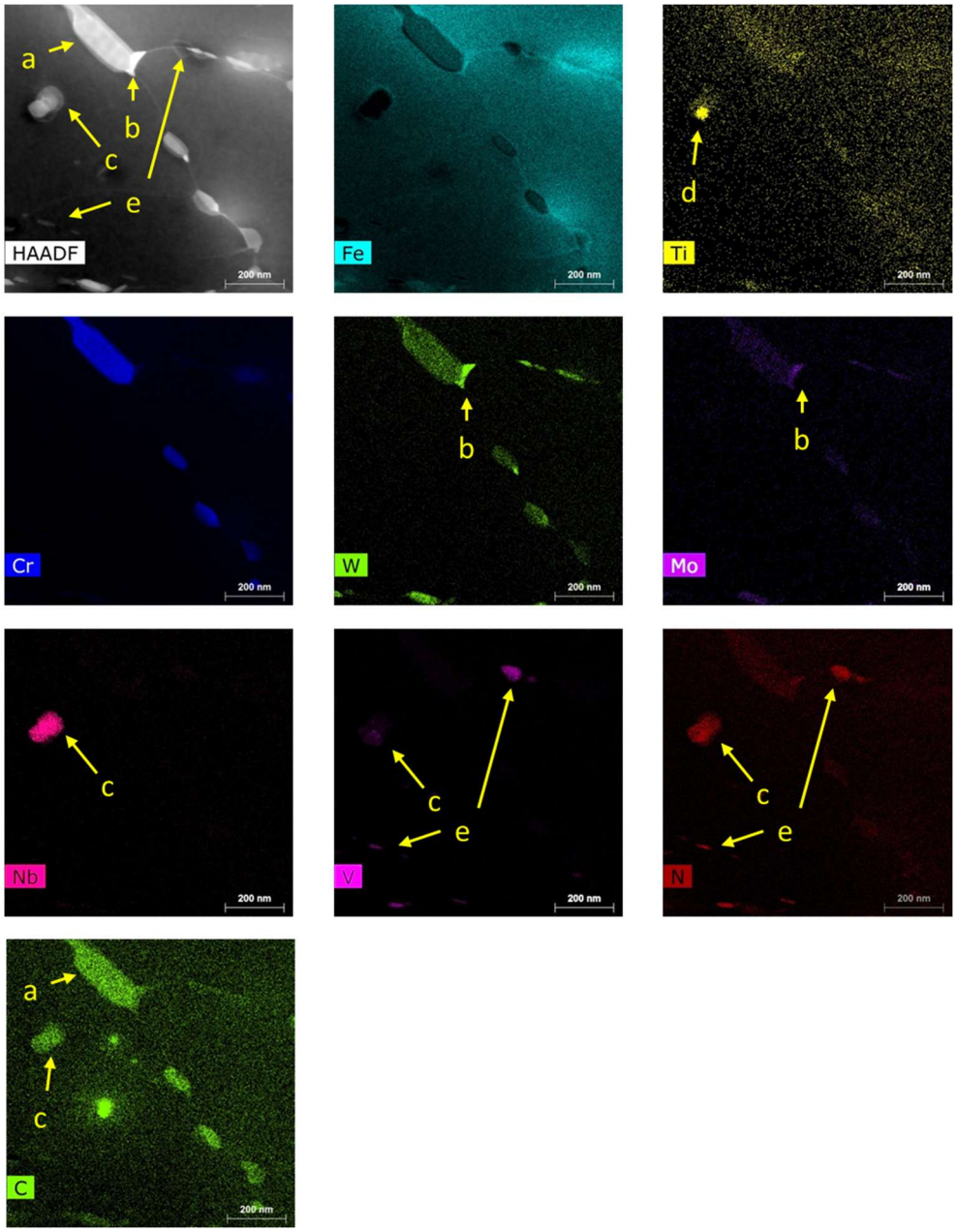

Figure 4. 4 HAADF STEM image and elemental EDS maps for T92, showing particles on PAGBs and interior grain : (a) (Cr, Mo, W) rich carbide, (b) (W, Mo)-rich intermetallics, (c) (Nb, V)-rich carbonitride, (d) Ti-rich carbonitride, (e) small V-rich carbonitride, (f) large V-rich carbonitride.

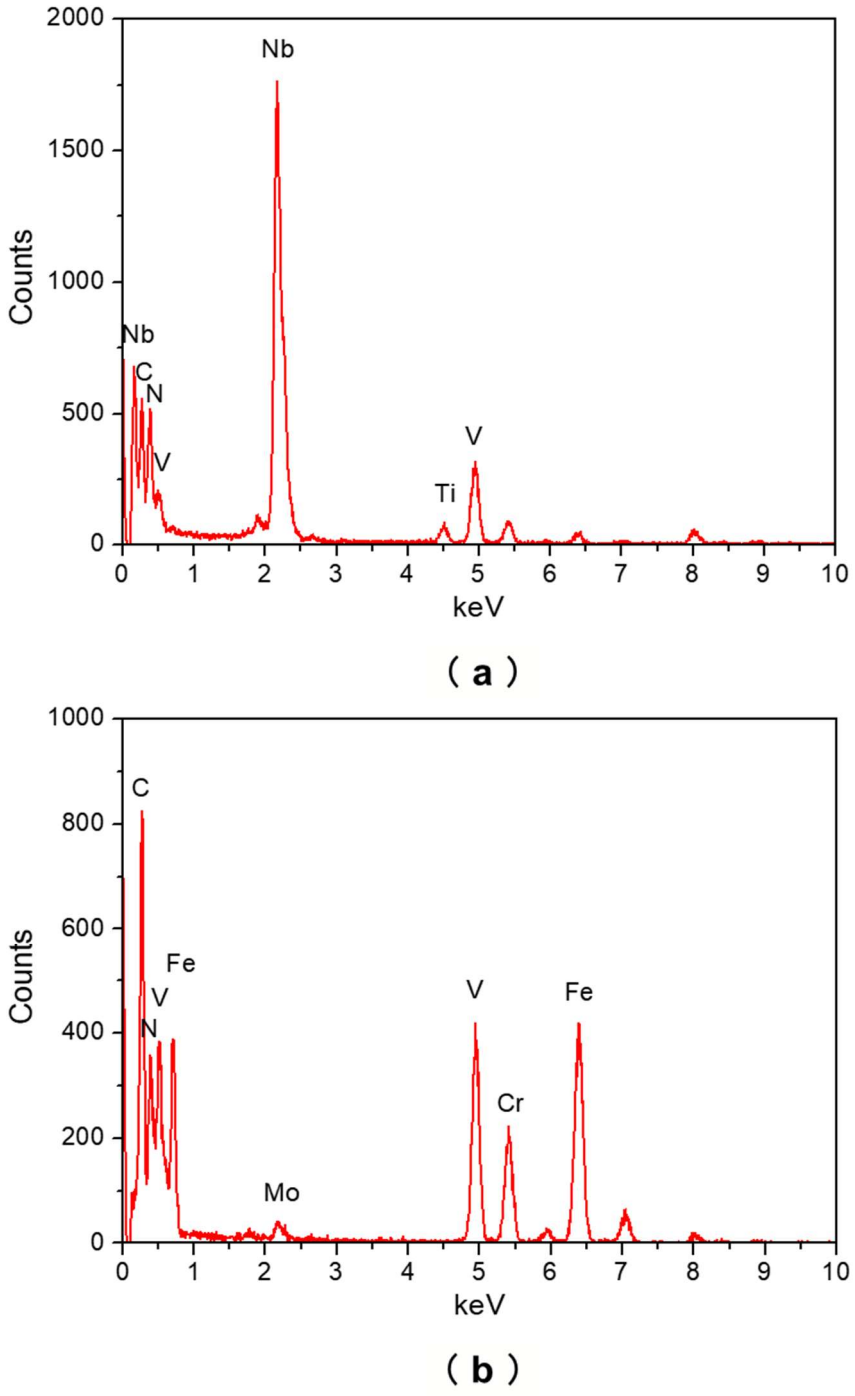

Figure 4. 5 EDS spectrum from a) (Nb, V)-rich carbonitride (Nb, V)(CN),b) V-rich carbonitride V(CN).

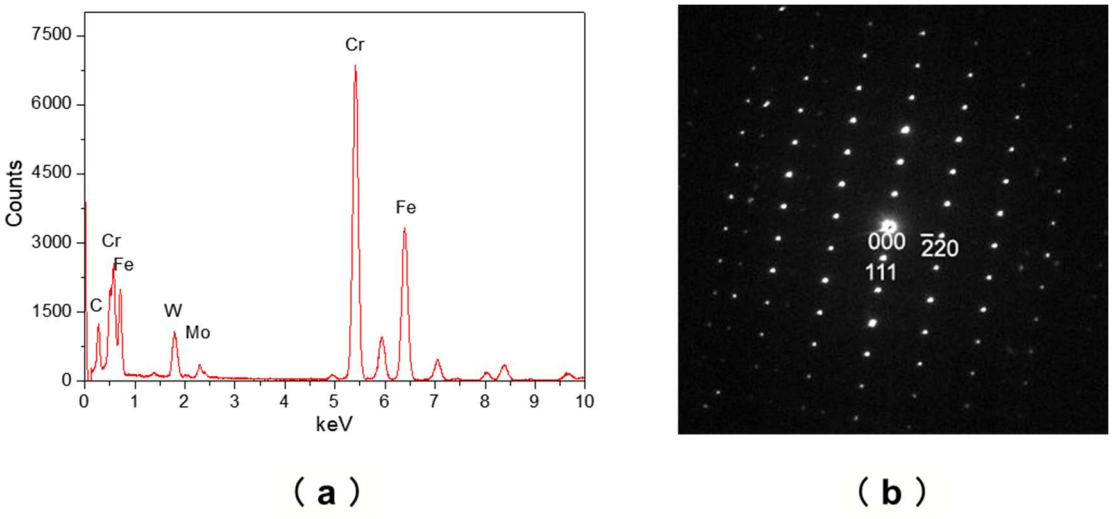

Figure 4. 6 a) EDS spectrum from the particle on the boundary and b) selected area diffraction pattern (SAD) of [11-2] from the carbide.

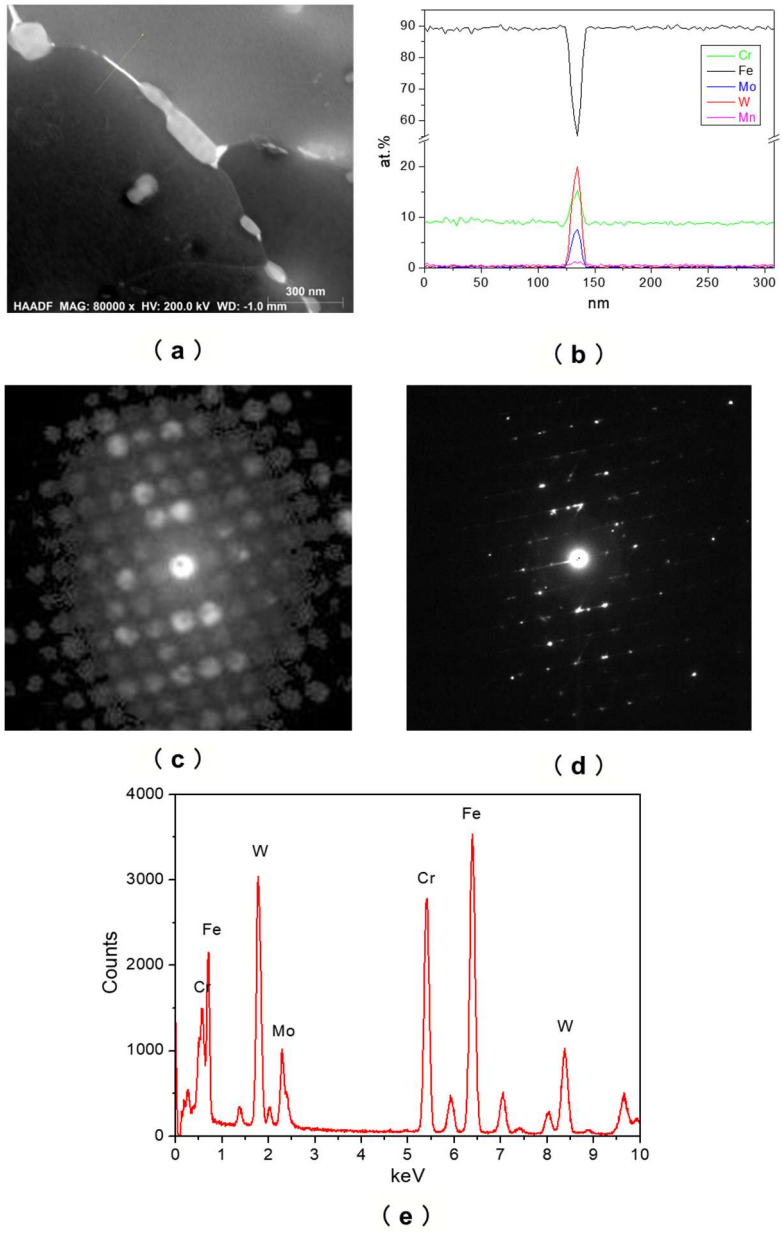

Figure 4. 7 a) HAADF image showing the line for EDS linescan, b) EDS linescan along the line in Figure 4. 7 a, c) convergent beam electron diffraction (CBED) of [-12-13] zone axis from the W and Mo rich carbide (Laves phase) and d) SAD of [-12-13] zone axis from W an d Mo rich carbide (Laves phase), e) EDS spectrum from the W an d Mo rich carbide (Laves phase).

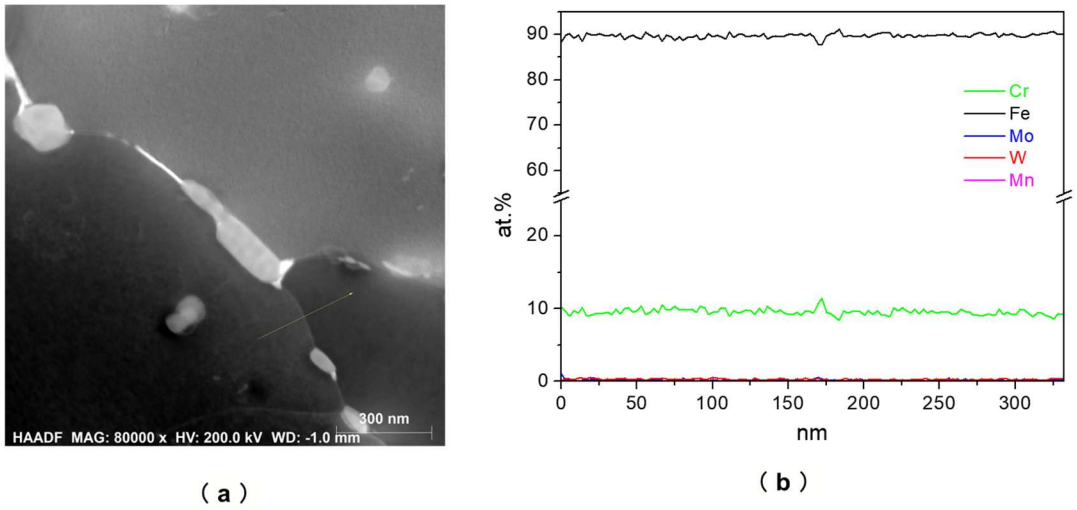

Figure 4. 8 a) HAADF STEM image showing the line for EDS linescan and (b) EDS linescan along the line in Figure 4. 8 a showing Cr enhancement at the boundary.

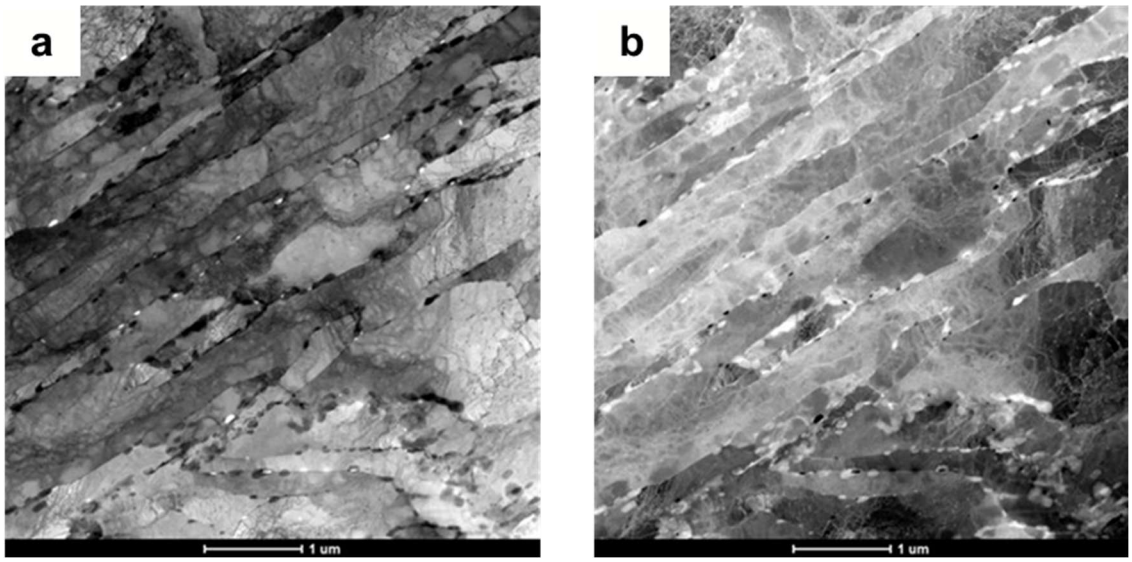

Figure 4. 9 TEM images of BG12Cr: a) BF-STEM image, b) HAADF-STEM image.

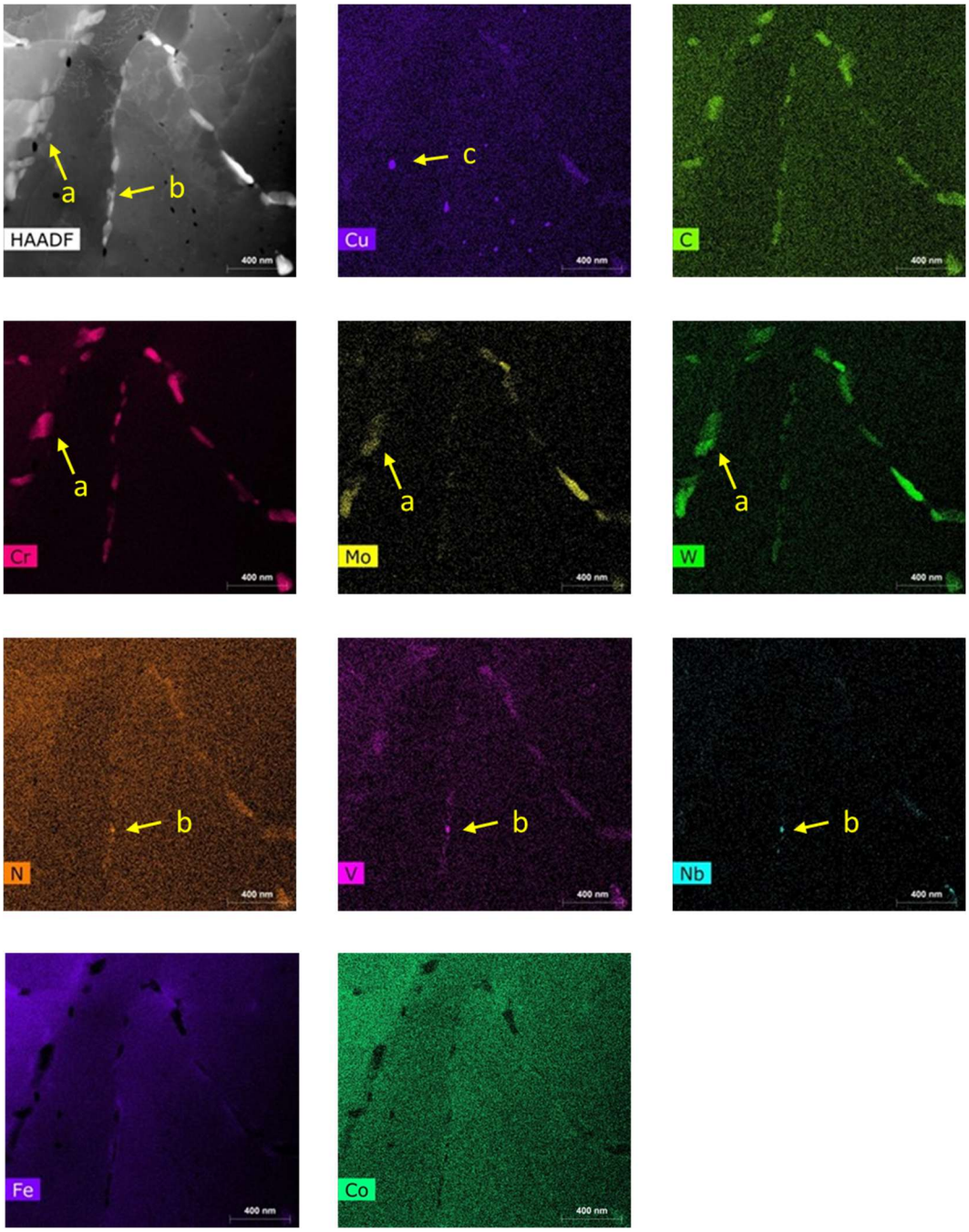

Figure 4. 10 HAADF STEM image and elemental EDS maps, showing particles on the boundary and interior grain. They are (Cr, Mo, W)-rich carbides at boundaries, (Nb, V)-rich carbonitrides at boundaries and Cu particles interior grain.

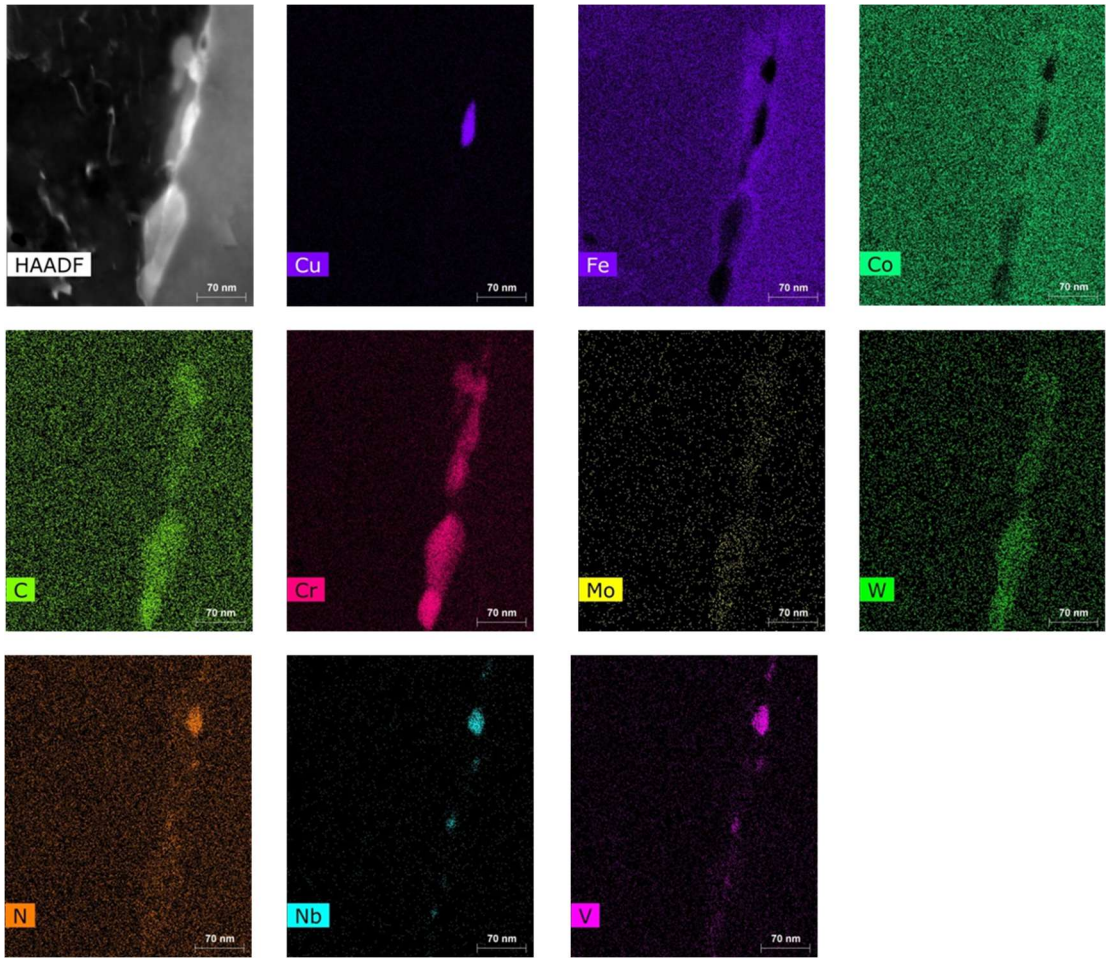

Figure 4. 11 High magnification HAADF STEM image and elemental EDS maps, showing particles on PAG.

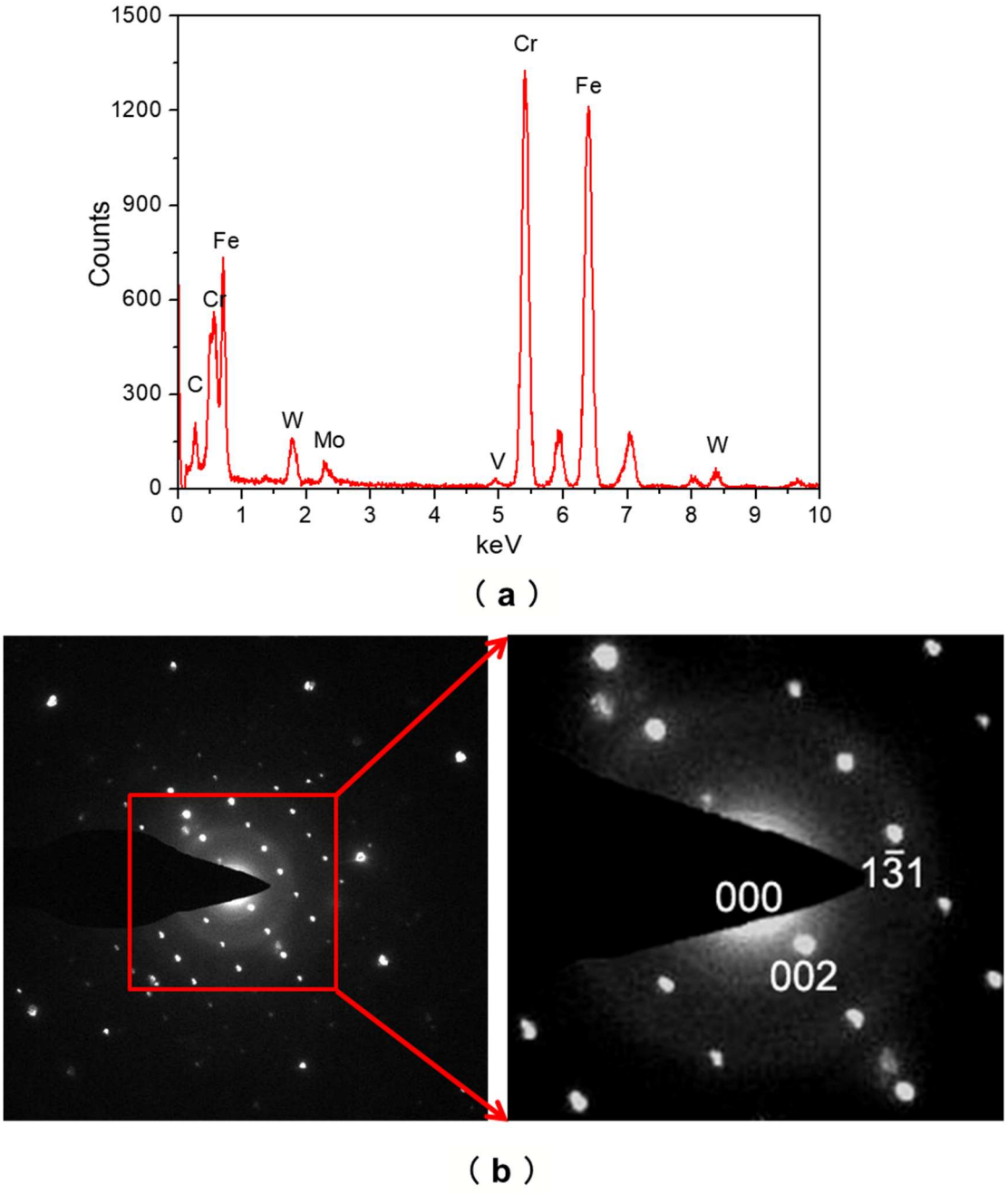

Figure 4. 12 a) EDS spectrum from a boundary carbide and b)SAD of [310] zone axis from the carbide.

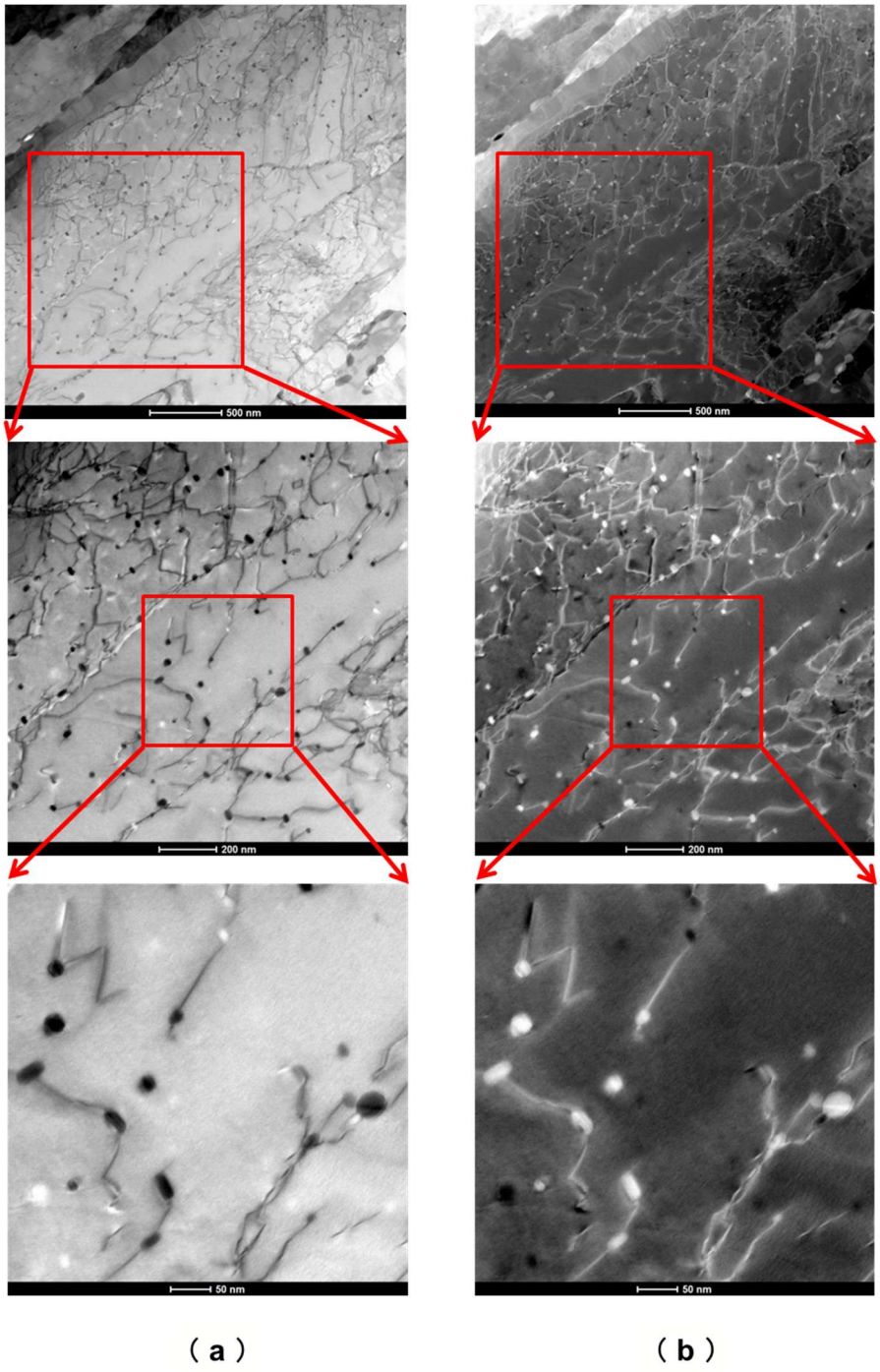

Figure 4. 13 a) BF-STEM images, b)HAADF-STE images show the dislocations interaction with small particles.

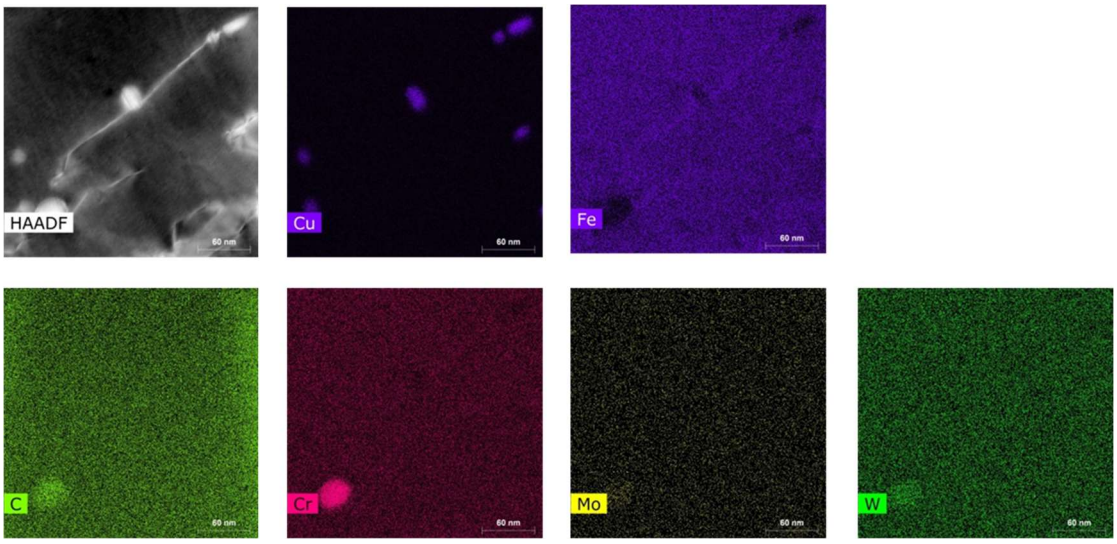

Figure 4. 14 EDS maps for the particle pinning dislocations. They are Cu particles and small (Cr, Mo, W)-rich carbide (i.e. $M_{23}C_6$).

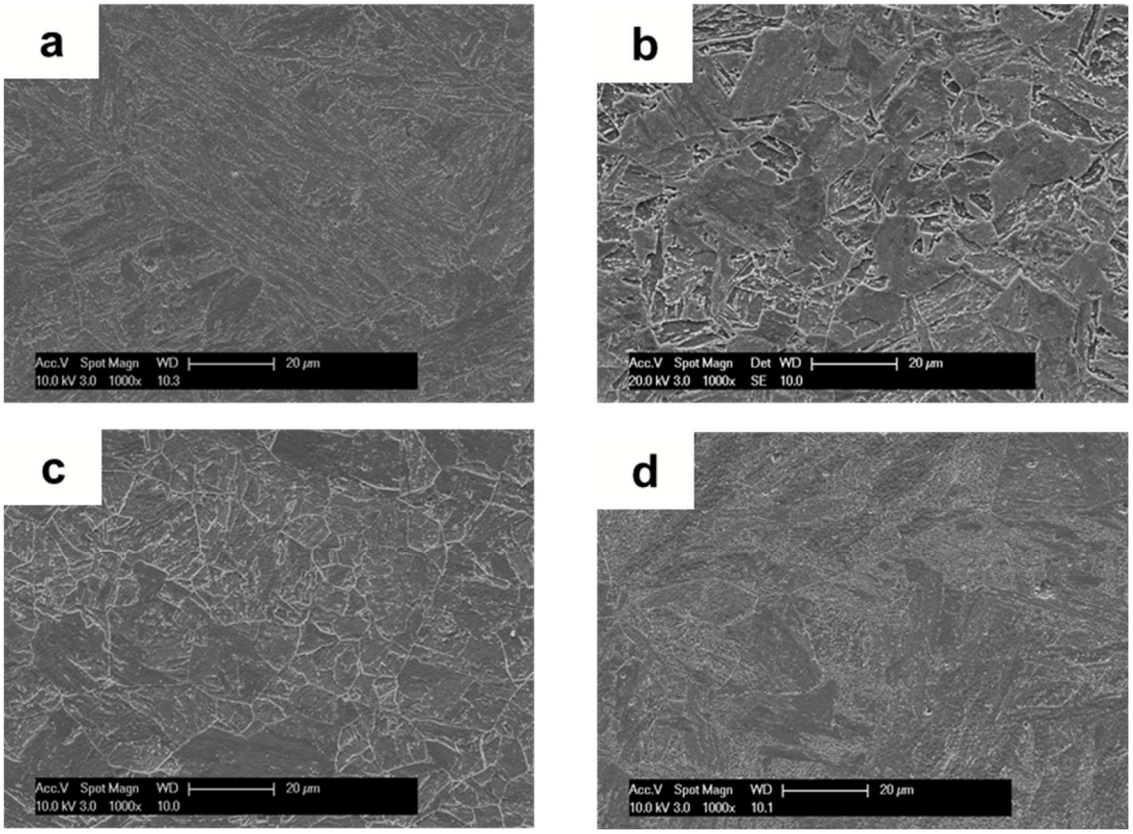

Figure 4. 15 SEM images showing the microstructure of T92 with different conditions: (a) T92 T760 (Tempered at 760°C (b) T92 T780 (Tempered at 780°C), (c) T92 T800 (Tempered at 800°C), T92 T820 (Tempered at 820°C).

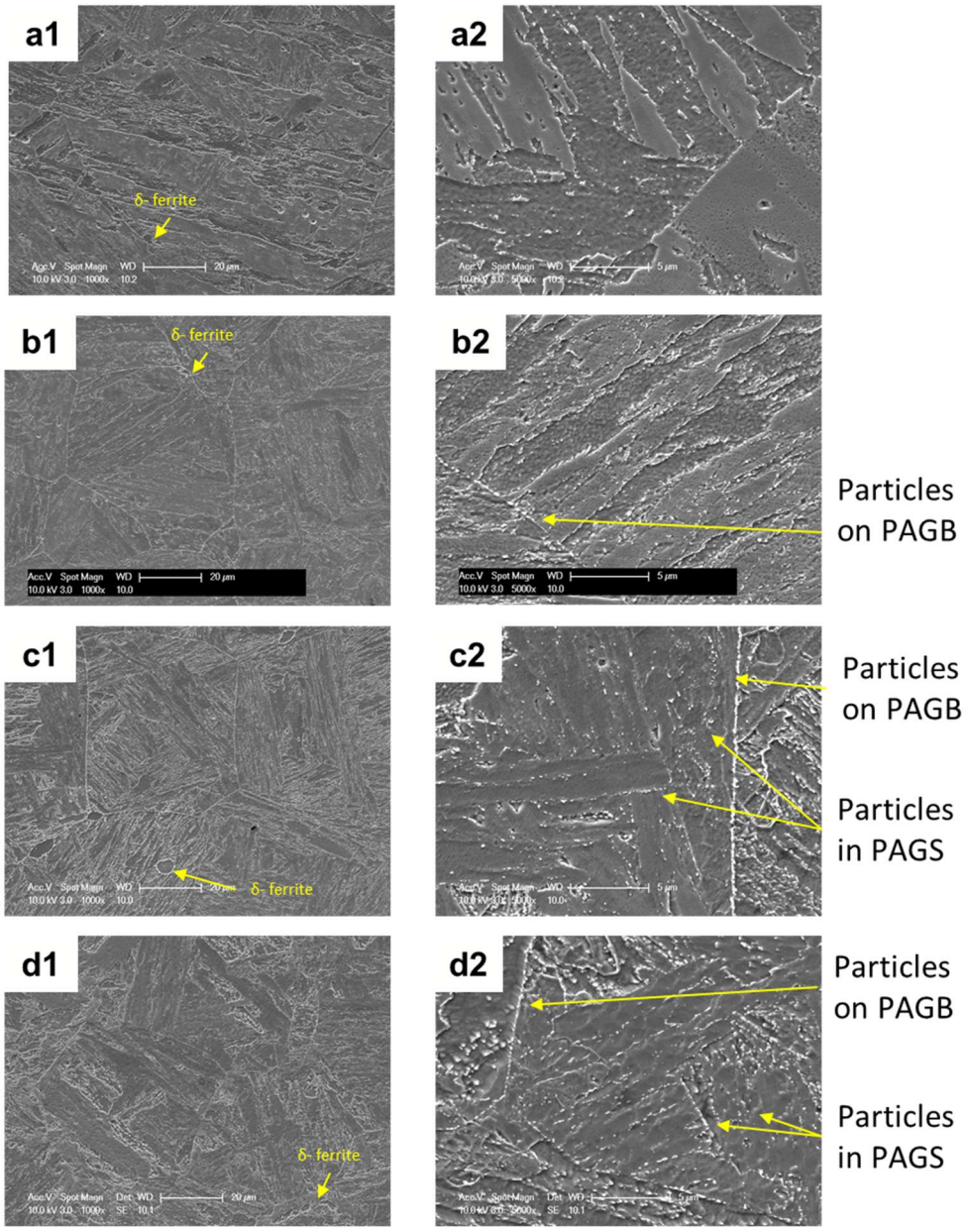

Figure 4. 16 SEM images showing the microstructure of BG12Cr with different conditions: (a) BG12Cr T760 (Tempered at 760°C), (1)1000x, (2)5000x, (b) BG12Cr T780 (Tempered at 780°C), (1)1000x, (2)5000x, (c) BG12Cr T800 (Tempered at 800°C), (1)1000x, (2)5000x, (d) BG12Cr T820 (Tempered at 820°C), (1)1000x, (2)5000x.

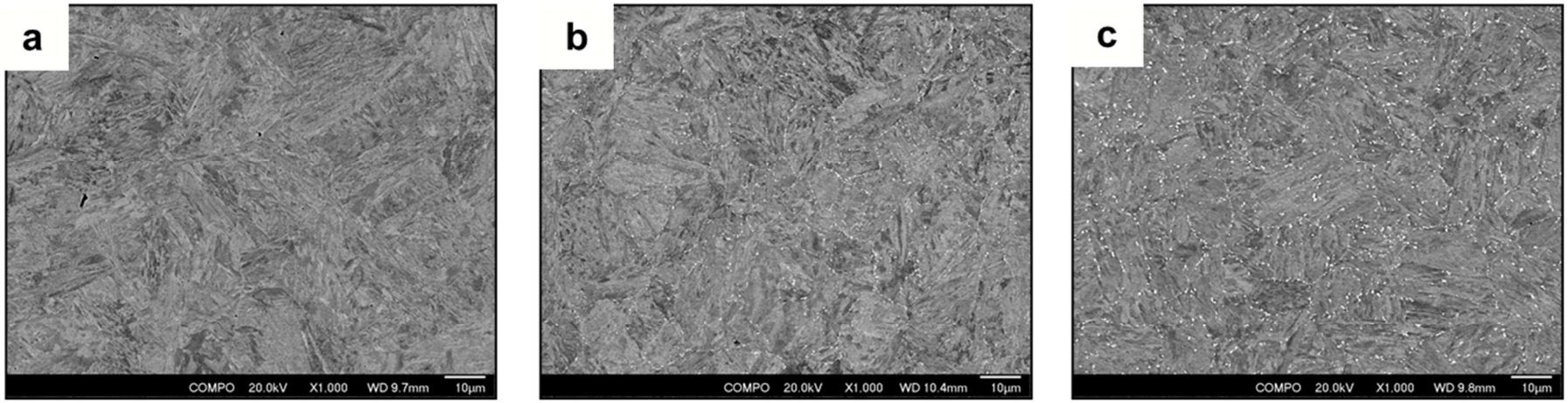

Figure 4. 17 Microstructure of as-received T92 and away from crack region after CCG tests on T92: (a) As-received, (b) 188h at 650°C with loading of 6 kN, (c) 2348.6h at 650°C with loading of 3 kN.

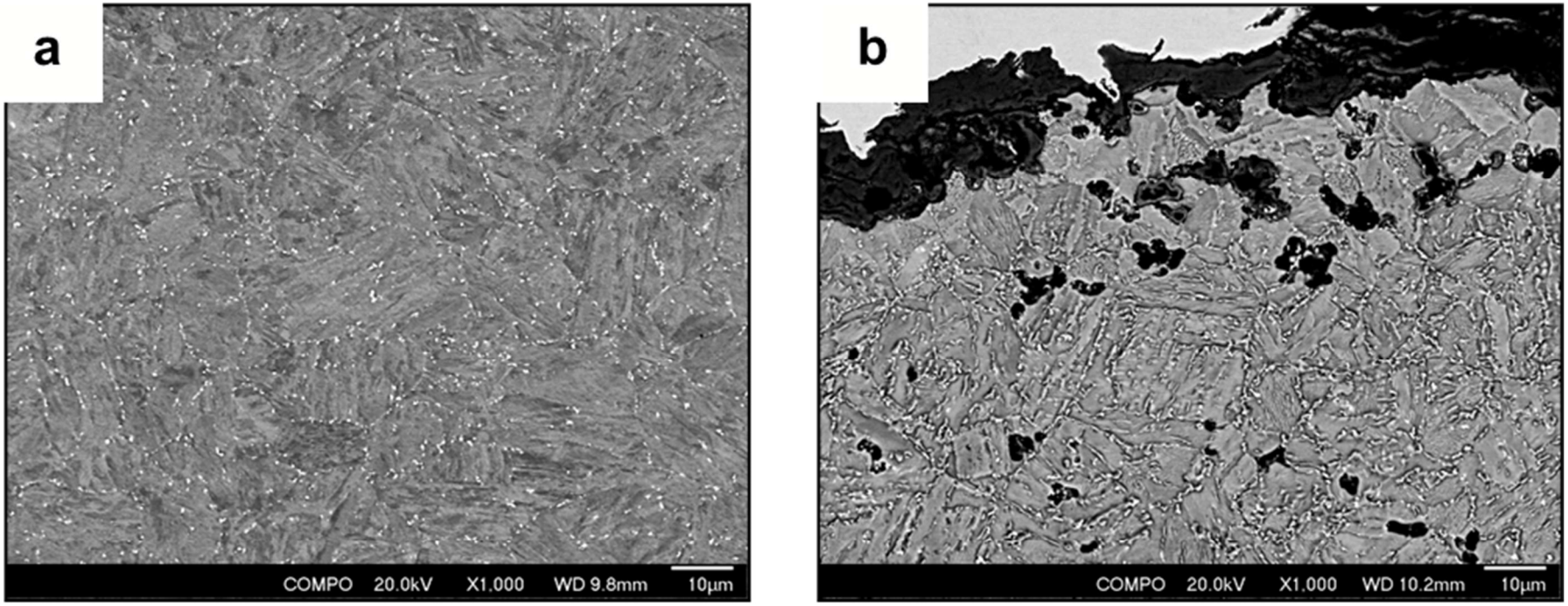

Figure 4. 18 Microstructure of T92 after tested at 650°C with the loading of 3kN (2348.6h): (a) Away from crack, (b) Near crack region.

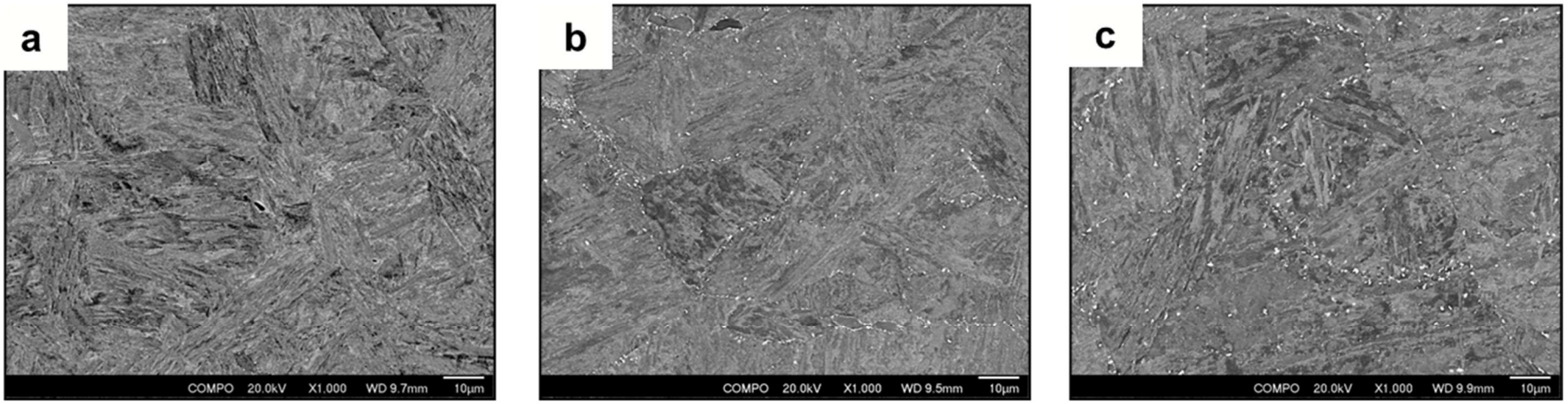

Figure 4. 19 Microstructure of as-received BG12Cr and away from crack region after CCG tests on BG12Cr: (a) As-received, (b) BG12Cr 650 6kN 886.9h at 650°C, (c) BG12Cr 650 3kN 2587.2h at 650°C.

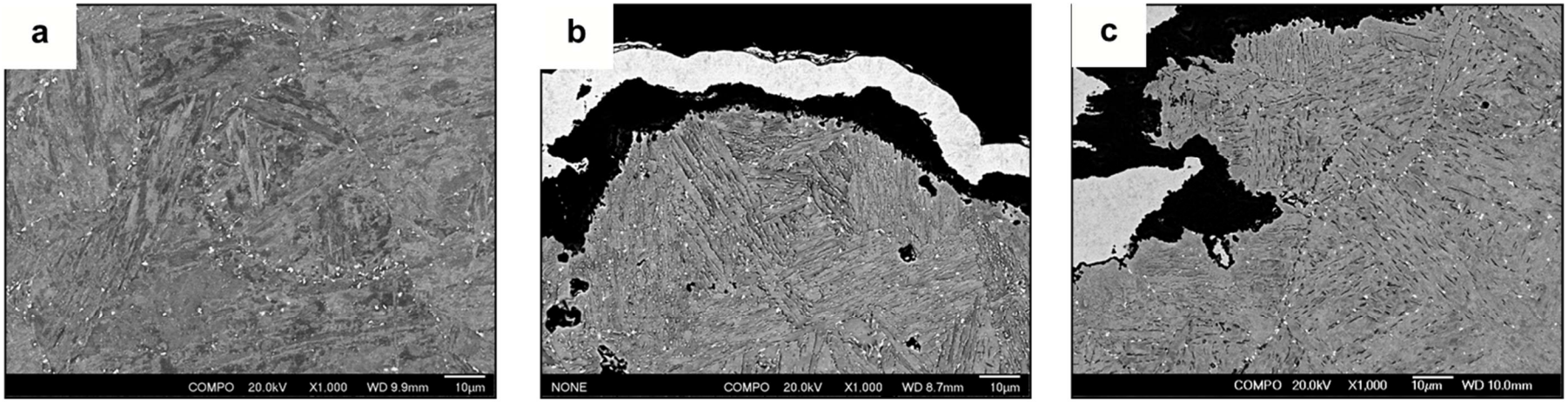

Figure 4. 20 Microstructure of BG12Cr after tested at 650°C with the loading of 3 kN: (a) Away from crack, (b) Near crack region (K_n=15.0 MPa√m), (c) Near crack region (K_n=14.3 MPa√m).

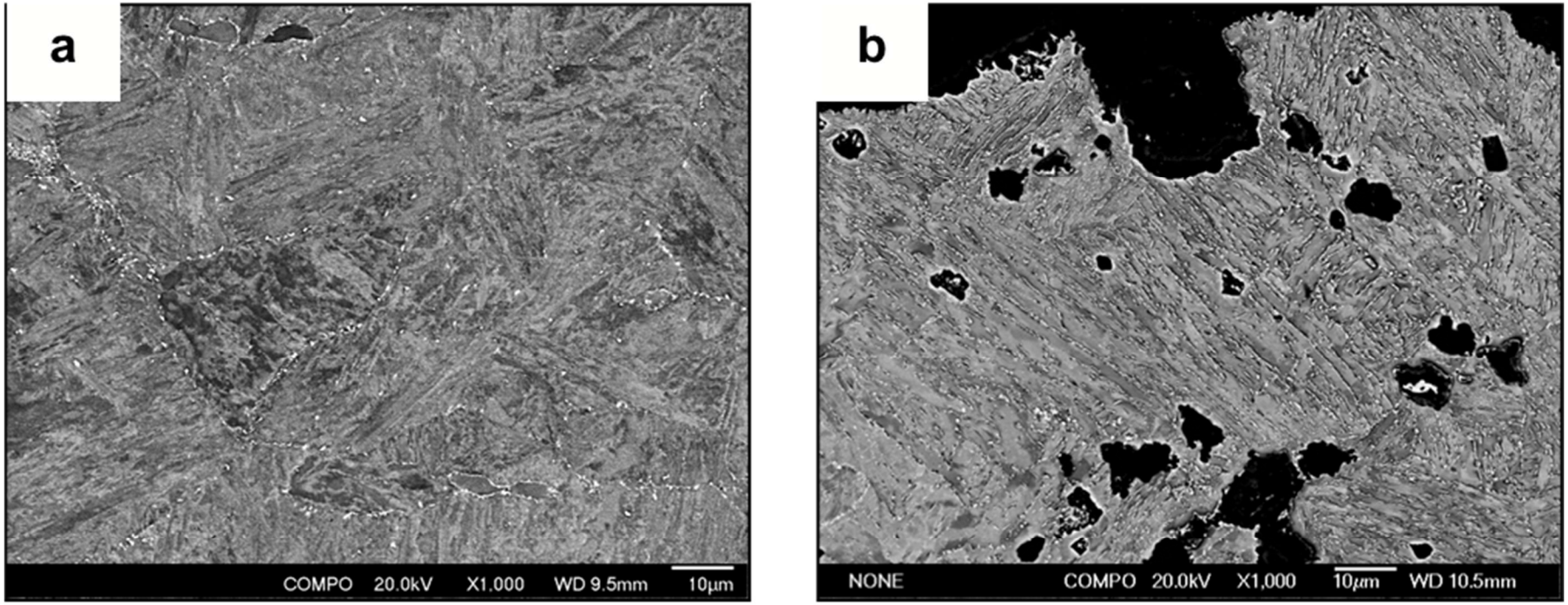

Figure 4. 21 Microstructure of BG12Cr after tested at 650°C with the loading of 6 kN: (a) Away from crack, (b) Near crack region.

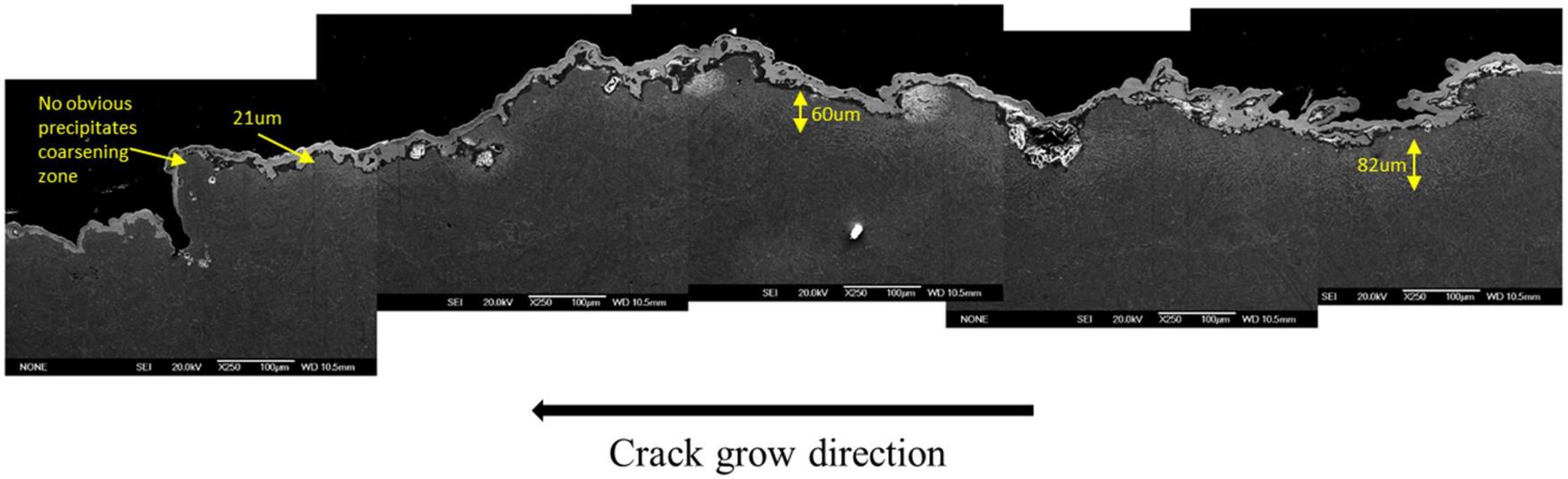

Figure 4. 22 Stitched SEM images show the whole creep crack of BG12Cr tested at 650°C with the loading of 3kN.

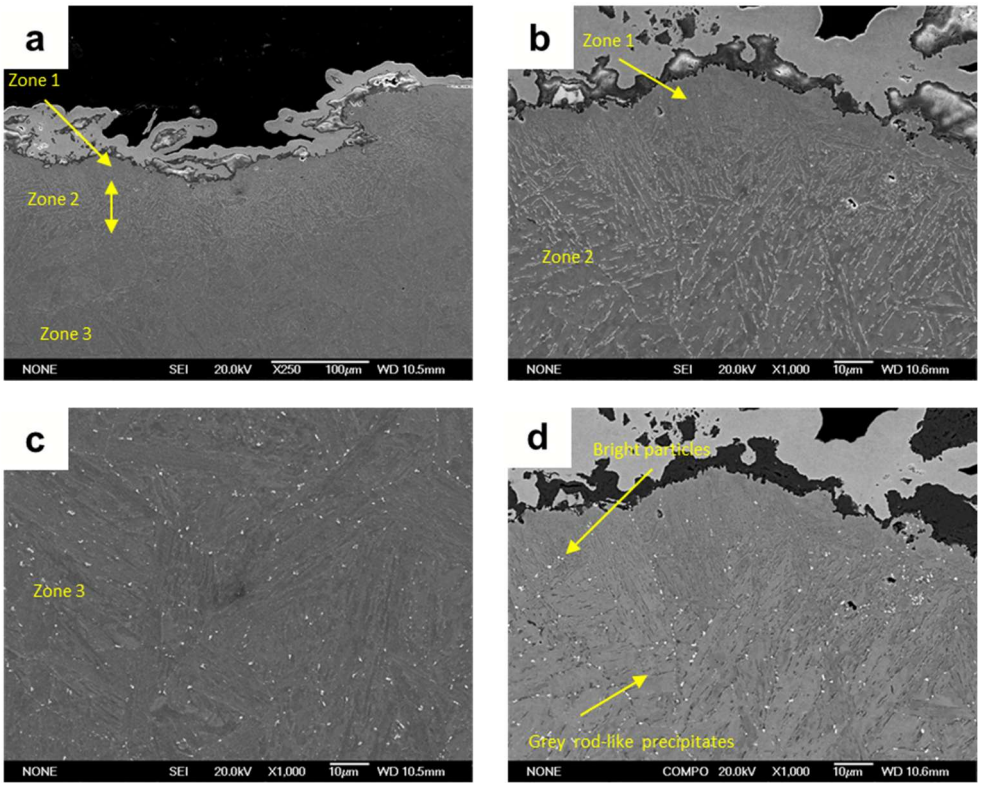

Figure 4. 23 Microstructure of BG12Cr tested at 650 °C with the loading of 3kN: a) low magnification sem image of the near crack region,b) high magnification sem image of the near crack region, c) away from the crack region, d) backscatter image. Zone 1: few or no obvious precipitates region. Zone 2: The region with a large number of precipitates included road-like precipitates.Zone 3: region away from the crack with large particles.

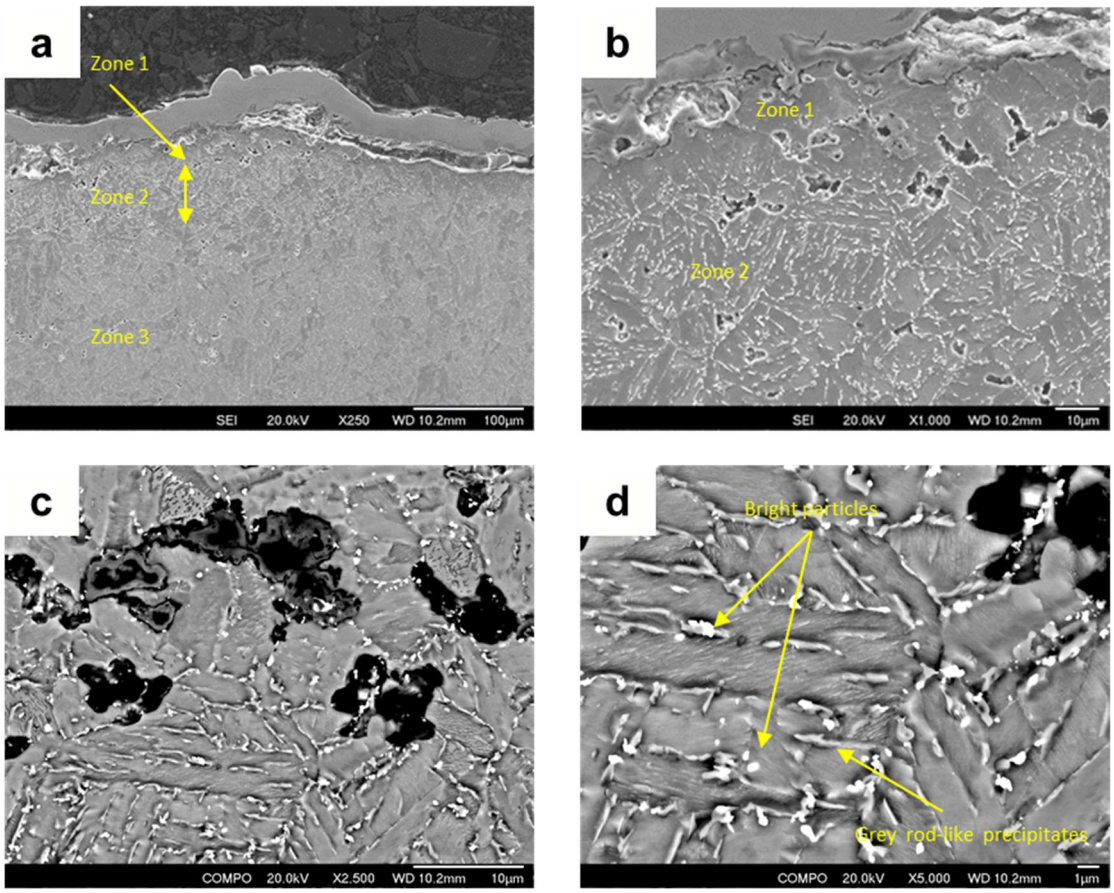

Figure 4. 24 Sem and backscatter images of etched T92 tested at 650 °C with the loading of 3kN: a) 250x magnification sem image, b)1000x magnification sem image, c) 2500x magnification backscatter image, d) 5000x magnification backscatter image.

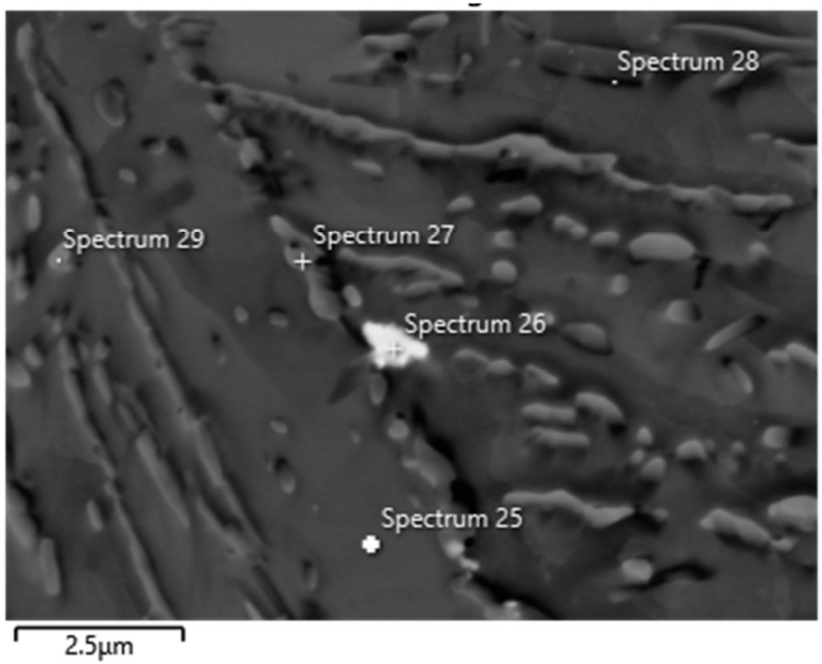

Spectrum	25	26	27	28	29
Element			Weight%		
B	0	0	0	0	0
C	3.7	5.02	3.89	3.25	4.13
N	0.19	1.92	5.11	3.37	1.01
Si	0.28	0.85	0.2	0.1	0.24
S	0	0.1	0.08	0	0.07
V	0.07	0.39	0.27	0.36	0.14
Cr	7.72	8.96	22.39	26.46	9.12
Mn	0.36	0.51	0.36	0.5	0.17
Fe	83.34	48.32	63.91	62.07	80.67
Co	3.36	1.7	2.19	2.71	3.06
Cu	0.11	0.56	0.51	0	0.44
Nb	0.04	0.18	0.11	0.01	0
Mo	0.28	9	0.39	0.65	0.32
W	0.56	22.5	0.6	0.51	0.62

Figure 4. 25 EDX Point scan of the near crack region on BG12Cr tested at 650°C with the loading of 3 kN. Spectrum 25: the matrix; spectrum 26: bright particle near the PAGB; spectrum 27: rod-like precipitate at PAGB; spectrum 28: rod-like precipitate in the lath; spectrum 29 grey particle in the lath.

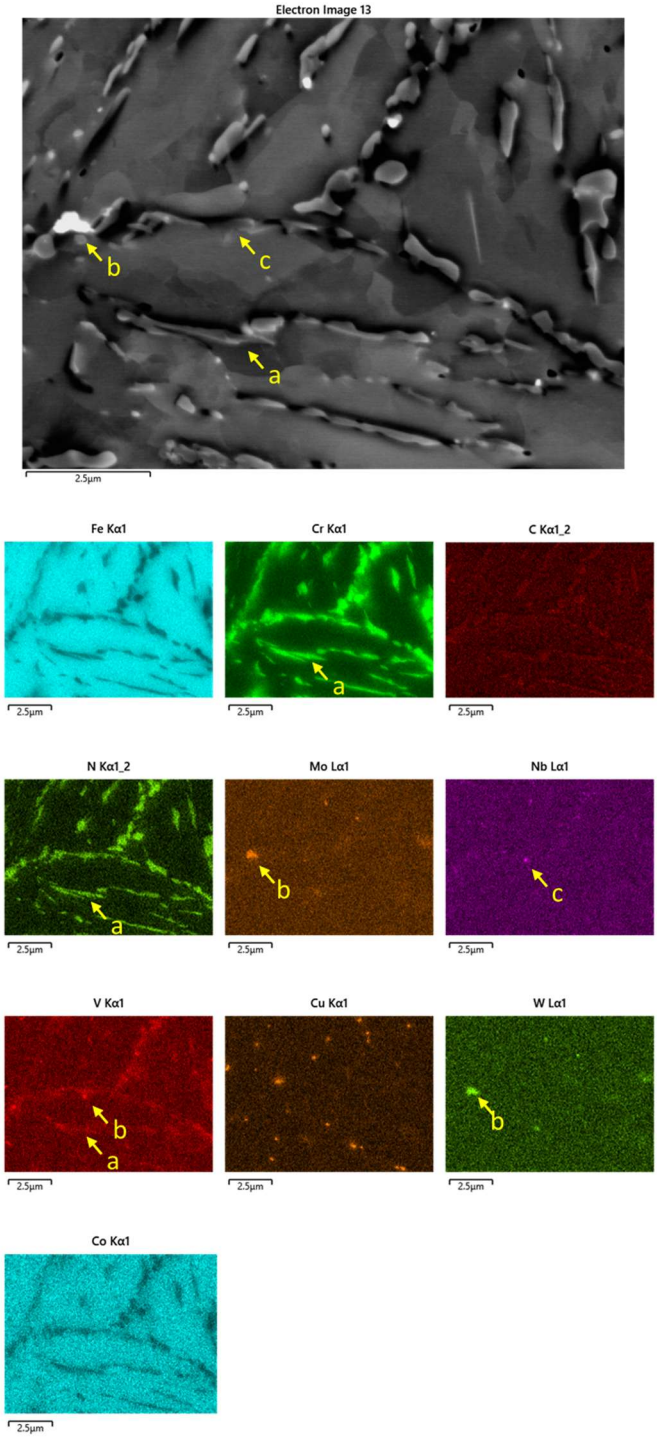

Figure 4. 26 EDX map scan result of the near crack region on BG12Cr tested at 650°C with the loading of 3 kN. Particle a: rod-like precipitate within PAG; Particle b: bright particle on the PAGB; Particle c: Nb-rich particle.

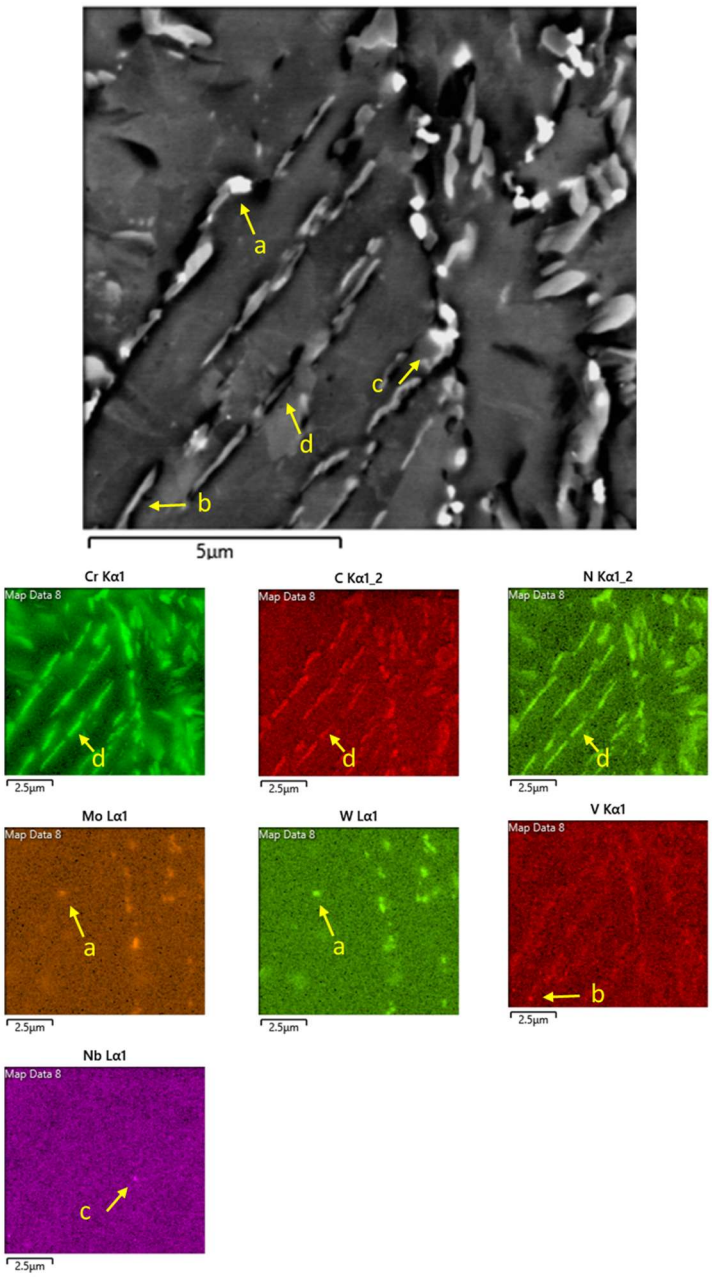

Figure 4. 27 EDX map scan result of the near crack region on P92 tested at 650°C with the loading of 3 kN. Particle a: bright particle on the PAGB; Particle b: small particle under rod-like particle within PAG: Particle c: small paticle on the PAGB; Particle d: rod-like precipitate within PAG.

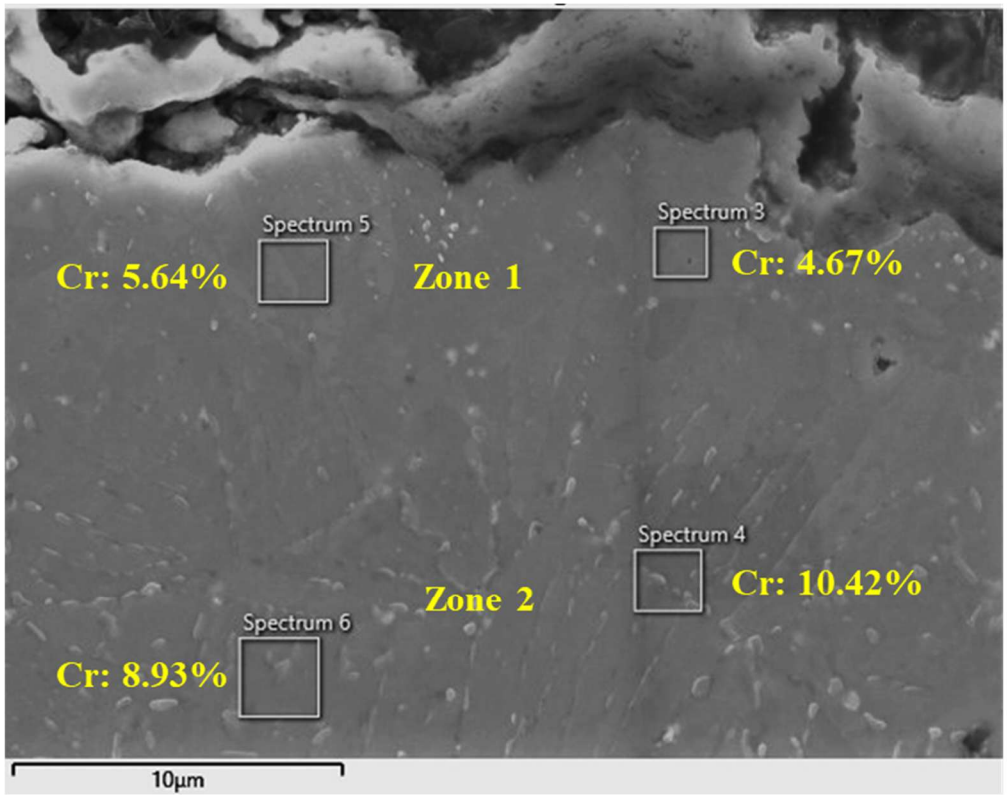

Spectrum	3	4	5	6
Element	Weight%			
C	1.01	1.18	1	1.03
Si	0.21	0.21	0.19	0.24
Cr	4.67	10.42	5.64	8.93
Mn	0.04	0.2	0.04	0.26
Fe	93.78	87.68	92.87	89.38
Mo	0.29	0.3	0.25	0.16

Figure 4. 28 EDX result shows the Cr content on Zone 1 and Zone 2 of P92 tested at 650°C with the loading of 3 kN.

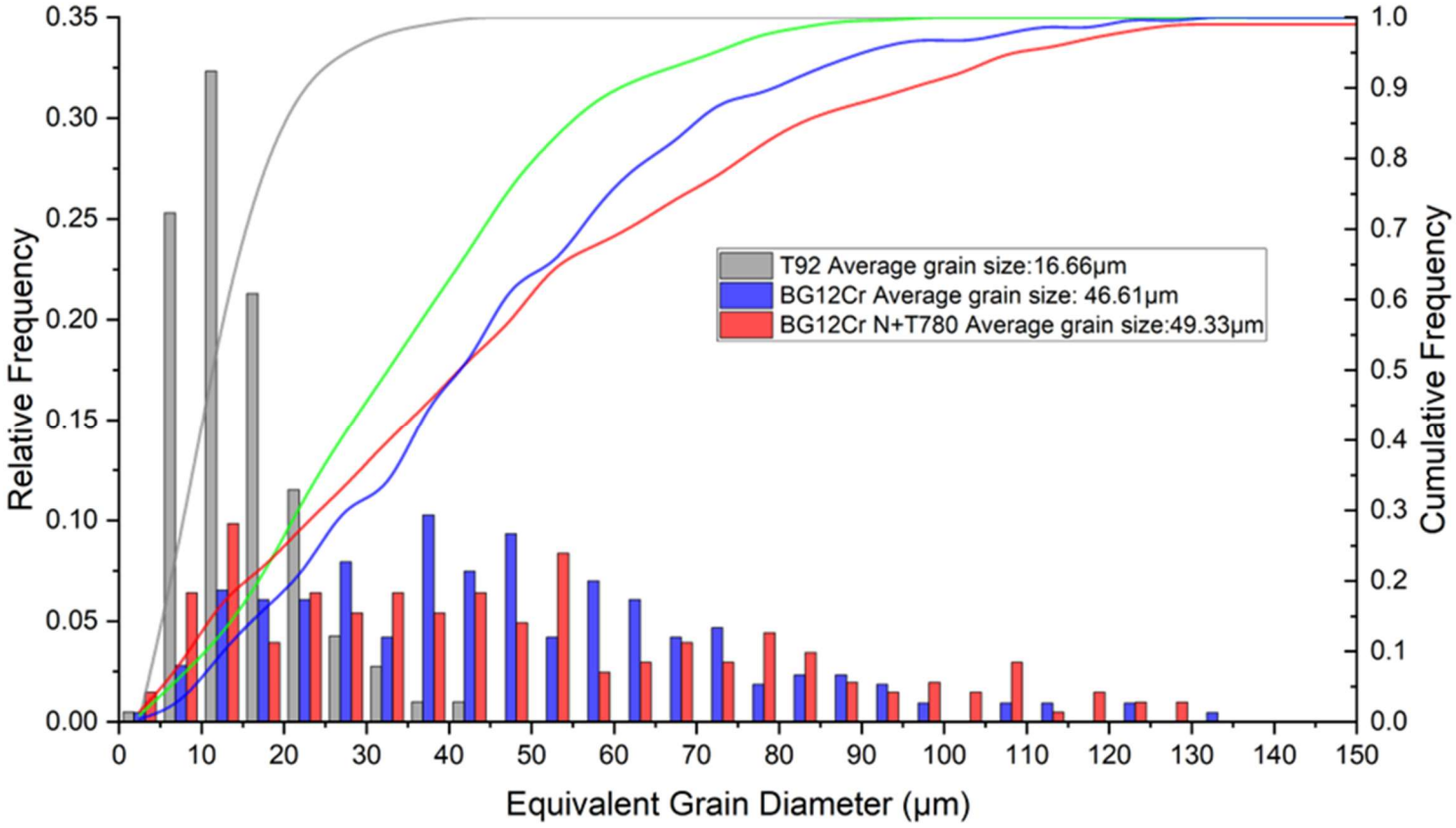

Figure 4. 29 The PAG size distribution of T92, BG12Cr and BG12Cr N+T780.

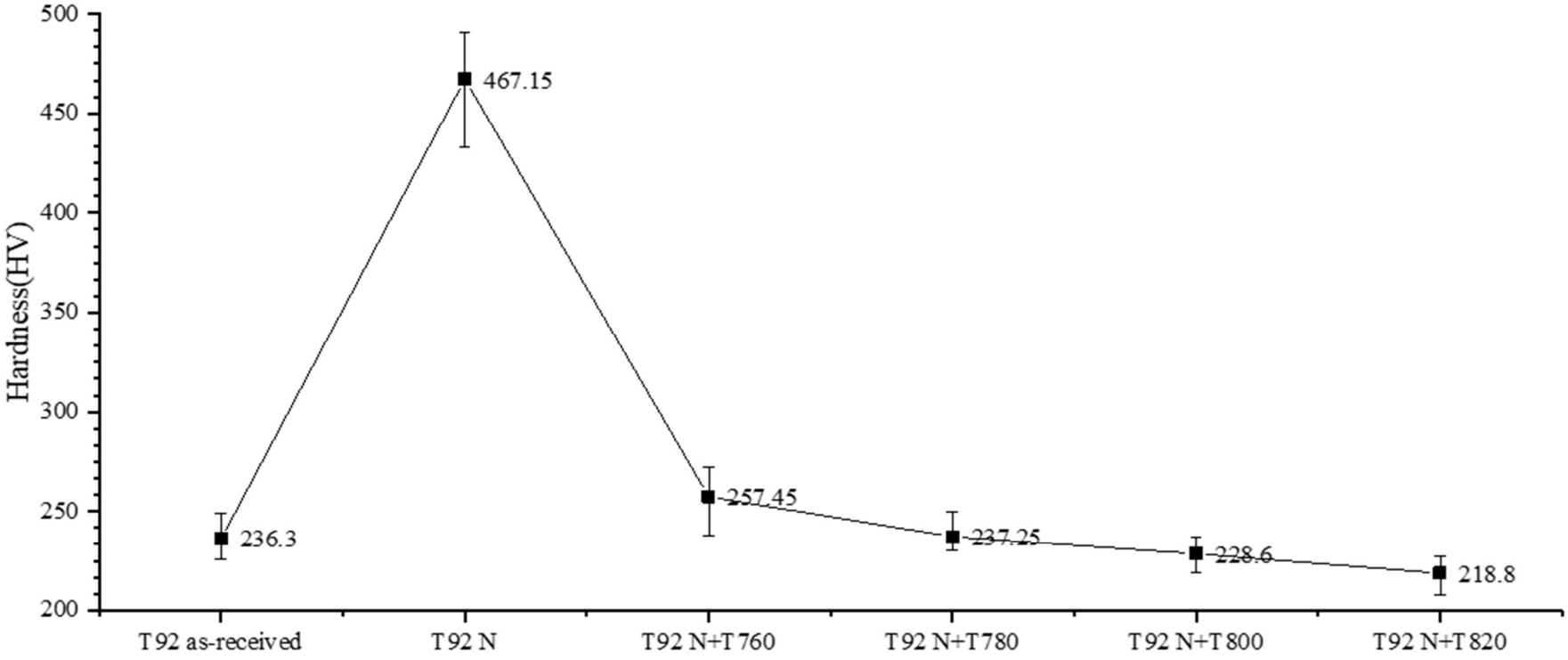

Figure 4. 30 Hardness of T92 samples with different heat treatments.

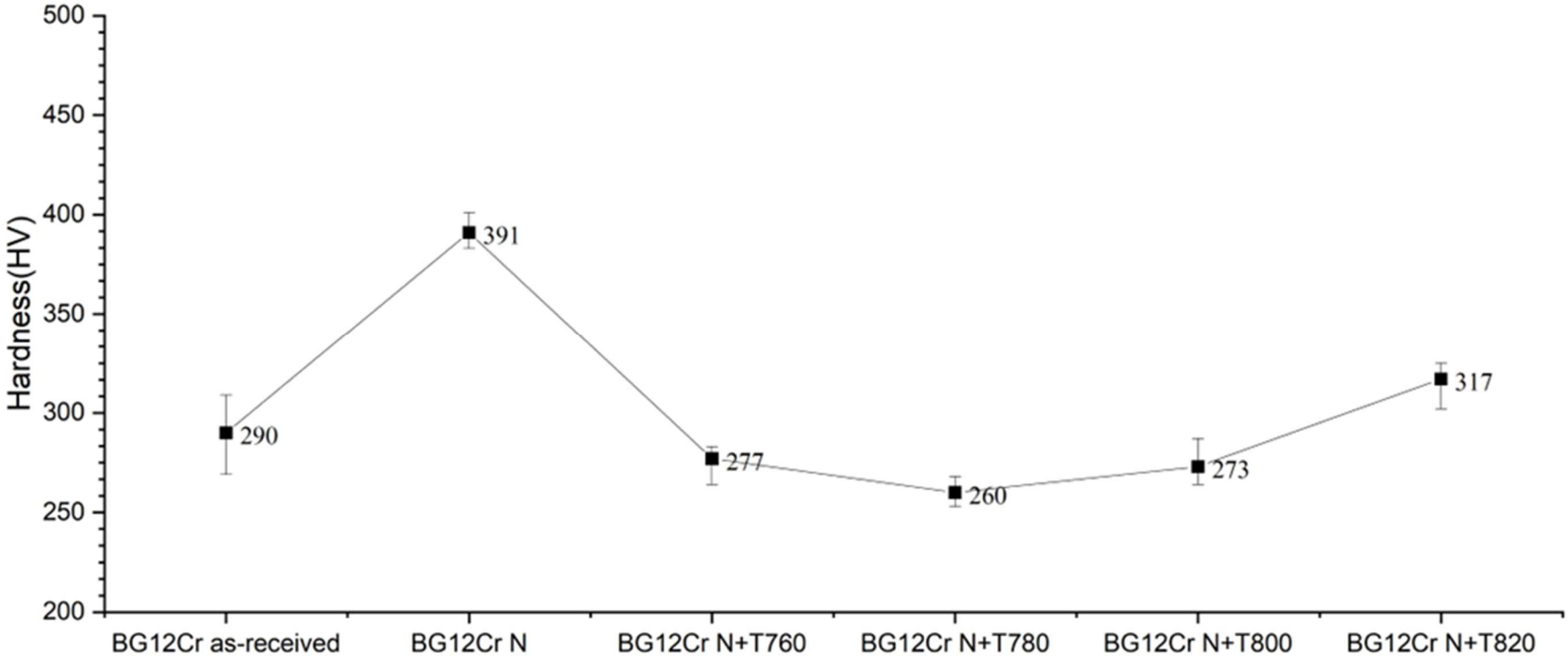

Figure 4. 31 Hardness of BG12Cr samples with different heat treatments.

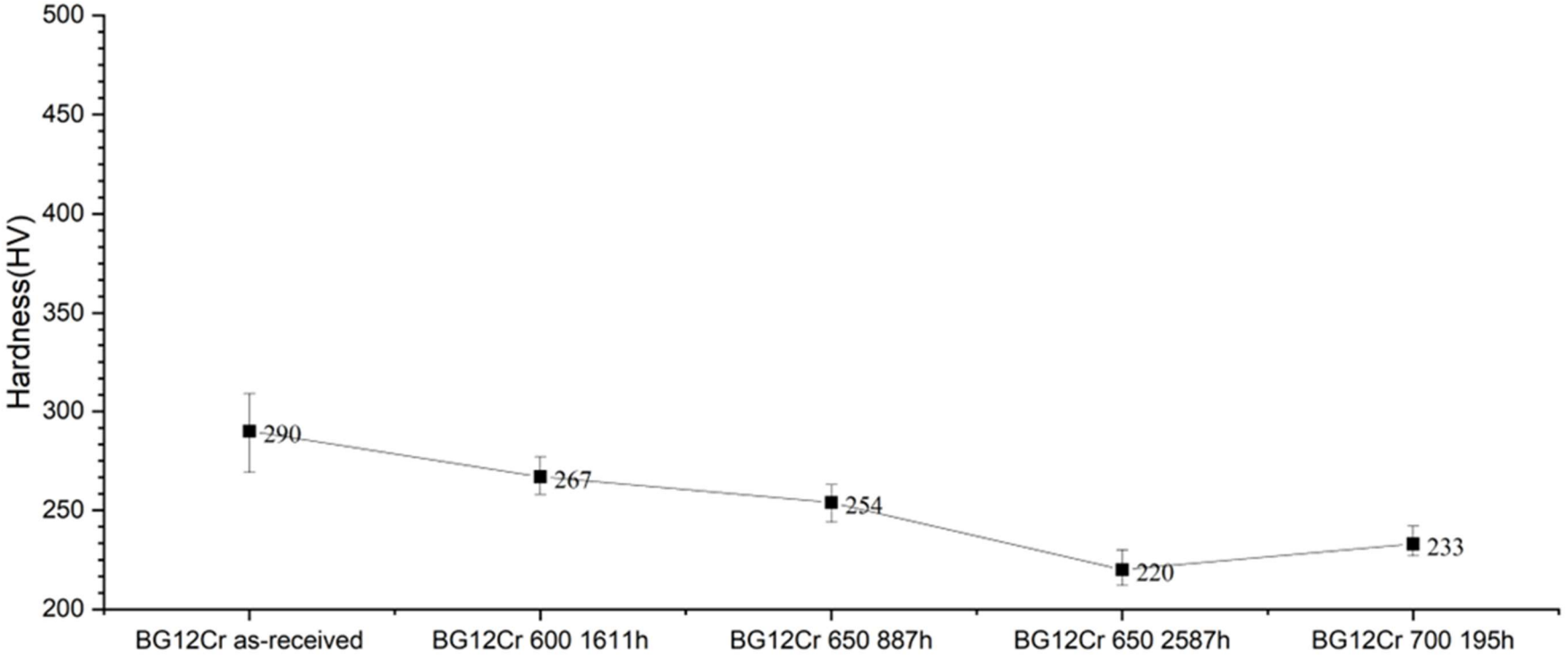

Figure 4. 32 Hardness of BG12Cr samples after tests with different temperture and time.

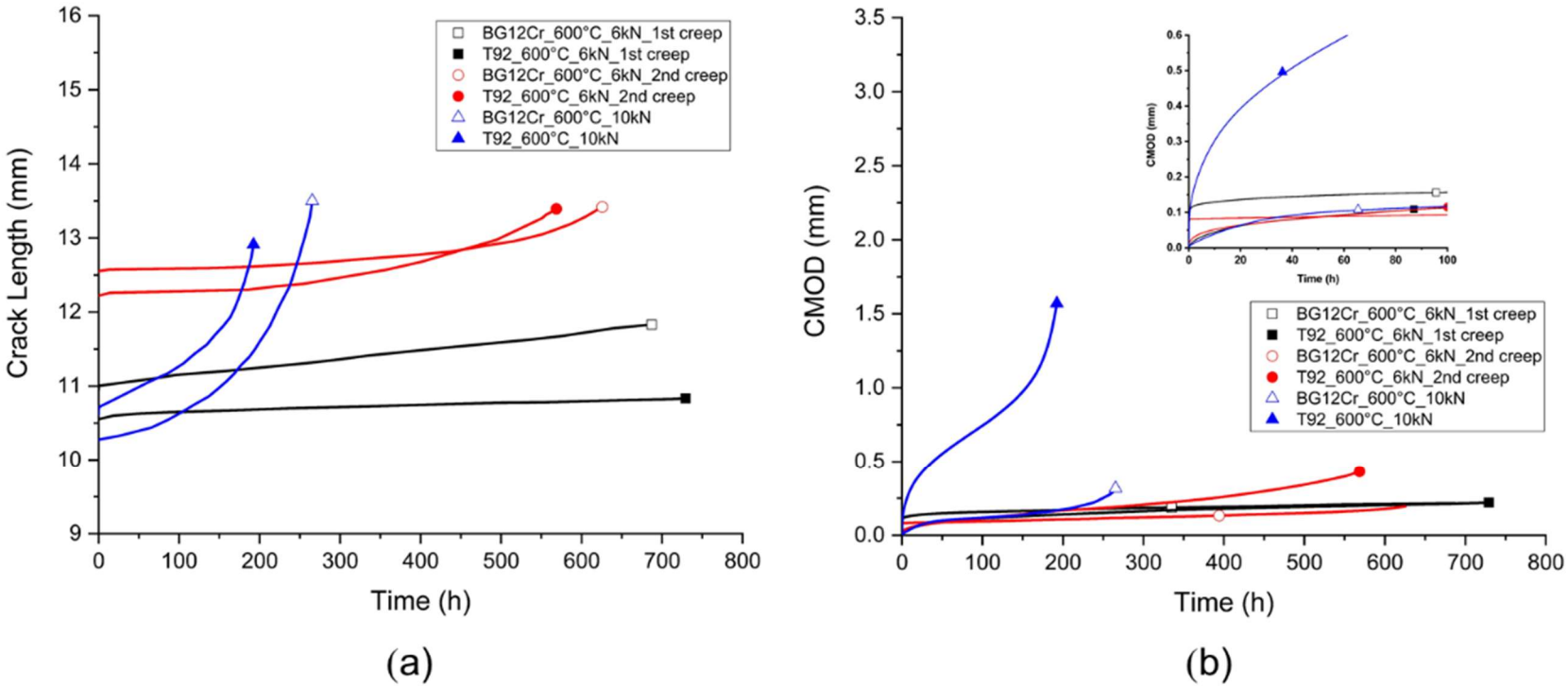

Figure 5. 1 Crack mouth opening displacement (CMOD) and crack length experimental results of creep crack growth in T92 and BG12Cr tested at 600°C: (a) Crack length, (b) CMOD.

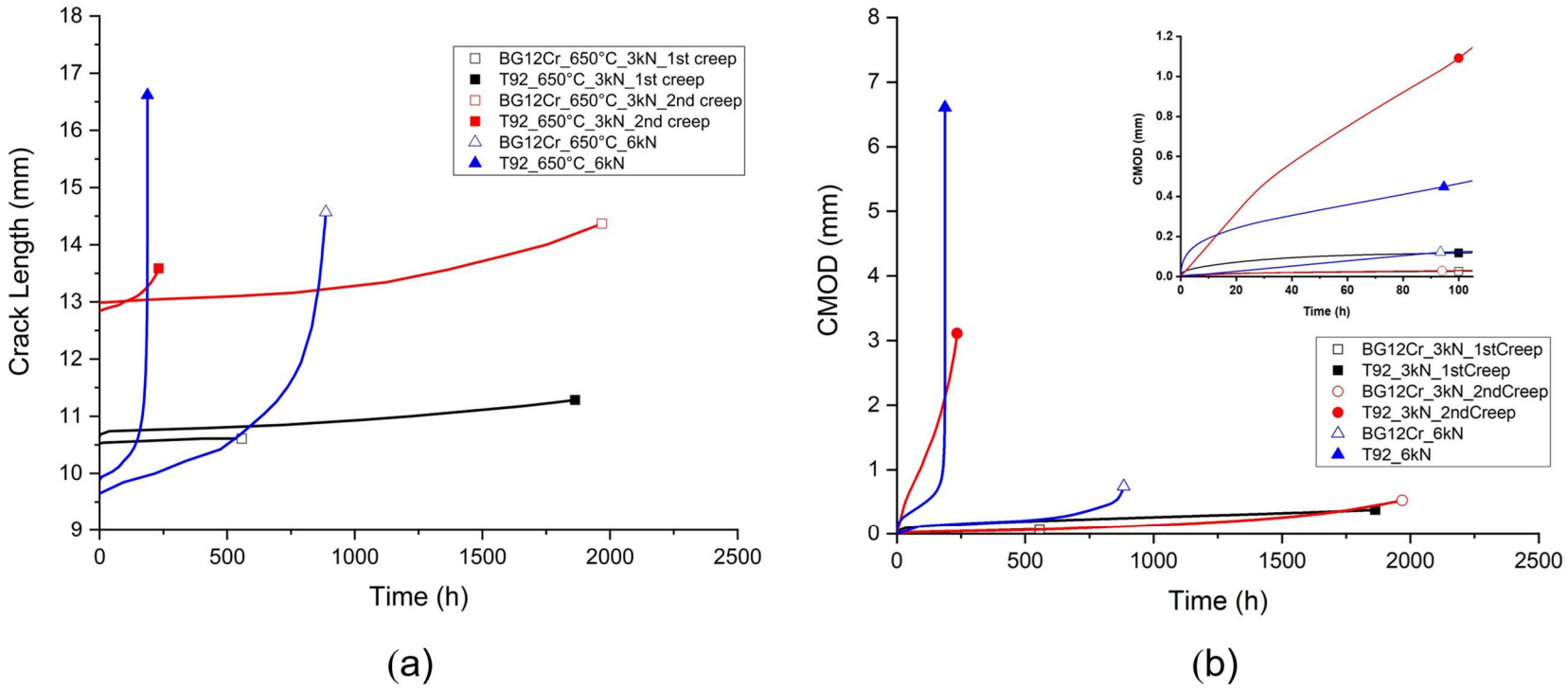

Figure 5. 2 Crack mouth opening displacement (CMOD) and crack length experimental results of creep crack growth in T92 and BG12Cr tested at 650°C: (a) Crack length, (b) CMOD.

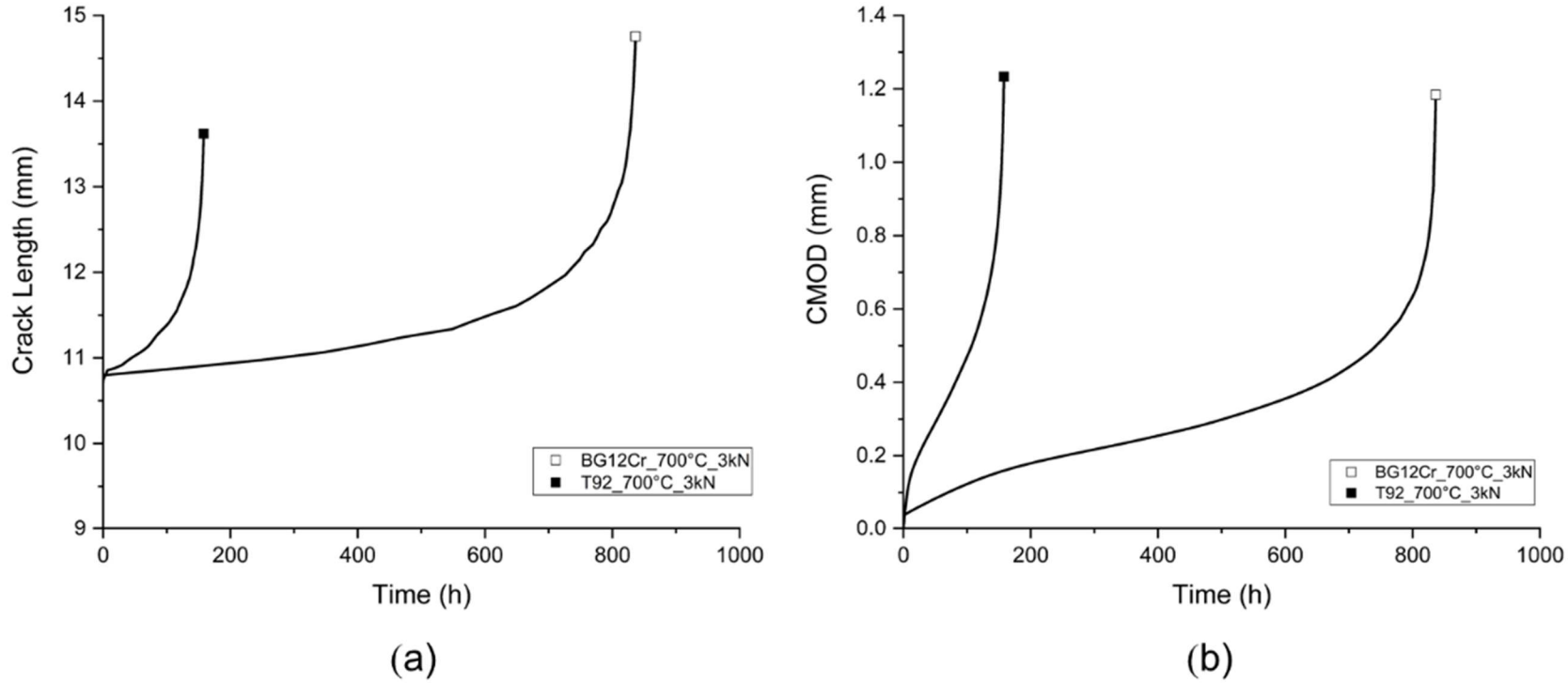

Figure 5. 3 Crack mouth opening displacement (CMOD) and crack length experimental results of creep crack growth in T92 and BG12Cr tested at 700°C: (a) Crack length, (b) CMOD.

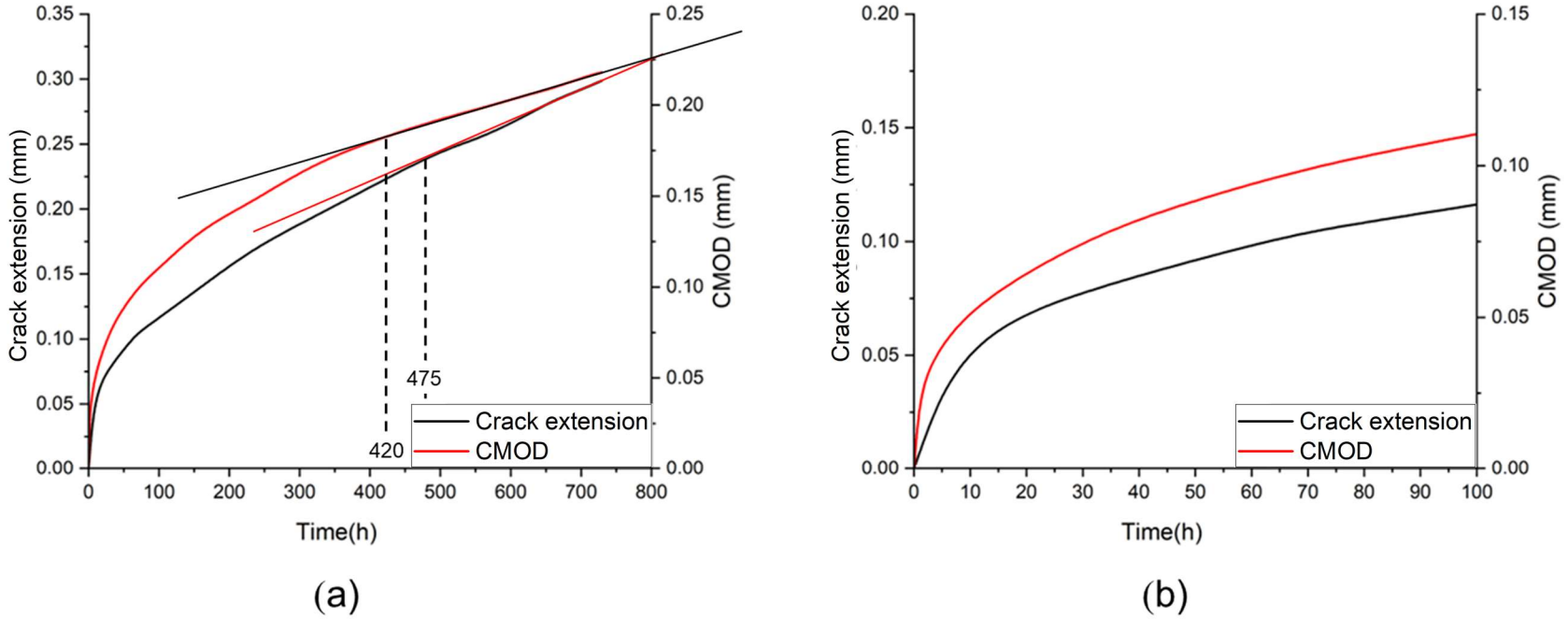

Figure 5. 4 Crack mouth opening displacement (CMOD) and crack extension in 1st creep region of T92 tested at 600°C with loading of 6kN : (a) 1st creep region, (b) first 100h. The onset of the steady-state (constant growth) stage is indicated.

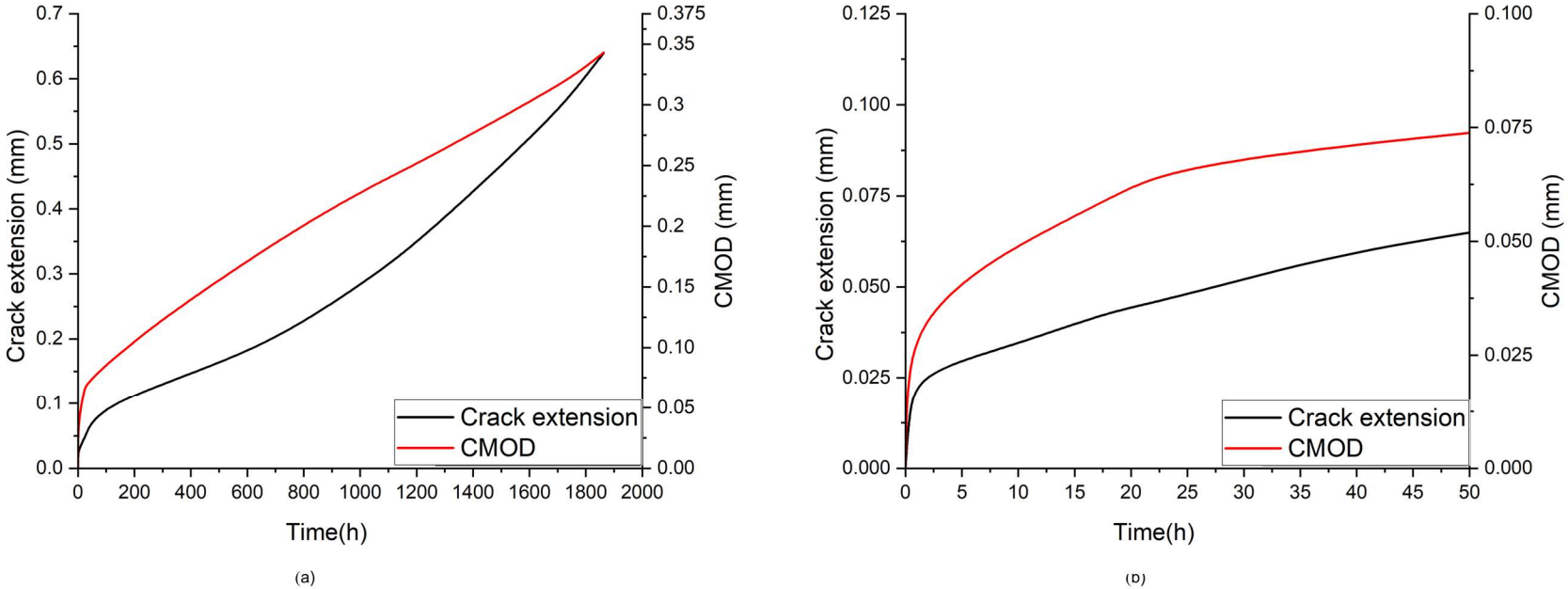

Figure 5. 5 Crack mouth opening displacement (CMOD) and crack extension in 1st creep region of T92 tested at 650°C with loading of 3kN : (a) 1st creep region, (b) first 50h.

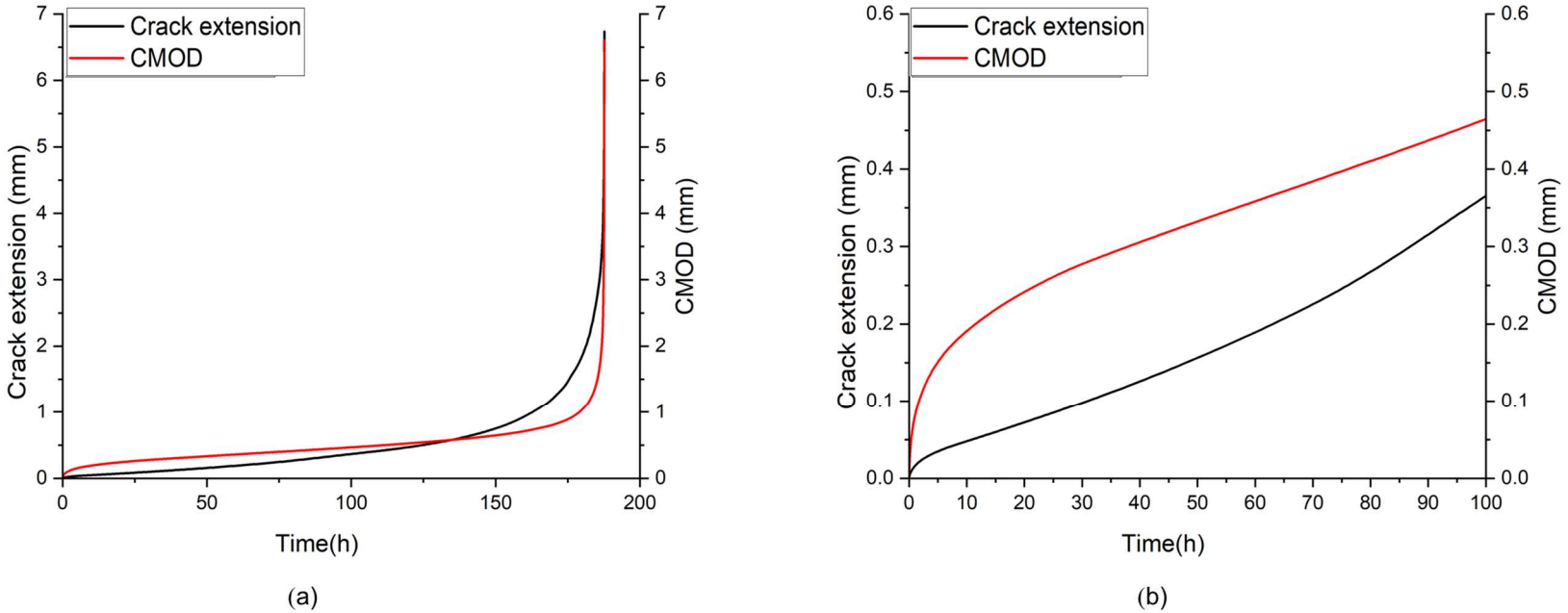

Figure 5. 6 Crack mouth opening displacement (CMOD) and crack extension in creep region of T92 tested at 650 with loading of 6kN : (a) whole creep region, (b) first 100h.

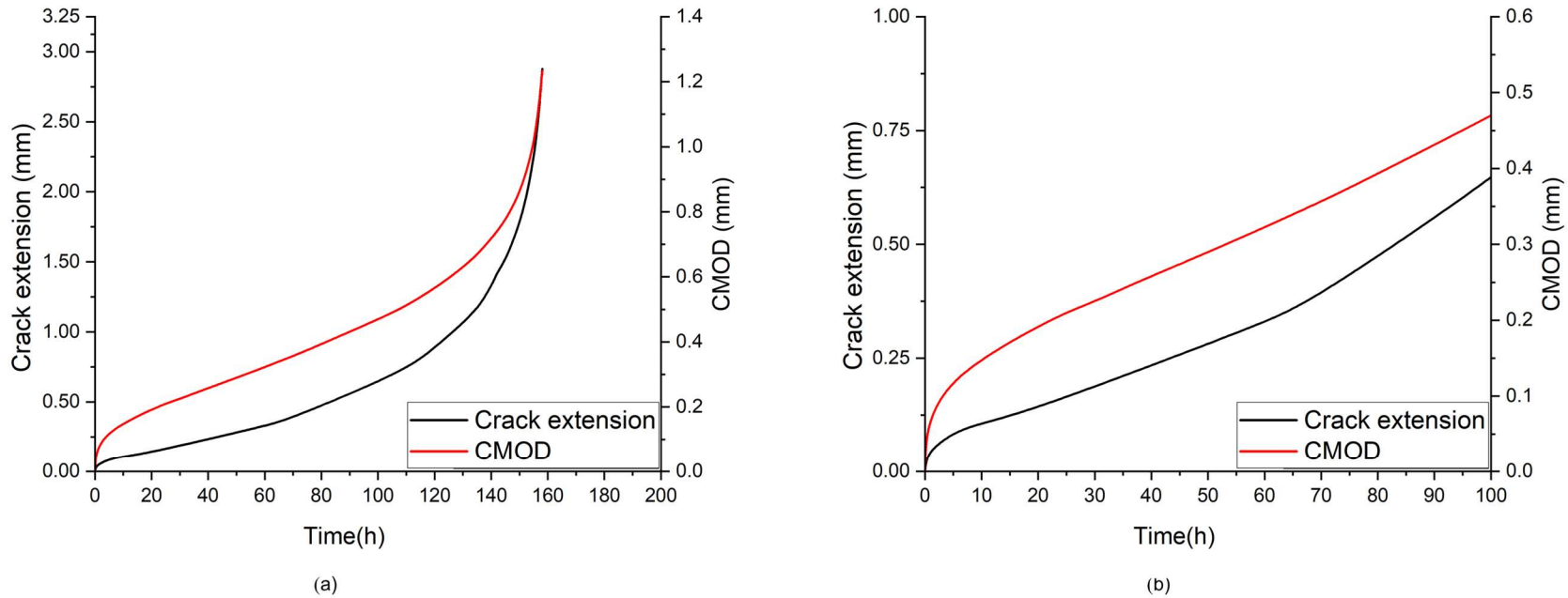

Figure 5. 7 Crack mouth opening displacement (CMOD) and crack extension in creep region of T92 tested at 700°C with loading of 3kN : (a) whole creep region, (b) first 100h.

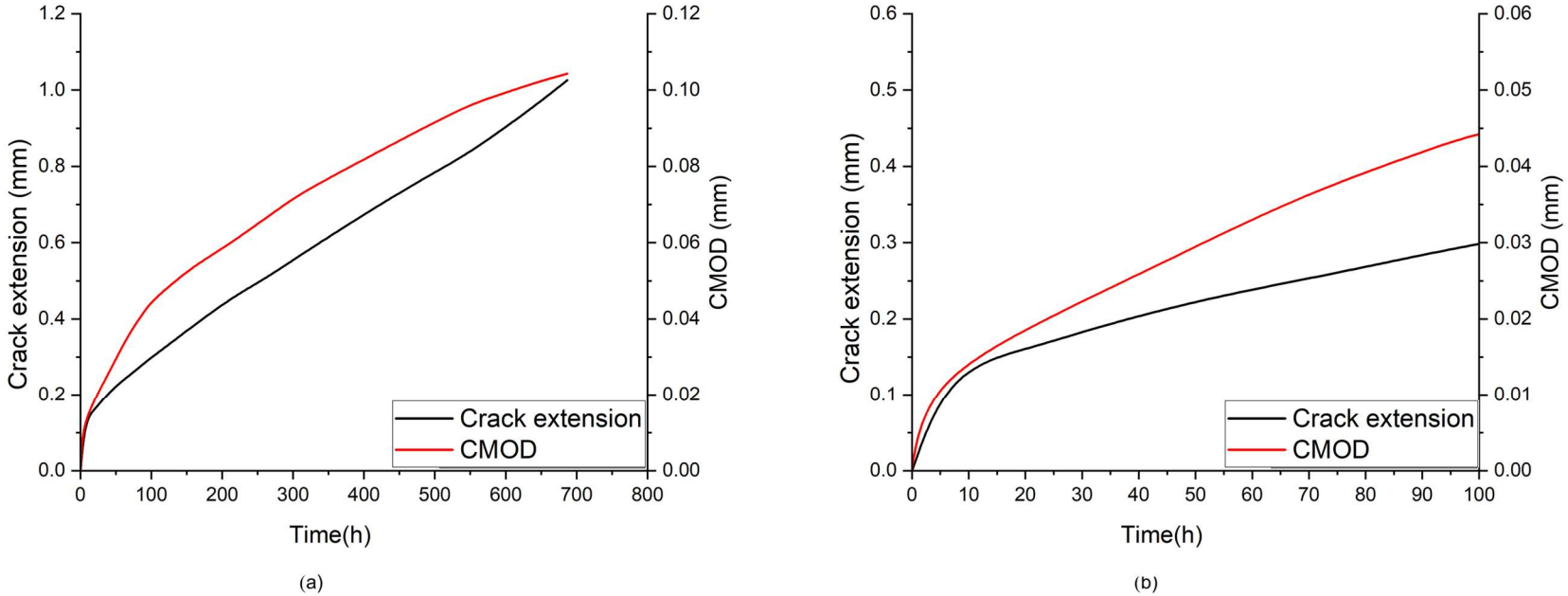

Figure 5. 8 Crack mouth opening displacement (CMOD) and crack extension growth in 1st creep region of BG12Cr tested at 600°C with loading of 6kN : (a) 1st creep region, (b) first 100h.

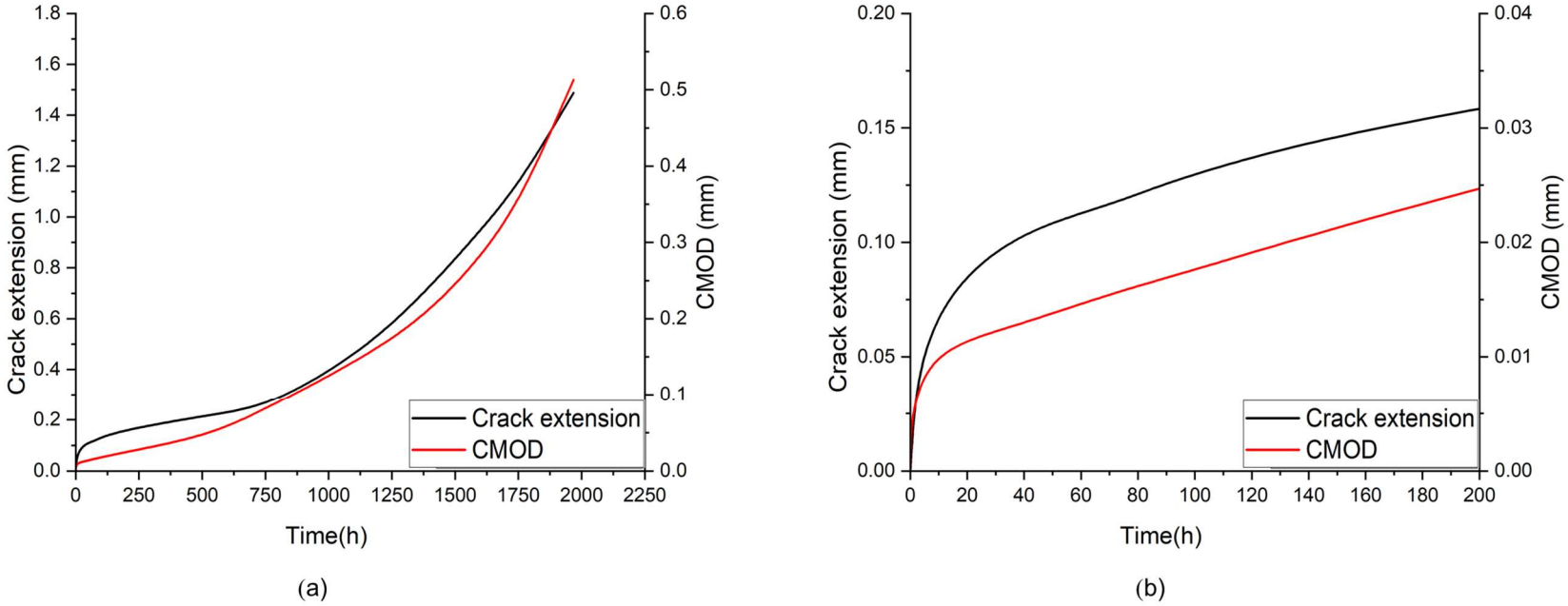

Figure 5. 9 Crack mouth opening displacement (CMOD) and crack extension in 1st creep region of BG12Cr tested at 650°C with loading of 3kN : (a) 1st creep region, (b) first 200h.

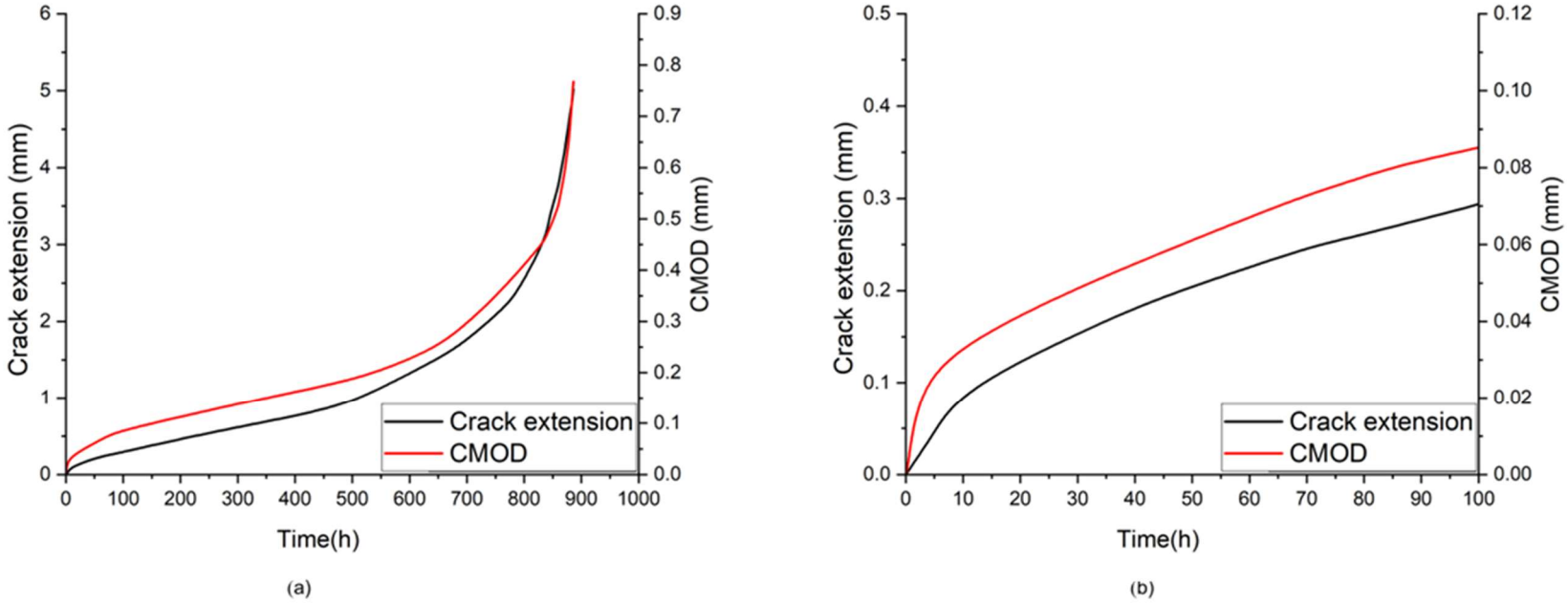

Figure 5. 10 Crack mouth opening displacement (CMOD) and crack extension in creep region of BG12Cr tested at 650°C with loading of 6kN : (a) whole creep region, (b) first 100h.

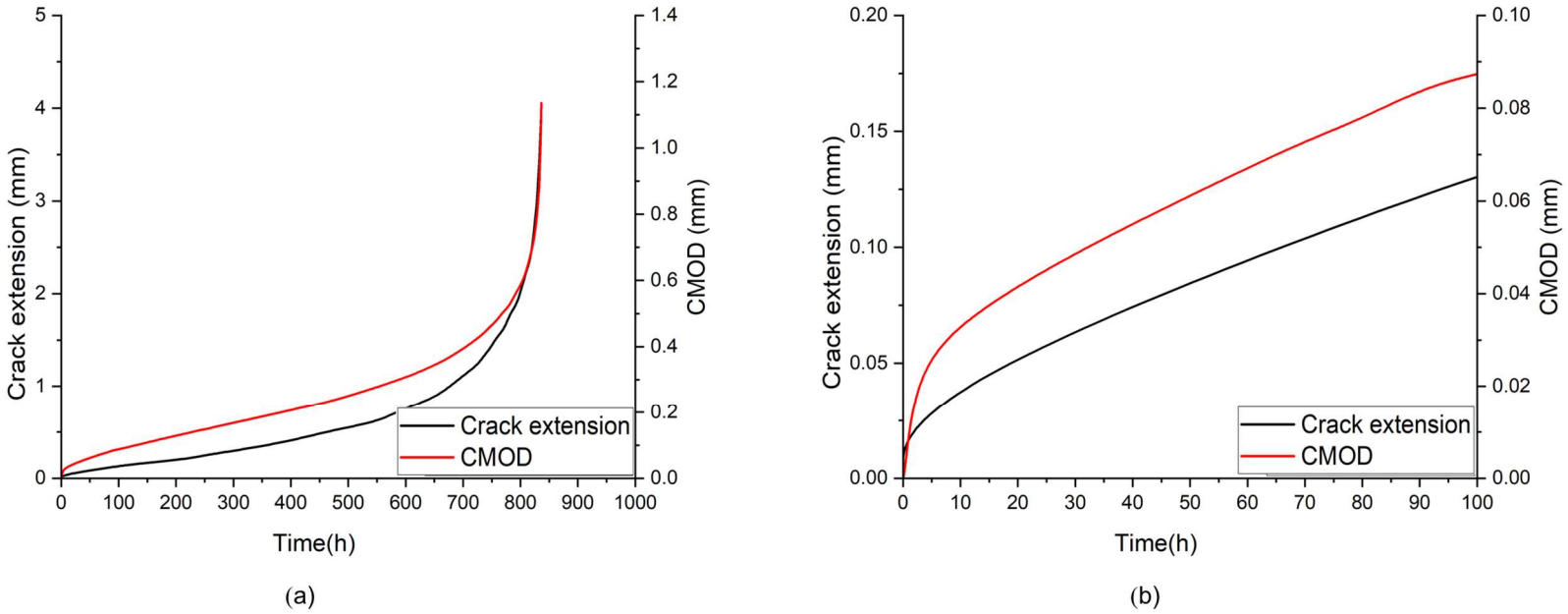

Figure 5. 11 Crack mouth opening displacement (CMOD) and crack extension in creep region of BG12Cr tested at 700°C with loading of 3kN : (a) whole creep region, (b) first 100h.

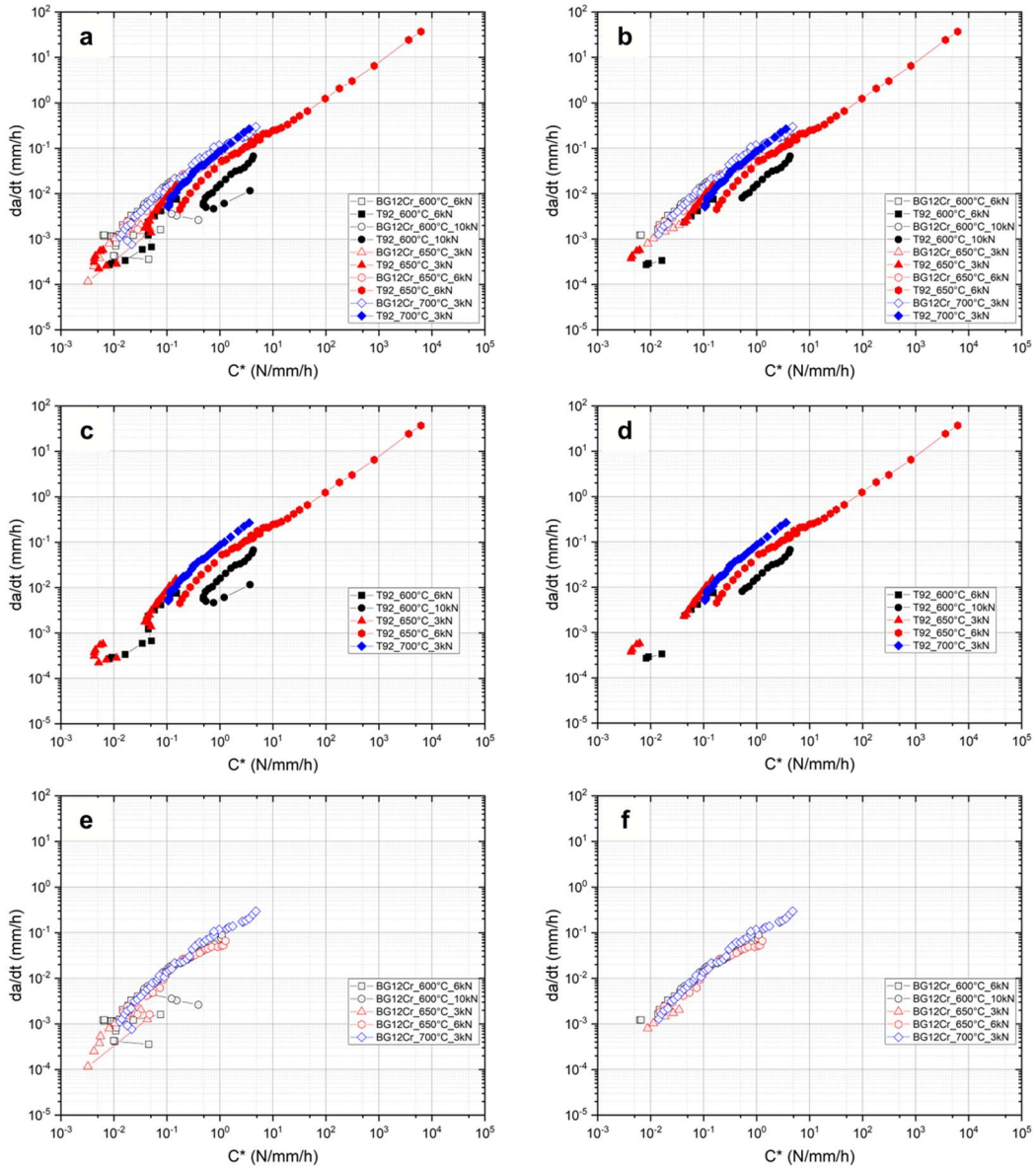

Figure 5. 12 Creep crack growth resistant curves of T92 and the BG12Cr tested in the form of da/dt – C*:a) T92 and BG12Cr with all data (include the data before extensive creep was established and $t_{0.2}$), b) T92 and BG12Cr, c) T92 with all data, d) T92, e) BG12Cr with all data, f) BG12Cr.

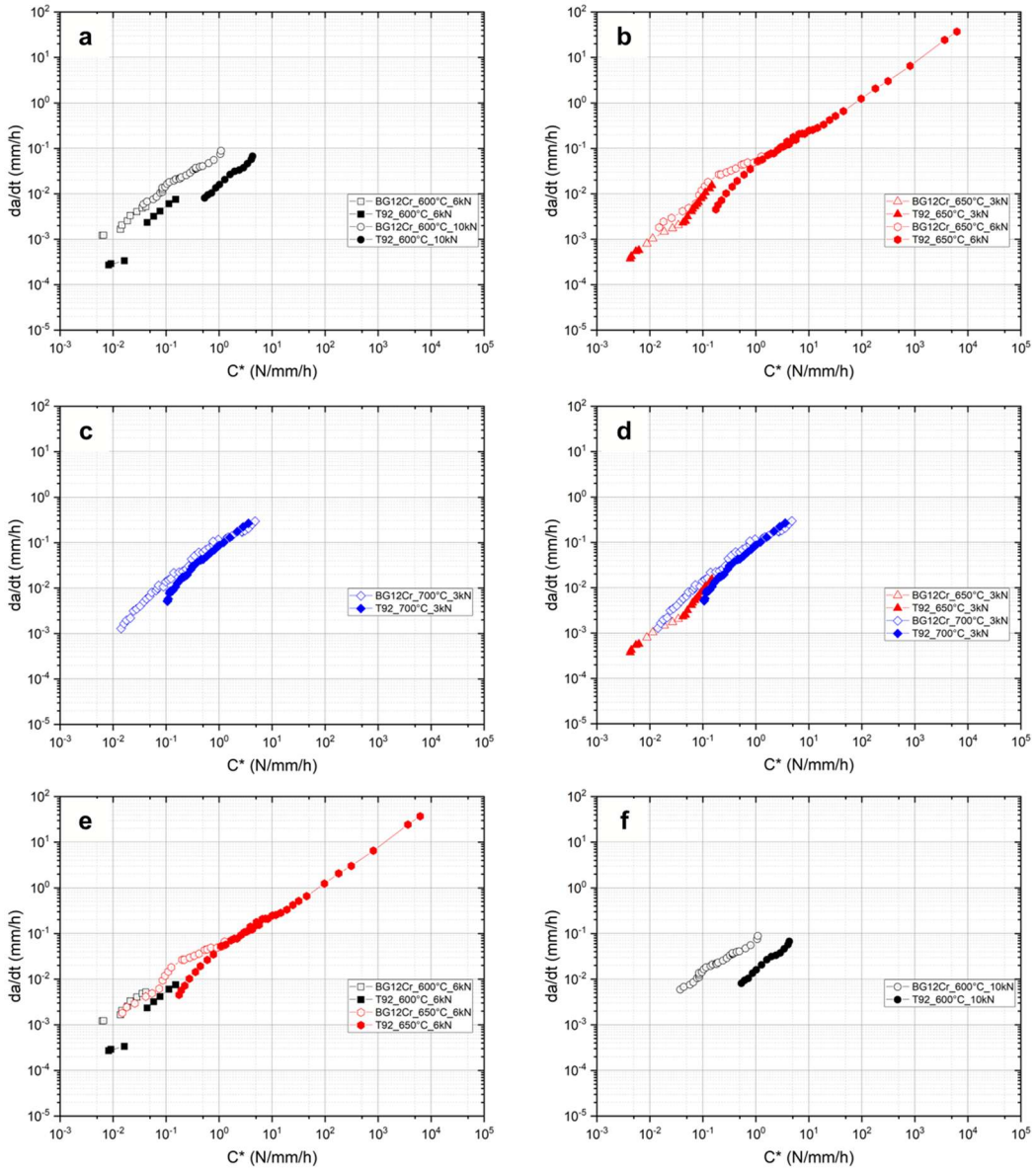

Figure 5. 13 Creep crack growth resistant curves of T92 and the BG12Cr tested in the form of da/dt – C*:a) 600°C, b) 650°C, c) 700°C, d) 3kN, e) 6kN, f) 10kN.

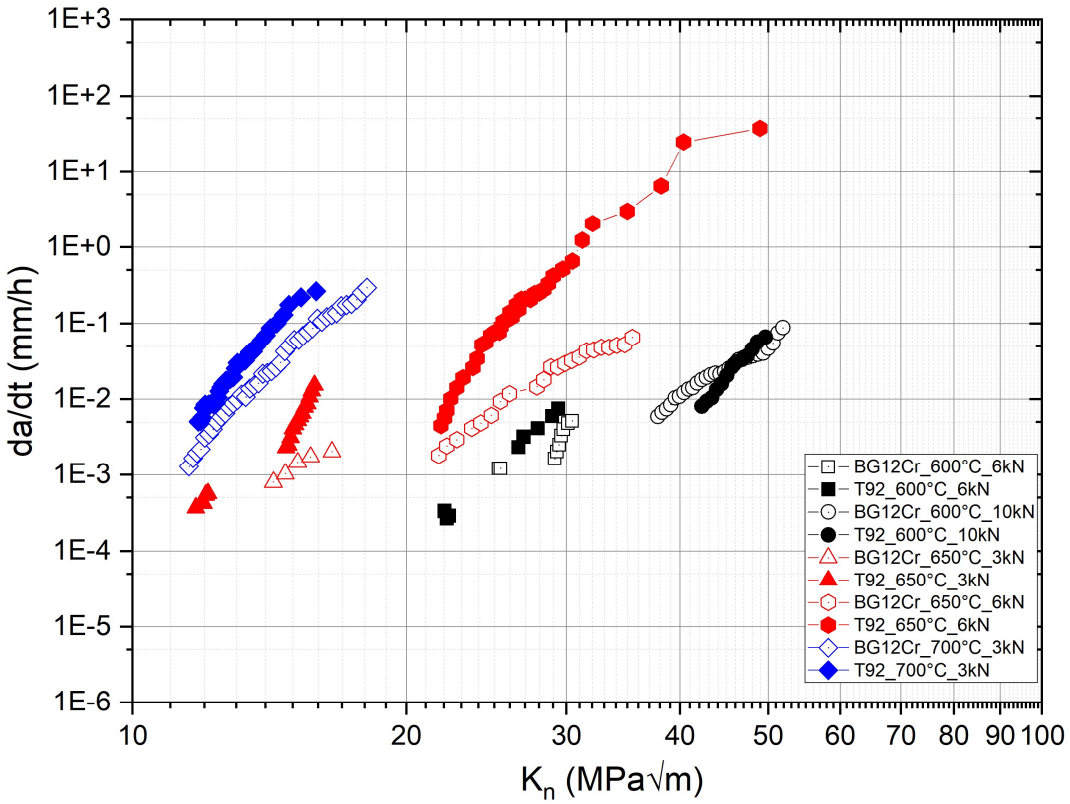

Figure 5. 14 Crack growth resistant curves of T92 and the BG12Cr tested in the form of $da/dt - K_n$.

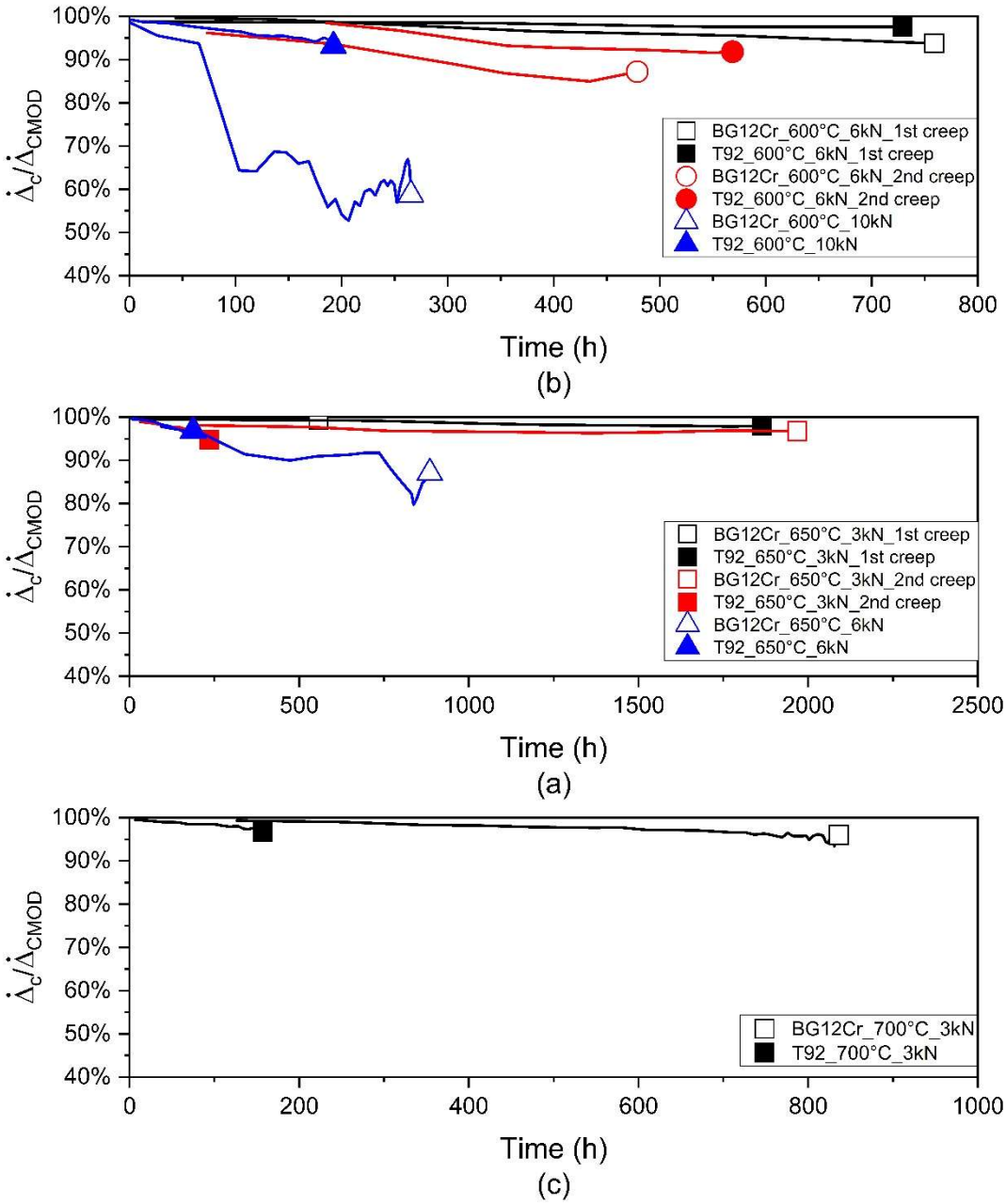

Figure 5. 15 Calculated proportion of creep-induced time-dependent CMOD rates ($\dot{\Delta}_c$) within the total CMOD rates ($\dot{\Delta}$) during testing.

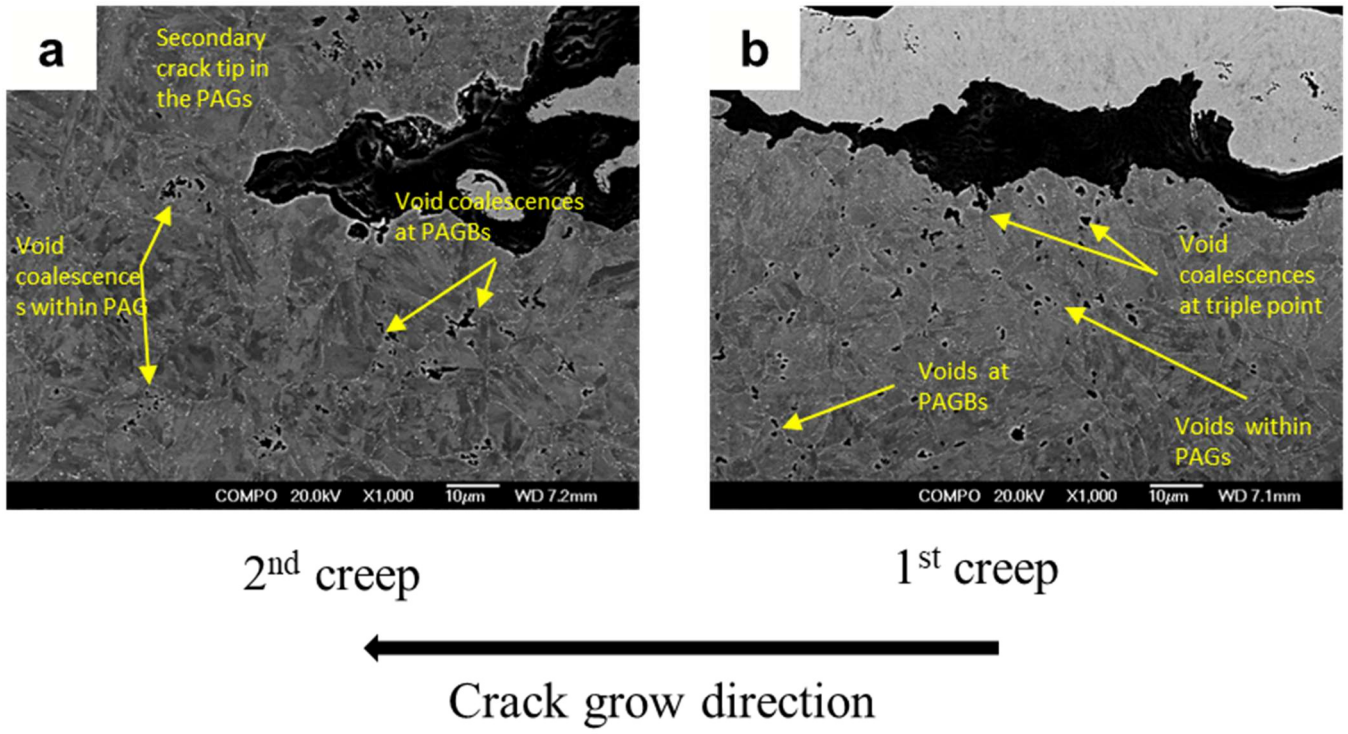

Figure 5. 16 Backscatter electron images of the cross-section views for creep crack growth regions on T92 at 600°C with the loading of 6kN on T92: a) 2nd creep region (K_n=26.5 MPa√m, C*=4.02E-02 N/mm/h), b) 1st creep region (Kn=21.7 MPa√m, C*=2.55E-01 N/mm/h).

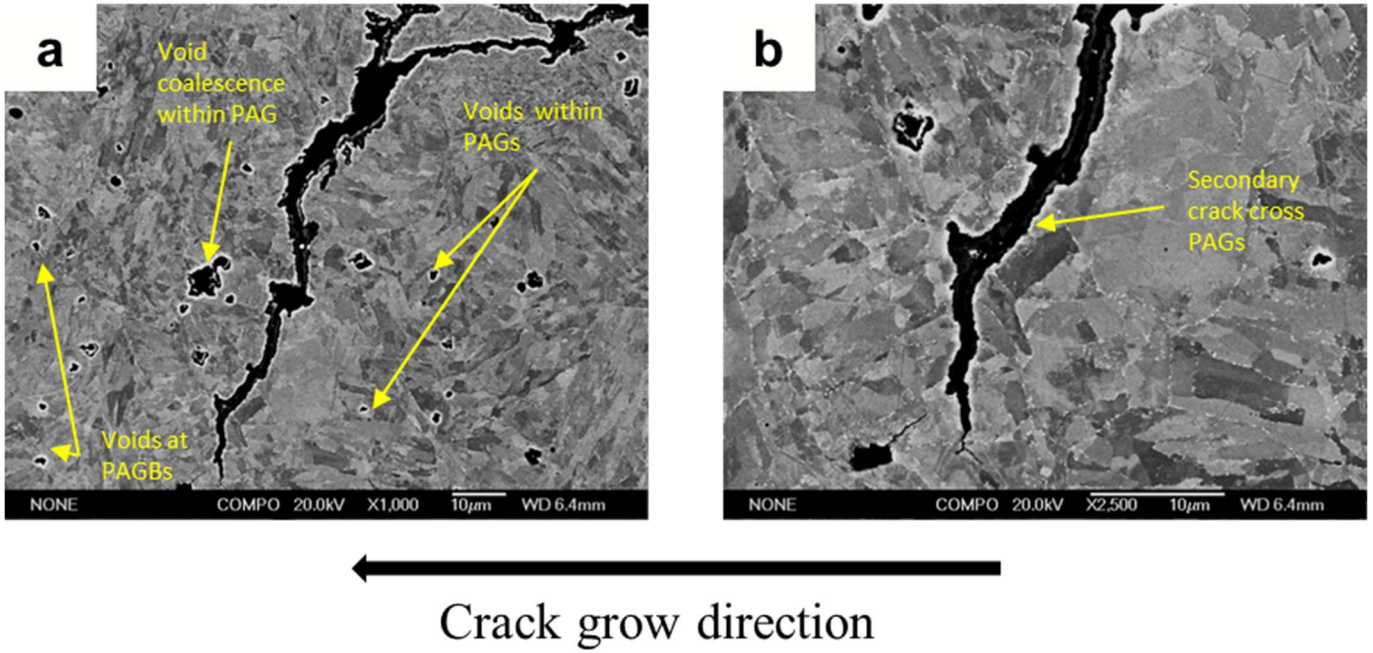

Figure 5. 17 Backscatter electron images of the cross-section views for creep crack growth regions on T92 at 600°C with the loading of 10kN: a) Low magnification image, b) High magnification image(K_n=47.4 MPa√m, C*=2.61E+00 N/mm/h).

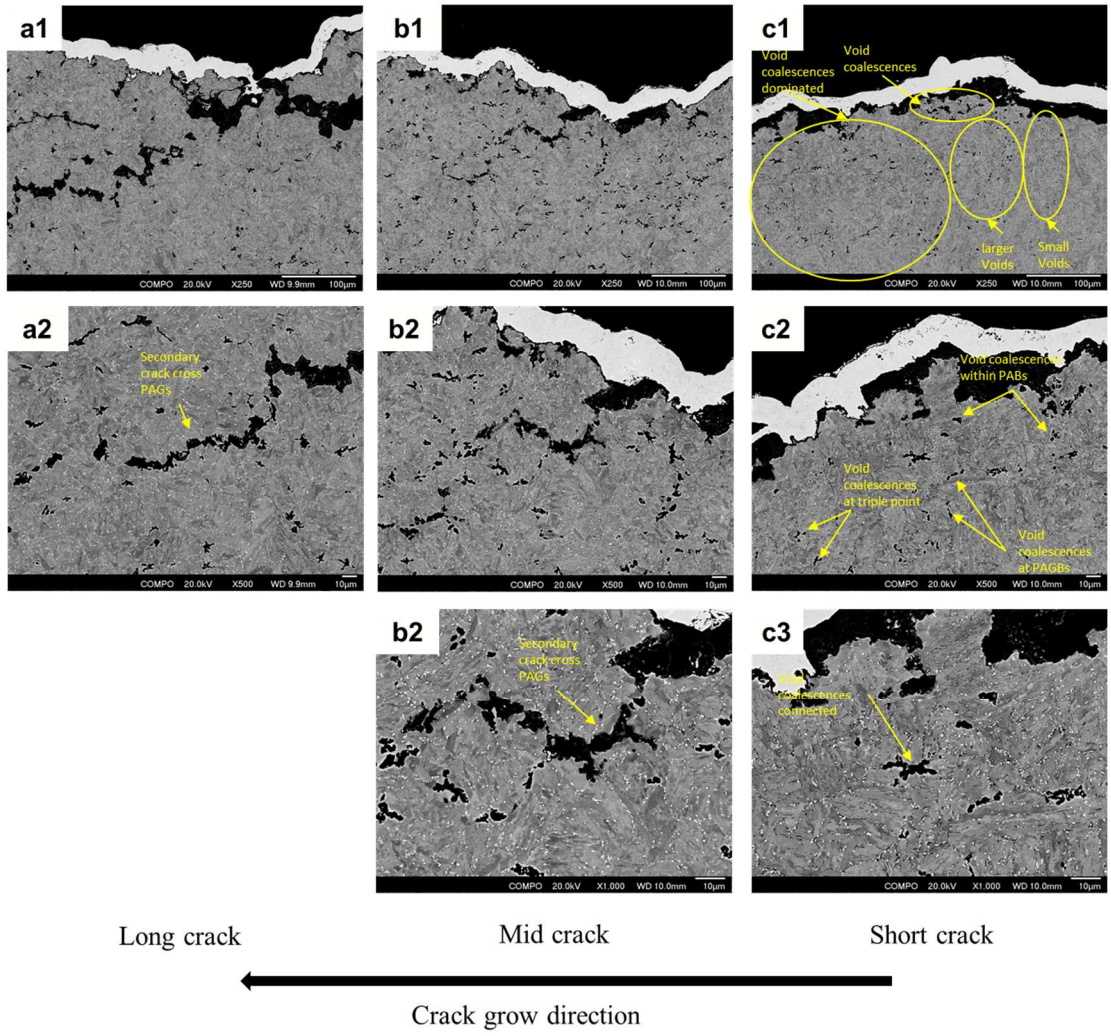

Figure 5. 18 Backscatter electron images of the cross-section views for creep crack growth regions on T92 tested at 650°C with 3kN: (a) Long crack of 2^{nd} creep (1)250x (2) 500x (3)1000x (K_n=15.7 MPa√m, C*=1.3E-02 N/mm/h), (b) Mid crack of 2^{nd} creep (1)250x (2) 500x (3)1000x(K_n=15.2 MPa√m, C*=7.11E-02 N/mm/h), (c) Short crack of 2^{nd} creep (1)250x (2) 500x (K_n=14.8 MPa√m, C*=4.71E-03 N/mm/h).

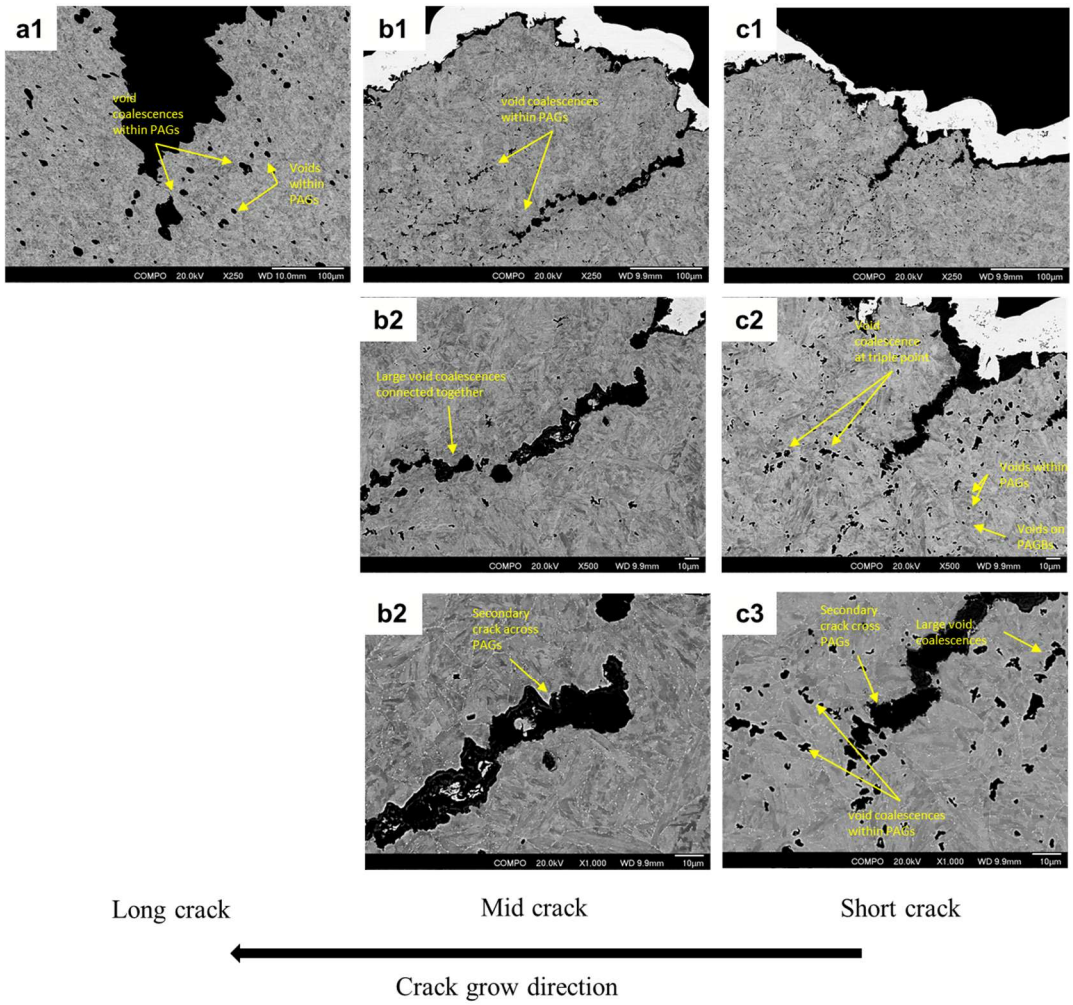

Figure 5. 19 Backscatter electron images of the cross-section views for creep crack growth regions on T92 tested at 650°C with 6kN: (a) Long crack of creep region (1)250x (2) 500x (3)1000x (K_n=38.1 MPa√m, C*=9.29E+02 N/mm/h), (b) Midcrack of creep region (1)250x (2) 500x (3)1000x (K_n=25.7 MPa√m, C*=3.72E+00 N/mm/h), (c) Short crack of creep region (1)250x (K_n=21.4 MPa√m, C*=3.42E-01 N/mm/h).

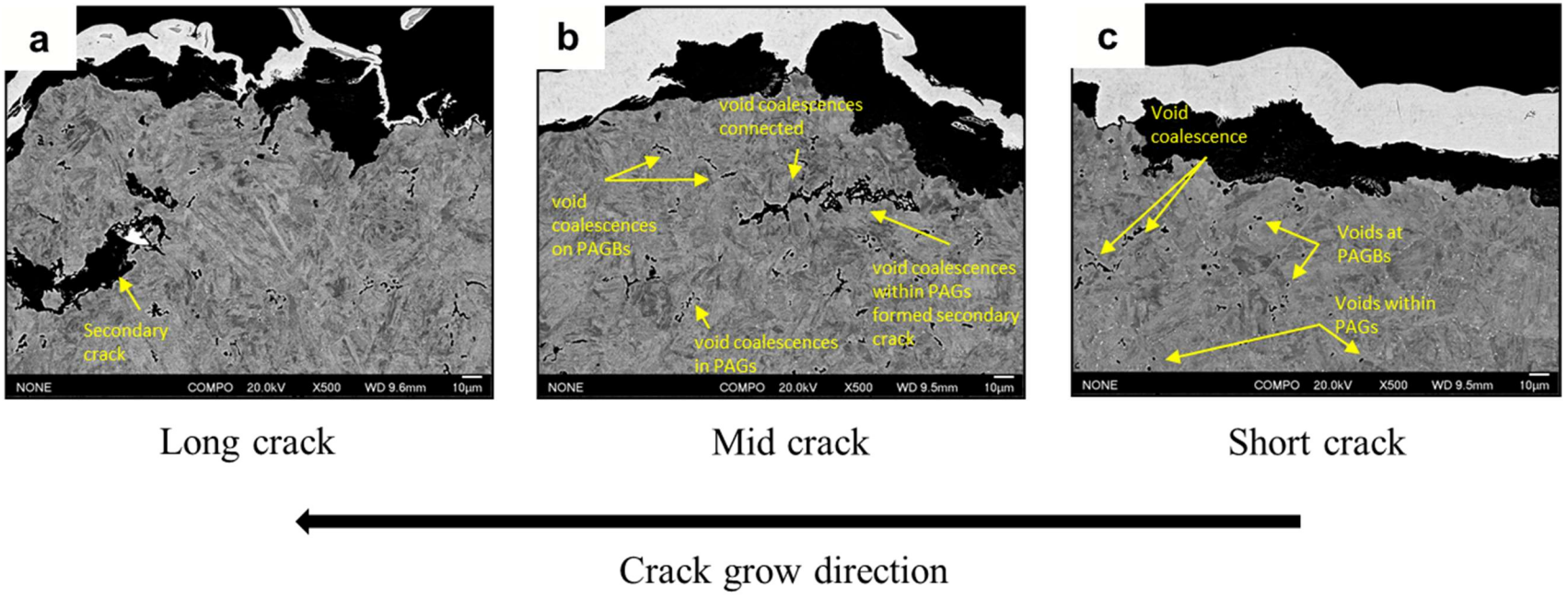

Figure 5. 20 Backscatter electron images of the cross-section views for creep crack growth regions on T92 tested at 700°C with 3 kN: (a) Long crack of creep region(K_n=13 MPa√m, C*=3.71E-01 N/mm/h), (b) mid crack of creep region (K_n=12.1 MPa√m , C*=1.46E-01 N/mm/h), (c) short crack of creep region (K_n=11.6 MPa√m, C*=7.72E-03 N/mm/h).

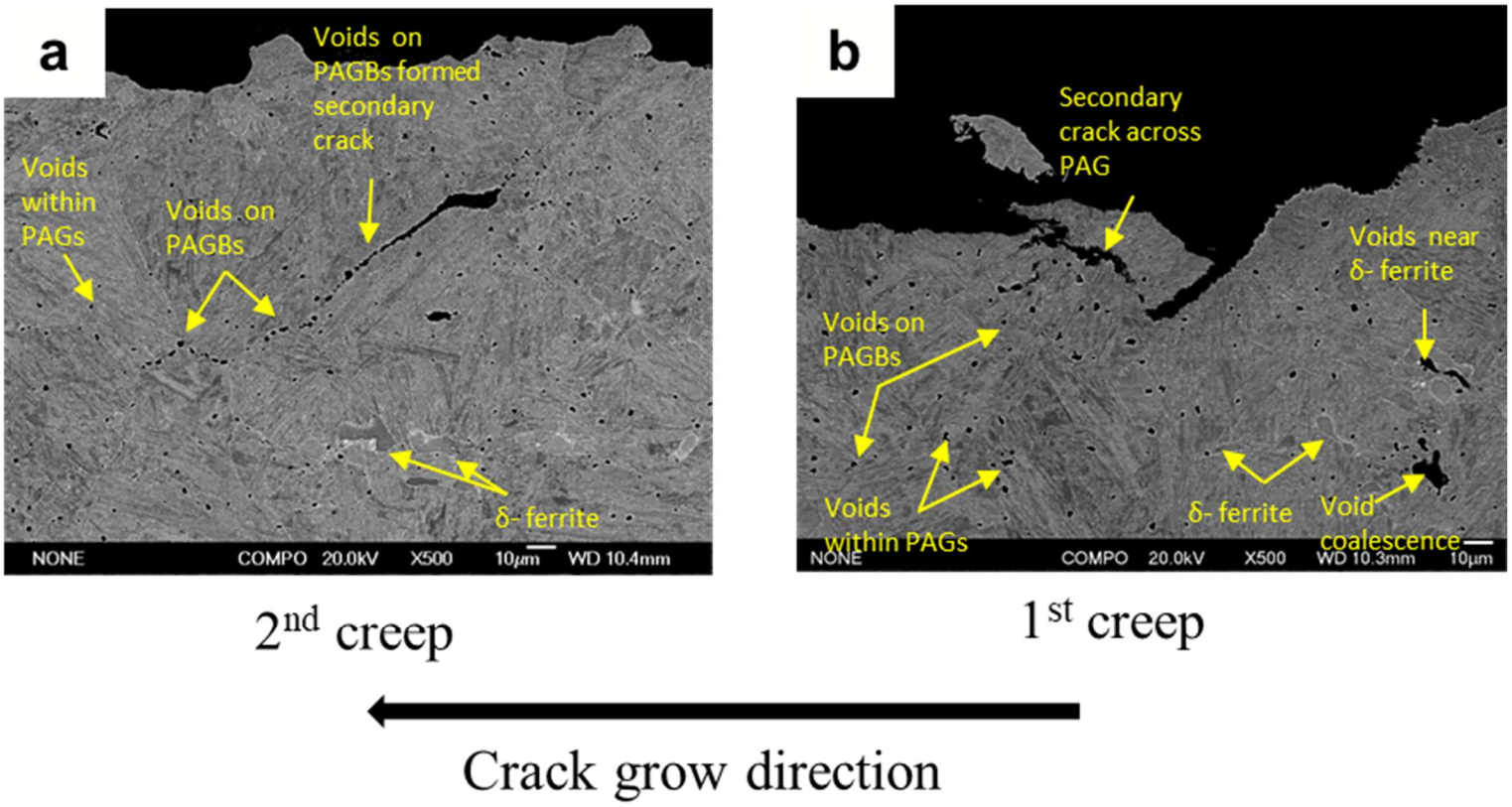

Figure 5. 21 Backscatter electron images of the cross-section views for creep crack growth regions on BG12Cr tested at 600°C with 6 kN: (a) 2nd creep region (K_n=28.7 MPa√m, C*=4.93E-01 N/mm/h). (b) 1st creep region (Kn=23.9 MPa√m, C*=6.9E-03 N/mm/h).

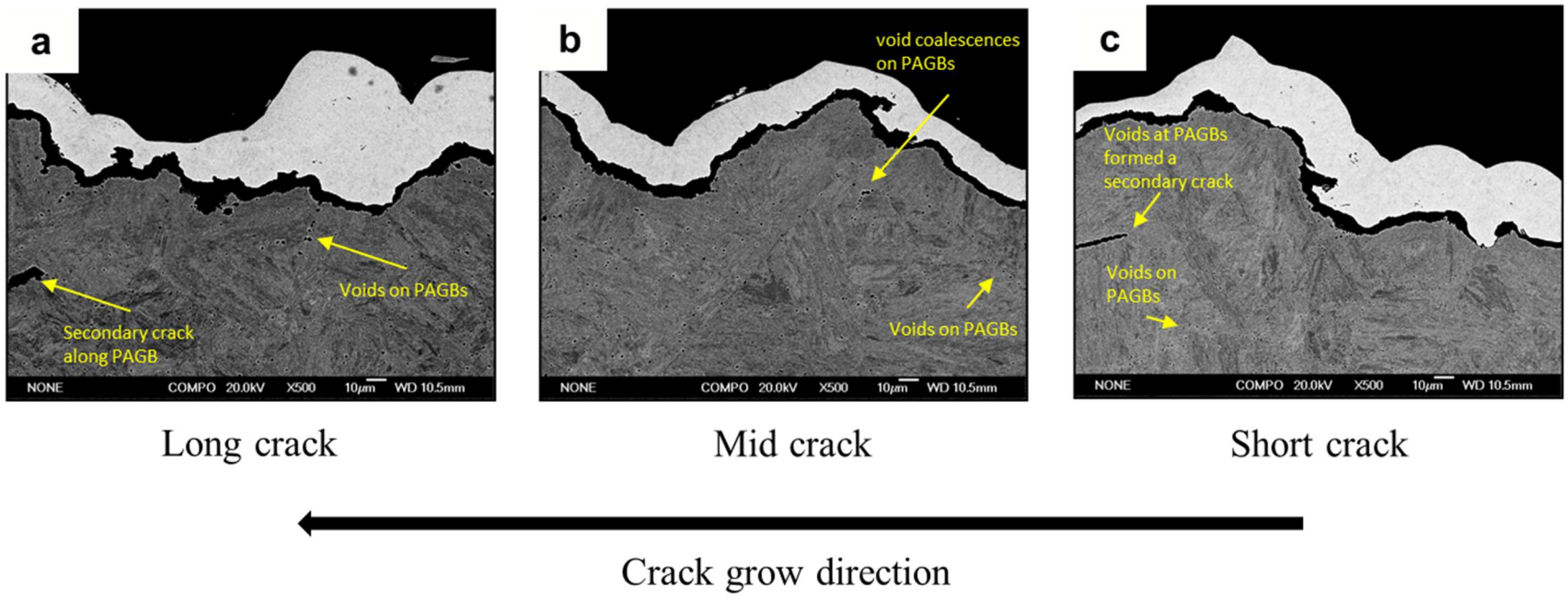

Figure 5. 22 Backscatter electron images of the cross-section views for creep crack growth regions on BG12Cr tested at 600°C with 10kN: (a) Long crack of creep region(K_n=43.7 MPa√m, C*=1.87E-01 N/mm/h), (b) Mid crack of creep region(K_n=40.9 MPa√m,C*=8.92E-03 N/mm/h), (c) Short crack of creep region (K_n=37.0 MPa√m, C*=1.28E-01 N/mm/h).

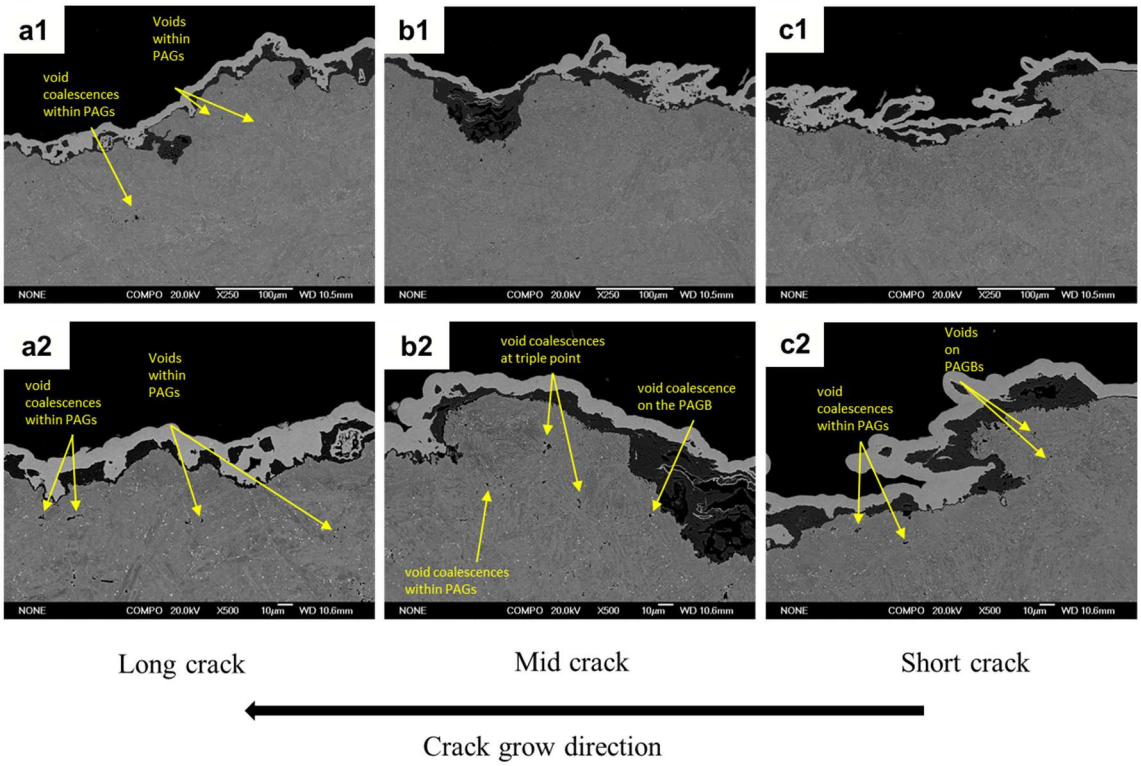

Figure 5. 23 Backscatter electron images of the cross-section views for creep crack growth regions on BG12Cr tested at 650°C with 3kN: (a) Long crack of 2nd creep region, (1)250x, (2) 500x (K_n=15.8 MPa√m, C*= 2.49E-02 N/mm/h), (b) Mid crack of 2nd creep region, (1)250x, (2)500x (K_n=15.0 MPa√m, C*=1.15E-02 N/mm/h), (c) Short crack of 2nd creep region, (1)250x, (2)500x (K_n=14.3 MPa√m, C*=8.18E-03 N/mm/h).

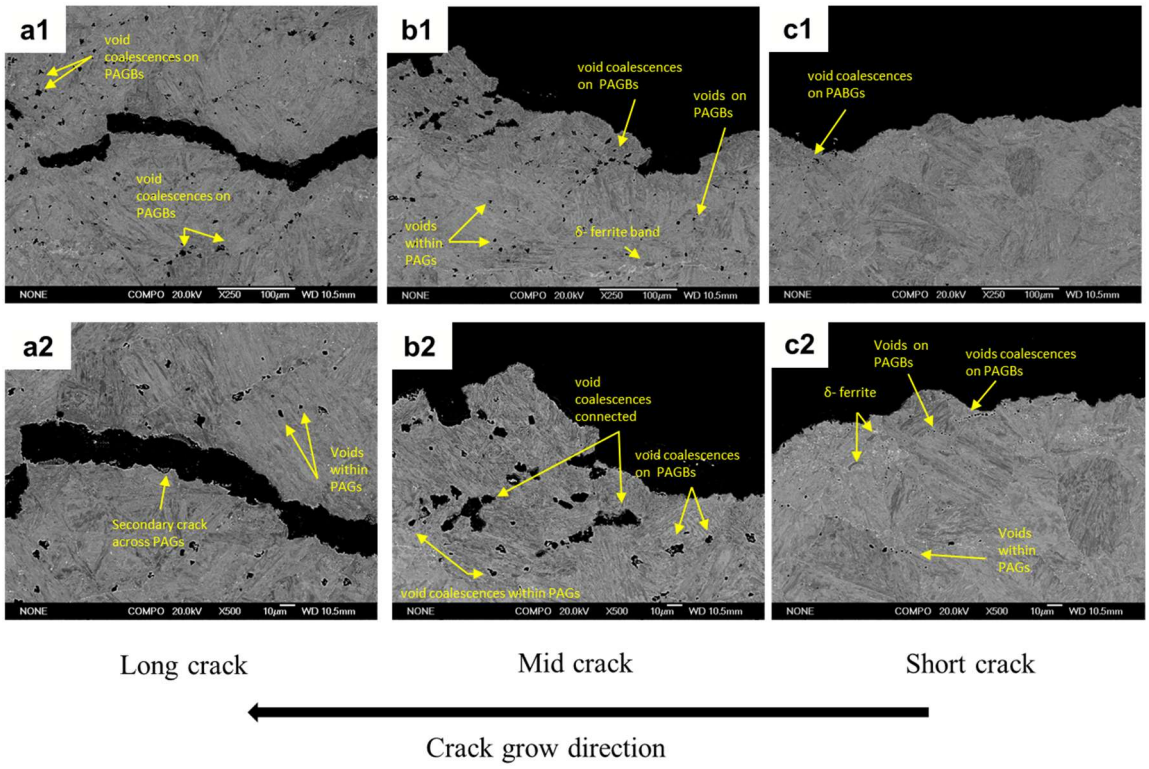

Figure 5. 24 Backscatter electron images of the cross-section views for creep crack growth regions on BG12Cr tested at 650°C with 6kN: a) Long crack of creep region, (1)250x, (2) 500x (K_n=30.4 MPa√m, C*=3.66E-01 N/mm/h), b) Mid crack of creep region, (1)250x, (2) 500x (K_n=26.0 MPa√m, C*=1.03E-01 N/mm/h), c) Short crack of creep region, (1)250x, (2) 500x (K_n=20.9 MPa√m, C*=5.07E-02 N/mm/h).

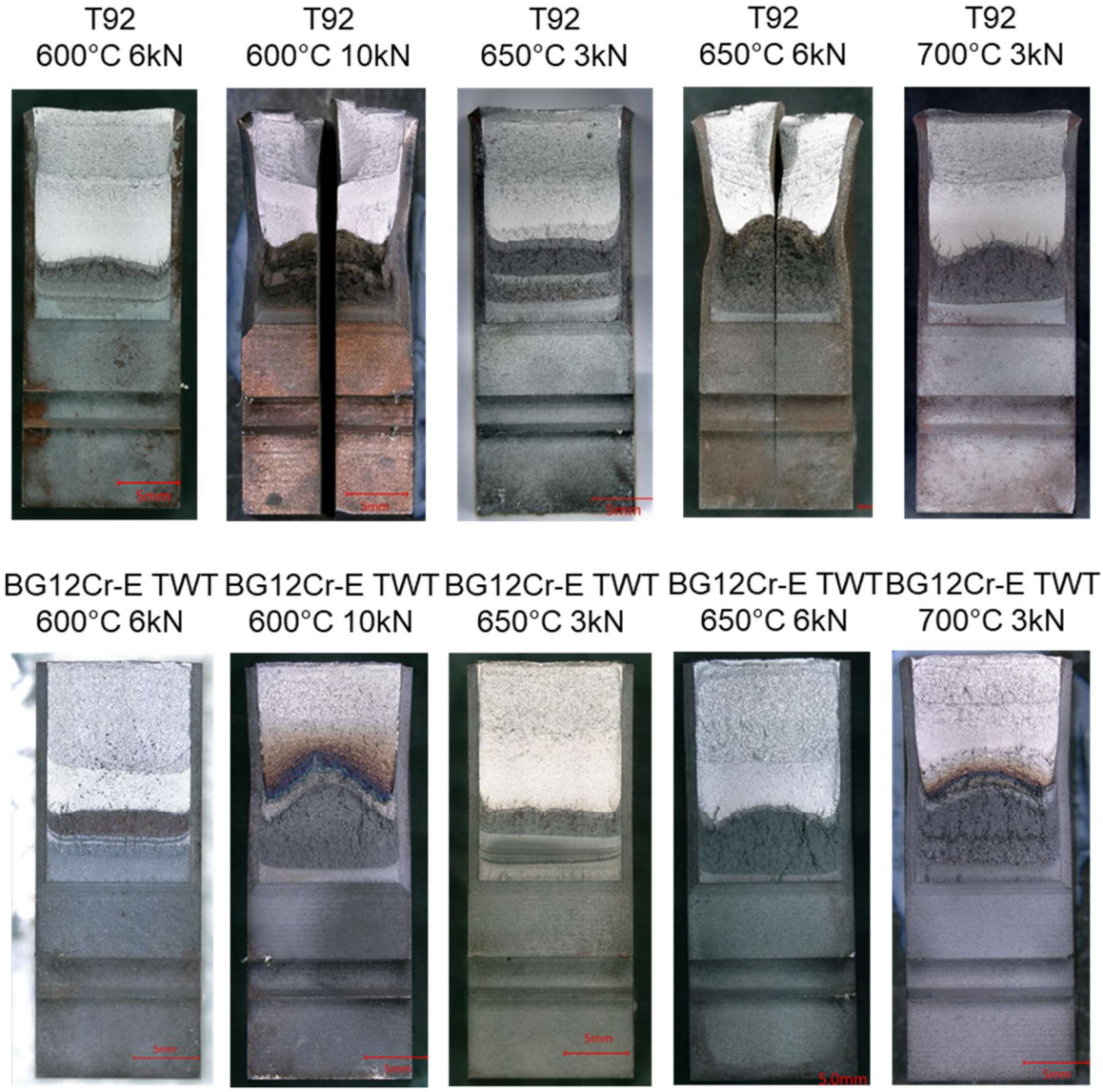

Figure 5. 25 Optical fractography of BG12Cr and T92 testpiece after creep crack growth tests.

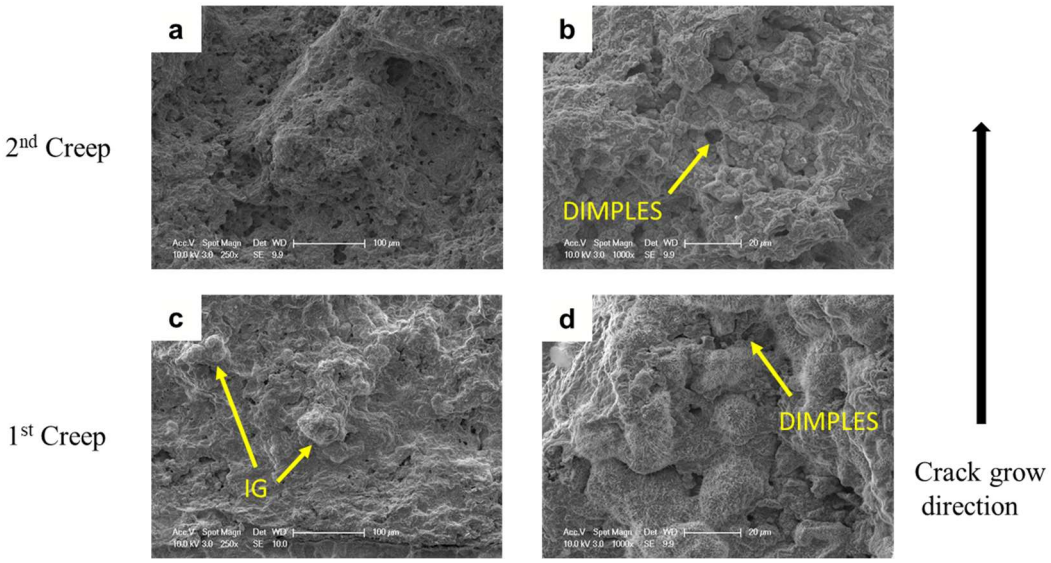

Figure 5. 26 Representative SEM fractography of creep crack regions tested at 600°C with the loading of 6 kN on T92: a) 2nd creep region, low magnification image, b) 2nd creep region (K_n=28.9 MPa√m, C*=8.39E-02 N/mm/h), high magnification image, c) 1st creep region, low magnification image, d) 1st creep region(K_n=21.9 MPa√m, C*=1.97E-02 N/mm/h), high magnification image.

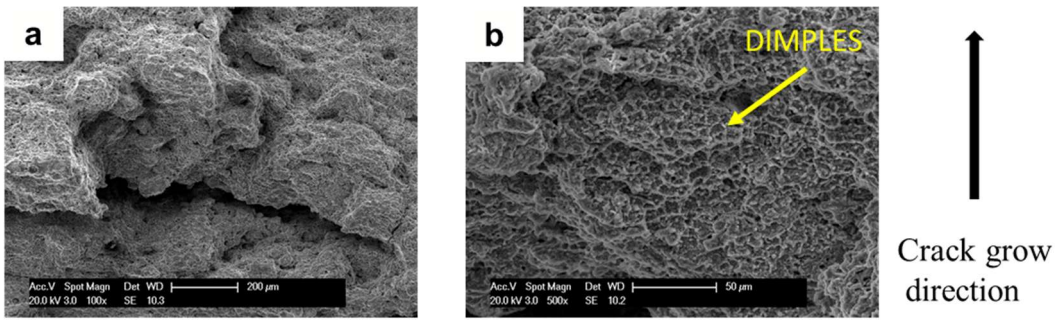

Figure 5. 27 Representative SEM fractography of creep crack regions tested at 600°C with the loading of 10 kN on T92: a) Low magnification image, b) High magnification image (K_n=42 MPa√m, C*=5.29E-01 N/mm/h).

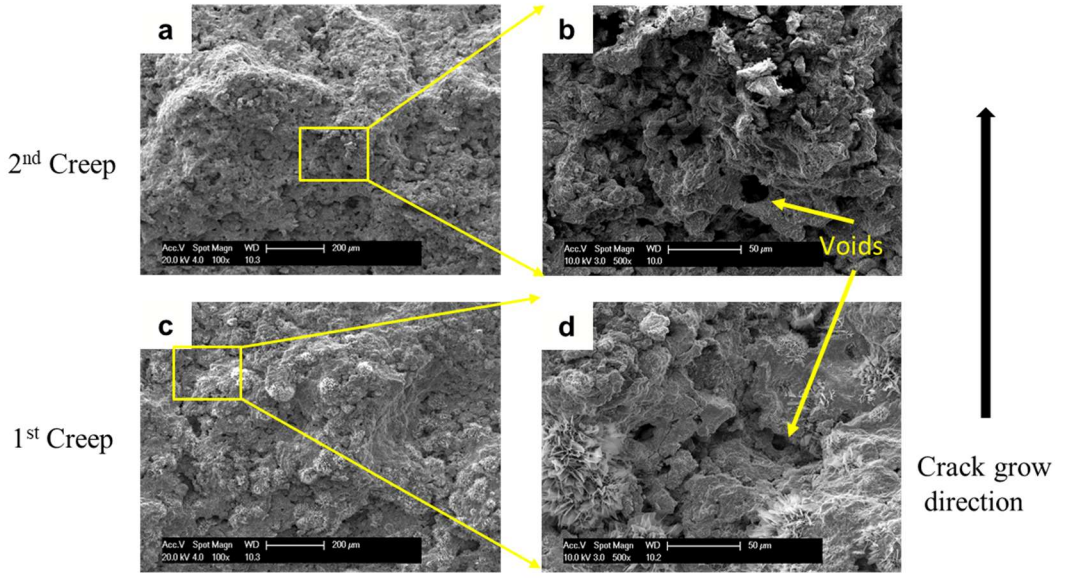

Figure 5. 28 Representative SEM fractography of creep crack regions tested at 650°C with the loading of 3 kN on T92: a) 2nd creep region, low magnification image, b) 2nd creep region (K_n=15.6 MPa√m, C*=1.01E-01 N/mm/h), high magnification image, c) 1st creep region, low magnification image, d) 1st creep region (K_n=12.1 MPa√m, C*=5.35E-04 N/mm/h), high magnification image.

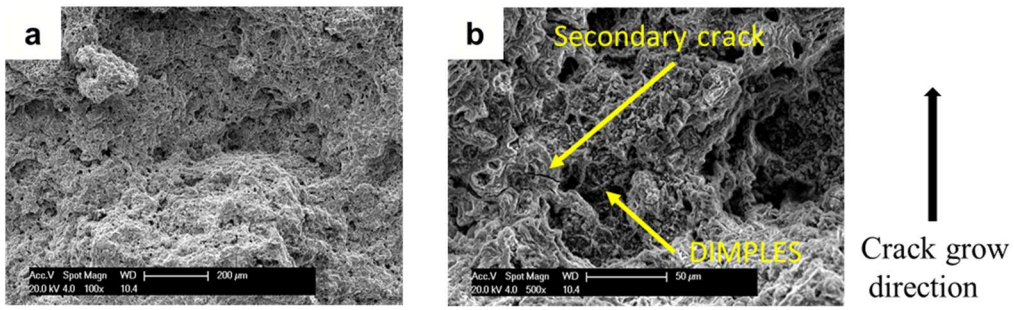

Figure 5. 29 Representative SEM fractography of creep crack regions tested at 650°C with the loading of 6kN on T92: a) low magnification image, b) high magnification image(K_n=22.6 MPa√m, C*=3.61E-01 N/mm/h).

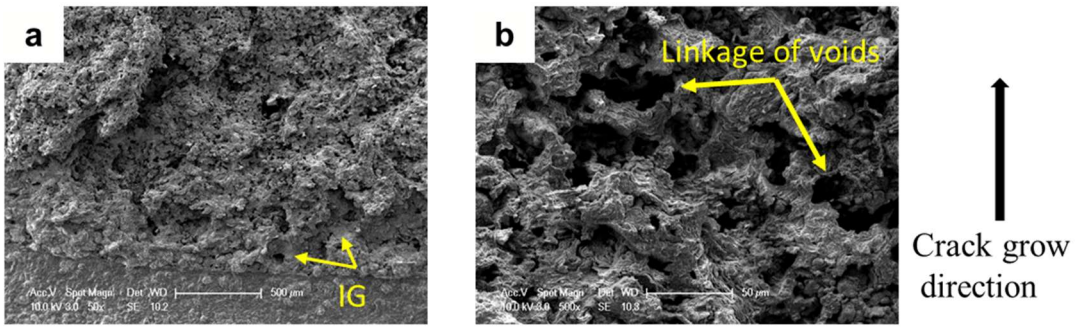

Figure 5. 30 Representative SEM fractography of creep crack regions tested at 700°C with the loading of 3kN on T92: a) low magnification image, b) high magnification image (K_n=14.2 MPa√m,C*=1.19 N/mm/h).

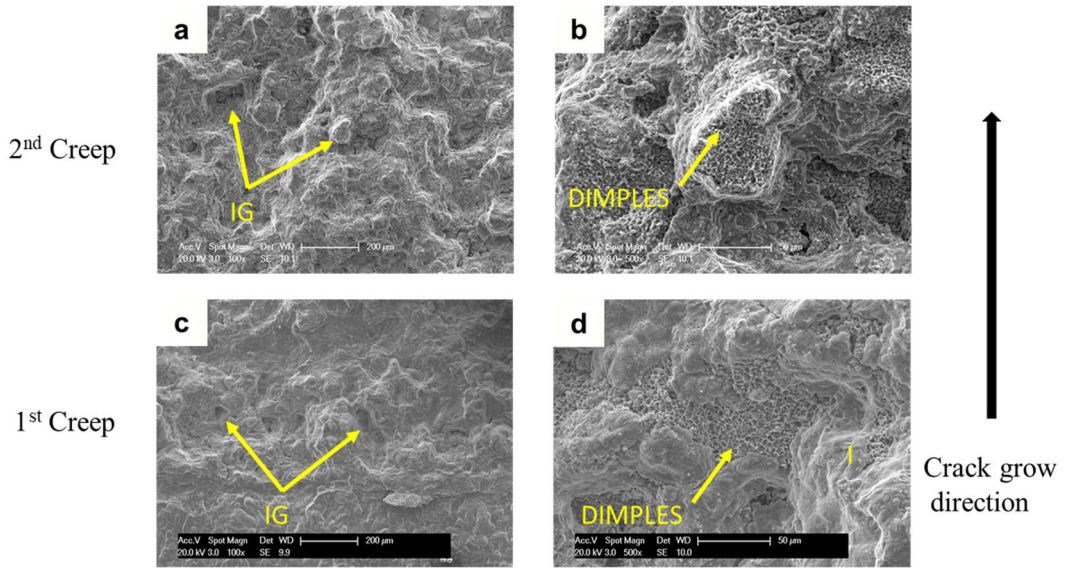

Figure 5. 31 Representative SEM fractography of creep crack regions tested at 600°C with the loading of 6 kN on BG12Cr: a) 2nd creep region, low magnification image, b) 2nd creep region (K_n=28.7 MPa√m, C*=4.93E-03 N/mm/h), high magnification image, c) 1st creep region, low magnification image, d) 1st creep region(K_n=24.2 MPa√m, C*=3.97E-03 N/mm/h), high magnification image.

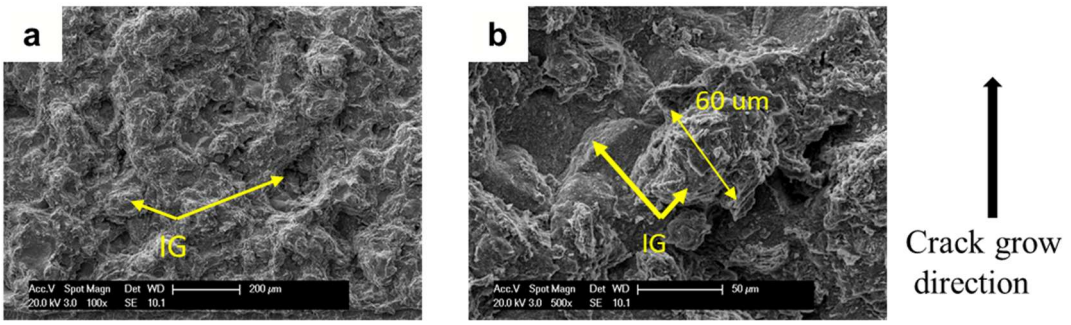

Figure 5. 32 Representative SEM fractography of creep crack regions tested at 600°C with the loading of 10 kN on BG12Cr: a) low magnification image, b) high magnification image(K_n=38.2 MPa√m, C*=4.60E-02 N/mm/h).

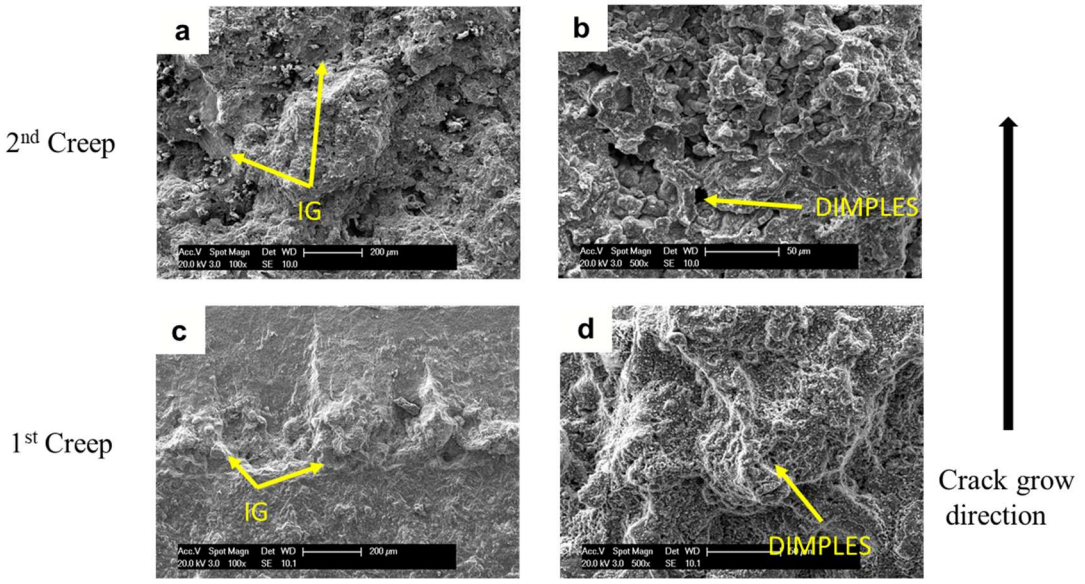

Figure 5. 33 Representative SEM fractography of creep crack regions tested at 650°C with the loading of 3kN on BG12Cr: a) 2nd creep region, low magnification image, b) 2nd creep region(K_n=10.9 MPa√m, C*=3.60E-02 N/mm/h), high magnification image, c) 1st creep region, low magnification image, d) 1st creep region(K_n=10.9 MPa√m, C*=3.60E-02 N/mm/h), high magnification.

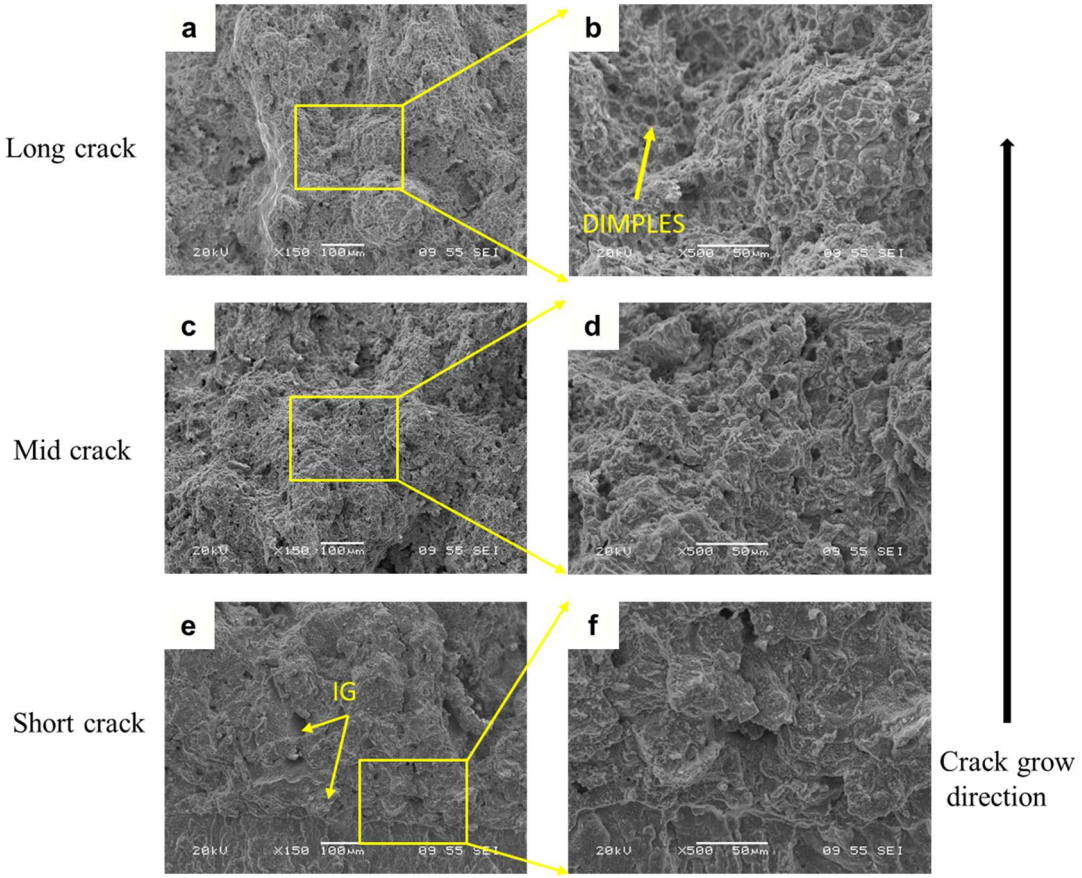

Figure 5. 34 Representative SEM fractography of creep crack regions tested at 650°C with the loading of 6 kN on BG12Cr: a) Long crack region, low magnification image, b) Short creep region (K_n=32.1 MPa√m, C*=6.41E-01 N/mm/h), high magnification image, c) Middle crack region, low magnification image, d) Middle crack region (K_n=26.8 MPa√m, C*=1.13E-01 N/mm/h), high magnification image, e) Short crack region, low magnification image, f) Short crack region(K_n=20.9 MPa√m, C*=5.07E-02 N/mm/h), high magnification image.

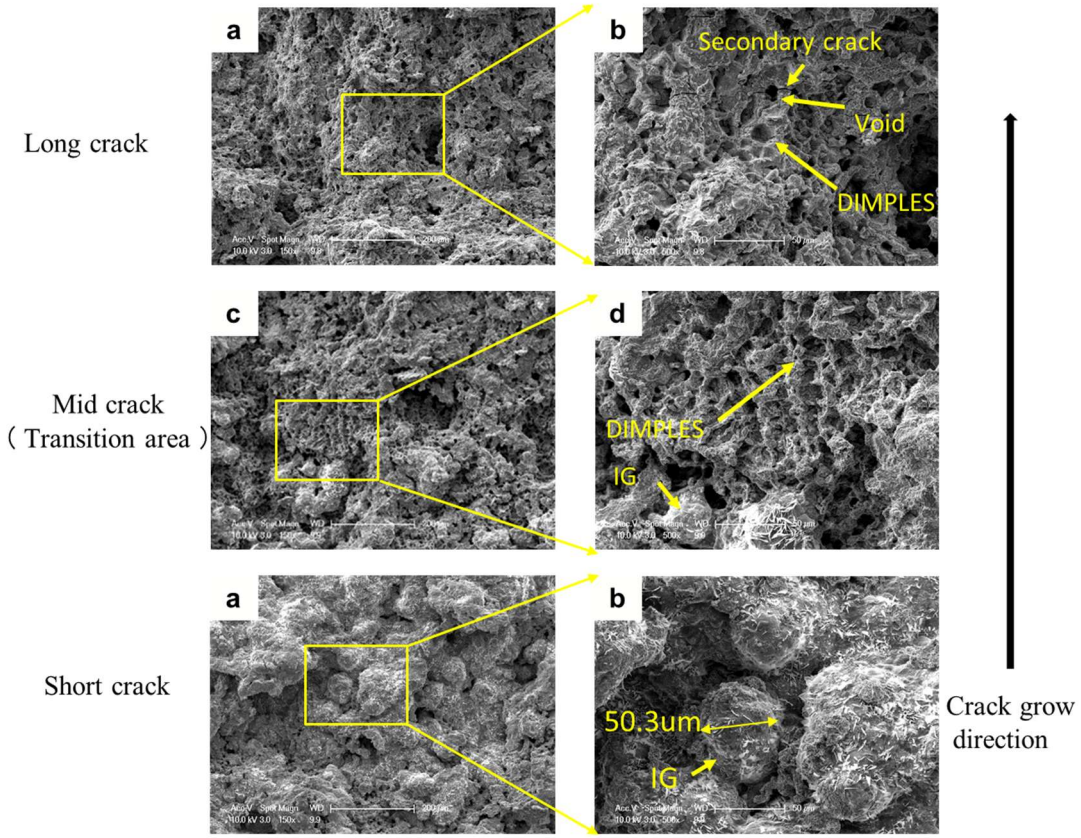

Figure 5. 35 Representative SEM fractography of creep crack regions tested at 700°C with the loading of 3 kN on BG12Cr: a) Long creep region, low magnification image, b) Long creep region(K_n=15.4 MPa√m, C*=4.61E-01 N/mm/h), high magnification image, c) Middle creep region, low magnification image, d) Middle creep region (K_n=13.4 MPa√m, C*=7.71E-02 N/mm/h), high magnification image, e) Short creep region, low magnification image, f) Short creep region(K_n=12.9 MPa√m, C*=4.81E-02 N/mm/h), high magnification image.

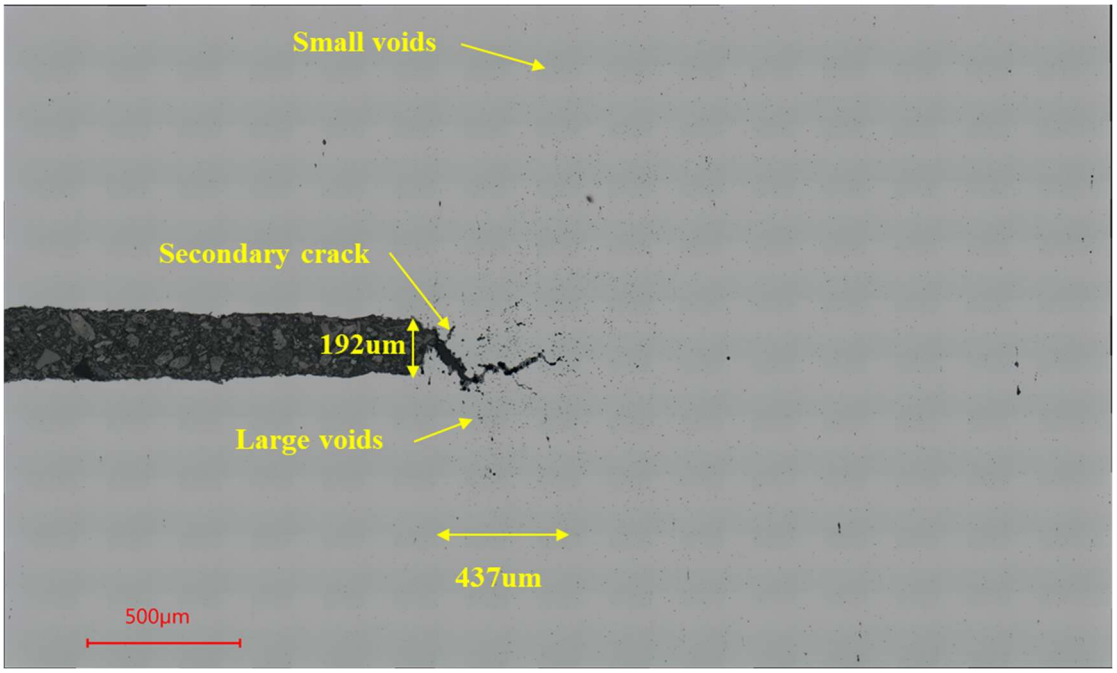

Figure 5. 36 Optical image shows the unbroken crack of the interrupted test on T92.

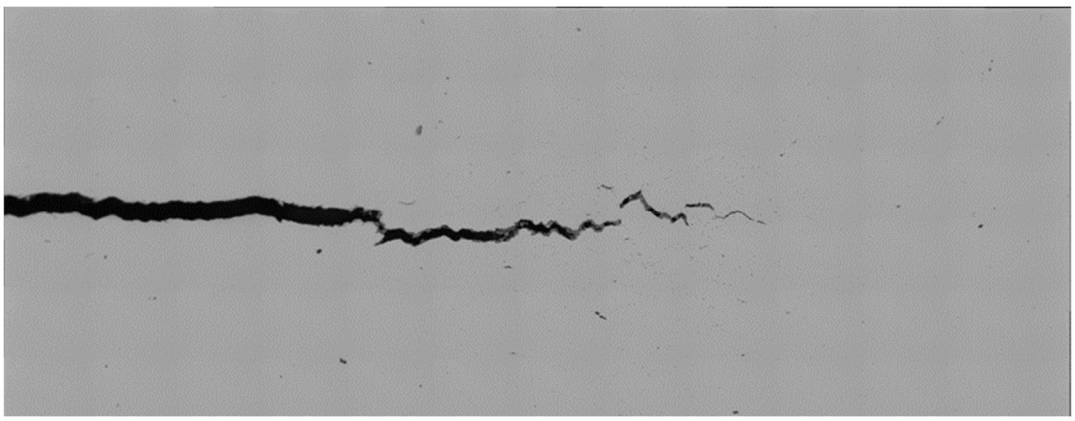

Figure 5. 37 Optical image shows the unbroken crack of interrupted test on BG12Cr.

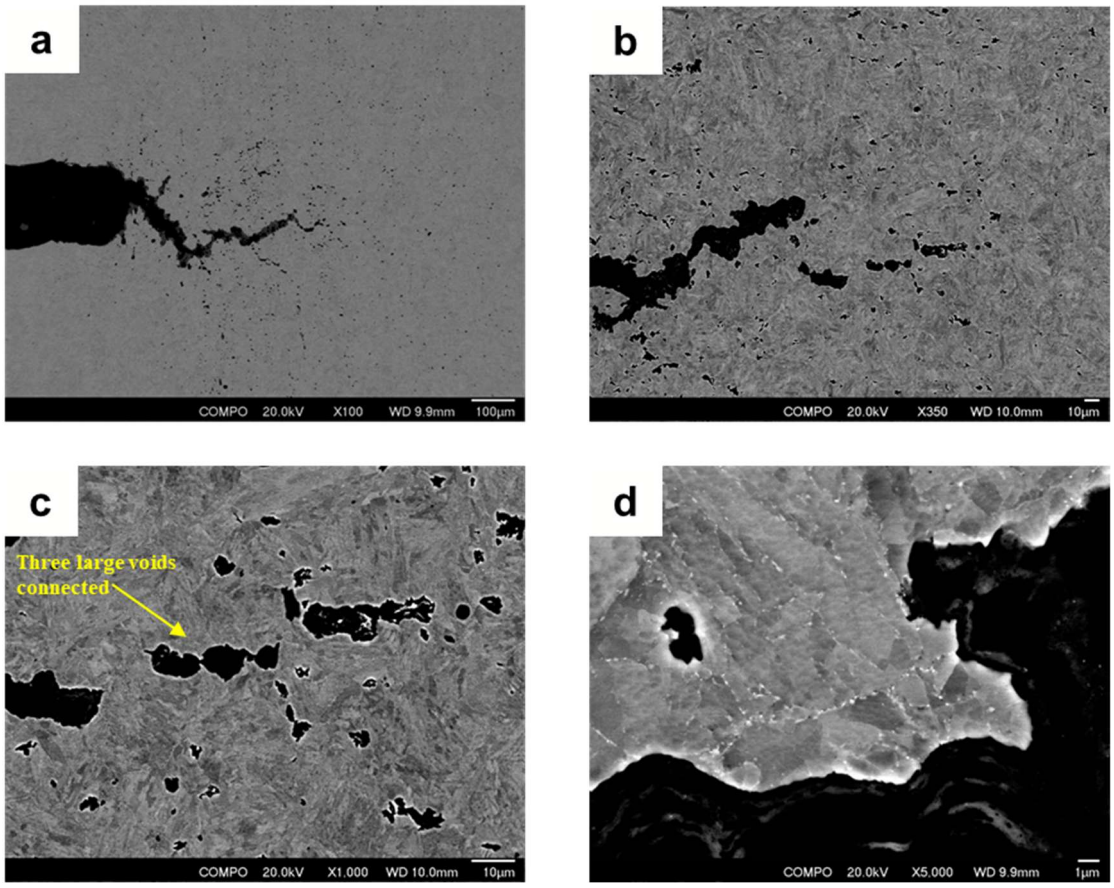

Figure 5. 38 SEM image and backscatter image show unbroken crack of interrupted test on T92: a) 100x, b) 350x, c)1000x, d)5000x. K_n=22.0 MPa√m at crack tip.

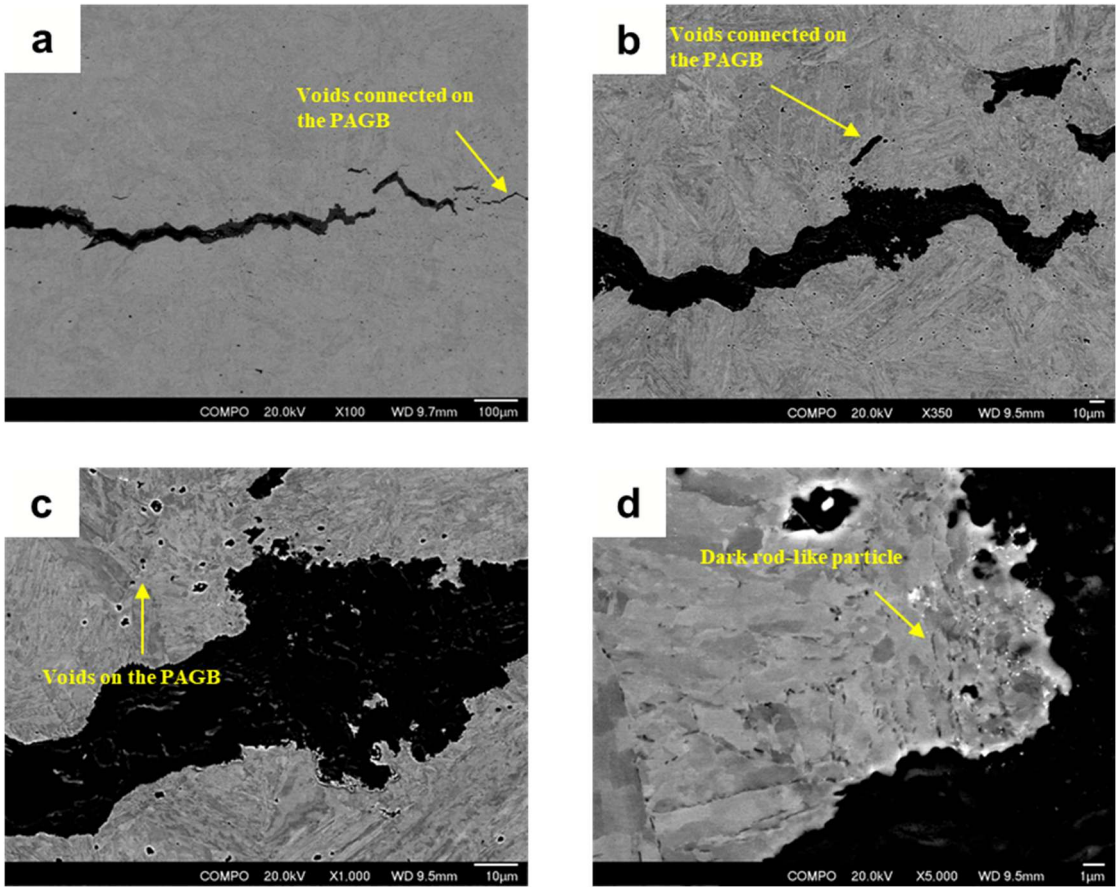

Figure 5. 39 SEM image and backscatter image show unbroken crack of interrupted test on BG12Cr: a) 100x, b) 350x, c)1000x, d)5000x. K_n=24.8 MPa√m at crack tip.

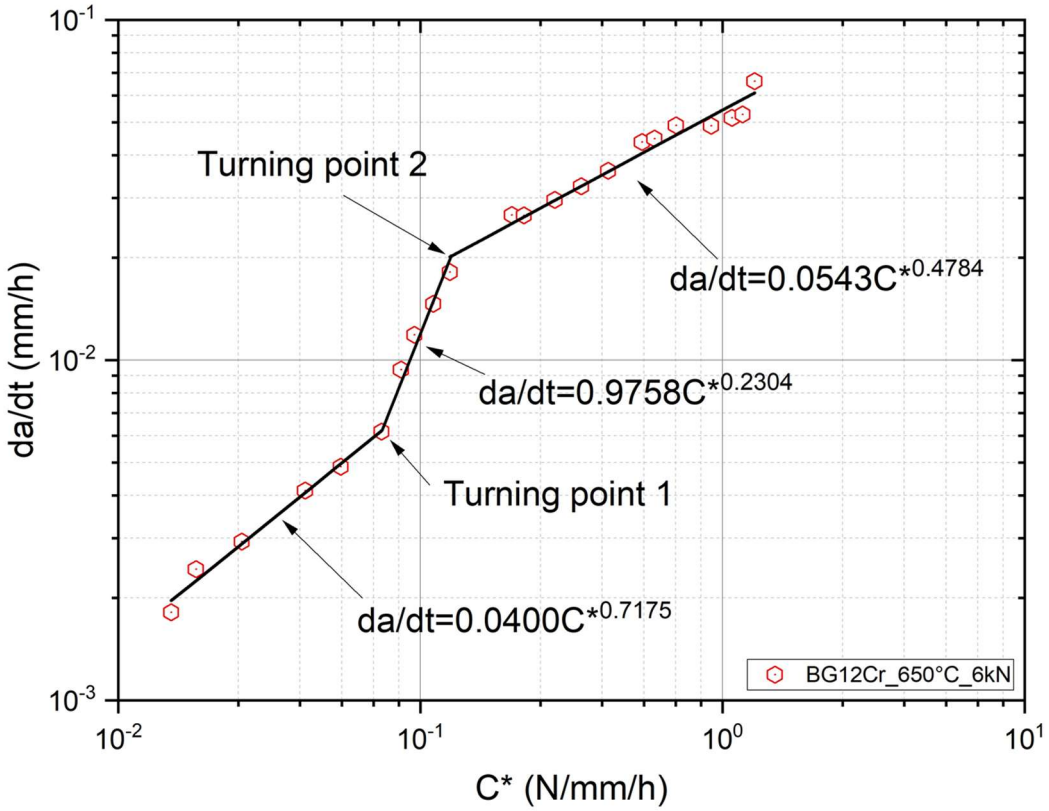

Figure 6. 1 The detailed C*-da/dt curves of BG12Cr 650 6kN.

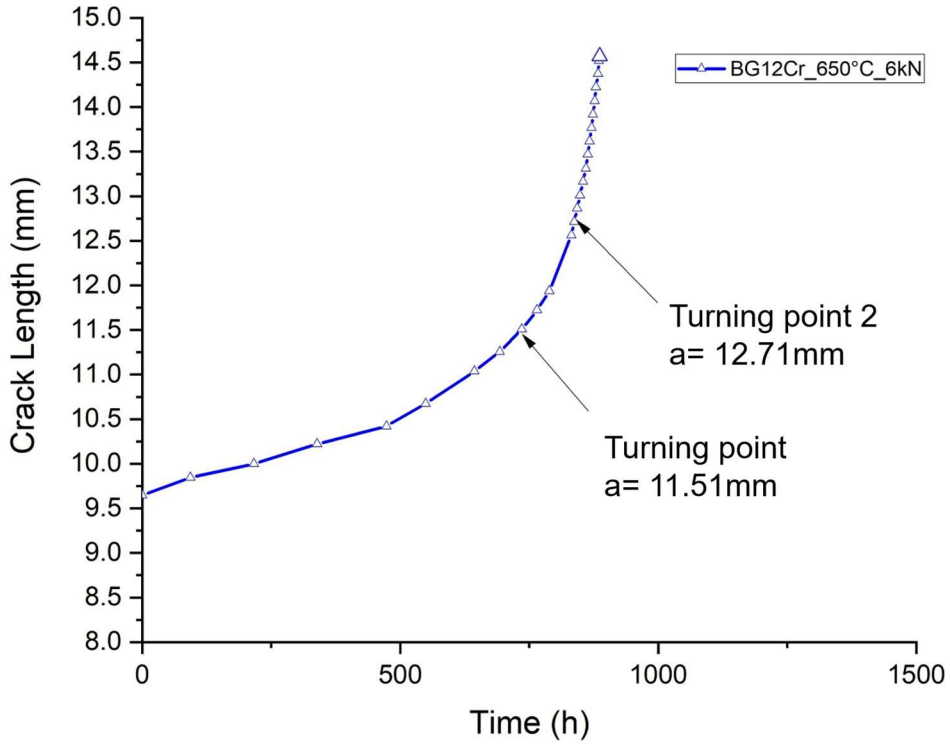

Figure 6. 2 The turning points on the crack length curves of BG12Cr 650 6kN.